Technische Universität München
TUM School of Computation, Information and Technology

Energy-selective processing of CT images for clinical applications

Ralf Steffen Gutjahr

Vollständiger Abdruck der von der TUM School of Computation, Information and Technology der Technischen Universität München zur Erlangung des akademischen Grades eines

Doktors der Naturwissenschaften (Dr. rer. nat.)

genehmigten Dissertation.

Vorsitz: Prof. Dr. Darius Burschka

Prüfer der Dissertation: Prof. Dr. Nassir Navab

Prof. Dr. Andreas H. Mahnken

Prof. Dr. Thomas G. Flohr

Die Dissertation wurde am 29.11.2023 bei der Technischen Universität München eingereicht und durch die TUM School of Computation, Information and Technology am 29.04.2024 angenommen.

Computer Aided Medical Procedures
Prof. Dr. Nassir Navab

Dissertation

Energy-selective processing of CT images for clinical applications

Ralf Steffen Gutjahr

TUM School of Computation,
Information and Technology
Technische Universität München

Ralf Steffen Gutjahr
Energy-selective processing of CT images for clinical applications
Technische Universität München
TUM School of Computation, Information and Technology
Lehrstuhl für Anwendungen in der Medizin
Boltzmannstraße 3
85748 and Garching bei München

Abstract

Computed Tomography (CT) serves as an essential diagnostic tool in the field of medical imaging, significantly contributing to the accurate detection and assessment of a wide range of medical conditions including trauma, stroke, cancer, pulmonary or vascular diseases. The ability of CT to provide detailed, non-invasive imaging of internal structures has redefined clinical practice. A fact that is also reflected in the documented use of this technology: Since its introduction the number of CT scans performed has experienced a consistent growth, with the total number exceeding 84 million in the United States alone in 2022.

Within CT, spectral imaging is a specialized approach which utilizes material-specific X-ray absorption properties to enable energy-selective image processing techniques. Yet, existing spectral CT scanning techniques come with certain limitations, including increased complexity in use, limits in their spectral sensitivity, restrictions in the measurement's field of view or the acquisition speed. The recent advent of photon counting detectors (PCDs) has introduced a novel spectral CT acquisition method, promising significant advancement in many aspects when compared to previous technologies, including an increase in spatial resolution, and improved radiation dose efficiency.

Yet, being on a rather early stage, thorough (pre-)clinical assessments and comparisons with existing technologies must be conducted. In a second step the practical and unique benefits and possible restrictions that come with PCD CT must be investigated. This includes the transfer of prior findings into the clinical practice. Ultimately, the question about new possible diagnostic applications arises.

This dissertation delves into a comprehensive array of evaluations and clinical studies centered around energy-selective CT imaging. The investigations carried out in this research encompass a variety of aspects, including the assessment of image quality, potential radiation dose reduction, and performance comparisons with conventional CT systems. An evaluation of these factors is the particular subject of the first contribution of this thesis. This study includes results from phantom evaluations and the very first measurement of a human using a PCD CT scanner in a clinical setting. By directly comparing with conventional CT, using so-called *energy-integrating detectors* (EID), measurements using PCD CT revealed an increased quantitative but also qualitative image quality.

The assessment of the ventilation and vascularization of a rabbit's lung is described in another study. Here two experimental contrast agents with different spectral sensitivity (based on xenon and gadolinium) were applied. The successful computation of virtual non-contrast images confirmed the potential to eliminate the requirement for actual non-contrast scans, ultimately contributing to a reduction in radiation dose. We present different analyses

of kidney stones, focusing on their morphology and mineral composition, as well as the distinction between various stone types — which is considered an essential information for choosing the appropriate treatment. Both qualitative and quantitative assessments confirmed non-inferiority using PCD CT when compared to EID CT in differentiating kidney stones (e.g., comparing uric acid kidney stones with non-uric acid-based kidney stones), while offering improved differentiation, particularly for larger patients.

Ultimately, we employed energy-selective CT imaging to quantify local concentrations of holmium injections within a rabbit model, showcasing the possibility of measuring activated holmium as a means for dosimetry in cancer treatment via internal radiation therapy.

Zusammenfassung

Computertomographie (CT) ist ein unverzichtbares diagnostisches Instrument im Bereich der medizinischen Bildgebung und trägt wesentlich zur genauen Erkennung und Beurteilung einer Vielzahl von medizinischen Zuständen bei, einschließlich Trauma, Schlaganfall, Krebs, Lungen- oder Gefäßerkrankungen. Die Fähigkeit von CT, detaillierte, nicht-invasive Bilder von inneren Strukturen zu liefern, hat die klinische Praxis neu definiert. Dies spiegelt sich auch in der dokumentierten Nutzung dieser Technologie wider: Seit ihrer Einführung ist die Anzahl der durchgeführten CT-Scans stetig gestiegen, wobei die Gesamtzahl im Jahr 2022 allein in den Vereinigten Staaten 84 Millionen überstieg.

Innerhalb der CT ist die spektrale Bildgebung ein spezialisierter Ansatz, der materialspezifische Röntgenabsorptionseigenschaften nutzt, um energie- und materialspezifische Bildbearbeitungstechniken zu ermöglichen. Dennoch weisen vorhandene spektrale CT-Bildaufnahmeverfahren gewisse Einschränkungen auf, wie zum Beispiel eine erhöhte Komplexität in der Anwendung, Grenzen ihrer spektralen Empfindlichkeit, Einschränkungen des Messfeldes oder der Untersuchungsgeschwindigkeit. Die jüngste Einführung von Photonenzähl-Detektoren (engl. *Photon Counting Detectors*, PCDs) hat eine neuartige spektrale CT-Aufnahmemethode eingeführt, die im Vergleich zu früheren Technologien erhebliche Fortschritte in vielen Aspekten verspricht, einschließlich einer erhöhten räumlichen Auflösung und verbesserter Strahlendosis-Effizienz.

Da sich diese Technologie noch in einem frühen Stadium befindet, müssen gründliche (pre-)klinische Bewertungen und Vergleiche mit bestehenden Technologien durchgeführt werden. In einem zweiten Schritt müssen die praktischen und einzigartigen Vorteile und mögliche Einschränkungen, die PCD-CT bietet, untersucht werden. Dies schließt die Übertragung bisheriger Erkenntnisse in die klinische Praxis ein. Letztendlich stellt sich die Frage nach neuen möglichen diagnostischen Anwendungen.

Diese Dissertation befasst sich eingehend mit Bewertungen und klinischen Untersuchungen, die sich auf die energie-selektive CT-Bildgebung konzentrieren. Die Untersuchungen dieser Arbeit umfassen verschiedene Aspekte, einschließlich der Beurteilung der Bildqualität, möglicher Strahlendosisreduktion und Leistungsvergleiche mit herkömmlichen CT-Systemen. Eine Bewertung dieser Faktoren ist das Hauptthema des ersten Beitrags dieser Arbeit. Dieser Beitrag enthält Ergebnisse von Phantomuntersuchungen sowie die erste Messung eines Menschen mit einem PCD-CT-Scanner in klinischer Umgebung. Durch den direkten Vergleich mit konventioneller CT mit sogenannten *energieintegrierenden Detektoren* (EID), zeigten Messungen mit PCD-CT in klinischer und nicht-klinischer Umgebung eine erhöhte quantitative und qualitative Bildqualität.

Die Beurteilung der Ventilation und Perfusion der Lunge eines Hasens wird in einer weiteren Studie beschrieben. Hier wurden zwei experimentelle Kontrastmittel mit unterschiedlicher spektraler Empfindlichkeit (basierend auf Xenon und Gadolinium) eingesetzt. Die erfolgreiche Berechnung virtueller Nativbilder bestätigte das Potenzial, die Notwendigkeit tatsächlicher Nativbilder zu beseitigen, was letztendlich zu einer Reduzierung der Strahlendosis beiträgt.

Wir präsentieren verschiedene Analysen von Nierensteinen und konzentrieren uns auf deren Morphologie und Mineralzusammensetzung sowie auf die Unterscheidung zwischen verschiedenen Steintypen - Informationen, die als wesentlich für die Auswahl einer angemessenen Behandlung gelten. Sowohl qualitative als auch quantitative Bewertungen bestätigten die Nichtunterlegenheit der PCD-CT im Vergleich zur EID-CT bei der Differenzierung von Nierensteinen (z. B. beim Vergleich von Harnsäure-Nierensteinen mit nicht Harnsäure-basierten Nierensteinen), während eine verbesserte Differenzierung, insbesondere für größere Patienten, geboten wurde.

Schließlich setzten wir energie-selektive CT-Bildgebung ein, um lokale Konzentrationen von Holmium-Injektionen in einem Hasenmodell zu quantifizieren und zeigten so die Möglichkeit auf, aktiviertes Holmium als Mittel zur Dosimetrie bei der Krebsbehandlung durch interne Strahlentherapie zu messen.

Acknowledgments

First and foremost, I wish to express my deep gratitude to Professor Dr. Nassir Navab and his esteemed chair for Computer Aided Medical Procedures and Augmented Reality at the Technical University of Munich. Thank your unwavering support, trust, and your patience. I am sincerely grateful for the opportunity you gave me to pursue my research.

Second, I want to take the opportunity to dedicate this work to my beloved parents, Hermann and Rosemarie Gutjahr. They are and they remain my enduring source of inspiration and motivation in every facet of my life. Thank you so much for that.

I want to extend my appreciation to my dear rest of the family. Thank you Gabriele, Ingo, Marie, Emily, Jochen, Ursl, Paul, Katharina.

Moreover, I want to acknowledge my professional partners and friends from Siemens Healthineers, that include Thomas G. Flohr, Bernhard Schmidt, Michael Grasruck, Bernhard Krauss, Martin Sedlmair, Christoph Polster, Tristan Nowak, Ulrike Haberland, and Ahmed F. Halaweish. Thank you for your expertise, insights, help, and companionship during the past years and for the next years to come.

At the Mayo Clinic, I had the privilege of working with a dedicated team of professionals who became my friends eventually. My sincere gratitude goes to Cynthia McCollough, J.G. Fletcher, Shuai Leng, Lifeng Yu, Nikki Weber, Andrea Ferrero, and Roy Marcus. You have taught me the true meaning of dedication to our profession.

To all the aforementioned individuals - and those I forgot to mention: I am profoundly grateful to know you in my life. This journey would not have been possible without each one of you, and I remain indebted for your contributions to my academic and personal growth.

Contents

Part I

Introduction and background

1 Introduction

> *Hält man die Hand zwischen den Entladungsapparat und den Schirm, so sieht man die dunkleren Schatten.*
>
> — **Wilhelm Conrad Röntgen**
> (1895)

1.1 Motivation

X-ray imaging and computed tomography (CT) have become indispensable tools in modern medicine, enabling non-invasive diagnosis for a variety of clinical conditions. As a form of electromagnetic radiation, X-rays can penetrate body materials, revealing valuable insights into the human body's internal structures. CT technology enhances these capabilities by capturing X-rays from multiple angles, generating cross-sectional images without superimposition of anatomical structures, and providing much greater detail and accuracy than traditional (planar) X-ray imaging.

This section gives an overview of the discovery of X-rays and the development of CT imaging. Key findings, and the eventual impact of these technologies on medical diagnosis will be highlighted.

1.1.1 X-ray imaging

The December 1895 proceedings of the Würzburg Physical-Medical Society report the lively discussion and immediate recognition of the importance of Wilhelm Conrad Röntgen's most famous discovery: the "New Kind of Rays" (orig: *Neue Art von Strahlen*) [276].

In his experimental setup, Röntgen noticed the appearance of fluorescence on a plate coated with barium plating cyanide after exposure through a *Crookes tube* (i.e. a cathode ray tube), which was covered with cardboard. Surprised by this observation, he concluded that these rays were capable of traversing matter. In the course of his following experiments, he found that these rays were able to pass through thick books and wooden boards with a thickness of 2-3 cm - still causing fluorescence on the plate. However, the intensity of fluorescence was reduced when several layers of tinfoil were placed in-between the tube and the plate [276].

With regard to the novelty of this finding and with reference to the mathematical unknown, Röntgen also called these rays *X-rays*. It was the Swiss-German anatomist and physiologist Rudolf Albert von Kölliker, a founding member of the Physical-Medical Society in Würzburg,

who suggested to name these rays *Roentgen rays* (orig: *Röntgen'sche Strahlen*) [276] - a nomenclature still used in many languages - not only German. In the year 1901, Röntgen was honored with the Nobel Prize in Physics [88]. After his discovery Röntgen conducted a series of experiments, one of which involved taking acquisitions of his wife's hand, showing the potential of X-rays to see through human tissue and demonstrating their use for medical purposes. Figure 1.1 depicts the first two documented X-ray radiographies of the human anatomy: (a) The hand of Röntgen's wife Anna Bertha Ludwig, and (b) the hand of Rudolf Albert von Kölliker.

(a) Possibly the hand of Röntgen's wife Anna Bertha Ludwig, acquired on December 22nd, 1895 [277].

(b) Hand of Rudolf Albert von Kölliker, acquired on January 23rd, 1896 [276].

Fig. 1.1. The first two documented X-ray radiographies.

Shortly thereafter, X-rays were used for the first time to examine the skeleton and later also to diagnose tuberculosis in patients before onset of symptoms [206, 276]. Today, planar radiographic imaging is used primarily for orthopedic issues (e.g. body statics or to exclude higher grades of joint degeneration), as well as for examining infections, presence and the trajectory of foreign material, or for the assessment of a patient's gastrointestinal passage.

1.1.2 History of CT imaging

The mathematical foundation for the reconstruction of tomographic slices was set by the Austrian mathematician Johann Radon in 1917 [260]. In his work he explained how three dimensional objects can be reconstructed using an infinite number of two dimensional projection planes[1]. His method is known as the *Inverse Radon transformation*.

[1]Whereas Radon's solution was then generalized to an n-dimensional Euclidean space and respective hyperplanes.

Later, and without knowledge of Radon's previous achievements [151], the South African-American physicist Allan MacLeod Cormack investigated the exponential absorption of (*pencil beam*) X-rays not in homogeneous, but in inhomogeneous matter, using line integral information (i.e. known intensity before and measured intensity after an object of interest) [45]. He emphasized the special importance of this approach not only for radiography (and ultimately tomography) but for radiotherapy, where knowing the local absorption coefficient of body materials is crucial, in order to apply intended doses of radiation to sick tissue and little radiation to healthy tissue.[2]

In 1967, the senior research scientist at EMI, Ltd, Central Research Laboratories, Godfrey Newbold Hounsfield, built the real first prototype CT scanner. His prototype was capable to reconstruction the two-dimensional distribution of an object's local X-ray attenuation coefficients within an image slice from knowing all line integrals of these absorption coefficients from different angles. The scanner was equipped with a gamma source and it took full 9 days to acquire sufficient data for a set of projections, while it took another 2.5 hours to reconstruct the corresponding tomographic images using a large main frame computer. Only the replacement of the gamma source with an X-ray tube reduced the acquisition time to *only* 9 hours [141].

On October 1st, 1972, Hounsfield and the neuroradiologist James Ambrose from Atkinson Morley's Hospital, London, used a new prototype scanner (*Mark I*) to generate the first clinical CT image of a patient with a suspected brain lesion in the frontal lobe (Figure 1.2 (a)). The image revealed the presence and the exact location of a cystic tumor [21, 141]. After more subsequent measurements it was found that the scanner provided sufficient image quality to not only assess a patient's (intra-)cranial anatomy and morphology, but various pathologic processes involving the brain, including tumors, infarcts, hemorrhages, and infections [14]. The first CT scan in the USA was performed on June 19th, 1973 at the Mayo Clinic in Rochester, Minnesota [21].

In a following project Hounsfield developed a full body CT scanner. He presented a CT image of his own abdomen on March 14th, 1975 (Figure 1.2 (b)).

Drs. Hounsfield and Ambrose received jointly the prestigious BJR Barclay prize in 1974. Together with Dr. Cormack, Hounsfield was honored with the Nobel Prize in Physiology or Medicine in 1979 [85]. In 1981 Hounsfield was knighted by the Queen of England [141].

Since its invention, CT has undergone significant development and improvements. A first one was done by Robert S. Lendley, a professor of physiology, biophysics and radiology at Georgetown University, who brought CT into a larger scale by developing the first clinical whole-body CT Scanner with a fan beam geometry in 1974 [176].

Slip-ring technology allowed CT images to be acquired with free rotation of the X-ray tube and the detector around the patient (cf. Section 2.1.1). This technology enabled the acquisition of CT images with a constant *table feed* or *pitch factor* (i.e. the table travel during rotation, in $\left[\frac{1}{\text{rot}}\right]$, or the table travel per rotation over the nominal beam width, respectively [205]), also

[2] In a second work he extended this thought to line integrals obtained from gamma ray coincidence counters after application of charged particles (i.e. positron emitting isotopes)[46]

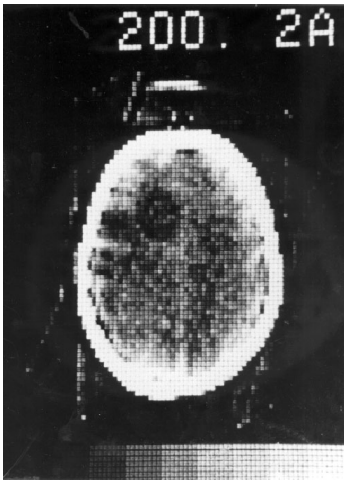

(a) First clinical head CT image, Atkinson Morley's Hospital, October 1st, 1971 [224].

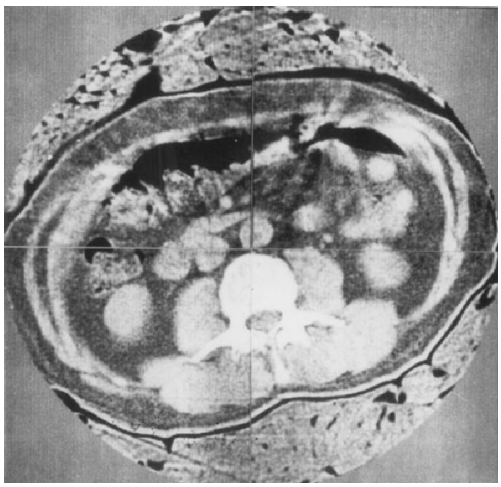

(b) First pre-clinical body CT image of Sir Godfrey N. Hounsfield's own abdomen, shown at Bemuda conference on March 14th 1975 [21].

Fig. 1.2. The first two CT images using two prototype EMI CT scanners.

known an *spiral* or *helical* CT [153]. Spiral CT brought many advantages of what was before called *sequential CT*: CT scans were performed much quicker, enabling the examinations of entire large organs such as the lung or the liver. It also reduced the amount of motion or misregistration artifacts due to the absence of inter-scan delays (especially for long scan ranges or in situations where patient breathing and swallowing cannot be controlled) [153].

At the end of the 1990's the *slice race* began. CT manufacturers started to increase the number of detector slices[3] and therefore increased the coverage of the CT detectors. This enabled much faster scanning of larger anatomies, and in particular scanning with much thinner slices to approach isotropic spatial resolution [80, 167, 203, 213].

In 2013, integrated CT detectors started to get implemented. In these detectors the photodiode, pre-amplifiers, and analog-digital converters were found on one chip, which on the same chip, obviating unnecessary analog connections and leading to more efficiency in signal determination and in reduced image noise eventually [62].

Today, CT scanners are widely used (with approximately 38,700 examinations per site per year in the United States [2]) and play a critical role in diagnosing and treating a wide range of clinical conditions (e.g., trauma, stroke, cancer diagnosis and treatment planning, assessment of vascularization and pulmonary ventilation, etc.). An overview of the procedure mix in the United States for 2022 is shown in Figure 1.3.

With the onset of COVID-19, annual CT procedures dropped to 73 million. Yet, in 2021, there was a resurgence with a 13% increase, totaling approximately 84.5 million CT examinations [2]. By 2022, the growth had tapered off, with the number of CT examinations rising by 0.9% to 85.3 million, as shown in Figure 1.4.

[3] 1995: 1×5 mm, 1998: 4×1 mm, 2001: 16×0.75 mm, 2004: 64×0.6 mm, 2008: 320×0.5 mm [274]

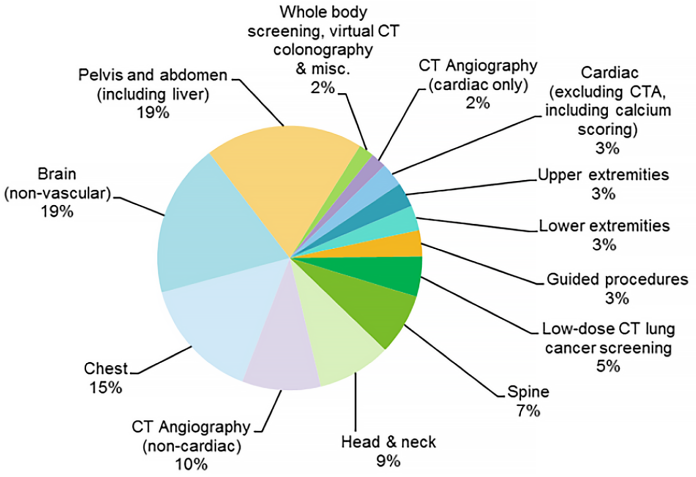

Fig. 1.3. Overview different CT procedures in the United States in 2022 (N = 85.3 million procedures, from [2]).

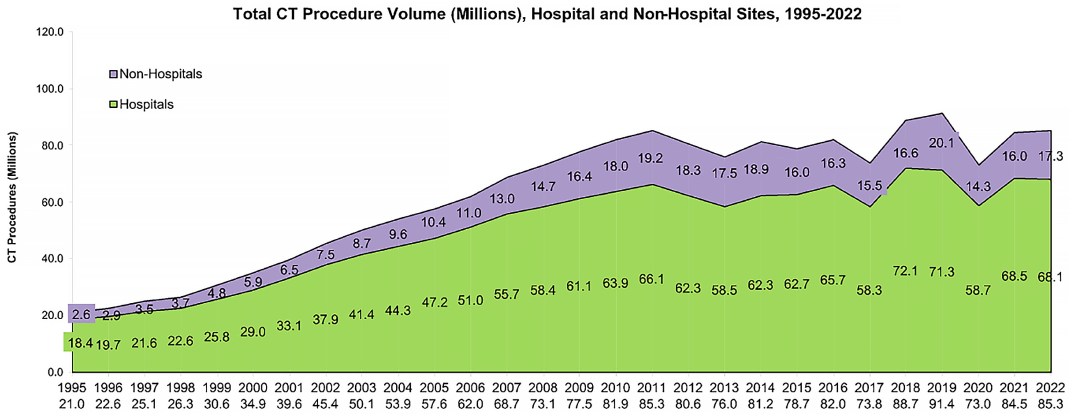

Fig. 1.4. Overview of annual total CT procedure volumes between 1995 and 2022 in the United States [2].

A recent, and probably one of the most important advances in the further development of clinical CT has been the development of spectral CT imaging technologies, i.e. the application and/or detection of different X-ray spectra, enabling energy-selective CT imaging. Spectral CT can be achieved by applying different acquisitions techniques, such as dual kV CT, slow/fast kV-switching CT, split filter CT, dual source CT, dual layer CT, and most lately, photon counting detector CT (PCD CT, cf. Section 2.4). The increase of availability of CT systems capable of acquiring energy-selective images, from 13% to 28% from 2014 until 2021, underlines the significance of this technology [57].

With spectral CT imaging energy-sensitive image acquisitions can be used to characterize and quantify body materials and therefore improve the range of possible diagnosis. A comprehensive overview of the latest advanced applications based on spectral CT can be found in Section 3.3.

1.2 Problem statement

During early non-clinical or pre-clinical evaluations, photon counting detectors (PCDs) have been found to provide increased spatial resolution and enhanced dose efficiency when compared against traditional energy integrating CT detectors [18, 158, 273, 322, 358, 359]. In addtion, PCDs an produce signals that correspond to different energy ranges of the registered X-rays, thereby enabling spectral processing. Nevertheless, prior to the adoption into clinical practice, certain questions about the characteristics and capabilities of these new detectors, as well as the potential opportunities they might offer, must be addressed:

- **Performance assessment: How does PCD CT compare against other spectral CT imaging techniques?**
  Previous feasibility studies have shown the potential advantages of prototype PCDs. However, to incorporate PCDs into clinical practice, it is necessary to carefully compare them with conventional detector technologies, in order to identify their exact advantages but also disadvantages, e.g. in terms of image quality and radiation dose. How do PCDs compare with traditional detectors in terms of contrast enhancement, noise characteristics, spatial resolution or spectral sensitivity? What is the impact of the applied and required radiation dose for specific clinical questions? How consistent are the findings across varying object/patient sizes? Answering these questions shall support the development of a comprehensive understanding of this technology.

- **Which practical benefits come with the use of PCD CT? How can the unique characteristics of this technology be successfully exploited?**
  Transferring the findings from prior performance assessments into clinical practice raises several important questions regarding the use of PCDs. For example, what are the implications of improved image quality and enhanced spectral sensitivity for optimizing the use of PCDs in achieving accurate and reliable diagnosis? Can the increased dose sensitivity of PCDs be harnessed to reduce radiation exposure in patients while maintaining a high image quality? What is the practical comparative advantage of PCDs over traditional spectral CT acquisition techniques in terms of imaging performance, radiation exposure, and ultimately patient management? The answers to these questions are vital to the realization of this technology's full potential and its future deployment into the clinical routine.

- **Which possible new applications could energy-selective CT bring?**
  PCD directly resolves impinging X-ray spectra by implementing energy-specific thresholds in the detector's readout electronics (cf. Section 2.1.3). These energy thresholds enable energy-sensitive measurements; whereas the application of multiple thresholds enables multi-energy imaging. In contrast to that, other established spectral CT acquisition methods are currently limited to detecting only two energy spectra. The increase in information provided by PCD CT can be utilized to improve existing and introduce new algorithms for processing the acquired data. Also, integrated readout electronics allow to set flexible thresholds, which could be adjusted for a special need, e.g. to allow for increased attenuation and therefore contrast enhancement of materials with increased absorption at a certain energy. The spectral sensitivity of a CT scanner, in terms of the

selection of the X-ray spectra and/or the selection of energy thresholds for given body materials and contrast media needs to be investigated.

This dissertation delves into a variety of evaluations and clinical experiments involving spectral CT imaging. The studies conducted encompass various aspects of the technology, including image quality assessment, potential radiation dose reduction, both compared against conventional CT systems. By examining the practical applications of spectral CT imaging in different clinical scenarios, we aim to provide insights into its potential benefits and limitations.

Furthermore, this dissertation discusses the potential for optimization and customization of spectral CT imaging to suit specific clinical needs, enabling more accurate and efficient diagnoses. It also explores the potential impact of this technology on the selection of adequate treatment.

Through a comprehensive analysis of the findings, as presented in this work, we aspire to contribute to the understanding and advancement of spectral CT imaging as a promising technology in medical imaging. By fostering a greater appreciation of its capabilities and potential clinical applications, we hope to concur to answer the above questions, while encouraging further research and development, paving the way for the widespread adoption of spectral CT imaging in clinical practice.

1.3 Thesis outline

Part I of this dissertation comprises of a general introduction and two technical chapters. Chapter 1 provides an holistic overview of the history of X-ray and CT imaging, with a particular focus on the most impactful developments underlying these imaging techniques. The introduction also outlines the motivation for the thesis and presents the problem statement. Additionally, an overview of the scientific contributions, as presented in this thesis, is included.

Chapter 2 depicts technical details on hardware components of a CT scanner, photon interactions relevant for clinical CT imaging, and a description of X-ray attenuation. Chapter 3 provides a comprehensive overview of methods of spectral CT image processing and an overview of their clinical applications including several examples.

Part II of this thesis comprises selected scientific contributions published in peer-reviewed scientific journals, as well as in national and international conferences. A particular focus was set on the physical and clinical evaluations of early PCD CT prototype research systems. This part of the thesis highlights its key contributions. The findings of the very first CT acquisitions of a human using a PCD CT system in a clinical setting is described in Chapter 4. The presented study features evaluations of image quality and artifacts, alongside phantom scans which showcase the advantages of PCD CT over conventional CT. The spectral assessment of the ventilation and vascularization of a rabbit's lung is described in Chapter 5. Chapter 6 discusses the potential to differentiate kidney stones based on their underlying material (uric acid,

calcium oxalate monohydrate, cystine, or apatite) using PCD CT image data. In Chapter 7 kidney stones are characterized using varying phantom sizes and tube voltages. The results of these findings were compared against results from conventional energy integrating CT systems. Chapter 8 describes the characterization of pure and mixed kidney stones, referring to results from micro CT acquisitions. Chapter 9 reports the quantification of holmium microspheres, specifically by determining the concentration of holmium injections in a phantom and rabbit model. The potential application of quantifying activated holmium, as a means of dosimetry in cancer treatment through internal radiation therapy, is described.

Finally, Part III concludes this thesis by critically summarizing its main findings. This part also includes the experienced limitations and provides recommendations for future research in the field of pre-clinical and clinical spectral CT image processing using PCD CT.

2 CT imaging - Technical background and state of the art

Today's CT imaging relies on the findings described in the previous chapter. This chapter will focus on the structure and the function of modern CT scanners. The generation and detection of X-rays are described. A special focus is set on the physical principles attenuation and scatter of X-ray photons, as they play an important role for spectral CT imaging. Ultimately, an overview on different spectral CT imaging techniques is provided. For further reading on more detailed insights to these topics, the following references are recommended: [35, 135, 151].

2.1 Hardware components

This subsection focuses on CT geometries and basic components of CT scanners. The structure and function of X-ray tubes and their use in conjunction with beam shaping filters will be described. At the end of the subsection three different X-ray detector principles (xenon ionization detectors, scintillator-based energy integrating detectors, semiconductor-based PCDs) will be outlined and explained in detail.

2.1.1 CT geometry

The geometry of Houndsfield's EMI Mark I CT scanner (cf. Section 1.1.1) marked the *first* generation of CT scanner geometries. It was characterized by the very narrow collimation of the X-ray beam. The initial X-ray cone was reduced to a so-called *pencil* beam. Images were acquired by linear *translation* and *rotation*: The X-ray source and the opposite detector (consisting of two single detector elements, allwing for the acquisition of two slices) were translated to acquire measurements *one by one* to cover an area of interest. After about 160 measurements both X-ray source and detector rotated around the isocenter by very small increments of 1° and the translation and rotation process was repeated. To acquire two CT images an measurement duration of around 5 minutes was needed [151].

The measurement time was reduced with the use of several adjacent detector elements and correspondingly wider collimation of the X-ray beam (30 such elements with the first scanner [79]). This *second* generation of CT geometries still followed the same principle as of its predecessor (rotation and translation), but both processes could be accelerated and acquisition time was reduced to only 18 seconds per scan [151].

The need cover large anatomies (e.g. the abdomen) and to improve the scan time even further led to the introduction of the *third* generation of CT geometries. Inside the CT gantry both

X-ray source and the diametrically opposed detector rotate around the patient. The collimation was opened even further (approx. 45-55°, with 700 or more detector elements), which led to a more efficient use of the X-rays [79]. With the advent of slip-rings in 1987[1], used to transfer measurement data from the detector[2] and supplying X-ray source and detector with the required energy, continuous measurements were feasible and scan times went down to 1 s (for a single slice scanner), 0.5 s (for a 4 slice scanner), and 0.33 s (for a 64 slice scanner)[79, 151]. A coveted goal was reached: To perform a CT scan within one breath hold. Figure 2.1 shows the structure and the main components of the third generation scanner geometry.

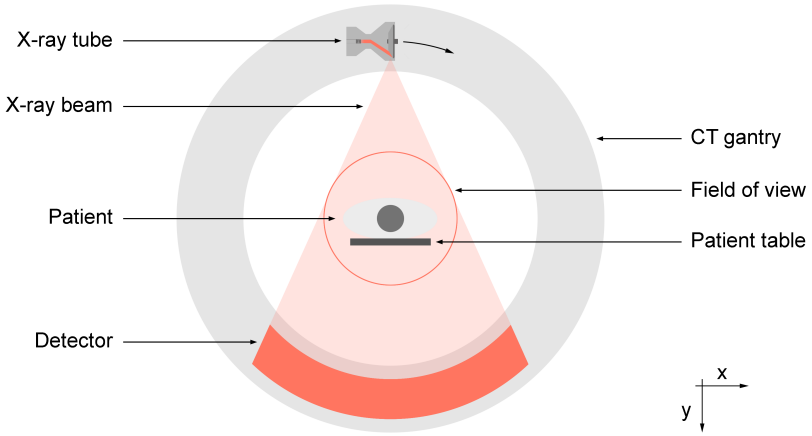

Fig. 2.1. Third generation CT geometry: A schematic view of a CT gantry and its internal components (X-ray tube and CT detector). The patient is located in the bore's isocenter and inside the field of view of the X-ray beam. Both X-ray tube and detector rotate around the patient during the examination, collecting projection information needed for image reconstruction.

Generation *four* of CT geometries came with a stationary detector ring and a rotating X-ray source. Despite the advantages this design has brought (reduced mechanics or the reduced propagation-effects caused by single erroneous detector signals), the costs of the design (due to the large number of detector elements) were too high and this approach has not been pursued for long [79].

With the *fifth* generation of scanner geometries, the so-called *electron beam CT* (EBCT), mechanically movable elements were completely dispensed. Instead both X-ray source and the detector were static. Just as with the fourth generation, a partial detector ring encircles the patient. The X-ray beam, first focused, gets deflected to the anode which also surrounds the patient [79, 198]. This design was firstly presented by Douglas P. Boyd and Martin J. Lipton in 1983 [29]. Due to its rapid measurements (36-54 images per second) Boyd and Lipton proposed this design to be used for cardiovascular imaging purposes; they even referred to the scanner as a *Cardiovascular CT* (CVCT). Due to the insufficient image quality, lack of adequate radiation dose reserves, and inherent complexity, the EBCT/CVCT-principle has meanwhile been given up.

Today all medical CT scanners use third CT scanner geometry.

[1] With the Siemens SOMATOM PLUS and Toshiba's TCT 900S [151].
[2] Modern slip-rings are capable of transferring up to 70 gigabytes of data per second.

2.1.2 X-ray generation

X-rays for CT imaging are generated in an X-ray tube (cf. Figure 2.2 (a)). Inside the tube a heating circuit generates an electrostatic field. A Wehnelt cylinder surrounds the cathode filament of the heating circuit, bundling the electrons to a beam which is generated by the *tube circuit* or *acceleration circuit*. Typical voltages for the tube circuit range from 70 kV to 150 kV; modern X-ray tubes achieve tube currents up to 1000 mA [97]. The electron beam is directed towards a tungsten anode where only a minor fraction is converted into X-rays, while the substantial fraction (approximately 99%) of the energy is transformed into heat.

The X-rays are created by three effects:

1. **Deflection:** Electrons are deflected and decelerated in the electrostatic field (i.e. *Coulomb field*) of the target atom when approaching its nucleus. The deceleration of the incoming electrons lead to the emission of *Bremsstrahlung*. The energy of the emitted X-ray photon is proportional the degree of deceleration. Therefore, Bremsstrahlung is characterized by a continuous energy spectrum, but is limited to the maximum kinetic energy of the electrons, which corresponds to the applied X-ray tube voltage.
2. **Collision with electrons:** Impinging electrons from the heating circuit remove electrons from the target atom of the anode material. Vacant holes are refilled with outer shell electrons and emit characteristic radiation depending on difference of the orbit energies of the involved shells[3]. This type of radiation is responsible for the peaks in X-ray energy spectra (cf. Figure 2.2 (b)).
3. **Collision with the nucleus:** The entire energy of the impinging electron translates into Bremsstrahlung (i.e. full deceleration). This type of interaction defines the upper limit of the X-ray spectrum.

The resulting X-ray beam exits the X-ray tube housing via a window and usually traverses additional filtration[4]. This filtration (e.g. a thin layer of tin, titanium, copper, or aluminum) is either used to remove low energy photons (with energies lower than around 30 keV) which would be stuck in the scanned object and which therefore would not contribute to the detected signal but to radiation exposure. Another important type of filter is referred to as the *bowtie-filter*. The bowtie-filter (made from materials with low effective atomic numbers but high density, e.g. aluminum) is designed to create additional attenuation in the peripheral (transversal) areas of the X-ray beam in order to compensate for cross-sections of patients or other scanned objects with less attenuation. Ultimately, specialized spectral K-edge pre-filtration, specifically designed for photon-counting CT scanners, have been suggested [12, 247, 250, 255, 256, 299]. These filters are designed with consideration for the specific detection features commonly seen in direct-converting CT detectors and yield for an improved spectral separation and enhanced quality of spectrally processed CT images.

More detailed information about the generation of X-rays, principles of beam filtration and technical specifications of modern X-ray tubes can be found at [35, 96, 97, 135, 151].

[3] Binding energies of tungsten, the most common anode material (due to its high potential for heat conductance), are K = 70 keV, L = 11 keV, M = 3 keV, N = 0.5 keV.
[4] The application of X-ray (pre-)filtration is sometimes referred to as *beam shaping*.

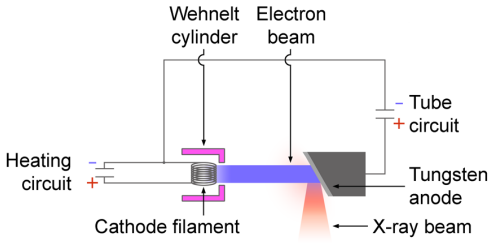

(a) X-ray tube and its main components. An electron beam is generated by a heating circuit and a Wehnelt cylinder. The beam hits the anode and X-ray emerges from the reflection.

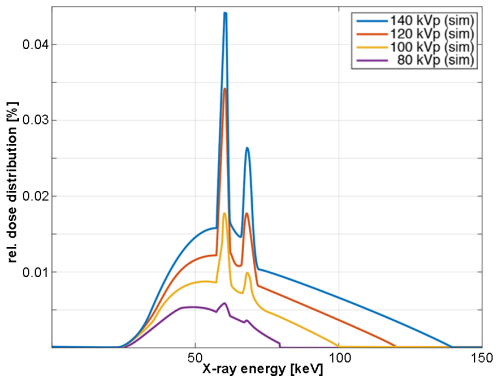

(b) Simulated pre-filtrated X-ray spectra at 140 kVp (blue, 120 kVp (red), 100 kVp (yellow), 80 kVp (purple) (modified from [105]). The y-axis depicts the dose distribution for each spectrum. Low energy photons are removed by the applied filter. The two respective peaks depict the characteristic radiation from the K_α- and K_β-transitions of tungsten.

Fig. 2.2. A schematic X-ray tube and exemplary X-ray spectra.

2.1.3 X-ray detection

Xenon ionization detectors

Xenon ionization detectors (XID) consist of isolated high pressure chambers filled with xenon gas. Every chamber comprises two high voltage collecting electrodes. Impinging X-ray photons hit xenon atoms and a photoelectric effect occurs, which leaves the original atom in an ionized state and leads to the ejection of an electron (cf. Section 2.2.3). The positively charged nuclei of the xenon atom moves towards the detector's negatively charged electrode, whereas the electron moves towards the corresponding positively charged electrode (Figure 2.3) [135, 350].

Depending on the energy of the X-ray photon multiple photoelectric effects can occur, which in turn creates a linear relationship between the number of events and the signal strength (Figure 2.3 (b)).

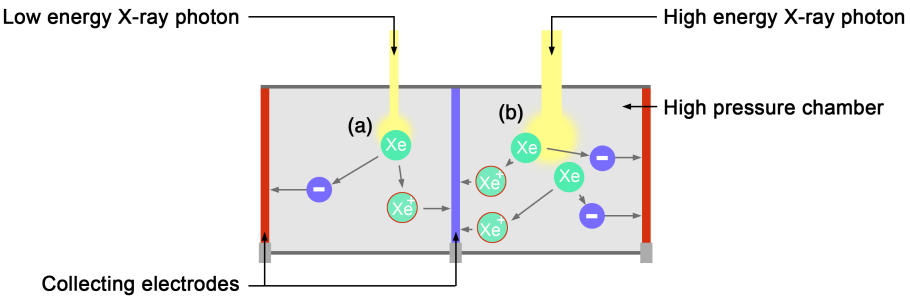

Fig. 2.3. Impinging X-ray photons interact with xenon atoms inside a high pressure chamber, causing photoelectic effects (cf. Section 2.2.3). The resulting xenon ions and electrons move towards high voltage collecting electrodes. A single event for a low energy photon is illustrated in (a). Higher energy photons can cause multiple photoelectric effects, leading to a greater detection signal.

The plain structure of these detectors provides comparable sensitivity across the single detector elements. However, when compared to energy integrating detectors, xenon ionization detectors only provide a reduced quantum efficiency (i.e. the sensitivity to detect single quanta), as X-ray photons can traverse through the chamber with the risk to not interact with xenon atoms [350]. Also, decay time and afterglow luminescence was proven to be inferior when compared to other detector technologies [90]. As single row CT scanners using such detectors were considered an efficient and cost-effective solution to detect X-rays, extending them to multi-row systems has proven difficult and too expensive [135, 151].

Energy integrating detectors

Energy integrating detectors (EID) or *solid-state scintillating detectors* measure X-ray photons via a *two step conversion*: An incoming X-ray ionizes inside a pixelized scintillating material, causing photoelectric effects, which lead to the emission of characteristic radiation in form of visible light (step 1), where the amount of light is proportional to the X-ray energy. Reflective septa are used to guide the light towards photodiodes while preventing the light to get detected by an adjacent detector element (*crosstalk*), which would reduce the spatial resolution of the detector. The photodiodes absorb the incoming light and produce electrical current in proportional correspondence to the light's intensity and hence the X-ray energy. Attached readout electronics amplify the current and convert it from an analog signal to a digital signal (step 2).

A 2D or 3D collimation grid on top of the detector prevent scattered photons from entering the detector (Figure 2.4, cf. Sections 2.2.1 and 2.2.2).

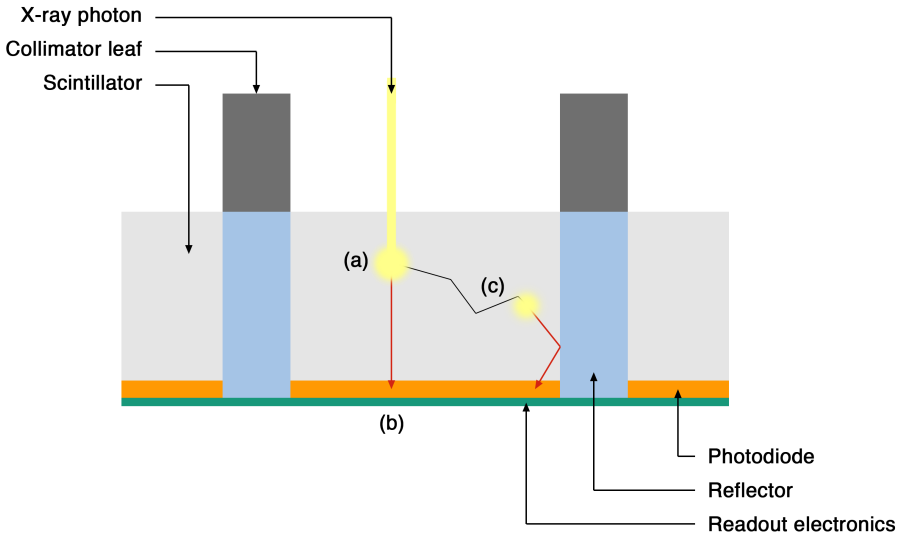

Fig. 2.4. A scintillating crystal material converts an impinging X-ray photon into visible light (a), which gets translated to an electrical current by a photodiode and attached readout electronics (b). Reflector septa scatter the light towards the photodiode while preventing crosstalk to adjacent detector elements (c).

Both the septa (e.g. made of titanium dioxide, TiO_2) and the collimator grid (e.g. made of tungsten, W) are geometrically aligned and direct towards the location of the X-ray source. As they cover an area that can not be used for detection, they diminish the overall geometric detection efficiency (i.e. the ratio of dose sensitive detector area over the total detector area) of the detector [82, 135].

Commonly, the scintillator is made of materials that provide a high stopping power even for photons from the higher energy range of the X-ray spectrum (e.g. gadolinium-oxide, Gd_2O_3, gadolinium-osysulfide, Gd_2O_2S, or caesium iodide, CsI) [127]. The compound specific signal output is described by the detector responsivity $D(E)$ (cf. Section 2.3.3).

$N(E)$ corresponds to the number of X-ray quanta registered at a specific energy E. Over a given sampling time all of these energy specific signals are integrated and weighted with the detector responsivity [82]:

$$S = \int_0^{E_{\max}} D(E) \cdot N(E) \mathrm{d}(E). \tag{2.1}$$

Ideal energy integrating detectors assume a linear proportionality of the detector response (i.e. light generation) and the energy of the X-ray photon, as the amount of light generated is proportional to the X-ray energy. This leads to

$$S \approx \int_0^{E_{\max}} E \cdot N(E) \mathrm{d}E. \tag{2.2}$$

This implies that signals from detected X-ray photons are weighted linearly based on their energy (i.e. low weights for lower energy photons, and high weights for high energy photons).

Photon counting detectors

PCDs generate signals without converting the X-ray photons into visible light. Instead, the photons interact with a semiconductor material, directly creating electron-hole pairs. A high voltage circuit (approximately 1 kV) connected to the detector forces the electrons to drift towards the pixelated anodes and the holes to drift towards the cathode.

The electron cloud (i.e. induction processes in the electrical field [124]) produces current pulses at the anode, which are in turn converted into voltage pulses by the pulse-shaping readout electronics (Figure 2.5). The full-width-at-half-maximum (FWHM) of such a pulse is between 10 and 15 ns.

By calibration proportionality of the pulse height to the corresponding energy of the detected electron cloud is ensured, and consequently, to the energy of the initial X-ray photon [127]. The direct conversion from the X-ray photon to electrical charge is also referred to as *one-step conversion*.

The electric pulse is counted as soon as it exceeds a threshold energy, technically realized by pulse height comparators. The simultaneous use of several pulse height comparators with different threshold energies allows for energy-sensitive measurements, as only pulse events that exceed the specified threshold are *counted* and contribute to the calculation of the reconstructed image (so-called *threshold images*). Also energy bins can be resolved by only considering measured pulses that lie between two energy thresholds (yielding so-called *bin images*).

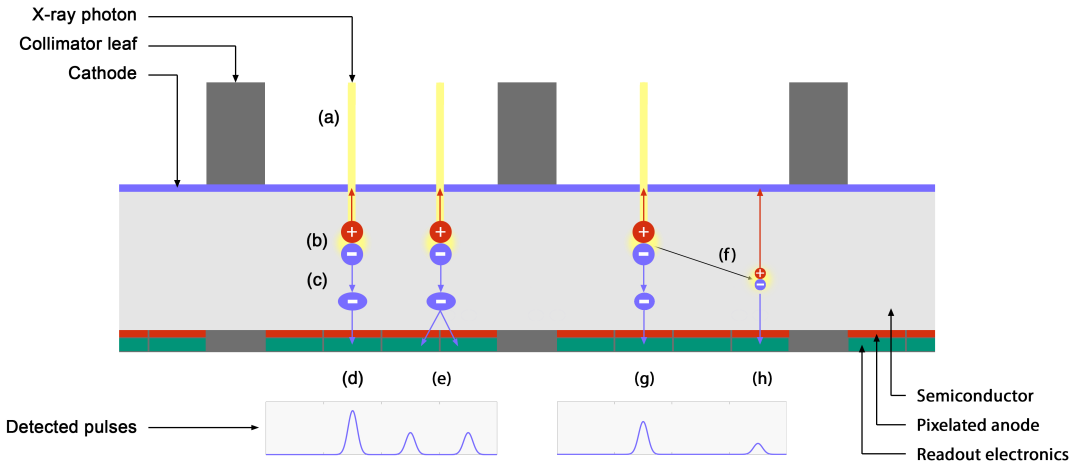

Fig. 2.5. An impinging X-ray photon (a) interacts inside a semiconductor detector material creating electron-hole pairs (b) which drift to the detector's cathode and pixelated anode, respectively (c). After detection and processing by the application-specific integrated circuit (ASIC) voltage pulses are generated (d). Charge sharing occurs when energy clouds are detected by adjacent pixel elements (e). K-fluorescence electrons interact at another location within the detector (f). The signals of the initial and the K-fluorescence electron are detected by different detector elements. The absence of optical septa between the single detector elements increases the geometric detector efficiency of PCDs [252].

Figure 2.6 depicts an exemplary signal over time. In this example two energy thresholds are applied. Three of the four indicated signals (2, 3, 4) exceed the first threshold ($T_2 = 25$ keV), whereas only signal 2 and 4 surpass the second threshold ($T_2 = 75$ keV). PCD also allow to read out signals of energy ranges between two thresholds. These ranges are referred to as *energy bins*. In the given example only signal 3 is detected in the energy bin determined by T_1 and T_2.

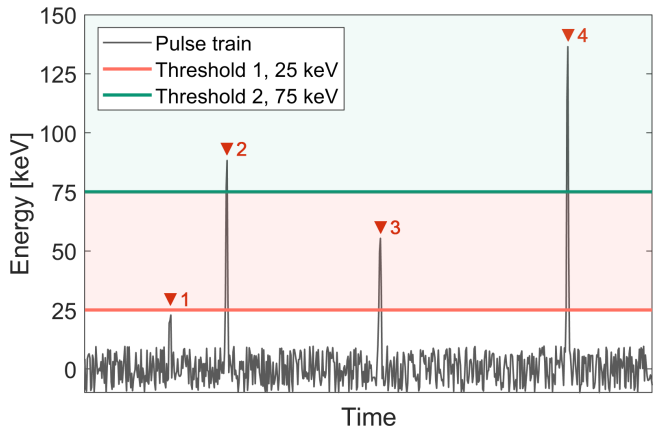

Fig. 2.6. An energy pulse train with four pulses. Two energy thresholds are applied (25 keV and 75 keV). The first pulse is not registered in any measurement. The pulses 2,3, and 4 exceed the first energy threshold. Pulses 2 and 4 exceed the second energy threshold. Images can also be reconstructed by only considering signals between two energy thresholds (*energy bin*).

The detection of electronic noise is omitted by design, as the noise level does not exceed the energy thresholds. This has a particular significance in situations where a reduced radiation dose is applied, or for patients with large body size [82, 360].

All X-ray quanta are counted with the same weight, as the detector's response remains nearly constant ($D(E) \approx c$) and accordingly independent of the energy of the measured photon. In reference to Equation 2.1 this yields to the following signal [82]:

$$S \approx c \int_{\mathrm{T_i}}^{\mathrm{E}_{max}} N(E)\mathrm{d}E. \tag{2.3}$$

for threshold-based measurements. With E_{max} depicting the maximum energy of the spectrum. And

$$S \approx c \int_{\mathrm{T_i}}^{\mathrm{T_{i+1}}} N(E)\mathrm{d}E. \tag{2.4}$$

for bin-based measurements, respectively. With $\mathrm{T_i}$ and $\mathrm{T_{i+1}}$ as adjacent energy thresholds.

Typical materials for PCDs are cadmium telluride (CdTe) and cadmium zinc telluride (CTZ). In experimental setups, silicon (Si) has also been utilized as a detector material [43, 104, 239, 289, 309]. The choice for the material depends on aspects of production, system integration and the physical requirements. Silicon, is easier to manufacture and, due to its pure form, offers favorable properties as a charge carrier and is less prone for polarization or charge trapping effects [51, 82]. However, the low atomic number of silicon ($\mathrm{Z_{Si}} = 14$) leads to a reduced absorption efficiency (cf. Section 2.3.1). Hence, an increased and unpractical detector thickness is required. CdTe/CTZ, as high-Z compound materials ($\mathrm{Z_{Cd}} = 48$, $\mathrm{Z_{Zn}} = 30$, $\mathrm{Z_{Te}} = 52$), provide high absorption efficiencies, allowing the integration of only thin crystal layers to a detector module. Yet, a complex manufacturing process and the very high requirement for material purity ($> 99.9999\%$) pose challenges in production.

The absence of impermeable septa increase the detector's geometric efficiency, allowing for hardware layouts with reduced pixel sizes and consequently acquisitions with increased spatial resolution down to 0.2 mm [120, 202, 281].

Several physical effects impair the quality of the pulse detection, leading to deterioration of the spatial and spectral sensitivity of the measurements, e.g. *K-fluorescense*, *charge sharing* or *pulse pile-up*.

The difference in atomic numbers also leads to a different distribution of the prevalent scatter- and absorption effects of the detector: Whereas the photoelectric effect is predominant for CdTe/CTZ-based detectors, most photons experience Compton scatter inside Si-based detectors. The photoelectric effect can lead to *K-fluorescence* or *K-escape* (Section 2.2.3), whereas Compton scatter causes multiple energy depositions at different locations before the photon gets annihilated (Section 2.2.2). The predominance of Compton scatter in Si-based detectors was found to lead to a degradation of the detector's quantum efficiency [240]. Both effects, however, potentially result in a degradation of the spatial and energy resolution [51, 239]. A case of K-fluorescence is outlined in Figure 2.5, where the fluorescent photon interacts at a different location (f), causing two detector events (g and h).

The event indicated in Figure 2.5 (e) is referred to as *charge sharing*. In this case one X-ray photon is absorbed close to a pixel boundary, and the resulting electric charge cloud is spread between two or more adjacent detector elements, such that multiple (lower) pulses are measured at different locations and with lower energies. The respective pulse heights correspond to the share of electrons that hit the single detector elements, which leads to a general underestimation of the detected energies, as only the sum of charges corresponds to the actual charge of the initial photon. Eventually, the distributed detection degrades the spectral resolution. Correction algorithms (e.g. *charge summing*) trying to overcome these limitations exist, particularly in the field of high-energy physics, where only single or a few photons are detected. These models utilize propagation assumptions of distributed adjacent signals to derive the actual location and energy of the original photon [16, 169, 171].

The high flux rate of clinical CT (about 10^9 events per second and square millimeter) require high sampling and readout rates from the PCD. *Pulse pile-up* describes the effect where two or more (nearly) coincidental pulses (with a finite width of about 10-15 ns) cannot be temporally resolved by the detector, leading to a combined detection and measurement of two or more pulses. As a result, there is an underestimation of the number of counted pulses and an overestimation of the detected energy [321, 323]. In Figure 8.1 two single pulses with 90 keV and 60 keV are measured as one pulse with 125 keV. This effect is more prominent for very high dose CT scans with increased tube current, but it does not play a practical role in current medical PCD CT scanners [271, 338, 364].

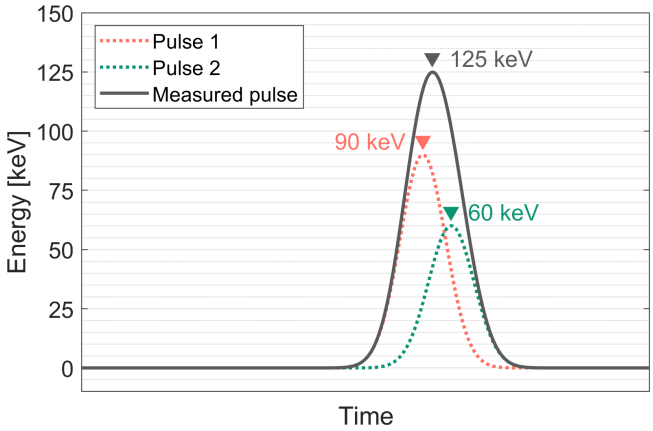

Fig. 2.7. Pulse pile-up occurs when the detector is not able to separate between two quasi-coincidental pulse signals. In this example two actual pulses with 90 keV and 60 keV are measured as one pulse with 125 keV. The non-linearity of the count rate will result in noisier (less photons) and spectrally distorted signals.

2.2 X-ray photon interactions

When traversing matter X-ray photons experience interactions, leading to deflection, scatter, or to their absorption. The extent of these effects defines the attenuation of X-ray photons. In the following the principal interactions relevant for CT imaging *Rayleigh scatter*, *Compton effect*, and *photoelectric absorption* are described.

A description of other interaction mechanisms, like *Thomson scatter*, *pair production*, or *photo-nuclear reactions* will be omitted, as they are negligible for the typical energy ranges of X-ray spectra (20-150 keV). Further information and elaborate explanations on interaction effects can be found at [35, 135].

2.2.1 Rayleigh scatter

Rayleigh scatter (also known as *coherent scatter* or *elastic* scatter) describes the deflection of an impinging photon while crossing a target atom (Figure 2.8 (a)). The photon excites the whole atom by causing in-phase oscillation of the atom's electrons, which leads to the emission of electromagnetic radiation and ultimately to the production of a photon with the same energy/wavelength as the initial photon, but with a deflected trajectory. During that process no loss of energy and hence no deposition of radiation dose occurs. The angle of the deflection mainly depends on the energy of the incoming photon, whereas the angle increases for lower energy photons and decreases for higher energy photons. For CT the Rayleigh scatter only has a limited relevance as it occurs mainly in the energy ranges between 15 and 30 keV - photons with energies within this range are usually removed by X-ray pre-filtration (cf. Section 2.1.2).

The likelihood of Rayleigh scatter to occur is proportional to the element's atomic number and inversely proportional to the square of the photon's energy [139]:

$$P_{\text{Rayleigh}} \propto \frac{Z}{E^2}. \tag{2.5}$$

Rayleigh scatter was discovered by John William Strutt Rayleigh, who later received the Nobel Prize in Physics for his investigations on gases and the discovery of argon [87].

2.2.2 Compton effect

Compton effect or *incoherent scatter* occurs when the energy of an impinging photon exceeds the binding energy of a target electron. During the interaction the electron (also referred to as the *Compton electron* or the *recoil electron*) ejects from its shell and the incident photon continues to traverse with deflected angle and with a decreased energy level (Figure 2.8 (b)). During this process and due to the loss of an electron the atom becomes ionized.

Compton scatter mostly occurs between the photon and outer valence shell electrons. The possible deflection angle of the photon ranges from 0° to 180° (so-called *back-scatter*), whereas higher energy photons have a greater chance to get deflected with a lower angle. Due to conservation of energy and momentum, the sum of the energy of the emitted photon and the kinetic energy of the ejected electron equals the initial photon energy.

The chance for the Compton effect to occur particularly can be formulated as [9]

$$P_{\text{Compton effect}} \propto Z \cdot f_{\text{KN}}(E), \tag{2.6}$$

The energy dependent cross-section of the Compton effect is described by the Klein-Nishina function $f_{\text{KN}}(E)$ [166]:

$$f_{\text{KN}}(\alpha) = \frac{1+\alpha}{\alpha^2}\left[\frac{2(1+\alpha)}{1+2\alpha} - \frac{1}{\alpha}\ln(1+2\alpha)\right] + \frac{1}{2\alpha}\ln(1+2\alpha) - \frac{(1+3\alpha)}{(a+2\alpha)^2}, \tag{2.7}$$

with $\alpha = E/510 \cdot 975$ keV. Thus, $f_{\text{KN}}(\alpha)$ shows only a slight dependence on the energy E.

Particularly for elements with lower atomic numbers, the relative attenuation due to the Compton effect increases. In case of high atomic numbers the photoelectric effect becomes dominant.

Yet, despite being the predominant effect occurring in the diagnostic energy range of CT, it is not the most responsible cause for energy deposition and therefore to radiation exposure to the patient, as only a fraction of the incident photon energy is deposited. Eventually, in the energy range for photon therapy (several MeV [269]), the Compton effect becomes the predominant photon interaction (cf. Section 3.3.5).

In CT, however, the Compton effect holds a great contribution to the degradation of the image quality as both, the possible strong deflection and the energy loss of the photon, do not allow to conclude the exact location of the interaction. Instead, the scattered photon gets ascribed to a different line integral, detected by another detector element, which ultimately results in increased noise and deteriorated spatial resolution. To reduce these artifacts, special mechanical and algorithmic scatter correction is required [202, 241].

The Compton effect is named after the American physicist Arthur Holly Compton, who received the Nobel Price in Physics in 1927 [86].

2.2.3 Photoelectric effect

The *photoelectric effect* occurs when the energy of an incoming (X-ray) photon exceeds the binding energy of a shell electron of a target material. During this process the entire energy of the initial photon is transferred to the electron, which leads to an annihilation of the incident photon and to an ejection of the electron, which is also referred to as the *photoelectron* (Figure 2.8 (c)). This effect is most likely to happen to electrons with binding energies greater or equal to the energy of the initial photon.

The kinetic energy of the photoelectron is equal to the difference of the kinetic energy of the initial photon and the electron's binding energy. Once ejected, the empty hole in the electron's orbit is refilled with an outer shell electron, which causes the emission of characteristic *X-ray fluorescence* radiation[5] or, as a secondary effect, an auger electron (see Figure 2.8 (c)). As the

[5] Corresponding to the sums of the different energy levels of the affected orbital shells.

energy of the emitted radiation/electron is rather small, consecutive interactions quickly lead to re-absorption. The initially affected target atom becomes positively ionized due to the net loss of at least one electron.

In general, the likelihood of the photoelectric effect to happen is proportional to the cubic of the (effective) atomic number of a given material, and it is inversely cubically proportional to the energy of the impinging photon [135, 211]:

$$P_{\text{photoelectric}} \propto \frac{Z^3}{E^3}, \tag{2.8}$$

Thus, for the purpose of differentiating between body materials with subtle differences in attenuation, the utilization of lower energy photons is of particular importance.

However, for materials with high atomic numbers the proportionality of these effects is perturbed with the presence of sharp absorption edges (slightly) around the material's specific (K/L/M/N) shell binding energies (as seen in Figure 2.9 (b)). Once the incident energy exceeds one of these binding energies, a strong increase in absorption occurs. This particular and material specific effect is utilized for radiation shielding or to increase local contrast in a clinical setting by applying iodine based contrast media. Naturally occurring elements in the human body, however, do not provide K-edges in the energy range relevant for CT.

The strong material and energy specific characteristics of the photoelectric effect facilitate a certain indication of the composition of a material when measured using X-rays [9] (cf. Chapter 3).

The photoelectric effect was firstly observed in 1887 by the German physicist Heinrich Hertz and later described in Albert Einstein's *theory of the photoelectric effect*, for which he received the Nobel Prize in Physics in 1921 [84].

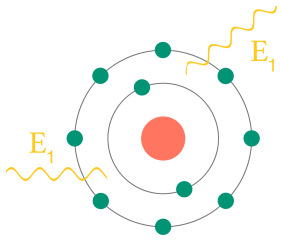

(a) Rayleigh scatter: An impinging photon deflects while crossing a target atom. The photon does not experience any loss in its initial energy.

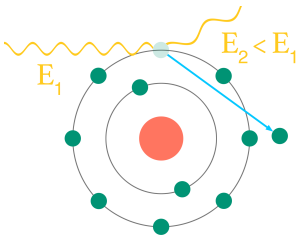

(b) Compton effect: An initial photon ejects an electron and continues to traverse with a deflected angle and with a decreased energy.

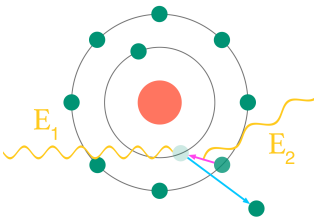

(c) Photoelectric effect: An incoming photon gets annihilated and ejects an inner-shell electron of the atom. The inner shell vacancy gets filled with an electron from an outer shell while emitting characteristic radiation or an auger electron.

Fig. 2.8. The predominant scatter and attenuation effects in clinical CT.

2.3 X-ray attenuation

The reduction of photons in an X-ray beam, referred to as *X-ray attenuation*, results from scatter effects and absorption effects as described above. In the following the linear attenuation coefficient and the mass attenuation coefficient are introduced. Both coefficients aim to depict the attenuation with respect to the thickness of an absorber, or to the thickness normalized to the local density, respectively. The *Beer-Lambert law* is used to describe the exponential decrease of X-ray intensity with respect to the distance and the mass attenuation of traversed materials.

2.3.1 Linear attenuation coefficient

The linear attenuation coefficient μ (in $\left[\mathrm{cm}^{-1}\right]$) is used as a metric to describe the net effect for a photon to interact with matter per unit thickness of a material. The value comprises a linear sum of the relative losses due to the described photon interaction effects. The linear attenuation coefficient depends on the energy E of the impinging photon, as well as the atomic number of the target element Z in the spatial coordinate $\vec{x}$ of a given event:

$$\mu\left(E, Z, \vec{x}\right) = \mu_{\text{Rayleigh}}\left(E, Z, \vec{x}\right) + \mu_{\text{Compton}}\left(E, Z, \vec{x}\right) + \mu_{\text{Photoelectric}}\left(E, Z, \vec{x}\right). \tag{2.9}$$

The chance for a photon to interact with matter depends on the local density (ρ in $\left[\mathrm{g} \cdot \mathrm{cm}^{-3}\right]$) along its trajectory. This yields to a linear proportionality of the linear attenuation coefficient to the density of a material.

2.3.2 Mass attenuation coefficient

The mass attenuation coefficient $\left(\frac{\mu}{\rho}\right)\left(E, Z, \vec{x}\right)$ (in $\left[\mathrm{cm}^2 \cdot \mathrm{g}^{-1}\right]$) normalizes the linear attenuation coefficient to the local density ρ [138], such that

$$\mu\left(E, Z, \vec{x}\right) = \left(\frac{\mu}{\rho}\right)\left(E, Z, \vec{x}\right) \cdot \rho. \tag{2.10}$$

Figure 2.9 depicts the mass attenuation coefficients for soft tissue and iodine in the energy range between 0 and 150 keV. Above 29 keV on the attenuation of soft tissue is mainly attributed to the Compton effect. For iodine the photoelectric effect is the predominant photon interaction. At 33.17 keV the binding energy of K-shell electrons is exceeded, which leads to a sudden increase in absorption.

An overview of mass attenuation coefficients for various elements and body tissues is provided by the International Commission on Radiation Units and Measurements (ICRU) [293, 346].

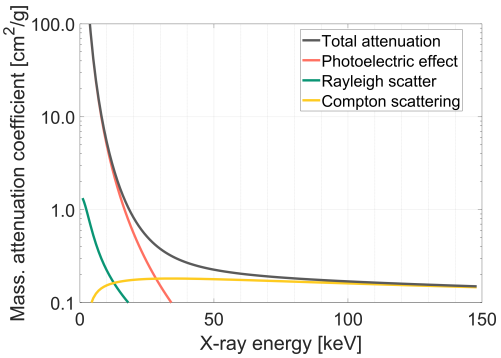

(a) The attenuation of soft tissue. The Compton effect becomes dominant at en energy of approximately 29 keV.

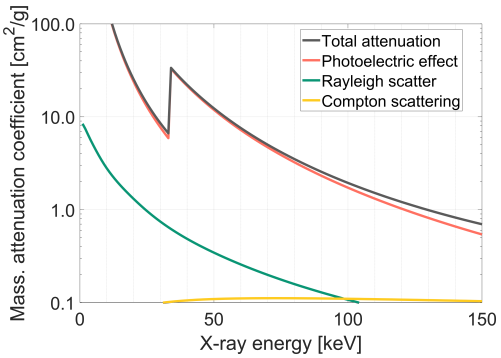

(b) In iodine (Z = 53) the photoelectric effect contributes mainly to the attenuation. The discontinuity at 33.17 keV is due to K-edge absorption.

Fig. 2.9. Mass attenuation coefficients within the energy range for clinical CT [138, 293].

2.3.3 Beer-Lambert law

The relationship between the initial beam intensity I_0 and a detected beam intensity I for a given photon traversing a material with a thickness Δx is described by the Beer-Lambert law [105, 127, 151]:

$$I_{\Delta\vec{x}} = I_0 \cdot e^{-\mu(\vec{x})\Delta x} \tag{2.11}$$

This equation provides information about the exponential loss of photons with a given energy while passing through a homogeneous absorber.

For an absorber comprising of inhomogeneous materials Equation 2.11 must be extended by the integration over the linear attenuation coefficients along a given line L:

$$I_L = I_0 \cdot e^{-\int_L \mu(\vec{x})\mathrm{d}x}. \tag{2.12}$$

To cover the use of polychromatic X-rays Equation 2.12 must be modified to include an additional integration over the individual energy levels E of a given X-ray spectrum:

$$I_{L,E} = \int_E I_0(E) \cdot e^{-\int_L \mu(E,\vec{x})\mathrm{d}x}\mathrm{d}E. \tag{2.13}$$

Finally, the so-called *System Weighting Function* (SWF) $w(E)$ is added to contribute for the characteristics of the X-ray source and the CT detector:

$$I_{L,E,w} = \int_E w(E) \cdot I_0(E) \cdot e^{-\int_L \mu(\vec{x},E)\mathrm{d}x}\mathrm{d}E, \tag{2.14}$$

with

$$w(E) = \frac{I_0(E) \cdot D(E)}{\int_E I_0(E) \cdot D(E)\,\mathrm{d}E}, \tag{2.15}$$

with $D(E)$ as the detector specific responsiveness to an impinging photon.

2.4 Spectral CT imaging techniques

Spectral CT imaging describes various methods to exploit the energy-dependence of the attenuation coefficient in order to derive material specific properties of the scanned object (cf. Chapter 3). A first approach on performing spectral X-ray was reported by Arne Enström in 1946, where he tried to depict material information in a histochemical level [65]. In 1953 Bertil Jacobson applied planar X-ray imaging using a monoenergetic X-ray source[6] to perform what he called *edge dichromography* (the application of X-ray energies that are slightly lower and higher than the K-edge of a material, cf. Section 2.2.3) or *continuous dichromography* (two monochromatic X-ray measurements with a great difference of energies.) [144]. In his groundbreaking report, Sir Godfrey Hounsfield indicated that the approximate determination of the atomic number is feasible using an X-ray machine [133].

Since then, technology has evolved tremendously, and to date, various different spectral acquisition techniques have found their way into clinical human imaging practice - and to the field of CT. Six spectral CT acquisition technologies will be presented in this section: *dual kV CT*, (*slow/fast*) *kV-switching CT*, *split filter CT*, *dual source dual energy CT*, *dual layer detector CT*, and *PCD CT*. An overview of the different methods is given in Figure 2.10. With the exception of PCD CT, all other CT technologies are limited to the acquisition of CT data in two different energy ranges (dual energy CT).

For further reading on the technologies, their characteristics and capabilities, the following references are recommended: [69, 82, 127, 137, 202, 221, 262, 368].

2.4.1 Dual kV CT

To perform *dual kV CT* (or *dual kVp CT* or *dual spin CT*) any type of CT scanner can be used, just by running two consecutive scans with different X-ray tube voltages (including or not including different beam filtrations (Figure 2.10 (a)) [127, 178, 202]. This approach provides great flexibility in clinical acquisition parameters by allowing sufficient time to change tube voltage, tube current to adjust the radiation dose, and beam filtering for spectral shaping. Additionally, all acquisitions are covering the entire field of view of the detector system, such that all scanned areas can be evaluated by their spectral properties.

[6] To obtain the monoenergetic X-rays they irradiated an element with a continuous X-ray spectrum. Together with the relatively small fractured mixed radiation they also attained a high fraction of primary radiation.

Changing the tube voltage or beam filtration results in a temporal delay between the two acquisitions. Unless the scanned object is not stationary, motion artifacts due to (internal or external) patient motion occur, which can only be partially corrected through registration algorithms. Additionally, spectral processing of contrast-enhanced CT scans as in CT angiography, or CT perfusion is not possible, as local contrast concentrations are varying between the two acquisitions [202].

2.4.2 kV-switching CT

In *kV-switching CT* the configuration of the single X-ray tube (voltage and current) alternates, such that two sets of images are acquired using alternating projections with two different X-ray spectra (low kV, e.g. 80 kV, and high kV, e.g. 140 kV). In *slow kV switching CT* the alternation happens after both X-ray tube and detector rotate 180° around the iso-center of the CT gantry (Figure 2.10 (b)).

In *fast kV* or *rapid kV switching CT* this alternation occurs rapidly with every two consecutive projections (approximately every 0.25 ms) (Figure 2.10 (c)). The acquired sets of projection data are nearly perfectly registered, providing a high level of temporal coherence and enabling spectral processing in the projection space [372]. Yet, with increased angular difference and longer switching times between the single measurements the number of projections per rotation becomes insufficient and the risk for streak artifacts increases [202].

With rapid kV-switching CT, two data sets at different mean X-ray energies are acquired, which both cover the same (full) field of view. However, whereas the tube voltage can be switched rapidly and almost instantly (which is necessary to achieve good spectral separation), the tube current cannot be changed rapidly between two projections. Depending on the setting, this limitation yields to either insufficient radiation dose and hence increased noise in the low energy data, or increased radiation dose for the high energy measurement and ultimately to an increased noise level in the spectrally processed images, caused by error propagation occurring during processing [164, 202]. To overcome this limitation asymmetric projection sampling (i.e. lower reading times for low kV measurements) was proposed (e.g. with GE's Discovery CT750 HD, GE Healthcare, Wauskesha, Wisconsin). However, this method requires a reduced speed, which consequently increases the risk for motion artifacts (e.g. for cardiac CT imaging [99]). Additionally, no spectral shaping of the high kVp X-ray beam to increase spectral separation is possible, because a corresponding pre-filter would have to be moved in and out of the beam too rapidly for an efficient technical realization [202].

A first prototype fast kV switching CT setup was reported in 1986 where a commercial CT Scanner (SOMATOM DR3, Siemens Healthcare GmbH, Forchheim, Germany) [152]. The first commercially available fast kV switching scanner was introduced in 2011 by General Electrics (GE Discovery CT750 HD, GE Healthcare, Milwaukee, Wisconsin) [368]. This system provided switching times that allowed a rotation speed down to 0.8 s.

2.4.3 Split filter CT

Split filter CT or *split beam CT* relies on modification of the X-ray spectrum by two different pre-filters without changing the kVp. Here a filter material (e.g. tin) covers one half of the X-ray beam, either in longitudinal or in azimuthal (Figure 2.10 (d)) direction, while another filter material (e.g. gold) covers the other half of the X-ray beam. Tin shifts the mean energy of the X-ray spectrum to higher values, while gold causes a slight shift to lower values. Split filter CT systems offer a cost effective solution for full field of view spectral CT imaging [56]. However, as both parts of the X-ray beam have to cover the full field of view at a sufficient number of different projection angles, only slow table feed (in case of spiral scan) is possible, which leads to prolonged acquisition times, unfavorable for fast contrast enhanced CT scans. Additionally, to maintain a sufficient radiation dose, the additional filtration requires the X-ray tube to run with an increased tube current and therefore an elevated tube load.

A first split filter CT system was presented in 1980 by Brian Rutt and Aaron Fenster [279]. Rutt and Fenster optimized the filter by its material (copper) and thickness (1 mm) by analyzing the image noise of the reconstructed CT images. They were also able to calculate beam hardening free virtual mono-energetic images. Since the first commercial introduction of CT scanners with split filter technique, multiple clinical evaluations have been published. Maso Di et al. successfully deliniated a pancreatic tumor using spectral CT data of a contrast enhanced scans acquired during the pancreatic and the portalvenous phase [56]. Just in 2021 Petritsch et al. compared a split filter CT scanner (SOMATOM Edge, Siemens Healthcare Gmbh, Forchheim, Germany) with a dual source CT System (SOMATOM Force, Siemens Healthcare Gmbh, Forchheim, Germany), investigating their capability to detect pulmonary embolism in CT pulmonary angiography scans. Whilst they found that both systems were capable of detecting the emboli, the performance of the split filter CT system was found inferior by different means: An increased level of image artifacts and slow acquisition times (9 s vs 2.5 s with a pitch of 0.25 and 0.55, respectively) led to significantly higher mean effective dose, a reduced detection accuracy and even to an increased number of non-diagnostic scans [243]. In a phantom study Euler et al. also found an overall reduced level of spectral separation when using a split filter CT-system compared to a dual source CT system [66].

2.4.4 Dual source dual energy CT

Dual source CT (DSCT) scanners have been introduced in 2006 [81]. DSCT scanners have two pairs of X-ray tubes and detectors embedded orthogonally to each other (about 90-95° offset) in one single CT gantry (Figure 2.10 (e)). For the acquisition of dual energy CT data, one X-ray tube is operated at a low kVp (e.g. 80 kVp), while the other X-ray tube is operated at a high kVp (e.g. 140 or even 150 kVp). Both X-ray tubes can be configured individually, both with tube voltage and tube current, which can be used to achieve similar radiation dose and hence similar noise levels in both acquired CT images. In addition both X-ray beams can be filtered individually, to further increase spectral separation. Both the improved spectral separation and the adjusted image noise contribute to low contrast-to-noise ratios (CNR) in spectrally processed images (e.g. material-specific) images [69, 81, 148, 202, 255].

The projection data acquired from the two distinct tube/detector systems exhibits a phase shift by design, therefore, spectral processing is performed in the image domain.

Another limitation of this setup is that scattered photons from one X-ray source can be detected by the other detector system (*cross scatter*), causing artifacts, leading to deterioration of the CNR and reduction of spectral separation of the low kV and high kV-images. Dedicated scatter correction is required to reduce the adverse effects of photon scatter (cf. Section 2.2.2).

Ultimately spectral processing is only possible in the area that is covered by both X-ray beams, i.e. by both fields of views. This congruent area is limited by the X-ray beam with the narrower width (Figure 2.10 (d), green circle).

2.4.5 Dual-layer detector CT

Dual/multi-layer CT (also *split detector* or *sandwich detector CT*) is characterized by a stack of detection layers, where X-ray photons with lower energies are absorbed and detected in the upper detector layer and higher energy X-ray photons detected by a detector layer underneath (Figure 2.10 (f)) - a setup enabling energy sensitive measurements within a single acquisition and a single CT detector.

An early dual-layer CT system was presented by Rodney A. Brooks and Giovanni Di Chiro in 1978 [31]. Their detector consisted of a stack of crystals made from calcium fluoride (providing a medium level of photoelectric absorption) and sodium iodide (with a very high level of photoelectric absorption), respectively, and was embedded in a EMI Mark 1 CT scanner (cf. Section 1.1.2). The observed spectral sensitivity was found superior to dual kV measurement with 100 and 140 kV.

Since then more advanced dual-layer based CT systems were introduced [7, 221, 264] and dual layer CTs found their way into clinical practice. The detectors comprise two scintillators based on yttrium garnet (upper layer) and on gadolinnium osysulfide (lower layer) [262].

CT images acquired using dual layer CT detectors are always perfectly registered - both temporarily and spatially, which facilitates spectral processing in both image space and projection space. Both acquisitions cover the same field of view, as every detected pixel acquires both low energy and high energy data. Unlike dual source dual energy CT, cross scatter effects don't degrade the spectral sensitivity of the measurements. However, detector-level crosstalk can occur [262]. Overall, the spectral separation of dual layer CT is found inferior to other acquisition techniques, such as kV switching CT, dual source dual energy CT or PCD CT [69, 164]. The number of absorbed photons per layer strongly depends on the fixed detector design (i.e. fixed materials and fixed thicknesses of each layer), but also on the absorption of the measured object, therefore the noise levels of the two sets of acquired images differ [269]. This leads to elevated noise levels in the spectrally processed CT images. The acquisition speed of such systems is mainly dependent on the longitudinal detector coverage and the rotation speed of the systems. The latest clinical dual layer CT systems achieve a pitch of 1.5.

2.4.6 Photon counting detector CT

Just as dual layer CT detectors, PCDs resolve one incoming X-ray spectrum, rather than detecting multiple different ones (Figure 2.10 (g)). Yet, only PCDs are capable of measuring the energy of an impinging X-ray photon and providing CT data in more than two different X-ray energy ranges. The basic principles of PCDs are described in Section 2.1.3.

PCDs have a long history of use in the field of high-energy physics, where they are well-suited for detecting single photons under well controlled measuring conditions. In medical CT imaging, however, specific requirements on design and implementation of these detectors exist. Here the detectors must be capable of resolving high photon flux rates with up to 10^9 events per second and square millimeter. The detectors must operate within a thermally stable environment (room temperature) and withstand mechanical stress emerging from the high rotation speeds of the CT gantry. Ultimately, the CT scanner must meet requirements on data transfer and data storage, as substantially large amounts of data are produced during acquisition[7].

Inherent to the detector's operating principle PCDs always resolve one X-ray spectra into multiple single spectra by applying adjustable energy thresholds, which facilitates an optimized system configuration for specific acquisition modes and particular clinical interests (cf. Section 3.3.8). All projections are perfectly registered and cover congruent information from the scanner's entire field of view [202, 262].

The incorporation of PCDs for medical CT imaging gained momentum in the recent years, with various pre-clinical assessments [43, 157, 161, 273, 367], first clinical installations and evaluations [111, 183, 273, 358, 360] and finally with the clearance of the first commercial PCD based CT scanner [83]. In a press statement on September 2022 the U.S. Food and Drug Administration stated the clearance of the "first major imaging device advancement for computed tomography in nearly a decade" [72]. Up to now multiple clinical applications of using PCD CT scanners have been reported [22, 121, 177, 281, 282, 304, 306, 345].

[7] The amount of data increases proportionally to the number of applied energy thresholds and to the corresponding increase in pixel numbers.

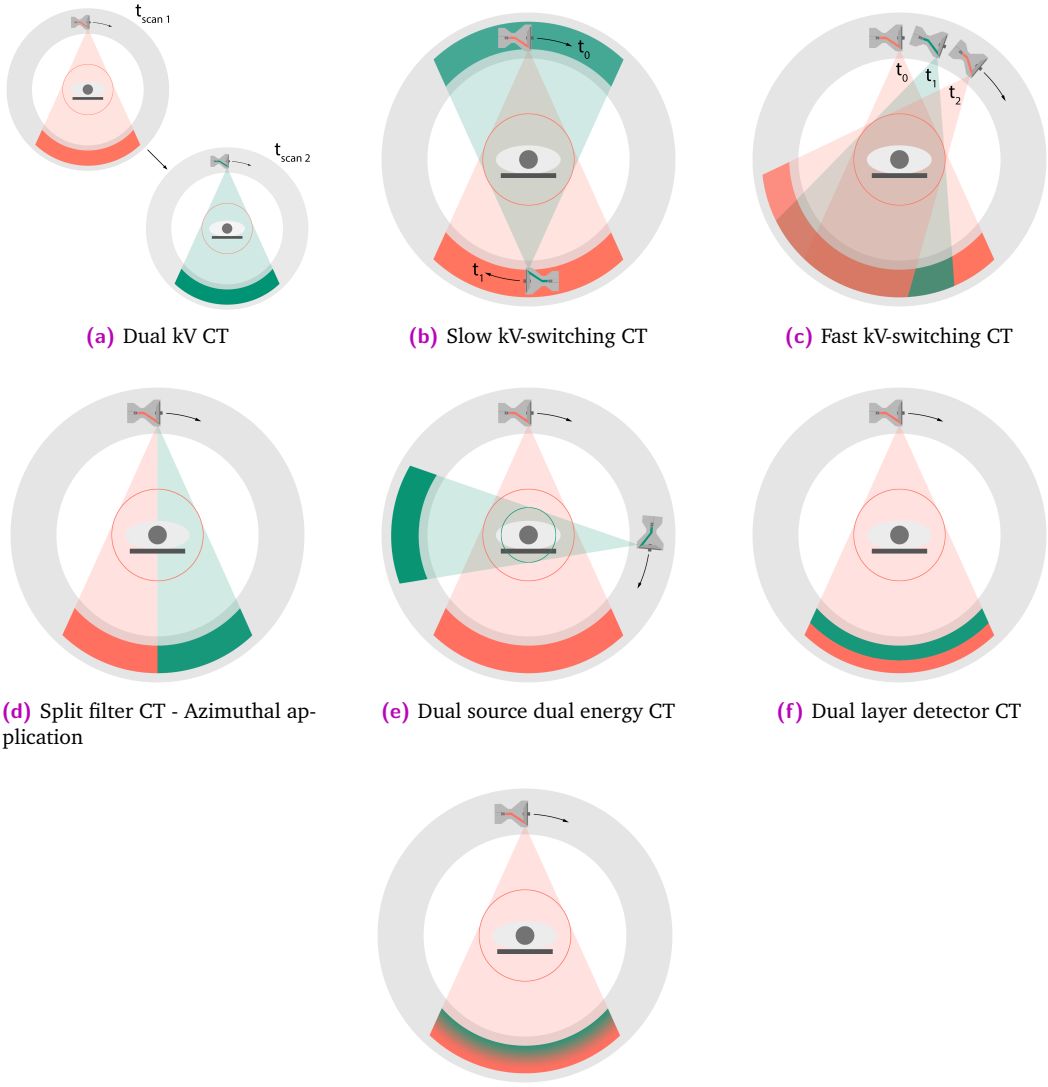

(a) Dual kV CT

(b) Slow kV-switching CT

(c) Fast kV-switching CT

(d) Split filter CT - Azimuthal application

(e) Dual source dual energy CT

(f) Dual layer detector CT

(g) Photon counting detector CT

Fig. 2.10. Overview of different spectral CT imaging technologies.

3 Spectral CT image processing and clinical applications

Spectral CT imaging techniques are based on the acquisition of two or more measurements in different X-ray energy ranges. The ability of spectral CT imaging to differentiate between different types of tissue and to quantify (contrast) materials makes it a valuable tool in both technical and clinical applications.

In the first part of this chapter, a comprehensive overview of the basic concepts and principles of material decomposition, both in the image domain and in the projection domain, is provided. Material labeling and material quantification is discussed in the second part of this chapter. The third part sets a particular focus on basic and advanced technical and clinical applications of spectrally sensitive CT imaging. Various examples and ongoing research are presented.

3.1 Energy selective base transformation of CT measurements

In an early study (1953) Bertil Jacobson showed that the characteristic attenuation properties of materials can be derived using X-ray technology (Section 2.2). In an experimental setup he used two monochromatic X-rays and he observed differences in absorption and distribution of material concentration. He referred to this method by calling it "dichromography" [144] - a spectral X-ray acquisition technique.

Later, in 1976, Alvarez and Macovski published a report in which they demonstrated that spectral information of a material, e.g. the contribution of the photoelectic effect and the compton effect, can also be derived from polychromatic X-ray spectra [9].

For this purpose they assume the attenuation coefficient to be a linear combination of attenuation (base) functions:

$$\mu(E) = a_1 \cdot f_1(E) + a_2 \cdot f_2(E) + \cdots + a_n \cdot f_n(E) \tag{3.1}$$

The choice of basis functions generally relies on empirical considerations. However, the authors chose two functions that correspond to the predominant photon interactions in CT: the photoelectric effect (cf. Section 2.2.3) and the Compton effect (cf. Section 2.2.2):

$$\mu\left(E\right) = \rho \cdot \left(\left(\frac{\mu}{\rho}\right)_{Photoelectric}\left(E, Z_{\text{eff}}\right) + \left(\frac{\mu}{\rho}\right)_{Compton}\left(E, Z_{\text{eff}}\right) \right) \approx \rho \cdot \left(\alpha_1 \cdot \frac{Z_{\text{eff}}^k}{E^n} + \alpha_2 \cdot Z_{\text{eff}} \cdot f_{\text{KN}}\left(E\right) \right), \tag{3.2}$$

where ρ depicts the local density. The scalar terms α_1 and α_2 are constants that consider the mass density, atomic weight and atomic number of the given material. The terms $\frac{Z_{\text{eff}}^k}{E^n}$ and $Z_{\text{eff}} \cdot f_{\text{KN}}\left(E\right)$ correspond to the probability for the occurrence (i.e. the *cross-section*) of the photoelectric effect (cf. Equation 2.8), and the Compton effect (cf. Equation 2.6), respectively.

Additional functions can be added that account for discontiuous absorption properties of materials with a K-edge absorption (cf. Section 2.2.3) within the typical energy range of CT X-ray spectrum [270]. This method is also referred to as *K-edge imaging*:

$$\mu\left(E, Z_{\text{eff}}\right) = \rho \cdot \left(\alpha_1 \cdot \frac{Z_{\text{eff}}^k}{E^n} + \alpha_2 \cdot Z_{\text{eff}} \cdot f_{\text{KN}}\left(E\right) + \sum_{i=3}^{n} \alpha_i \cdot f_{\text{K-edge},i}(E, Z_{\text{eff}}) \right). \tag{3.3}$$

Equation 3.3 enables a separation into n different materials. In order to solve this equation (without additional constraints, e.g. mass conservation [189] or volume conservation [188, 191, 275]) at least n CT measurements are required.

The proposed decomposition method can be used to associate and quantify densities and compositions of materials, which, as Alvarez and Macovski recognized already, has a significant purpose for medical imaging.

Rodney A. Brooks and Lehmann et al. demonstrated that the principle of the described decomposition method can also be applied in the image domain by using n material-dependent and spectrum-specific base vectors [32, 178]:

$$\mu\left(E, Z_{\text{eff}}\right) = \sum_{i=1}^{n} \left(\frac{\mu}{\rho}\right)_i \left(E, Z_{\text{eff}}\right) \cdot \rho_i. \tag{3.4}$$

In 2007 Ewald Roessl and Roland Proska applied the described material decomposition method to projection domain data (i.e. data before image reconstruction), generated by a PCD CT simulation. Based on the generated measurements they decomposed attenuation coefficients a_i (Equation 3.1), corresponding to the photoelectric effect, Compton effect and the mass attenuation of a K-edge material [272].

In their work, Roessl and Proska assume independent Poisson distributions for measured photons within N energy bins, as well as absence of electronic noise and noise from incomplete charge collection. They calculate the expectation value λ_i of the number of photons per energy bin as follows:

$$\lambda_i\left(A_1, A_2, A_3\right) = \int_0^\infty S_i\left(E\right)\Phi\left(E\right)\mathrm{e}^{-\sum_{a=1}^{3} f_a(E)A_\alpha} D\left(E\right)\mathrm{d}E, \tag{3.5}$$

with A_α as line integral of the scalar coefficients a_i from Equation 3.1, and S_i as bin sensitivities, expressed as rectangular Heaviside functions determined by two adjacent energy thresholds. $\Phi(E)$ denotes the X-ray photon flux and $D(E)$ describes the detector responsivity (Section 2.1.3).

In case where the number of acquisitions exceed the dimension of the base functions, optimized parameters can be determined via least squares methods (e.g. by variance minimization using the *Best Linear Unbiased Estimator* [93]) or by methods of maximizing likelihood/minimizing negative log-likelihood [272].

After optimization base function specific images (e.g. material specific images) can be reconstructed by applying conventional reconstruction methods.

3.2 Spectral CT image processing: Material labeling and material quantification

Spectral CT acquisitions produce measurements yielding two or more distinct CT values for each voxel. Specifically in dual energy acquisitions, the measured CT values pertain to both low energy and high energy acquisitions. The measured CT values can be displayed in a so-called *dual energy plot* (or *low-high-kV diagram*, or *CT-value diagram*), where usually the CT values of the low energy acquisition are plotted along the y-axis, while the corresponding CT values of the high energy acquisition are plotted along the x-axis. The ratio between both values (i.e. CT value of the low energy acquisition divided by the CT value of the high energy acquisition) is defined as the *Dual Energy Ratio* (DER). The appearance of the plot is by definition dependent on the combination of the applied or resolved energy spectra (including beam hardening) and the measured materials (cf. Section 2.3). The CT values for a specific material also vary based on its density or local concentration. Neglecting image noise, changes in density or concentration will result in CT values that align along a specific vector in the dual energy plot.

Within the dual energy plot, materials can either be distinguished (material labeling) or quantified (material quantification).

3.2.1 Material labeling

Material labeling is used to discriminate, label, or classify materials and tissues in spectral CT images. It can be used to determine the presence or absence of specific materials and structures with otherwise (i.e. in single energy CT acquisitions) indistinct morphologies. The method behind material labeling relies on a threshold slope which originates on a reference material in the dual energy plot (e.g. water or soft tissue). Measured materials are labeled with respect

to their location relative to the separation threshold within this plot. CT-values located in exclusion/cutoff areas are not considered in the labeling. A comprehensive illustration of this methodology is provided in Figure 3.1 (a).

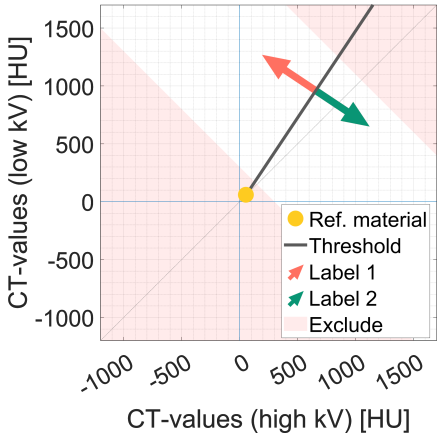

(a) The algorithm utilizes a threshold slope (gray line) based on a reference material (yellow) in the dual-energy plot, such as water or soft tissue. Materials are assigned labels (orange/green) according to their positioning in relation to the plot's separation threshold. CT values that fall within the exclusion or cutoff regions (red) are excluded from the labeling process.

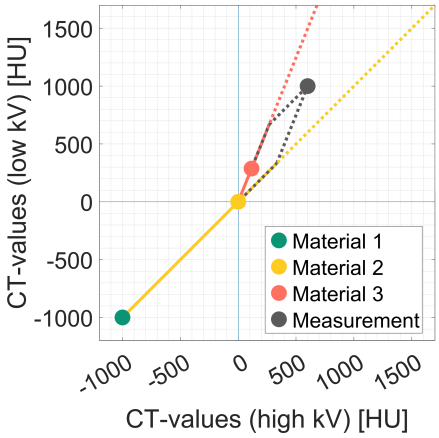

(b) Principle of spectral CT material quantification: Two base vectors are defined by three different materials, e.g. air (green), water (yellow), and iodine (orange). A calibration scan with known concentration of material 3 indicates an amount (scalar) to the respective base vector. Any measured pixel (gray) is represented as a linear combination of the base vectors. Material quantification is enabled by projecting the relative contribution of this linear combination to the respective base vectors.

Fig. 3.1. The principles of material labeling and material quantification.

The results of this method can be visualized either as color coded overlays with corresponding lookup tables, or with replacements or masks of the CT-values. Material labeling is particularly useful in distinguishing between different bone types, such as trabecular versus cortical bone [313, 316]. It is also employed in bone removal for angiographic imaging (cf. Section 3.3.1), to distinguish fat tissue from cartilage, tendons or ligaments [263], or to differentiate among different types of kidney stones (cf. Section 3.3.2).

3.2.2 Material quantification

Material quantification relies on the definition of multiple base materials (or *base material vectors*), which are defined by their CT-values in the dual energy plot. Lehmann et al. illustrated that measurements of materials can be expressed as linear combinations of the coefficients of base materials, allowing for the separation into their relative contributions to the measured material [178]. With additional calibration scans (i.e. prior measurements of materials with known concentrations) quantitative measurements are feasible.

In dual-energy CT, it's possible to separate two materials because two measurements allow for the calculation of two mass fractions. However, clinical relevant applications, such as the quantification of contrast uptake in tumors, or measuring iron in a patient's liver, necessitate the decomposition into three base materials. To achieve this, additional constraints must

be applied. An initial method presumed a constant volume fraction for the three materials. However, this presumption holds true only for solid materials or solutions in which the volume displacement (or the molecular interaction) upon mixing is precisely known [189]. In contrast to a material's volume fraction, its mass faction (i.e. its concentration) remains after mixing, following the law of conservation of mass. Liu et al. demonstrated that the individual mass fractions of three materials can be determined from dual-energy CT scans by adhering to the principle of mass-fraction conservation [189].

Figure 3.1 (b) illustrates an example of material quantification. It shows the projection, or decomposition, of a measured pixel (gray) into its component that aligns with the base vector typical for contrast agents with high atomic numbers (orange), and the respective component along another material vector representing water (yellow). Prior knowledge about the scale of the contrast material vector allows for the precise determination of the contrast concentration, while the projection on the water-vector facilitates the calculation of so-called *virtual non-contrast* (VNC), or *virtual un-enhanced* (VUE) images (cf. Section 3.3.7).

With the acquisition of more spectral CT data the quantification of materials can extended even further by considering additional base material vectors, including vectors of heavy elements (cf. Section 3.3.8).

In the result image, the separated or quantified materials can be visualized blended (i.e. superimposed) monochromatic, or color-coded images, as shown in the following examples.

3.3 Clinical applications for spectral CT image processing

The following section presents a wide range of practical examples that demonstrate the utility of spectral CT imaging in clinical practice. These applications involve material labeling and the quantification of different materials, aiming to enhance the diagnostic quality of the acquired CT images.

3.3.1 CT angiography and bone/plaque removal

CT angiography (CTA) is a medical imaging technique used to evaluate the vascular system of a patient. This method allows for the visualization of contrast enhanced blood vessels, including the arteries and veins, in a non-invasive manner. CTA is particularly useful in the diagnosis and assessment of peripheral arterial diseases (PAD) or other pathologies, such as thoracic, abdominal, or intracranial aneurysms. PAD summarizes various conditions that impair the blood flow in the limbs, often caused by the buildup of plaque in the vessels, a condition known as atherosclerosis. Atherosclerosis can lead to local stenosis, or narrowing of the blood vessels. By using CTA adequate treatment of PDA or aneurysms, whether surgical or non-surgical, can be planned.

Typical CTA acquisitions cover large scan ranges (e.g. pelvis to toes) and are reconstructed with thin slices (1-2 mm) to allow the detection of small stenosis; this results in the generation of large data sets. To reduce the time for reading and diagnosis CTA images are volumetrically-rendered [313] and displayed using *maximum intensity projections* (MIPs), which is a projective visualization showing only voxels with the highest attenuation along a linear viewing trajectory [223]. However, in MIPs the strong X-ray attenuation of bone and bony structures leads to superposition of bones on vessels. This circumstance can be particularly critical for the assessment of vessels with close proximity to bones (e.g. intercostal or intervertebral arteries) [34]. The virtual *removal* of bony structures facilitates a *angiography-like* visualization out of CT images [313].

Several methods of virtual bone removal have been proposed; Single CT-value threshold-based methods lack the ability to differentiate between real bone, plaques or contrast enhanced vessels and therefore lead to increased false positive or false negative segmentations [290]. Both *dual scan subtraction* [307] and *dual scan masking* [335] rely on a prior unenhanced CT scan, which is used to identify bones that are either subtracted or, respectively, masked (affected voxels are set to -1000 HU) from a subsequent contrast enhanced scan. However, these methods are sensitive to patient motion and require an additional scan with additional radiation dose.

Dual energy based methods, however, utilize the absorption properties of base materials, such as soft tissue, iodine (for the enhanced vessels) and bony structures (including density ranges from porous trabecular bone to solid cortical bone) [148, 181, 291, 339, 340]. Studies have shown that dual energy based masking methods provide a higher sensitivity for bone and increased contrast to noise ratios, when compared to threshold-based or subtraction-based methods [316]. An example showing the results of a threshold-based approach vs. a dual energy-based method is depicted in Figure 3.2.

The automated nature of these methods also lead to a reduction of reading time by almost 32% (173 ± 53 s vs. 253 ± 12 s) of efficient dual energy based methods, when compared to threshold based methods [212].

While digital subtraction angiography (DSA) remains the gold standard to assess the patient's vascular system, the findings of CTA still provide a high level of correlation to those of DSA [34]. CTA also allows fast, minimal-invasive, as well as cost-effective diagnosis, particularly for time-critical situations as in patients with acute stroke [34]. However, the imaging of calcified plaques remains a challenge, as they are usually located in thin vessels and provide very high CT-values causing streak artifacts (so-called *calcium blooming*). Applying bone removal to plaques can lead to an overestimation of stenosis and an underestimation of the vessel's lumen [34, 261, 313, 369]. Just recently a novel algorithm was proposed, aiming to overcome this limitation by omitting calcified contributions (from calcified lesions, bone, etc.) while maintaining all other material contributions [6]. In a first step virtual monoenergetic images (cf. Section 3.3.6) are generated, used as an input for a final blending with an iodine image. In parallel a spectral material decomposition (cf. Section 3.3.7) into iodine and calcium is performed and a virtual non-calcium CT image is generated, comprising voxel-wise contributions from all materials but calcium. The complementary calcium image is used as a so-called *calcium map*, containing voxel-wise weighting functions for the monoenergetic

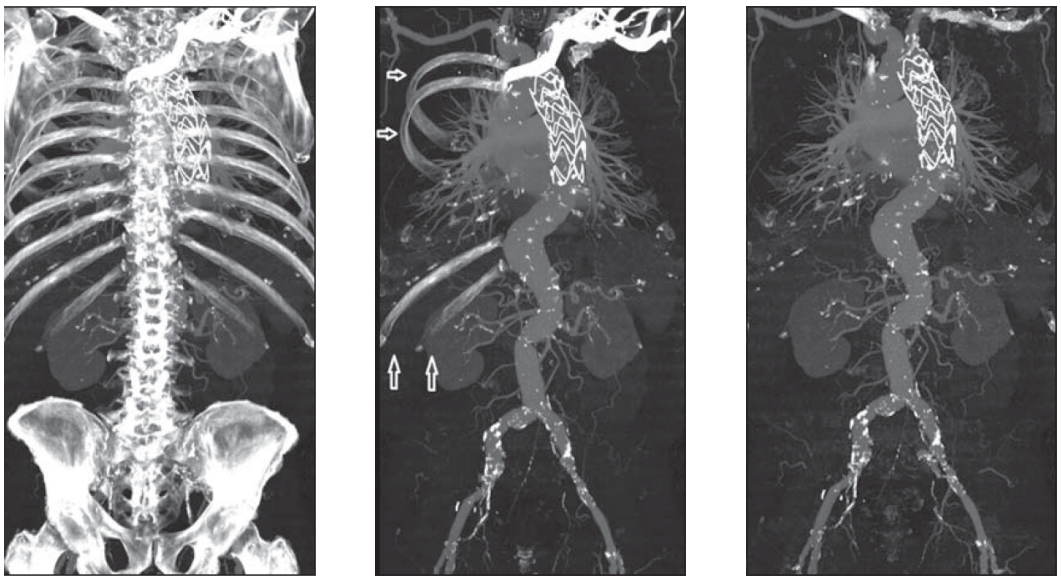

(a) Without bone removal.

(b) With attenuation-based automatic bone removal. Some bones were not removed (arrows).

(c) With spectral automatic bone removal (dual energy mode).

Fig. 3.2. 56-year-old man with implanted stent graft in the descending thoracic aorta. Frontal maximum-intensity-projection CT angiograms (from [290]).

image and the iodine-image. Finally a soft tissue-offset considers voxels without contribution of iodine or calcium, in order to facilitate normalized and physically meaningful CT-values within the Hounsfield scale. The results of a cardiac motion-phantom study indicates more accurate estimations of occlusions and free lumen, when compared to solely monoenergetic images (50% for the novel algorihtm vs. 56% for the monoenergetic image at a 50% stenosis, and 32.5% for the novel algorihtm vs. 36% for the monoenergetic image at a 25% stenosis) [6].

3.3.2 Kidney stone differentiation

Kidney stones (or *renal calculi*, *nephrolithiasis*, *urolithiasis*) are solid masses that form in the kidneys. Uric acid (UA) based kidney stones are composed of light chemical elements ($C_5H_4N_4O_4$). Other types of kidney stones are comprised of heavier elements as in of calcium-based stones (mainly calcium oxalate, $CaC_2 \cdot 2O_4$, or calcium phosphate $Ca_3\,(PO_4)_2$), struvite (NH_4MgPO_4), cystine ($(SCH_2CH\,(NH_2)\,CO_2H)_2$), or brushite ($CaHPO_4 \cdot 2H_2O$).[1]

The origins of kidney stones can be manifold, e.g. resulting from an increased purine intake and unhealthy diet (UA, calcium), after development of too much ammonia in the urine (struvite), from metabolic defects (cystine), or when brushite does not translate to hydroxypatite [60, 61, 173, 185].

[1] Atomic numbers for the mentioned elements: $Z_H = 1$, $Z_C = 6$, $Z_N = 7$, $Z_O = 8$, $Z_{Mg} = 12$, $Z_P = 15$, $Z_S = 16$, $Z_{Ca} = 20$

CT is accepted as an effective and efficient tool to identify and localize kidney stones, as it is fast and available [102]. However, knowing where the stone is located is insufficient for the planning of subsequent treatment. Additional information about the density and composition help to triage different treatment approaches [30]. For example, while the physical destruction of kidney stones by *external shock wave lithotripsy* (ESWL) can be applied to stones of mixed composition and to struvite-based stones, cystine and calcium-based stones are resistant to this form of therapy [30, 54, 126]. Some treatments, such as ESWL and invasive urinary procedures, carry a risk of renal bleeding and fibrosis. They are not appropriate for stones that can be treated pharmacologically, such as stones based of cystine or UA [68].

Early approaches to the characterization of kidney stones relied solely on the measurement of the CT value [208, 215], but depending on the composition and density of the stone, as well as the X-ray spectrum used (tube voltage and filtration), it can be concluded that the CT value is not a reliable measure [254]. Spectral CT introduced stability in the differentiation of different stones. The different stone types provide stable DER for fixed combinations of tube voltages and patient sizes. Even changes in density (solid vs. porous stones) align on the specific material vector [254]. Based on prior calibration the separation of UA-based stones to other types of stones yield accuracies and sensitivities of 95% and 88% or higher [74, 102, 113, 208, 254]. With the use of PCD CT, the differentiation of cystine from calcium oxalate and calcium phosphate has also been demonstrated [113].

An example of the differentiation of uric acid and calcification is shown in Figure 3.3. Here, spectral processing of the data reveals the heterogeneity of the stone as it comprises of UA and calcified components.

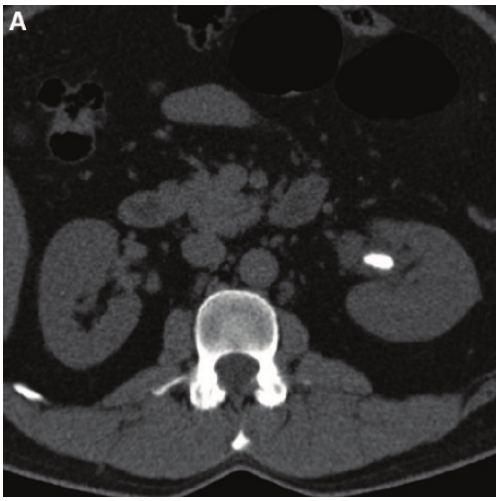

(a) 11 mm urolith in the left renal pelvis in a 40-year-old male patient. Analysis of the stone composition was not possible based on the HU values of the stone.

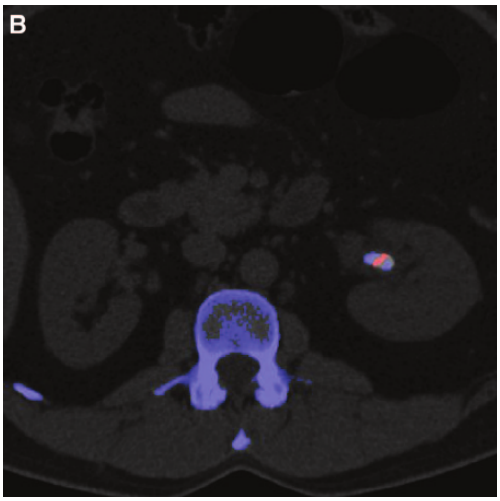

(b) The corresponding DECT color coded image shows that the calculus has uric acid and calcified components. Chemical analysis yielded 20% uric acid, 40% of calcium oxalate monohydrate, and 40% of calcium oxalate dihydrate.

Fig. 3.3. Exemplary kidney stone characterization (from [102]).

3.3.3 Lung perfused blood volume measurement

Ventilation/perfusion scintigraphy (also known as *V/P scintigraphy* or *V/Q lung scan*[2]) is considered the gold standard to detect impairments in lung ventilation and perfusion. The V/P scintigraphy consists of two separate measurements and the application of two tracers: First, an aerosol tracer (e.g. graphite crucible micro-aerosol particles labelled with technetium-99m pertechnetate (known as *Technegas*)) is applied using a respiration mask. The signal of this tracer is detected by a gamma camera. The acquired images represent the ventilation of the aerosol in the patient's lung. In a second step a second tracer (e.g. Technetium-99m labelled macroaggregated albumin (^{99m}Tc-MAA) is intravenously injected. Again, the signal is detected by a gamma camera and the output image reflects the patient's local perfusion of the lung parenchyma. An assessment of the correlating signals allows the physicians to understand whether a pulmonary emboli is present (when correlated) or not (when not correlated) [327]. The long acquisition time of ventilation/perfusion scintigraphy yields to a decreased detail in spatial resolution of the findings.

CT can be used to assess the morphological structure of a lung, but also its vasculature, and, when spectral CT is applied, its local contrast perfusion[3] [98, 327]. A dedicated application is used to detect local perfusion defects and defect patterns across the lung parenchyma, which allows to draw conclusions about underlying pathological reasons, e.g. pulmonary thromboembolic disease or interstitial lung disease [251, 328]. The application utilizes dual energy CT acquisitions and applies a pixel-wise two material decomposition into the material vectors air-soft tissue and air-iodine, specific for the applied/detected X-ray spectra [148, 327]. Additional HU-based clipping thresholds are applied to exclude highly attenuating pulmonary vessels and soft tissue [98]. The resulting contrast-map serves as a colored overlay blended over the CT image, visually mapping local contrast uptake to its corresponding morphology [98, 327].

A typical application is the detection of perfusion defects caused by pulmonary emboli (PE). Such defects can lead to pulmonary arterial hypertension and right heart failure [98]. The information obtained by the perfusion map can be used to determine the relevance of a detected pulmonary emboli for local blood oxygenization and disease/treatment prognosis [327]. Figure 3.4 (a) shows the perfusion defect caused by a pulmonary emboli, which is indicated in Figure 3.4 (b).

Thieme et al. evaluated the correlation of perfusion measurements from spectral CT scanning to perfusion scintigraphy [327]. In their findings they determined a per patient accuracy for detecting PE with a sensitivity of 75%, specificity of 80% and a negative predictive value (true negative findings over true negative and false negative findings) of 66%. For a detection of PE per lung segment they reached a sensitivity of 83%, specificity of 99% and a negative predictive value of 93%. They concluded that the CT findings of perfusion defects are in good agreement with the results from scintigraphic measurements.

[2] *Q* for *quantity* was used by initially used by French scientists to refer to the blood flow rate and is now used as a symbol for several other types of perfusion [53].

[3] There is an ongoing discussion whether the term *perfusion* is justified, as the measurement only represent results for one point it time. *Lung perfused blood volume* is found the preferred terminology which takes the temporal state of the acquisition into account [131, 327].

In another study Thieme et al. investigated the use of iodine maps from spectral CT acquisitions to differentiate between occlusive or non-occlusive PE [328]. The sensitivity for detecting occluding PE reached 100%, with a specificity of 95%. However, the sensitivity of non-occlusive PE only reached 58%, with a sensitivity of 92%. An example of a lung with a perfusion defect caused by an occluding embolus is shown in Figure 3.4.

Whether local iodine uptake correlates with the presence of *ground-glass opacities* (GGO) with vascular origin was investigated by Pontana et al. [251]. GGO appear as hazy hyperattenuating opacities and in conventional CT images. While their pathogenic origin is non-specific, they can either be caused by alveolar origin by filling of airspaces and/or interstitial thickening, which could be caused by infections pneumonia, hemoptysis, or cardiogenic edema, or due from a vascular origin caused by increased local capillarization, e.g. from pulmonary thromboembolic disease or asthma [251]. As GGO of vascular origin provide an increased iodine uptake, the detection with lung perfused blood volume measurement yield a detection sensitivity of 99.5% and specificity of 88.3%.

The CT based perfusion measurements benefit from the fast acquisition time, its availability and its spatial resolution, as conventional CT images are used as high-resolution morphological maps below the iodine map overlay [327]. In conjunction with the functional images, the conventional CT images can be used for differential diagnosis of interstitial lung disease, represented as emphysematous areas or tissue fibrosis [327]. However, artifacts caused by motion (e.g. heart, diaphragm, patient motion) can lead to to spectral distortion and therefore to false perfusion information. This effect was found strongest in the proximity of the heart [98]. Also, especially for spectral CT acquisitions using dual source CT systems the limited field of view causes restrictions on the area where spectral processing is possible [327, 328]. In their study Thieme et al. found that 18% of the known PE could not be seen in the reduced FOV [327]. Yet, this limitation can be overcome using full FOV spectral CT acquistion techniques. The high resolution of PCD CT could also support the detection of small emboli, as the prognostic implication is more influenced by small occlusive emboli, than large non-occlusive ones [98].

3.3.4 Lung ventilation measurement

Typical pulmonary function tests (e.g. spirometry or plethysmography) are often found to provide only insufficient sensitivity and specificity for the conduction of comprehensive clinical diagnosis. The results from these measurements allow for global but not local assessment of ventilation defects in the respiratory system [131, 168, 172]. Fast acquisition speeds and the availability of spectral imaging enabled CT to be used as an instrument to assess local lung ventilation. An exemplary application is the assessment of lung ventilation applying spectral material decomposition using air-soft tissue and air-xenon as base material vectors. For the practical use dedicated xenon control systems apply mixtures of xenon gas and oxygen ($30\% - 50\%$ of xenon and $70\% - 50\%$ of oxygen, respectively [114, 131, 168, 172]) to a patient via a positive-pressure ventilation mask [168]. Xenon is a stable and radiopaque gas with similar attenuation properties as iodine ($Z_{\text{Iodine}} = 53$, $Z_{\text{Xenon}} = 54$). Within the lung it is assumed that every measured pixel in a CT acquisition is a mixture of air, xenon and soft tissue. An additional cutoff function is applied to exclude materials that are presumed to be

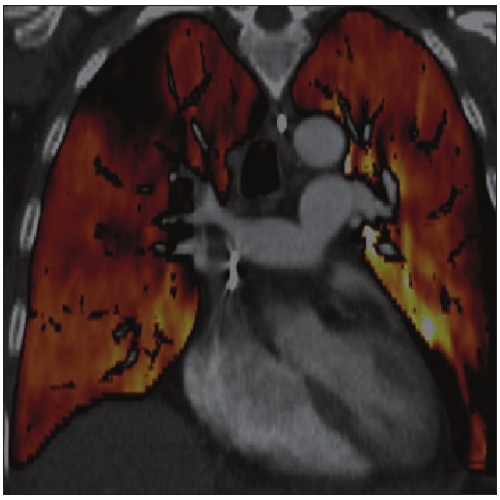

(a) Iodine map image shows segmental defect indicating occlusive pulmonary embolism in the right upper lobe.

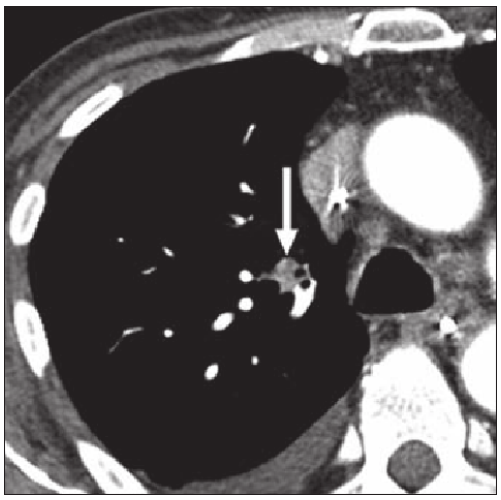

(b) Axial CT angiogram shows occlusive embolus (arrow) in posterior segment of right upper lobe.

Fig. 3.4. 41-year-old woman with pulmonary embolism (from [328]).

not a mixture of the aforementioned materials [114, 172]. Figure 3.5 depicts a the xenon distribution within the lungs of a healthy person (a) and the xenon distribution of a patient suffering from pulmonary emphysema (b).

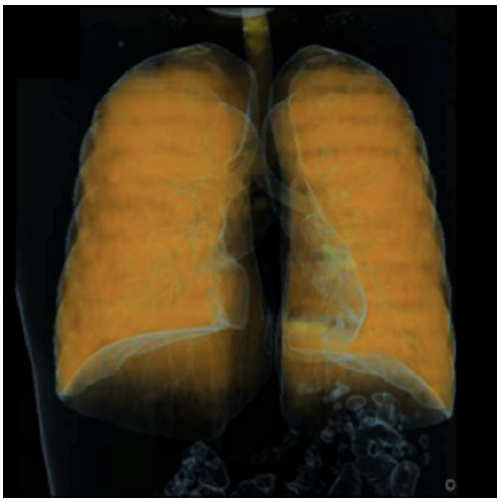

(a) Healthy volunteer.

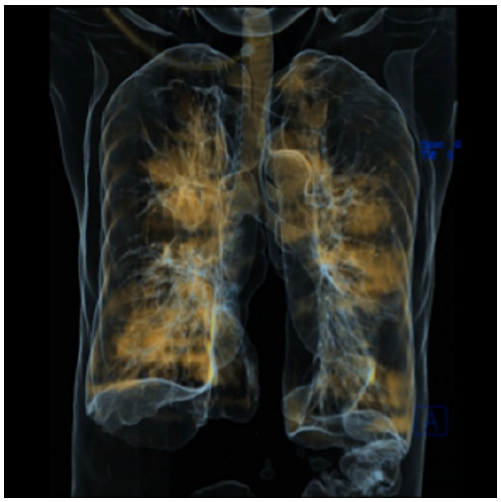

(b) Pulmonary emphysema.

Fig. 3.5. Virtually rendered images of xenon ventilation CT (from [168]).

However, to infer a diagnosis solely by considering functional images depicting the lung's ventilation is insufficient. Additional information about the morphology of the lung or its vascularization must be correlated with the functional data, especially in diagnosis with pathological effects perturbing the lung's ventilation, such as lung consolidation, infarction, or pulmonary masses [168].

Xe-based ventilation assessment can be applied to diagnose various clinical conditions, like *chronic obstructive pulmonary disease* (COPD), asthma, or pulmonary embolism: COPD describes an irreversible and progressive airway obstruction characterized by the destruction of lung parenchyma caused by local inflammation [168]. Whereas conventional pulmonary function tests are used to assess the severity of COPD, no local information or progression of disease or treatment can be derived. Whereas conventional high resolution CT is used to assess local airway wall thicknesses, functional CT (i.e. Xe-based ventilation assessment) can be used to assess the homogeneity of Xenon and the overall Xe-induced contrast enhancement, whereas the homogeneous distribution and increased enhancement is linked to the absence of COPD [168].

For asthmatic patients conventional CT support the evaluation of bronchial hyperresponsiveness, airway wall inflammation and airway remodelling. To consolidate the diagnosis of asthma detected ventilation defects can be utilized, as they correlate with local airflow reductions [42, 168]. Decreased local lung ventilation can also hint the presence of particularly small and peripheral pulmonary emboli [168].

Despite the advantages of lung ventilation measurements, such measurements remain challenging, as xenon control devices and spectral CT scanners might not be available and both the application of xenon and the monitoring of the patient (e.g. respiratory rate, oxygen saturation, blood pressure) pose elaborated requirements on the setup of the examination. Also, reported adverse reactions (anesthetic effects, but also headache, seizures, nausea [175]) after the application of xenon to a patient have deterrent effects towards the clinical acceptance of this technique.

Also, when using a Dual Source CT scanner the area of possible assessment is restricted by the FOV covered by both X-ray tube and detector-systems. Temporal sensitive spectral CT acquisition techniques using the full FOV (e.g. fast kV-switch CT, split filter CT, dual layer CT, PCD CT) can overcome this limitation, as demonstrated in [114].

3.3.5 Spectral imaging in radiation oncology

Radiation oncology (also known as *radiation therapy* or *radiooncology*), describes the medical field of radiation based cancer treatment, often applied in conjunction with surgical resection and/or chemotherapy [269]. Internal radiation therapy includes interventional treatments such as brachytherapy (i.e. the insertion of radioactive beads in close proximity to tumorous tissue, often used to treat cancers in the head/neck, cervical cancer, or prostate cancer [191, 371]) or radio-embolization (i.e. localized intra-arterial or intra-venous delivery of radionuclides to blood vessels supplying a tumor or metastasis, primarily in the liver [1, 28, 154, 214, 225]). External radiation therapy uses ionizing radiation (*photon therapy*) or heavy particles, such as protons or carbon ions (*particle therapy*), to damage the DNA of cancer cells. Every form or radiation therapy targets a maximal deposition of energy inside the tumor, while sparing surrounding healthy tissue [20].

To develop an individual therapy plan, image data from different modalities are used, e.g. *magnetic resonance imaging* (MRI), *ultrasound* (US), CT, *positron emission tomography* (PET),

or *single-photon emission computed tomography* (SPECT). Among these modalities, CT provides the highest temporal and spatial resolution, which makes it an important tool used for the delineation of tumors and the definition of margin tissues, or to derive local energy depositions of internal or external radiation therapy. CT is also used to monitor the progress of the different therapy approaches over time.

In a recent study spectral CT imaging has been used to detect and quantify holmium microspheres in phantoms and animal models (cf. Chapter 9) [107]. Information about local depositions and the activity of beta-emitting radioactive Holmium can be used to perform accurate radiation dosimetry (cf. Chapter 9).

Spectral CT can also be used to determine *relative electron densities* (REDs) and effective atomic numbers (Z_{eff}) on a voxel-by-voxel basis [197, 204, 269, 278]. This allows conclusions to be drawn about the respective attenuation caused by photoelectric effects and Compton effects. Information about REDs are of particular importance for photon therapy, as the Compton effect is the predominant photon interaction in the respective energy range (cf. Section 2.2.2).

For particle therapy, however, not only the REDs are important, but also the so-called local *mean excitation potential* (MEP) of tissue, as both are used to determine the eventual *stopping power ratio* (SPR) of the particle. The SPR is described by the product of RED and the tissue specific *relative stopping number* (RSN), which is derived from heuristic conversion methods [209, 269]. The precision in determining an accurate SPR is particularly crucial for particle therapy. This is because the particles release the bulk of their energy at the termination of their trajectory, a phenomenon known as the *Bragg Peak*, which must occur within the tumor region and not its surroundings. Conversely, the necessity for SPR accuracy in photon therapy is significantly less critical due to the exponential absorption of radiation along its path.

Figure 3.6 depicts two examples for the determination of REDs and effective atomic numbers using a Gammex-phantom (*Advanced Electron Density Phantom*, Sun Nuclear, Wisconsin, USA) with iodine and calcium inserts, respectively.

3.3.6 (Virtual) monoenergetic imaging

Spectral CT images can be used to derive the spectral information of a given material (cf. Section 3.1). In their early work, Alvarez and Macovski postulated that, knowing these constants, linear attenuation coefficients can be reconstructed for any energy within the diagnostic energy range [9]. Today this method is referred to *virtual* (or *synthesized*, *pseudo*, *artificial*) *monoenergetic imaging* (VMI) [101, 178].

VMI techniques process one resolved or two detected polychromatic X-ray spectra (*low energy* and *high energy*, cf. Section 2.1.2) to differentiate the local attenuation separated into the respective contributions of the Compton effect and photoelectric effect (Equation 3.3), or alternatively, representative base materials (Equation 3.4). Low energy acquisitions are characterized by improved enhancement of high-Z materials, such as calcium and iodine. However, depending on the spectral separation and the size of the absorber, low energy

(a) Gammex phantom with iodine inserts (0.2 - 20 mgI/mL).

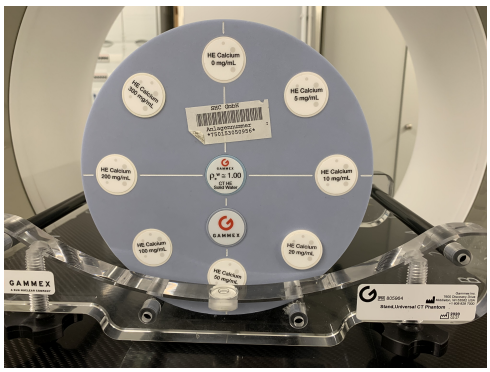

(b) Gammex phantom with calcium inserts (5 - 300 mgCa/mL).

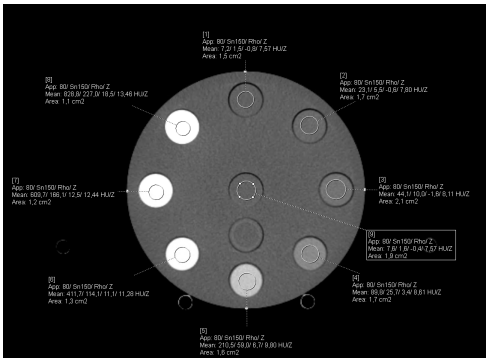

(c) Mixed image of the Gammex phantom with iodine inserts.

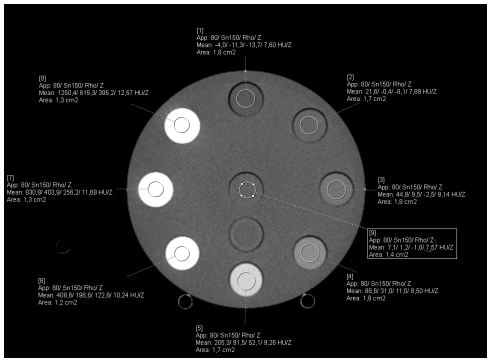

(d) Mixed image of the Gammex phantom with calcium inserts.

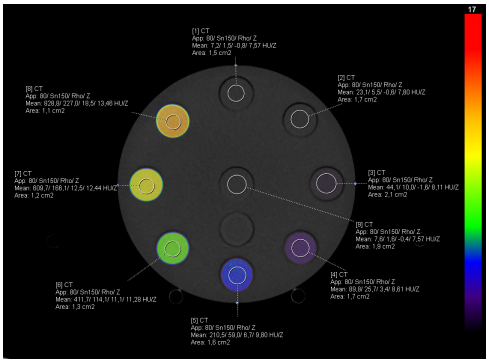

(e) Z_{eff} overlay image on the measured Gammex phantom with iodine inserts.

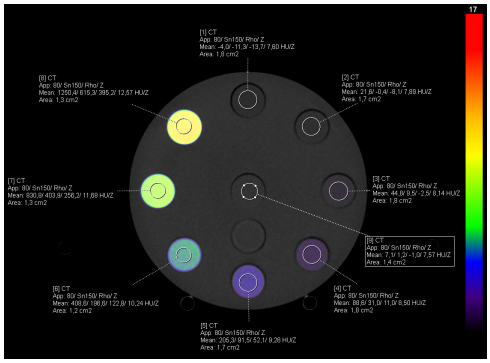

(f) Z_{eff} overlay image on the measured Gammex phantom with calcium inserts.

Fig. 3.6. Two examples for decompositions into the REDs and effective atomic numbers of iodine (left) and calcium (right) inside a Gammex phantom. Both scans were performed on a dual source CT system (SOMATOM X.ceed, Siemens Healthcare GmbH) at 80 / 150Sn kV. The electron density equals the RED with water as the reference. The elevated effective atomic numbers result from the increasing contribution of iodine to the water equivalent Gammex-material.

measurements can suffer from increased noise as the spectrum experiences beam hardening, i.e. loss of lower energetic photons and a shift towards a higher mean energy. High energy acquisitions, on the other hand, provide lower contrasts, but also tend to have lower noise levels, as photons with higher energy have a higher potential to fully traverse the scanned object.

In general VMI images can be calculated in the projection space or in the image space [178, 356]. For projection-based processing the two detected low/high energy sinograms are used in conjunction with material-, size- and energy-specific calibration scans to derive the local mass density for each base material. Respective mass attenuation coefficients (e.g. from the *National Institute of Standards and Technology* (NIST) [293]) are used to calculate the local mass attenuation for any desired energy (typically in the range of 40 and 190 or 200 keV). For image-based processing (used where the respective projections don't align, e.g. dual source CT) two sets of acquired and reconstructed CT images are used to directly solve for the local mass density. In practice, VMIs are calculated by a weighted addition of the low energy and the high energy input images. The weighting factors depend on the selected keV of the VMI and are chosen to exactly represent the attenuation of a specific material, mostly iodine, at the selected keV, which can be obtained from NIST tables.

Particularly for bigger patients, VMI images at lower energies tend to show increased contrast but also increased image noise. This observation can be explained by the fact that as the deviation from the mean energy of the spectrum in the target energy level increases, it necessitates a corresponding increase in the weights applied to both the low and high input images to attain the desired attenuation. Consequently, a surge in these weights amplifies the noise, owing to the quadratic dependence of the variance on these weights [41, 140]. Grant et al. introduced a method to improve the noise propagation, which is based on a *frequency-split* technique where the lower spatial frequencies, i.e. the object information, of a lower keV image is stacked to a high-pass filtered image, providing optimized noise levels, yielding an improved image quality in terms of increased CNR [101]. The CNR can also increase with the use of iterative/deep learning based reconstruction methods [25, 136, 174, 265].

Detailed descriptions and comparisons of the presented methods, including comparisons using dose-equivalent polychromatic acquisitions can be found at [3, 143, 295, 356].

VMI reconstructions can be used to reduce beam hardening artifacts caused by medical implants (e.g. coils, stents, pacemakers, prostheses, dental fillings, orthopedic devices, etc.) or external sources for metal artifacts (e.g. ECG cables, glasses, etc.), particularly at higher energies [3, 9, 356]. Figure 3.7 depicts an example of the reduced severity of metal artifacts caused by screws in the spine and in the tibia with increased selected energy for the VMI.

Residual artifacts in the lower energy ranges are caused by strong beam hardening effects in the low energy acquisitions and even photon starvation across the entire energy range (i.e. full attenuation of X-ray photons along their path) [41, 140]. Yet, in absence of photon starvation VMI reconstructions provide enhancement independent of the size of the absorbing object and with higher values as with low kV polychromatic acquisitions [9, 33, 132, 180, 283, 286, 334, 341, 355, 366]. Ensuring constant radiation dose, VMI reconstructions can also be used to omit low kV CT aquisitions, as same CNR-values can be achieved [101]. The possibility to adjust the local enhancement, by selecting an energy close to the K-edge absorption of a material, can be utilized to save contrast doses up to 80% [3] or to increase the conspicuity of local leasions, as exemplary depicted in Figure 3.8.

An elaborated overview of optimized pathology- and use case-specific energy selections for VMI can be found at [3].

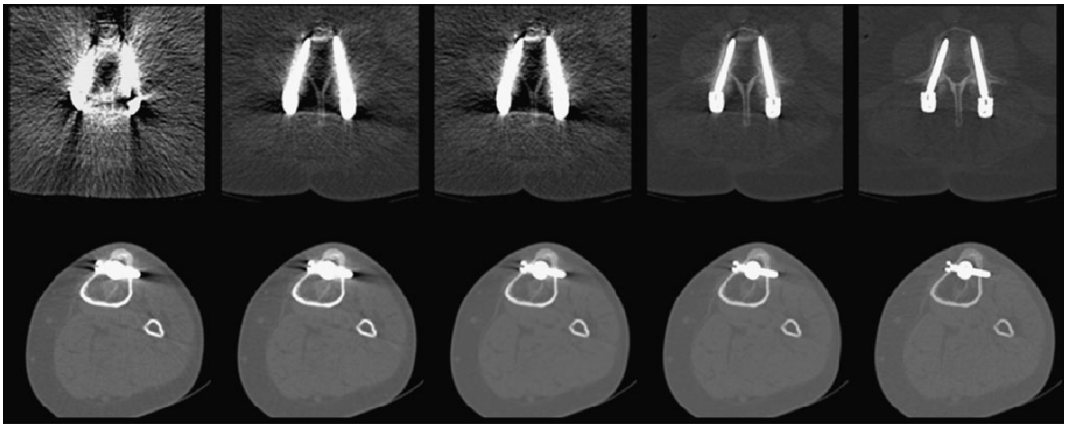

Fig. 3.7. Two sets of images showing screws in the spine and in the tibia reconstructed at 64, 69, 88, 105 and an optimal keV setting (left to right). Note that the spinal canal the thin layer of bone covering the left screw are only discernible in the two reconstructions at the highest energy. Similarly, the screw in the tibia is optimally depicted in the rightmost image (from [17]).

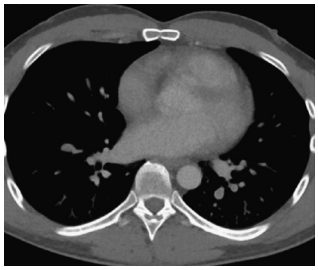

(a) Assessment of PE is substantially hampered in standard linear blended series (m = 0.6).

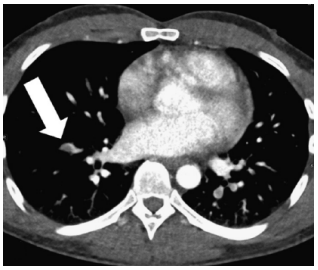

(b) Reconstructions using the VMI+ algorithm at 40 keV show considerable increased attenuation of the pulmonary arteries and thus facilitate the delineation and detection of multiple segmental emboli of the middle and lower lobe of the right lung (arrow). Luminal filling defects of left lower lobe segmental arteries are also better appreciated using 40 keV VMI+.

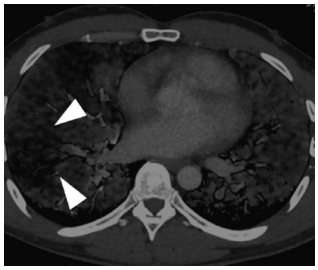

(c) DECT perfusion maps reveal corresponding lung perfusion defects (arrowheads) and provides information regarding the hemodynamic relevance of vessel obstruction.

Fig. 3.8. Axial reformattet DE-CTPA images of a 40-year-old man (BMI, 25.3 $\frac{kg}{m^2}$) with poor contrast due to transient interruption of contrast. Assessment of PE is substantially hampered in standard linear blended series. All observers assigned higher scores regarding diagnostic confidence for all central, segmental, and overall PE assessment using protocol 3 including VMI+ reconstructions and DECT-PM. Window settings in both reconstructions were: level, 70 HU; width, 800 HU (from [179]).

3.3.7 Material quantification and (virtual) non-contrast imaging

With spectral CT imaging techniques, CT enhancement values can be represented as as linear combinations of a set of base materials (cf. Section 3.1). *Virtual non-contrast* (VNC), or *virtual un-enhanced* (VUE) imaging refers to a digital reduction of the dimensionality of this linear combination, usually generating a quantitative *contrast map* (i.e. a colored overlay representing local concentrations of a contrast media), and a *VNC image* mimicking a native

true non-contrast (TNC) CT scan (i.e. a CT scan without the use of contrast media). The principle of VNC imaging is shown in Figure 3.1 (b).

For visualization purposes, the contrast map is displayed as an overlay on one of the input images or on a linearly weighted mixture of the input images. The separation into a contrast map eases the assessment of local contrast uptake, which can be specific for present pathologies: Hypervascular lesions provide an increased enhancement and are easy to differentiate from hypovascular cysts [103]; tumor necrosis can be identified with a decreased contrast uptake, over the course of oncological therapy (cf. Section 3.3.5). Hypoperfused regions can also indicate vessel occlusions or (active) hemorrhages (cf. Section 3.3.3).

High quality VNC images, on the other hand, may allow to omit native CT scans, e.g. for multi-phase acquisitions of the pancreas or the liver [326]. Studies showed that this can lead to radiation dose savings of 35% or more. A high accuracy of the CT-values in the calculated VNC images is achieved with modern spectral CT scanners [103, 282, 330], however, deviations were observed in case of presence of beam hardening artifacts in the input images [73, 330].

To generate contrast maps and VNC images (so-called *idealized* [242]) base materials within the Hounsfield space need to be defined. As only air and water provide fixed reference values in the Hounsfield space, other materials require calibrations specific to the applied or resolved energy spectra, and to the size of a measured object.

The base materials can either define a range (i.e. with a minimal or a maximal amount), or an open one (i.e. dependent on the quantity). Examples for limited space are vectors described by fat and soft tissue; urine over porous UA-based kidney stones, to solid UA-based stones (cf. Section 3.3.2); lung tissue filled with air and lung tissue saturated with xenon (cf. Section 3.3.4); or trabecular and cortical bone (cf. Section 3.3.1). Within the clinically reasonable amount of injectable contrast media (with negligible volume fraction but very high absorption), respective base vectors can be considered open. Known concentrations, however, can be used as scalars to their energy- and size-specific vector. Once determined, these material vectors provide a fixed slope for the calibrated system. The quality of the resulting images depends on the level of distinction among these vectors [69, 116, 118].

Examples of typical combinations of base materials are:

1. **Fat, soft tissue, iodine:** E.g. to distinguish cysts from tumorous lesions in the liver [218, 282, 286, 311, 332, 351]. An example a contrast enhanced scan of a liver during portal venous phase, a TNC scan, and a VNC image is shown in Figure 3.9.
2. **Air, water, iodine:** For CT urography, to determinate urinary calculi in the renal collecting system [103, 192, 325], or to assess the transit time of contrast over the arterial and excretoy (pyelographic) phase of both kidneys in case of acute pyelonephritis [326]. These materials are also used in the context of pancreatic imaging, e.g. to investigate for the presence or absence of pancreatic ductal adenocarcinoma [56, 222, 258] or the diagnose acute pancreatitis [196, 222].
3. **Trabecular bone, cortical bone, soft tissue:** To create masks for the virtual removal of bone (cf. Section 3.3.1), or to evaluate the possible edema [5, 24, 40, 89, 145, 229].
4. **Air, soft tissue, iodine:** To assess lung perfusion (cf. Section 3.3.3).

5. **Cerebrospinal fluid, hemorrhagic tissue, iodine:** To spare the TNC scan in case of suspected brain hemorrhage , to differentiate hemorrhage from iodinated contrast in different intracranial compartments, or to detect calcifications and ossifications [73, 244].
6. **Lung and air, lung and xenon, soft tissue:** To assess the ventilation capacity of the lung (cf. Section 3.3.4 and Chapter 5).

Contrast maps and VNC images can be generated with all presented spectral CT acquisition techniques[4]. However, the decomposition of contrast media in early injection phases require high temporal coherence. The quality of the decomposition particularly depends on the spectral resolution of the CT acquisitions, as well as the discriminability of the base vectors.

(a) Contrast enhanced CT scan in the portal-venous phase.

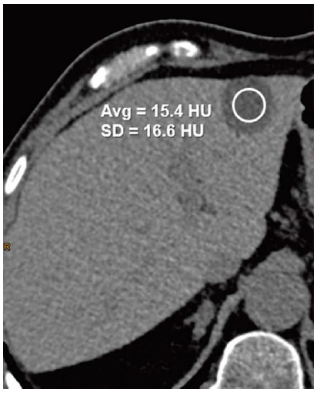

(b) TNC image.

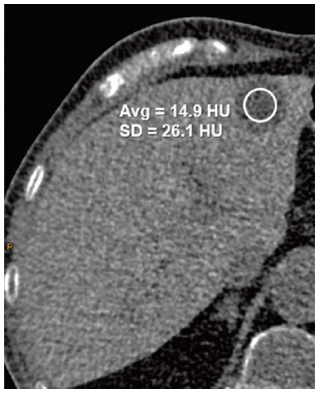

(c) VNC image.

Fig. 3.9. Magnified axial CT slice of a 79-year-old male patient with a cystic lesion in the left liver lobe with a diameter of 28 mm (modified from [282]).

3.3.8 Multimaterial decomposition and K-edge imaging

X-ray imaging offers only a very low intrinsic sensitivity for the differentiation of soft tissue within the human body, as these materials provide very similar mass attenuation coefficients (cf. Figure 3.10 (a)). Contrast media is used for the delineation of blood vessels and organs within the body from their surrounding tissue. The enhancement of contrast media depends it's material-specific properties (namely the mass attenuation coefficient, cf. Section 2.3.2), it's density, the applied X-ray spectrum, the beam hardening of the measured object, and the responsiveness of the CT detector. Figure 3.10 (b) and Table 3.1 list a selection of elements which provide K-edges within the energy range of X-rays used in clinical CT. However, currently only iodine-based contrast agents are clinically approved to be used in CT imaging.

Separation and quantification of contrast media and body materials is achieved via material separation algorithms, as described in Section 3.1. Without further constraints on mass or volume conservation, the number of possible base materials is limited by the number of detected X-ray spectra (cf. Section 3.2.2). Thus, most spectral CT techniques can only provide information for material separation into two base materials. Photon-counting CT

[4] A good overview of the performances of different spectral CT acquisitions techniques on image-based material decomposition can be found at [69].

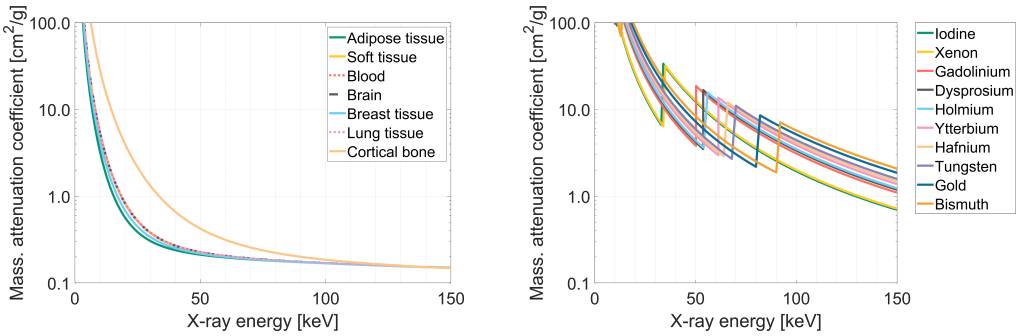

(a) Selection of body materials.

(b) Elements with existing/potential use as contrast media for CT (cf. Table 3.1)

Fig. 3.10. Mass attenuation coefficients of body materials and heavy elements with K-edges within the energy range for clinical CT [138, 293].

Tab. 3.1. Overview of elements with existing/potential use as contrast media for CT.

Atomic number (Z)	Symbol	Element	K-edge [keV]
53	I	Iodine	31.82
54	Xe	Xenon	34.57
64	Gd	Gadolinium	50.24
66	Dy	Dysprosium	53.79
67	Ho	Holmium	55.61
70	Yb	Ytterbium	61.33
72	Hf	Hafnium	65.35
74	W	Tungsten	69.52
79	Au	Gold	80.73
83	Bi	Bismuth	90.53

scanners, on the other hand, can produce multiple energy-specific images that can be used to decompose more then just two materials. However, the quality of the decomposed images may deteriorate as the number of base materials selected increases, or as base materials with similar attenuation properties are selected [118, 189, 303].

The general gain of enhancement (and therefore the potential of radiation dose saving) of different contrast media with respect to the energy spectra and patient size was quantified by Nowak et al. [228]. Their findings revealed the complexity of how the given factors interact: For smaller patients, hafnium-based contrast media and tube voltages of 120 kVp yielded the greatest enhancement. For larger patients, however, the greatest enhancement was observed with gold or bismuth-based contrast media and tube voltages of 140 kVp. The authors reasoned that optimal enhancement results from the shift of the mean energy of the attenuated X-ray spectrum toward the K-edge of the material. Decomposition of more than two materials is only feasible if these materials exhibit K-edges within the applicable energy range for CT. The differentiation of three or more materials without K-edges in this energy

range (for instance, iodine, calcium, and water) is unattainable, because if two base materials are chosen for material decomposition, any third material can as well be a linear combination of the base materials.

With the advent of the latest prototype and commercially available PCD CT systems, research into new possible contrast media and new contrast-related applications has increased [150].

In an experimental setting, Dangelmaier et al. evaluated the separation of iodine, gadolinium, and calcium as a basis for the discrimination of endoleaks and intra-aneurysmatic calcification within aneurysms [50].

In another study Symons et al. successfully demonstrated the potential of using multi-energy CT data from a PCD CT scanner to visualize iodine and gadolinium in cardiac imaging to delineate the border between infarcted myocardium and the blood pool in the left ventricle (cf. Figure 3.11) [318]. They applied a sequence of injections (a gadolinium-based contrast agent 10 minutes prior to a diagnostic scan, and iodine 1 min before the same scan, respectively) to achieve late enhancement in the organ parenchyma and first-pass iodine enhancement.

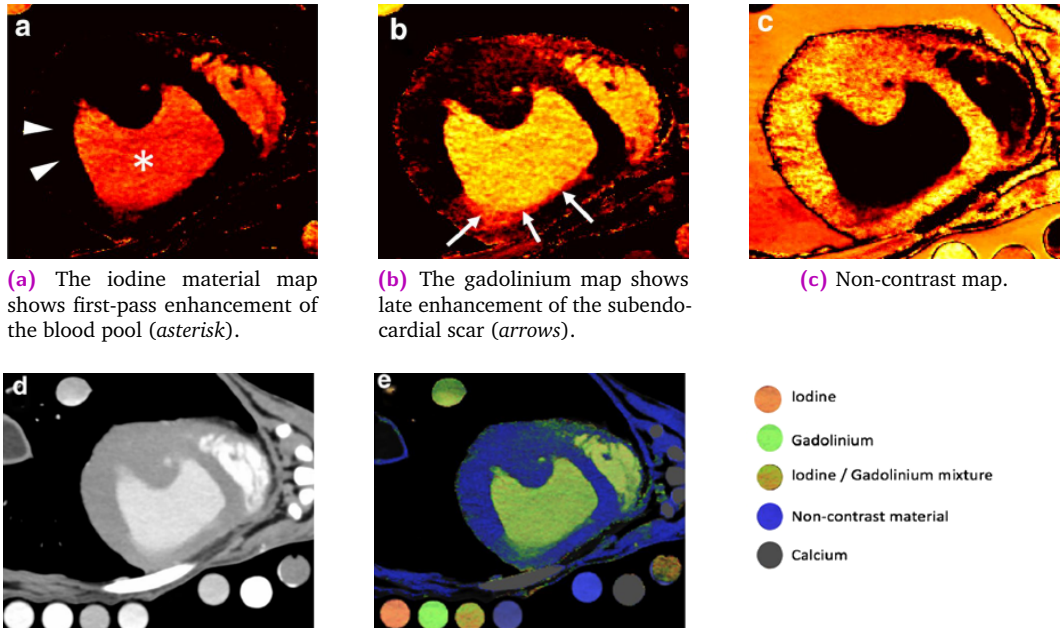

(a) The iodine material map shows first-pass enhancement of the blood pool (*asterisk*).

(b) The gadolinium map shows late enhancement of the subendocardial scar (*arrows*).

(c) Non-contrast map.

(d) PCD gray-scale image.

(e) Mult-material concentration map. Differentiation between the infarcted myocardium (*arrows*), remote myocardium (*arrowheads*), and the left ventricle (LV) blood pool (*asterisk*) is possible with high CNR.

Fig. 3.11. Sample results of material decomposition of PCD CT images after injection of iodine and gadolinium to highlight infarcted myocardium and the blood pool in the left ventricle (modified from [318]).

In an *ex-vivo* experiment Grönberg et al. demonstrated an unconstrained projection-based material decomposition of iodine, calcium and soft tissue using image data of a human heart containing calcified plaques in its coronary arteries, obtained by a Si-based PCD [104]. The increased spatial resolution and the reduction of beam hardening effects, both characteristic

of PCDs, have proven to be particularly beneficial for imaging and spectral evaluation of small vessels.

Muenzel et al. investigated the use of PCD CT for a simulated laxative-free colonography [216]. In their experimental setup, they used a 3D-printed model of a human colon filled with iodine solution (as a surrogate for labeled feces) and capsules filled with gadolinium (mimicking polyps) located on the colon wall. The resulting separated contrast maps clearly differentiated the both materials. The virtual removal of the iodinated contrast media facilitates *electronic cleansing*, which is used to improve the visibility of colonic polyps and omits physical cleansing of the colon and the associated discomfort for the patient [39].

The simultaneous visualization of two contrast agents in the small bowel has been demonstrated by Ren et al. [268]. In their study they administered a solution of bismuth and saline orally to a swine, followed by an intravenous injection of iodine. After material decomposition they found clear separation between the enteric enhancement of the bismuth and the arterial enhancement in the bowel wall. Their findings suggest a potential use of spectral multi-material decomposition in differentiating between extravasation of labeled intestinal fluid or bleeding caused by vessel rupture.

The potential to replace multi-phase CT image acquisitions of the kidney or the liver was suggested by different groups [217, 267, 305, 319]. Symons et al. administered bismuth 24-72 hours before imaging to mongrel dogs. Right before scanning, additional injections with gadolinium-based contrast media and iodine-based contrast media followed. They succeeded in imaging three different contrast phases (corticomedullary, nephtrogenic, and excretion phase) with one single CT scan [319]. Si-Mohamed et al. were able to simultaneously image the arterial and portal venous phase of a rabbit's liver, after sequentially applying a gadonlinium-based contrast agent (to enhance portal venous phase) and iodine (for highlighting the arterial phase) [305]. As the decomposed images result from the very same acquisition, a perfect tempo-spatial resolution is given, which omits the use of potentially erroneous registration algorithms and therefore improves the detection of small (< 2 mm) focal liver lesions, as possibly prevalent in case of hepatocellular carcinomas. In a similar procedure Ren et al. also applied a dual-phase contrast injection, but they improved their results by applying an additional CNN-based denoising algorithm to the acquired CT images before material separation [267]. The resulting reduction of noise (60-80%) yielded a quantification accuracy of iodine and gadolinium with respective root-mean-square deviations of only 0.75 mgI/mL and 0.45 mgGd/mL. All authors concluded, that in addition to the accurate discrimination and quantification of contrast media, the replacement of multi-phase CT scan protocols by single CT acquisitions yield to substantial radiation dose savings.

The development of new contrast media is currently hampered by restrictions on biocompatibility, low osmolality and viscosity, toxicity and the requirement to be renally excretable [10, 11, 19, 52, 59, 64, 100, 150, 165, 210, 245, 352]. Even the use common gadolinium-based contrast agents for MRI was met with skepticism after Kanda et al. firstly observed accumulations of gadolinium-based contrast media in human brains [155, 156] - a finding that was confirmed a year later by investigations using inductively coupled plasma mass spectroscopy [155]. In 2017, as a response to these findings, the *European Commission* (EC) followed the recommendation of the *European Medicines Agency* (EMA) to ban the use of some linear

gadolinium-based contrast agents within the European Union as a precautionary measure. To date, there are no known adverse health effects associated with the use of linear contrast media [288]. However, subsequent investigations revealed that such accumulations were not found in the use of macrocyclic gadolinium based contrast media.

Methods to encapsulate otherwise toxic elements have been proposed (e.g. nanotubes, fulerenes, or nanoparticles [13, 27, 47, 259, 310]). Yet, with these bio-compatible encapsulations the effective density of the materials diminishes and the contrast enhancement decreases. Encapsulation also increases the average core diameter of such materials to sizes that cannot be renally excreted, which leads to hour long or permanent persistency of these contrast media particles in the patients' blood pool [38, 48, 59, 314].

Despite these difficulties, research into new contrast agents continues to be useful, as it is anticipated that with technological advances in medical imaging systems, the use of optimized contrast agents may meet or exceed current clinical requirements.

Part II

Scientific contributions

4

Human Imaging With Photon Counting-Based Computed Tomography at Clinical Dose Levels: Contrast-to-Noise Ratio and Cadaver Studies

Ralf Gutjahr, MSc,[1,2] Ahmed F. Halaweish, PhD,[2] Zhicong Yu, PhD,[3] Shuai Leng, PhD,[3] Lifeng Yu, PhD,[3] Zhoubo Li, BS,[3] Steven M. Jorgensen, BSEE,[4] Erik L. Ritman, MD, PhD,[4] Steffen Kappler, PhD,[5] and Cynthia H. McCollough, PhD[3]

[1]Computer Aided Medical Procedures (CAMP), Technical University of Munich, Munich, Germany
[2]Siemens Healthcare–Imaging and Therapy Systems, Malvern, PA
[3]Department of Radiology, Mayo Clinic, Rochester, MN
[4]Department of Physiology and Biomedical Engineering, Mayo Clinic, Rochester, MN
[5]Siemens Healthcare, Forchheim, Germany

Copyright statement

Contributions

The author of this thesis contributed to the conceptualization and methodology development shaped the research. He supported the experiment preparation by assisting prior dose measurements, performing system calibrations, organizing the cadaver. His involvement in data curation included the conduction of scans, performing reconstructions and data analysis. The author also developed the software for data evaluation and visualization. The author

played a key role in writing, reviewing, and editing this article, ensuring its quality and impact.

The co-authors supported the formal analysis and participated in the investigation process, providing their expertise and insights. They were also involved in providing resources, which facilitated the study's smooth execution. Their contributions extended to the conceptualization and methodology development, helping shape the research's direction and design. Furthermore, they played a significant role in supervising the project, ensuring proper guidance and mentorship. Finally, the co-authors were involved in reviewing and editing the article.

Abstract

Objectives: The purpose of this work was to measure and compare the iodine contrast-to-noise ratio (CNR) between a commercial energy-integrating detector (EID) computed tomography (CT) system and a photon-counting detector (PCD) CT scanner capable of human imaging at clinical dose rates, as well as to determine clinical feasibility using human cadavers.

Materials and Methods: A research dual-source PCD-CT scanner was used, where the "A" tube/detector subsystem used an EID and the "B" tube/detector subsystem used a PCD. Iodine CNR was measured in 4 anthropomorphic phantoms, simulating 4 patient sizes, at 4 tube potential settings. After biospecimen committee approval, PCD scans were performed on a fresh-frozen human head and a whole body cadaver using clinical dose rates. Scans were repeated using the EID and identical parameters, and qualitative side-by-side comparisons were performed.

Results: For the same photon fluence, phantom measurements demonstrated a mean increase in CNR of 11% , 23% , 31% , 38% for the PCD system, relative to the EID system, at 80, 100, 120, and 140 kV, respectively. Photon-counting detector CT additionally provided energy-selective imaging, where low- and high-energy images reflected the energy dependence of the iodine signal. Photoncounting detector images of cadaveric anatomy demonstrated decreased beam hardening and calcium blooming in the high-energy bin images and increased contrast in the low-energy bins images relative to the EID images. Threshold-based PCD images were qualitatively deemed equivalent in other aspects.

Conclusions: The evaluated research PCD-CT system was capable of clinical levels of image quality at clinical dose rates. It further provided improved CNR relative to state-of-the-art EID-CT. The energy-selective bin images provide further opportunity for dual-energy and multienergy analyses.

Keywords

Computed Tomography, Photon-counting CT, Spectral CT, Multienergy CT, Photon-counting detectors

4.1 Introduction

Photon-counting detectors (PCDs) have been proposed for use in computed tomography (CT) as a method of reducing radiation dose and improving material composition analysis [142, 199, 272, 287, 322]. However, technical limitations have heretofore restricted investigations to micro- and small-animal CT systems [170, 230, 284, 336]. In addition, problems with detector stability and high count rates have presented significant technical challenges for the development of systems capable of human imaging [284, 322, 323].

Unlike conventional energy-integrating detectors (EIDs), PCDs are capable of resolving incoming x-ray photons according to their individual energy. In PCD technology, impinging x-ray photons produce electron hole pairs inside a semiconducting material. A bias voltage applied to the detector creates a strong electric field in the bulk material and attracts the electrons toward a pixelated anode, where an application-specific integrated circuit transfers and shapes the charge pulses into voltage pulses. The amplitude of the pulses is approximately proportional to the energy of the absorbed incident x-ray photon [159, 322, 323].

The energy-resolving nature of these PCD modules facilitates the generation of energy-specific images. For each measured pulse, the amplitude is compared with a set of user-specified energy thresholds. Pulses with energies greater than the specified low-energy threshold, but lower than the specified high-energy threshold, are used to form images that correspond to a specific energy bin [159]. An ideal energy bin only considers photons between the specified lower and higher thresholds; thus, only photons with energy values between 2 neighboring energy thresholds contribute to the signal of an energy bin. In practice, however, the ability to perfectly separate photons of different energies using PCD is impaired by physical effects such as K-escape, charge sharing, detector polarization, charge trapping, and high pulse rate effects in a high-flux scenario, such as clinical CT imaging [35, 125, 127, 159, 160, 170, 219, 284, 297, 320, 322, 323, 333]. However, PCD-CT acquisitions can provide fewer beam-hardening effects, do not suffer from the sharp increase in noise (e.g., electronic noise) at low photon counts, and offer an increase in dose efficiency [23, 127, 160, 287, 297, 322, 342].

A research PCD-CT system has been in development for several years [157, 158, 159] and was recently installed at the Mayo Clinic in Rochester, MN. A complete physics evaluation of image quality and dose performance has been previously performed [358]. These studies indicate the potential for use in human imaging at clinical dose rates. The purpose of this work was to measure and compare the iodine contrast-to-noise ratio (CNR) of a commercial EID-CT system and our research PCD-CT scanner, which is capable of human imaging at clinical dose rates, as well as to demonstrate clinical feasibility using human cadavers.

4.2 Materials and Methods

4.2.1 Scanner Description

The research PCD-CT scanner used for this study, which is capable of human imaging at clinical dose rates, is based on a commercially available 128-slice dual-source CT system (SOMATOM Definition Flash; Siemens Healthcare, Forchheim, Germany). Using a commercial 78-cm wide gantry opening, the system is capable of imaging human-sized objects. The primary difference between the commercial and the research systems is the replacement of one of the dual-source scanner's 2 EID arrays with 1 CdTe-based PCD array. This has been previously reported [157, 158, 159]. The x-ray tubes and beam-shaping filters of both systems are identical; however, the in-plane field of view (FOV) of the PCD array is smaller (275 mm) than that of the EID detector (500 mm). This means that while the whole body can be positioned in the gantry, a smaller FOV is used for PCD imaging. There is no fundamental limitation requiring a smaller FOV for the PCD array; the limited size is merely a choice that was made in the design of this particular research system.

Quantitative evaluation of the research system's PCD tube/detector pair was previously performed and compared with the physics performance of the EID tube/detector pair of the research scanner, the latter being identical to a commercially available SOMATOM Definition Flash scanner [358]. The specifications of the research PCD-CT scanner, its 2 tube/detector subsystems, and the adjacent commercial EID-CT system used for comparison are given in Table 4.1.

Tab. 4.1. Overview of the Specifications of the Commercial and Research Scanners.

Specification	Commercial Subsystem A	Commercial Subsystem B	Research Subsystem A	Research Subsystem B
Detector type	EID	EID	EID	PCD
Tube type	Straton®			
Tube voltages, kV	70, 80, 100, 120, 140		80, 100, 120, 140	
Rotation time, s	1.0, 0.5, 0.33, 0.28		1.0, 0.5	
Projections/rotation	2304			
Gantry opening, mm	780			
In plane FOV, mm	500	325	500	275
Detector pixel size in Z-dim., mm	0.6	0.6	0.6	0.5
Maximum Z collimation, mm	64×0.6	64×0.6	64×0.6	32×0.5
Z coverage, mm	38.4	38.4	38.4	16.0

EID indicates energy-integrating detector; PCD, photon-counting detector; FOV, field of view.

The PCD-CT system was composed of 1.6-mm-thick CdTe semiconducting sensors. Each detector pixel was composed of 16 (4×4) subpixels, each with an effective individual pitch of

0.225 mm. An antiscatter collimator grid was placed between each pixel (every fifth subpixel) for in-plane scatter suppression. The effective pixel size along the z axis at the isocenter was 0.5 mm.

To image objects with sizes exceeding the PCD FOV, the truncated projections of the PCD subsystem were filled in with data acquired in a separate acquisition using the 500-mm FOV EID array. This second scan acquisition using the EID array is referred to as a data completion scan (DCS). This technique results in PCD data within the PCD FOV, EID data outside the PCD FOV, and avoids truncation artifacts that would otherwise occur from imaging an adult patient with the smaller FOV of the PCD array.

Each subpixel of the PCD array provides 2 energy thresholds; the lower threshold T_L is adjustable in a range from 20 to 50 keV and the higher threshold T_H is adjustable in a range from 50 to 90 keV. In this work, the energy-resolved readout of the PCD array occurred in this so-called macro mode, in which every subpixel used identical low- and high-energy thresholds. Reconstructed data from this mode provided 4 image sets: 2 threshold-based image sets and 2 bin-based image sets, where the bin 1 image set was reconstructed using all photons between T_H and TL, and the bin 2 image set was reconstructed using only measurements where the photon energy exceeded T_H (hence bin 2 images are equivalent to T_H images).

4.2.2 Measurement of Contrast, Noise, and CNR

This study was designed to measure the iodine CNR of the PCD-CT system as a function of tube current-time product and tube potential, and to compare the results to those from a commercial EID-CT scanner (SOMATOM Definition Flash). Four anthropomorphic abdominal phantoms (CIRS, Inc, Norfolk, VA) with lateral widths of 10.6, 20.5, 30.0, and 38.7 cm were used to mimic a newborn, a 10-year-old, a small adult, and a large adult, respectively (Fig. 4.1 (a)). Each phantom contained 4 Lucite vials filled with 4 iodine solutions with concentrations of approximately 5, 10, 15, and 20 mg I/mL. The solutions were chosen to provide CT values of approximately 150, 300, 450, and 600 HU for a reference scan of the 20.4 cm phantom on the EID-CT using a tube voltage of 120 kV. A spine-mimicking material was located posteriorly, with a CT number of approximately 740 HU at 120 kV. All phantoms were aligned with the center of the phantom positioned at scanner isocenter.

Measurements were acquired on both the commercial EID-CT system and the research PCD-CT system with tube potentials of 80, 100, 120, and 140 kV. Data were collected for tube current-time product values of 50, 100, 150, 200, 250, 300, 350, 400, 500, and 550 mA for each tube potential and phantom size on both the EID and PCD systems. All scans used a clinical abdominal sequential protocol with an identical body beam-shaping ("bow tie") filter, ensuring identical photon fluence to both detectors. The rotation time was 1 second for both systems to achieve very high tube current-time products. The collimation was set to 32×1.2 mm for the EID system and 32×0.5 mm for the PCD system (identical collimation settings were not available). Neither collimation setting used the flying focal spot technique. Table 4.2 details the scan parameters used for the phantom scans. The volume CT dose index ($CTDI_{vol}$) reported by the scanner console, which was previously verified with ionization chamber measurements by our clinical physics group, was recorded for each acquisition (Table 4.3).

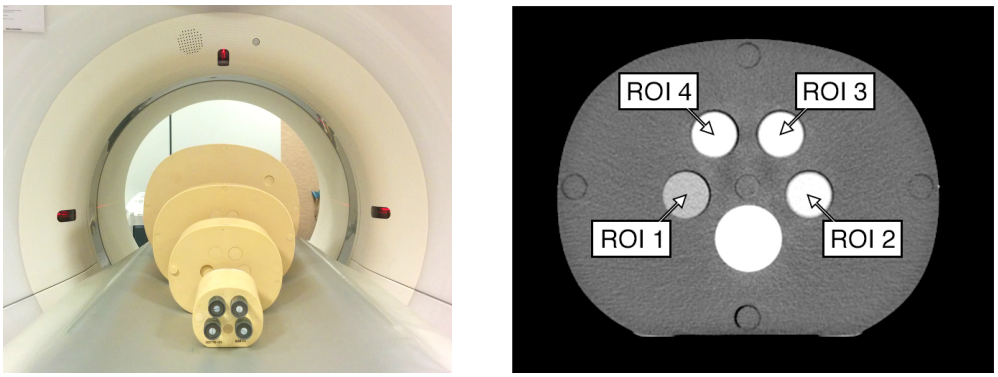

(a) (b)

Fig. 4.1. (a) Experimental setup. Four anthropomorphic phantoms containing 4 different iodine solutions in each phantom. Each phantom was scanned separately to center each phantom at scanner isocenter. (b) In a reference scan (EID system, 120 kV, 200 mA), the solutions provided CT numbers of approximately 150 HU in ROI 1, 300 HU in ROI 2, 450 HU in ROI 3, and 600 HU in ROI 4.

The differences in $CTDI_{vol}$ for the same tube current-time product and tube potential, using the same x-ray tube, geometry, and bow tie filter, are due to decreases in dose efficiency (hence higher $CTDI_{vol}$ values) for more narrow collimations.

Tab. 4.2. Acquisition and Reconstruction Parameters Used to Scan the Phantoms.

Parameter	System A (EID)	System B (PCD)
Detector collimation, mm	32×1.2	32×0.5
Tube potential, kV	80, 100, 120, 140	
Tube current, mA	50, 100, 150, 200, 250, 300, 350, 400, 500, 550	
Rotation time, s	1.0	
Detector collimation, mm	500	275
Scan mode	Sequential	
Image thickness, mm	6.0	
Image interval, mm	6.0	
Reconstruction kernel	D40	
Reconstruction FOV, mm	275	

EID indicates energy-integrating detector; PCD, photon-counting detector; FOV, field of view.

The PCD system was operated with energy thresholds of $T_L = 25$ keV and $T_H = 65$ keV; these settings provide approximately equal photon counts in each of the low- and high-energy bins at a tube potential setting of 140 kV. The final images were reconstructed applying a weighted filter back projection algorithm using a quantitative, medium sharp reconstruction kernel (D40) [44, 344]. This reconstruction method ensures a firm basis for image quality comparison because it avoids nonlinear effects on the contrast, noise, and spatial resolution of the reconstructed images. An image thickness of 6 mm was selected for analysis to use the same image thickness for both the 0.5 and 1.2 mm collimation data while also fully utilizing all acquired photons (i.e., it was the smallest image thickness that could be divided into integer

Tab. 4.3. $CTDI_{vol}$ (32 cm) for 4 Different Tube Potentials and a Tube Current-Time Product of 100 mAs.

Tube Potential, kV	EID $CTDI_{vol}$, mGy	PCD $CTDI_{vol}$, mGy
80	2.0	2.2
100	4.2	4.6
120	6.9	7.6
140	10.1	11.1

$CTDI_{vol}$ values for higher tube current-time products scale linearly. The small difference between the 2 systems is due to the different detector collimations used (EID, 32×1.2 mm; PCD, 32×0.5 mm). The EID detector's total detector coverage is greater, hence the $CTDI_{vol}$ is about 10% less, as wider collimation settings are more dose efficient. $CTDI_{vol}$ indicates volume CT dose index; EID, energy-integrating detector; PCD, photon-counting detector.

multiples of the 2 underlying collimations). The EID system used the same reconstruction algorithm as that of the PCD system such that in plane spatial resolution was matched when reconstruction kernels of the same name were selected on both systems.

The CNR values in each EID-CT image and each low-energy threshold PCD-CT image were calculated for each phantom size and contrast vial by first measuring the mean of CT numbers in each region of interest (ROI) shown in Figure 4.1 (b). Measurements were repeated in 10 consecutive images, and mean values were recorded. The image noise was measured in 2 adjacent images that were subtracted from each other to remove any structured noise components. The resulting noise measurement was divided by the square root of 2 to compensate for the quadrature noise addition that occurs when images are subtracted from one another [128]. Iodine contrast was calculated as the difference between the mean CT number of iodine and the tissue-mimicking phantom material, and CNR was then calculated as the ratio of the mean iodine contrast to the measured noise. The CNR values as a function of tube current-time product were compared between the EID-CT and PCD-CT systems.

4.2.3 Energy-Selective Bin Image Data

Each PCD-CT scan resulted in 2 threshold image sets and 2 bin image sets (because T_H thresholds images are equivalent to bin 2 images, this results in only 3 unique image sets per scan). The CT numbers were measured in each vial for all images using the 4 ROIs shown in Figure 4.1 (b). These values represent the iodine contrast for the specific photon energies used to form the image. The CT numbers of the iodine vials in the PCD images were compared with the CT numbers in iodine in the EID images.

4.2.4 Human Cadaveric Scanning

With approval of Mayo Clinic's institutional biospecimen committee, a human cadaver was obtained from the local department of anatomy. The unembalmed, frozen cadaver was of a 76-year-old woman who had died from metastatic lung cancer and had donated her body for medical research. A separate fresh-frozen human head was also obtained. This patient died from end-stage chronic obstructive pulmonary disease.

Using typical clinical parameters, CT scans of the cadaver's head, thorax, abdomen and pelvis, and extremities were performed on both the EID and the PCD subsystems of the research PCD-CT systems (Table 4.4). This ensured that the specimens were in the identical position for the EID and PCD scans. For the PCD subsystem, macro mode was used to acquire the data and both threshold and bin images were produced. Images were reconstructed using the weighted filter back projection technique. This process was repeated for scanning of the separate human head (Table 4.5). A different pitch was used for the EID subsystem only because that value was programmed into the scanner as the default value and did not get adjusted to match the default values for the PCD subsystem; there was no specific reason for the pitch values to differ. Fortunately, because the Siemens' scanners are designed to maintain constant image quality (e.g., noise, in plane and z axis resolution) as pitch is varied, we do not consider this a limitation of the results presented here.

Tab. 4.4. Acquisition and Reconstruction Parameters Used to Scan the Whole-Body Cadaver.

Parameter	System A (EID)	System B (PCD)
Detector collimation, mm	32 × 1.2 (thorax); 32 × 1.2 (A/P); 64 × 0.6 (legs)	32 × 0.5
Tube voltage, kV	140	
Tube current (head), mA	Not performed	400
Tube current (body), mA	180 (thorax); 240 (A/P); 250 (legs)	
$CTDI_{vol}$ (head, 16 cm), mGy	Not performed	101.4;
$CTDI_{vol}$ (body, 32 cm), mGy	17.7 (thorax); 23.6 (A/P); 24.6 (legs)	20.0 (thorax); 26.6 (A/P); 27.7 (legs)
Rotation time, s	1.0	
Acquisition FOV, mm	500	275
Scan mode, s	Spiral	
Spiral pitch	1.2 (thorax); 0.6 (A/P); 0.8 (legs)	0.5
Image thickness, mm	5.0	
Image interval, mm	5.0	
Reconstruction kernel	D30	
Reconstruction FOV (head), mm	200	
Reconstruction FOV (body), mm	275	

All parameters were identical for the head and body scans, unless otherwisenoted.

EID indicates energy-integrating detector; PCD, photon-counting detector;

$CTDI_{vol}$, volume CTDI; FOV, field of view; A/P, abdomen/pelvic.

Board-certified radiologists specializing in imaging of the head (neuroradiologists) and body (thoracic and abdominal radiologists) independently reviewed the images in a blinded fashion and were asked to state whether the images were essentially equivalent to each other, or, if one set was superior to the other, to identify the superior images.

Tab. 4.5. Acquisition and Reconstruction Parameters Used to Scan the Isolated Cadaveric Head.

Parameter	Subsystem A (EID)	Subsystem B (PCD)
Detector collimation, mm	64×0.6	32×0.5
Tube voltage, kV	140	
Tube current, mA	550	
$CTDI_{vol}$ (head, 16 cm), mGy	124.5	139.4
Rotation time, s	1.0	
Acquisition FOV, mm	500	275
Scan mode	Spiral	
Spiral pitch	0.6	
Image thickness, mm	5.0	
Image interval, mm	5.0	
Reconstruction kernel	D40	
Reconstruction FOV, mm	200	

EID indicates energy-integrating detector; PCD, photon-counting detector; $CTDI_{vol}$, volume CTDI; FOV, field of view.

4.2.5 Statistical Analysis

The mean iodine contrast, image noise, and iodine CNR were compared between PCD and EID systems for each tube potential and dose level. The coefficients of variation for these measurements were determined by expressing the standard deviation as a percentage of the mean values. At each tube potential, a Wilcoxon signed rank test was performed to compare the iodine CNR between PCD and EID systems, with $P < 0.05$ considered to be statistically significant.

4.3 Results

4.3.1 Contrast, Noise, and CNR

The CT number of iodine (Figure 4.2), image noise (Figure 4.3), and CNR (Figure 4.4) measured in the EID and PCD data (plotted vs tube current-time product for Figures. 4.3, 4.4) for each tube potential and/or phantom size demonstrated the following key results:

At low tube potentials, the difference in iodine contrast between the EID and PCD systems was minimal. As tube potential increased, the contrast in the PCD system exceeded that of the EID system. Even though absolute contrast values decreased with increasing tube potential and increasing phantom size, the relative decrease was smaller for the PCD system than for the EID system. This behavior was unaffected by increasing or decreasing the tube current time product (data not shown).

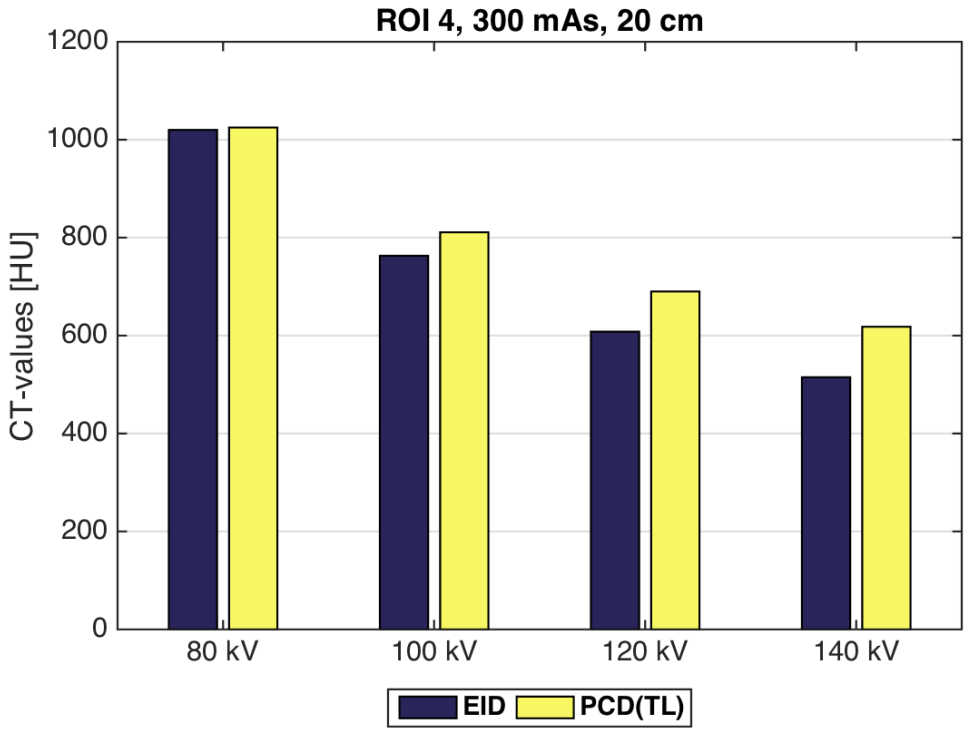

Fig. 4.2. Comparison of the CT numbers measured in ROI 4 for the EID and the low-energy threshold (TL = 25 keV) image from the PCD for 4 tube potentials (80, 100, 120, 140 kV). At 80 kV, the iodine signal is nearly the same for the EID and PCD (TL) images. However, as the tube potential increases, the iodine signal in the PCD (TL) images is increasingly greater than the iodine signal in the EID images. Shown here are the CT values for the 20-cm phantom at 80, 100, 120, or 140 kV and 300 mA.

Noise behaved as expected in both systems. Specifically, noise increased with increasing phantom size and decreasing tube potential and current (Figure 4.3 shows the results for the 40-cm phantom). The noise versus tube current-time product data points followed the expected exponential relationship, with a power of around -0.5 (fitted lines in Figure 4.3). At lower tube potential settings, photon starvation artifacts were observed for measurements obtained in the largest phantom size. For all tube current-time products and phantom sizes evaluated per tube potential setting, the difference in image noise between the EID and PCD system was minimal, ranging from 0.0 to 3.8 HU for 80 kV, 0.0 to 3.0 HU for 100 kV, 0.0 to 2.8 HU for 120 kV, and 0.1 to 2.2 HU for 140 kV.

The values for the coefficient of variations for ROI measurements (contrast, noise, and CNR) were small, and hence error bars were not shown in Figures. 4.3 to 4.5. Typical values for the coefficients of variation were below 1%, with a maximum value of 2.5%.

Contrast-to-noise ratio was significantly ($P < 0.05$) higher in the PCD system relative to the EID system for all tube potentials, the mean ± SD improvement was 11% ± 11%, 23% ± 18%, 31% ± 28%, and 38% ± 24% at 80, 100, 120, and 140 kV, respectively. The increase in CNR for the PCD system relative to the EID system was greatest at higher tube potential settings. The CNR versus tube current-time product data points followed the expected exponential relationship, with power close to 0.5 (fitted lines in Figure 4.4).

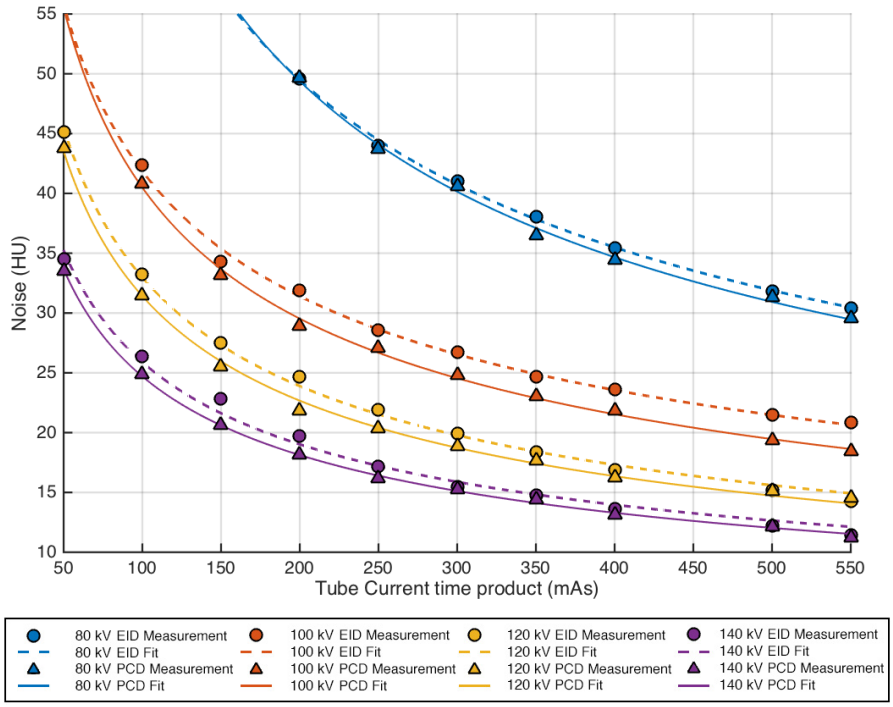

Fig. 4.3. Comparison of image noise versus tube current-time product between the EID images and the low-energy threshold (TL) images from the PCD for the 40-cm (large adult) phantom. The noise was very similar between the 2 systems, albeit consistently a small amount higher for the EID system. The 4 curves are for the 4 tube potential settings (80, 100, 120, 140 kV).

4.3.2 Energy-Selective Bin Image Data

The CT numbers of the iodinated contrast material that were measured in the low-energy bin images of the PCD system were higher in all cases than those measured for the EID system (Figure 4.5 illustrates these results for the mean CT numbers of ROI 4 in a 20-cm phantom). Conversely, the CT numbers in the iodinated contrast material that were measured in the high-energy bin images of the PCD system were lower in all cases than those measured for the EID system (Figure 4.5). Comparing CT numbers among the 4 PCD data sets, low-energy bin images have the highest CT number, followed by the low-energy threshold images. The high-energy bin and high-energy threshold images, which are identical by definition, both had lower CT numbers than the low-energy bin images and low-energy threshold images. These data demonstrate the energy dependence of CT numbers in PCD images.

4.3.3 First PCD-CT Images of Human Anatomy

The images of a human body acquired with a PCD subsystem were deemed to have equivalent clinical image quality relative to current EID subsystem (Figure 4.6). The thorax, abdomen, and pelvis images, where the anatomic dimensions exceed the PCD subsystem's FOV of 275 mm, were free of truncation artifacts. Smaller areas, such as the extremities, did not demonstrate artifacts associated with pulse pileup or other high-flux effects, which might be

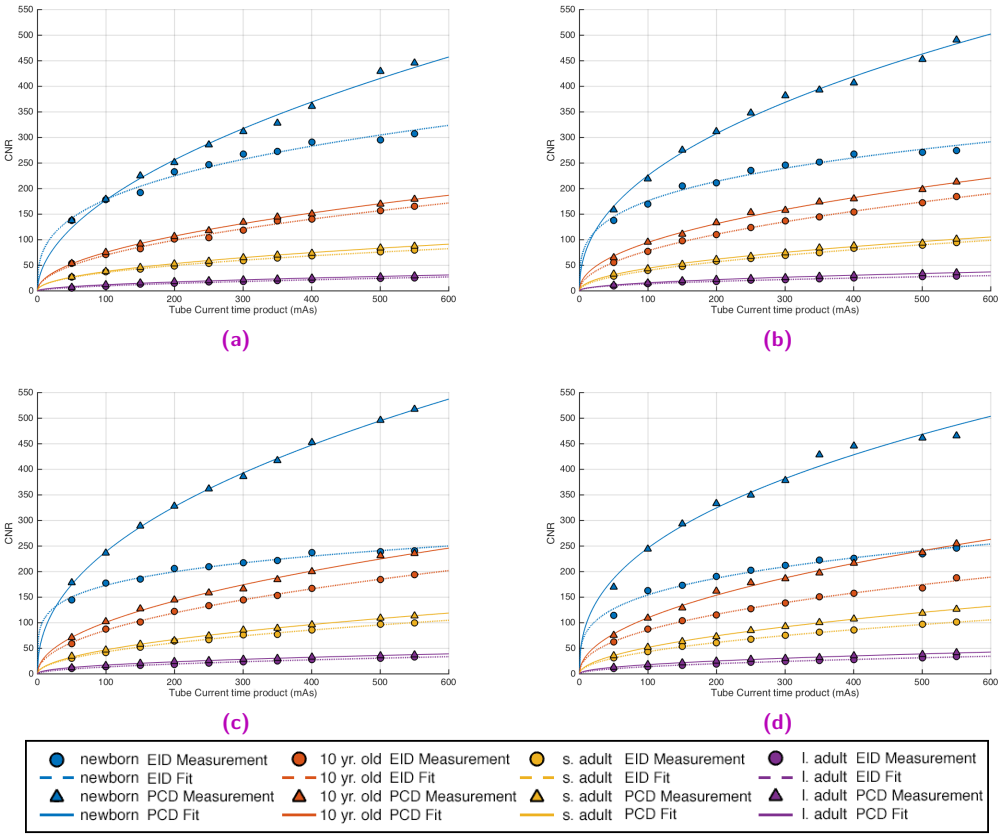

Fig. 4.4. Comparison of CNR versus tube current-time product (milliampere-seconds) in each of the 4 phantom sizes between the EID images and the low-energy threshold (TL) images from the PCD (A, 80 kV; B, 100 kV; C, 120 kV; D, 140 kV). The iodine CNR in the PCD (TL) images was consistently greater than the iodine CNR in the EID images; s. adult indicates small adult; l. adult, large adult.

expected at the higher flux measured through thinner anatomy. All images were free of ring artifacts.

Comparing the PCD images to the EID images, the following differences were noted:

1. The bin 2 (high energy) images of the posterior fossa showed considerably less beam-hardening artifact between the areas of dense bone (Figure 4.7) than the EID images and the bin 1 PCD images. Note: algorithmic water beam-hardening corrections were applied to the images, but second order bone beam-hardening corrections were not. Thus, beam-hardening artifacts that normally required additional processing to remove were not present in the unprocessed high-energy PCD data.

2. The high Z material contrast (bone) of the bin 1 (low energy) PCD images was higher than that of the EID system, in agreement with the phantom measurements (Figures. 4.7, 5.2).

3. The skull/brain interface was much sharper in the bin 2 (high-energy images) of the PCD system compared with the EID system and bin 1 of the PCD system (Figure 5.2). This was presumably due to decreased calcium-blooming effects.

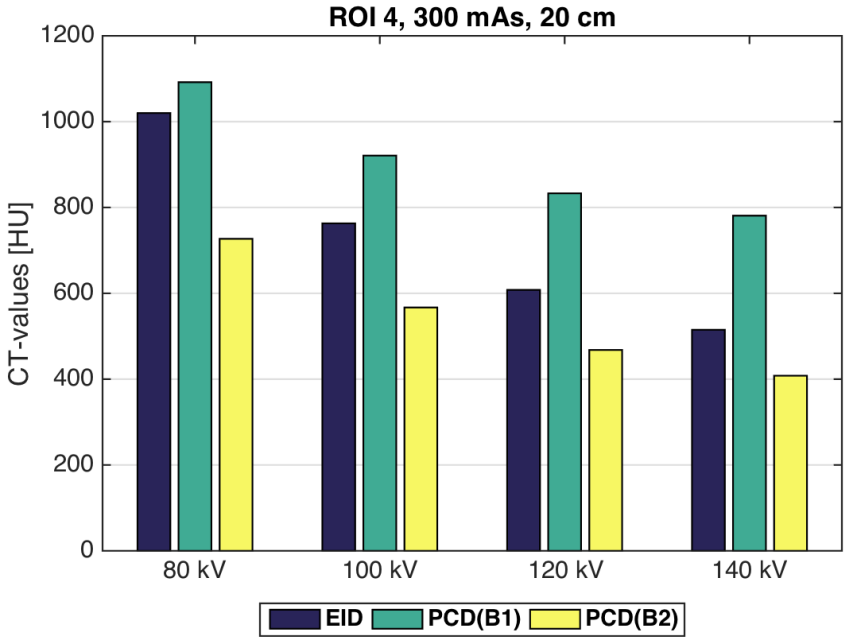

Fig. 4.5. Computed tomography numbers measured in ROI 4, which contained iodinated contrast media, show an increase in CT numbers in the lower energy bin 1 (B1) of the PCD system and a decrease in the higher energy bin 2 (B2) of the PCD system relative to the energy integrating (EID) system. Shown here are the CT values for the 20-cm phantom at 300 mA.

4.4 Discussion

Several characteristics of PCDs make them of significant interest for medical CT imaging, including relative immunity to electronic noise, enhanced iodine contrast, and decreased beam-hardening and calcium blooming artifacts. In addition, their ability to resolve photons of different energy ranges allows for acquisition of multienergy data sets, which can be used for material decomposition and quantitative material analyses. In this work, we demonstrated 3 important findings. First, the iodine contrast and CNR were superior for PCD relative to EID, particularly at higher tube potentials, which are necessary when imaging moderate to extremely large size patients. This may allow, for example, reduction of the applied radiation dose while maintaining the same iodine CNR. Second, PCD-CT produced images in energy-selective energy bins. In the example provided here with 2 energy bins, dual-energy processing from a single, simultaneous data acquisition would be possible. This avoids the need for a second x-ray source, dual layer detector, or the use of tube potential switching. The energy thresholds can be freely chosen (within the allowable ranges) to tailor the acquisition to the desired dual-energy or multienergy analysis. In this study, our thresholds were chosen to obtain similar photon statistics in each bin image for a tube potential of 140 kV. Other choices would allow, for example, techniques such as k-edge subtraction. Third, we have shown the first images of a human body acquired using a PCD-CT system capable of operating at clinical photon flux levels (e.g., 550 mA). These images demonstrated equivalent image quality relative to an EID-CT system. With respect to the contrast of high Z materials, and beam-hardening or calcium-blooming artifact, the high-energy PCD images were superior to the EID images.

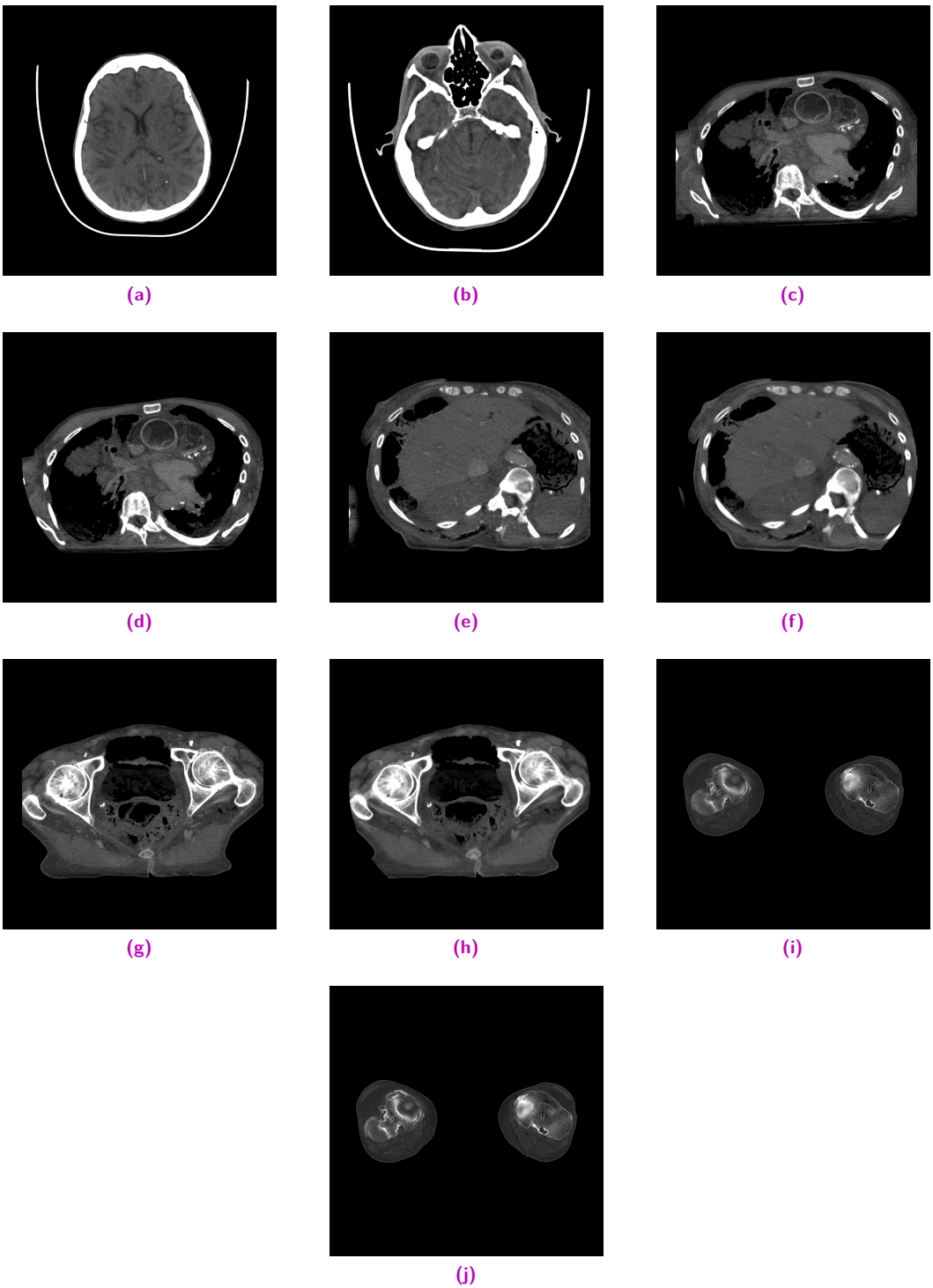

Fig. 4.6. Cerebrum (a), posterior fossa (b), thorax ((c) and (d)), abdomen ((e) and (f)), pelvis ((g) and (h)), and legs ((i) and (j)) of a female human cadaver scannedwith the EID ((c), (e), (g), (i)) and PCD((a), (b), (d), (f), (h), (j)) subsystems. The image quality was deemed to be equivalent between the 2 subsystems by the radiologist viewers. Energy-integrating detector head images were not acquired at the same settings as for the PCD subsystem and are thus not included. Figures. 4.7 and 5.2 provide EID to PCD comparisons for the head.

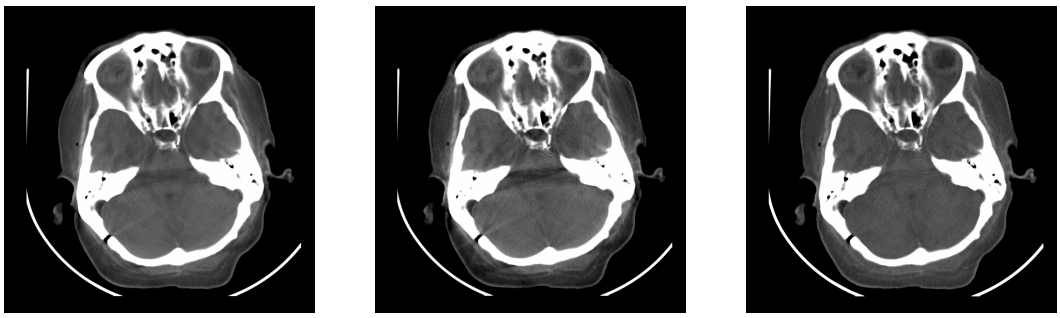

(a) (b) (c)

Fig. 4.7. Images of a cadaver head. Energy-integrating detector images (a), PCD images (low-energy bin; (b)), and PCD images (high-energy bin; (c)). The high-energy images of the posterior fossa acquired using the PCD subsystem showed considerably less beam-hardening artifact between the areas of dense bone than the EID image and low-energy PCD image. While water beam-hardening corrections were applied to the images as part of the normal image reconstruction, second order bone beam-hardening corrections were not applied here. This was done to demonstrate that beam-hardening artifacts that normally require algorithmic correction were not present in the uncorrected high-energy PCD image.

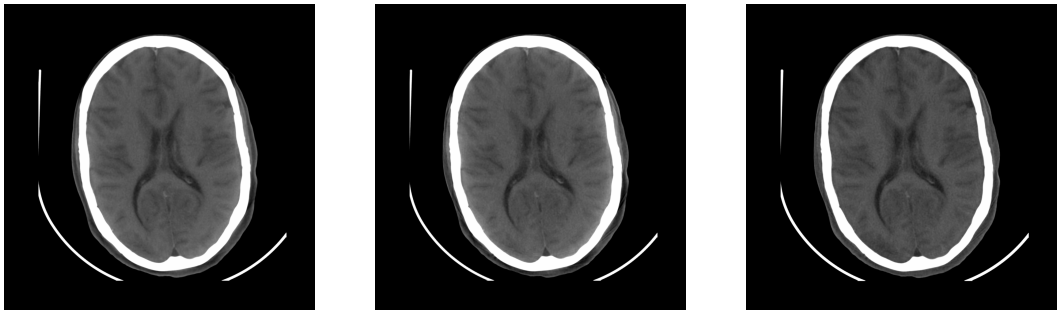

(a) (b) (c)

Fig. 4.8. Images of a cadaver head. Energy-integrating detector images (a) PCD images (low-energy bin; (b)) and PCD images (high-energy bin; (c)) The skull/brain interface was much sharper in the high-energy bin PCD image compared with the EID image and low-energy bin PCD image.

In conventional EID systems, detector signal is proportional to the energy deposited by the incoming photons; consequently, higher energy photons are more strongly weighted than lower energy photons. The detector signal in PCD systems, however, is proportional to the number of detected photons. Therefore, lower energy photons have higher weights in PCD system compared with EID system, which consequently generates higher contrast for high Z materials. Results from our study demonstrated the increased contrast and CNR of iodine solutions using PCD-CT in comparison with EID-CT. We also found that the contrast improvement was more obvious for examinations performed at high tube potentials, where the spectrum covered a wider range of photons; it was less obvious for examinations performed at low tube potentials due to the more narrow and predominantly low energy spectrum of the beam. In addition to this fundamental advantage of PCD systems (i.e., weighting by photon count rather than photon energy), researchers have also investigated other schemes and found that CNR can be further improved by assigning higher weighting to the lower energy photons [37, 95, 287, 298].

Previous studies in bench-top PCD-CT systems have demonstrated the capability of multienergy CT using PCDs to perform quantitative material composition analyses [8, 36, 284]. Such analyses result in material specific images in which the pixel value represents the concentration of the specified material. However, due to the limited size of these systems, the work has been restricted to small animals only (e.g., mice or rabbits) [76, 230, 284]. Our work with the described research PCD-CT system extends the capabilities of PCD-CT to the inner 275-mm diameter of the human body. To avoid data truncation artifacts, a separate DCS acquisition is required on this research system. Using the A tube, projection data acquired from the EID system were converted to the format of the PCD system projection data and added to the PCD projection data outside of the 275-mm FOV. Note that the DCS is only to complete the PCD data to avoid truncation artifact, it is not to extend the FOV of PCD data. Although extra dose is required for this additional DCS acquisition, it can be performed at a very low dose. It was found in a separate study that the DCS scan can be performed with a $CTDI_{vol}$ around 1 mGy (which was the minimum value achievable in the abdomen protocol) without sacrificing the quality of PCD images. It is essential to note that there is no fundamental limitation to the FOV of the PCD array. Rather, as a research scanner, it was decided to only cover this FOV; the addition of more PCD modules to the B detector would overcome this limitation and remove the need for a DCS.

Our study is limited in several aspects. First, we limited our evaluation to that of the macro acquisition mode, where each 4×4 detector pixel array is read out as a single pixel value. The underlying improved spatial resolution of the described PCD array is not captured in this mode. There is no fundamental limitation to reading out each subpixel individually. For this research scanner, at this stage of its development, this feature has not yet been enabled, primarily due to data rate transfer limitations, as essentially 16 times more data would be delivered in the same time frame as the system on which the research scanner was based reads out only 1 detector pixel. Evaluation of subpixel data sets will be the subject of future work. Second, we did not seek to take advantage of the energy-selective properties of the acquired data. Although we demonstrated the different CT numbers of iodine due to the different energy spectra captured by bin 1 and bin 2, we did not perform any material decomposition analyses, as the energy thresholds that were used were not chosen to optimize spectral separation but rather to provide similar noise characteristics at 140 kV. Also, our development of multienergy material decomposition algorithms is ongoing. Third, the decreased beam hardening and calcium blooming in the high-energy bin comes at the cost of increased noise, as only a portion of the photon spectrum was used to form the high-energy bin image. Ongoing work with iterative reconstruction and energy domain noise reduction techniques is focused on retaining the positive aspects of the high-energy bin image while decreasing the noise level to that of the low-energy threshold image [363].

In summary, this work quantitatively demonstrated in phantoms the improved iodine CNR and the energy sensitivity of PCDs, and showed in images of the human body that the image quality is as good as state-of-the-art EID-CT systems. To the best of our knowledge, these are the first images of human anatomy acquired with a high-flux capable PCD-CT system. The improved CNR could be used directly to improve conspicuity of subtle enhancing lesions, such as those in the liver. Alternatively, the dose of radiation or iodinated contrast material could be reduced such that the same CNR as the EID system was achieved. Dose reduction is one potential application of PCD technology. Another potential application is the reduction of

beam-hardening and calcium-blooming artifacts. Finally, the energy-selective information acquired in the separate bin images could be used with dual-energy algorithms to perform analyses similar to those currently in use [202], including quantitative material concentration analyses. New multienergy algorithms are under development in our laboratory and elsewhere to take advantage of the data from more than 2 energy bins. Thus, PCD technology makes possible new techniques and clinical applications, while delivering image quality equivalent to current state-of-the-art EID-CT systems.

Acknowledgements

The authors sincerely thank André Henning and Friederike Schöck for their assistance in data acquisition.

4.5 References

[8] R. E. Alvarez. "Dimensionality and noise in energy selective x-ray imaging". In: *Medical Physics* 40.11 (2013), p. 111909

[23] J. Beutel, H. L. Kundel, Y. Kim, R. L. Van Metter, and S. C. Horii. *Handbook of medical imaging*. Vol. 3. Spie Press, 2000

[35] J. T. Bushberg and J. M. Boone. *The essential physics of medical imaging*. Lippincott Williams & Wilkins, 2011

[36] J. Butzer, A. Butler, P. Butler, P. Bones, N Cook, and L Tlustos. "Medipix imaging-evaluation of datasets with PCA". in: *2008 23rd International Conference Image and Vision Computing New Zealand*. IEEE. 2008, pp. 1–6

[37] R. Cahn, B Cederström, M. Danielsson, A Hall, M Lundqvist, and D Nygren. "Detective quantum efficiency dependence on x-ray energy weighting in mammography". In: *Medical Physics* 26.12 (1999), pp. 2680–2683

[44] J. A. Christner, K. Stierstorfer, A. N. Primak, C. D. Eusemann, T. G. Flohr, and C. H. McCollough. "Evaluation of-axis resolution and image noise for nonconstant velocity spiral CT data reconstructed using a weighted 3D filtered backprojection (WFBP) reconstruction algorithm". In: *Medical Physics* 37.2 (2010), pp. 897–906

[76] S. Feuerlein, E. Roessl, R. Proksa, G. Martens, O. Klass, M. Jeltsch, V. Rasche, H.-J. Brambs, M. H. Hoffmann, and J.-P. Schlomka. "Multienergy photon-counting K-edge imaging: potential for improved luminal depiction in vascular imaging 1". In: *Radiology* 249.3 (2008), pp. 1010–1016

[95] J. Giersch, D. Niederlöhner, and G. Anton. "The influence of energy weighting on X-ray imaging quality". In: *Nuclear Instruments and Methods in Physics Research Section A: Accelerators, Spectrometers, Detectors and Associated Equipment* 531.1 (2004), pp. 68–74

[125] J. A. Heanue, D. A. Pearson, and R. E. Melen. “CdZnTe detector array for a scanning-beam digital x-ray system”. In: *Medical Imaging 1999: Physics of Medical Imaging*. Vol. 3659. SPIE. 1999, pp. 718–725

[127] B. J. Heismann, B. T. Schmidt, and T. G. Flohr. “Spectral computed tomography”. In: SPIE Bellingham, WA. 2012

[128] W. Hendee and E. Ritenour. *Medical Imaging Physics*. Wiley, 2003

[142] J. S. Iwanczyk, E. Nygard, O. Meirav, J. Arenson, W. C. Barber, N. E. Hartsough, N. Malakhov, and J. C. Wessel. “Photon counting energy dispersive detector arrays for x-ray imaging”. In: *IEEE Transactions on Nuclear Science* 56.3 (2009), pp. 535–542

[157] S Kappler, F Glasser, S Janssen, E Kraft, and M Reinwand. “A research prototype system for quantum-counting clinical CT”. in: *International Society for Optics and Photonics Medical Imaging*. International Society for Optics and Photonics. 2010, 76221Z–76221Z

[158] S Kappler, T Hannemann, E Kraft, B Kreisler, D Niederloehner, K Stierstorfer, and T Flohr. “First results from a hybrid prototype CT scanner for exploring benefits of quantum-counting in clinical CT”. in: *International Society for Optics and Photonics Medical Imaging*. International Society for Optics and Photonics. 2012, pp. 83130X–83130X

[159] S Kappler, A Henning, B Krauss, F Schoeck, K Stierstorfer, T Weidinger, and T Flohr. “Multi-energy performance of a research prototype CT scanner with small-pixel counting detector”. In: *International Society for Optics and Photonics Medical Imaging*. International Society for Optics and Photonics. 2013, 86680O–86680O

[160] S Kappler, A Henning, B Kreisler, F Schoeck, K Stierstorfer, and T Flohr. “Photon counting CT at elevated X-ray tube currents: contrast stability, image noise and multi-energy performance”. In: *International Society for Optics and Photonics Medical Imaging*. International Society for Optics and Photonics. 2014, pp. 90331C–90331C

[170] T. Koenig, J. Schulze, M. Zuber, K. Rink, J. Butzer, E. Hamann, A. Cecilia, A. Zwerger, A. Fauler, M. Fiederle, et al. “Imaging properties of small-pixel spectroscopic x-ray detectors based on cadmium telluride sensors”. In: *Physics in Medicine and Biology* 57.21 (2012), p. 6743

[199] C. H. McCollough, G. H. Chen, W. Kalender, S. Leng, E. Samei, K. Taguchi, G. Wang, L. Yu, and R. I. Pettigrew. “Achieving routine submillisievert CT scanning: report from the summit on management of radiation dose in CT”. in: *Radiology* 264.2 (2012), p. 567

[202] C. H. McCollough, S. Leng, L. Yu, and J. G. Fletcher. “Dual-and multi-energy CT: principles, technical approaches, and clinical applications”. In: *Radiology* 276.3 (2015), pp. 637–653

[219] M. E. Myronakis and D. G. Darambara. “Monte Carlo investigation of charge-transport effects on energy resolution and detection efficiency of pixelated CZT detectors for SPECT/PET applications”. In: *Medical Physics* 38.1 (2011), pp. 455–467

[230] D. Pan, E. Roessl, J.-P. Schlomka, S. D. Caruthers, A. Senpan, M. J. Scott, J. S. Allen, H. Zhang, G. Hu, P. J. Gaffney, et al. “Computed tomography in color: NanoK-enhanced spectral CT molecular imaging”. In: *Angewandte Chemie* 122.50 (2010), pp. 9829–9833

[272] E Roessl and R Proksa. “K-edge imaging in x-ray computed tomography using multi-bin photon counting detectors”. In: *Physics in Medicine and Biology* 52.15 (2007), p. 4679

[284] J. Schlomka, E Roessl, R Dorscheid, S Dill, G Martens, T Istel, C Bäumer, C Herrmann, R Steadman, G Zeitler, et al. “Experimental feasibility of multi-energy photon-counting K-edge imaging in pre-clinical computed tomography”. In: *Physics in Medicine and Biology* 53.15 (2008), p. 4031

[287] T. G. Schmidt. “Optimal “image-based” weighting for energy-resolved CT”. in: *Medical Physics* 36.7 (2009), pp. 3018–3027

[297] P. M. Shikhaliev. “Computed tomography with energy-resolved detection: a feasibility study”. In: *Physics in Medicine & Biology* 53.5 (2008), p. 1475

[298] P. M. Shikhaliev. “Energy-resolved computed tomography: first experimental results”. In: *Physics in Medicine & Biology* 53.20 (2008), p. 5595

[344] “Weighted FBP—a Simple Approximate 3D FBP Algorithm for Multislice Spiral CT With Good Dose Usage for Arbitrary Pitch”. In: *Physics in Medicine and Biology* 49.11 (2004), p. 2209

[320] C. Szeles, S. A. Soldner, S. Vydrin, J. Graves, and D. S. Bale. “CdZnTe semiconductor detectors for spectroscopic x-ray imaging”. In: *IEEE Transactions on Nuclear Science* 55.1 (2008), pp. 572–582

[322] K. Taguchi and J. S. Iwanczyk. “Vision 20/20: Single photon counting x-ray detectors in medical imaging”. In: *Medical Physics* 40.10 (2013), p. 100901

[323] K. Taguchi, M. Zhang, E. C. Frey, X. Wang, J. S. Iwanczyk, E. Nygard, N. E. Hartsough, B. M. Tsui, and W. C. Barber. “Modeling the performance of a photon counting x-ray detector for CT: Energy response and pulse pileup effects”. In: *Medical Physics* 38.2 (2011), pp. 1089–1102

[333] T. Tumer, M Clajus, G. Visser, S Yin, P. Willson, L D’Aries, K. Parnham, B Glick, J. Perry, T Gamble, et al. “Preliminary results obtained from a novel CdZnTe pad detector and readout ASIC developed for an automatic baggage inspection system”. In: *IEEE Nuclear Science Symposium Conference*. Vol. 1. IEEE. 2000, pp. 4–36

[336] A. de Vries, E. Roessl, E. Kneepkens, A. Thran, B. Brendel, G. Martens, R. Proska, K. Nicolay, and H. Grüll. “Quantitative spectral K-edge imaging in preclinical photon-counting x-ray computed tomography”. In: *Investigative Radiology* 50.4 (2015), pp. 297–304

[342] T Weidinger, T. Buzug, T Flohr, G. Fung, S Kappler, K Stierstorfer, and B. Tsui. “Investigation of ultra low-dose scans in the context of quantum-counting clinical CT”. in: *Medical Imaging 2012: Physics of Medical Imaging*. Vol. 8313. SPIE. 2012, pp. 1207–1215

[358] Z. Yu, S. Leng, S. M. Jorgensen, Z. Li, R. Gutjahr, B. Chen, X. Duan, A. F. Halaweish, L. Yu, E. L. Ritman, and C. H. McCollough. “Initial results from a prototype whole-body photon-counting computed tomography system”. In: *International Society for Optics and Photonics Medical Imaging*. International Society for Optics and Photonics. 2015, 94120W–94120W

[363] Z. Yu, S. Leng, Z. Li, E. L. Ritman, and C. H. McCollough. “Spectral PICCS Reconstruction for PCCT”. in: 2nd Workshop on Medical Applications of Spectroscopic X-ray Detectors (CERN, Geneva, Swiss). 2015

5

Material Decomposition and Virtual Non-Contrast Imaging in Photon Counting Computed Tomography - An Animal Study

Ralf Gutjahr, MSc,[1,2] Christoph Polster, Dipl.-Phys.,[2,3] Steffen Kappler, PhD.,[2] Hubertus Pietsch, MD,[4] Gregor Jost, PhD.,[4] Katharina Hahn, PhD,[2] Friederike Schöck, PhD,[2] Martin Sedlmair, PhD,[2] Thomas Allmendinger, PhD,[2] Bernhard Schmidt, PhD,[2] Bernhard Krauss, PhD,[2] and Thomas G. Flohr, PhD[2]

[1]CAMP, Technical University of Munich, Garching (Munich), Germany
[2]Siemens Healthcare GmbH, Forchheim, Germany
[3]Institute of Clinical Radiology, Ludwig-Maximilians-University Hospital, Munich, Germany
[4]Bayer Pharma AG, Berlin, Germany

Copyright statement

Contributions

The author of this thesis was responsible in conceptualizing the study and developing its methodology. His involvement in the experiment preparation included the conduction and processing of prior calibration scans for the two contrast media (Gd, Xe) and various object sizes, as well as ensuring logistics for animal measurements. The author was responsible for the formal evaluation of the study's results. The author's efforts in data curation encompassed data conversion from a prototype format into a format readable by the evaluation software. The author was also the main responsible person for writing and presenting the results of this work.

The co-authors participated the study's conceptualization and method development, helping to shape its direction and framework. Their expertise was crucial in guaranteeing the ethical treatment of the investigated animal, adhering to established guidelines and best practices. Moreover, the co-authors played an important role in reviewing and editing the article, They also supplied essential resources and supervision, ensuring the research's quality and seamless execution.

5.1 Abstract

The energy resolving capabilities of Photon Counting Detectors (PCD) in Computed Tomography (CT) facilitate energy-sensitive measurements. The provided image-information can be processed with Dual Energy and Multi Energy algorithms. A research PCD-CT firstly allows acquiring images with a close to clinical configuration of both the X-ray tube and the CT-detector. In this study, two algorithms (Material Decomposition and Virtual Non-Contrast-imaging (VNC)) are applied on a data set acquired from an anesthetized rabbit scanned using the PCD-CT system. Two contrast agents (CA) are applied: A gadolinium (Gd) based CA used to enhance contrasts for vascular imaging, and xenon (Xe) and air as a CA used to evaluate local ventilation of the animal's lung. Four different images are generated: a) A VNC image, suppressing any traces of the injected Gd imitating a native scan, b) a VNC image with a Gd-image as an overlay, where contrast enhancements in the vascular system are highlighted using colored labels, c) another VNC image with a Xe-image as an overlay, and d) a 3D rendered image of the animal's lung, filled with Xe, indicating local ventilation characteristics. All images are generated from two images based on energy bin information. It is shown that a modified version of a commercially available dual energy software framework is capable of providing images with diagnostic value obtained from the research PCD-CT system.

Keywords

CT, Dual-Energy CT, Multi-Energy CT, Spectral CT, Photon-Counting CT, Material Decomposition, Virtual Non-Contrast

5.2 Purpose

The attenuation of X-rays depends on the material of the penetrated object and the applied X-ray spectrum - this is the key characteristic utilized in Spectral Computed Tomography (Spectral CT). The idea to associate X-ray measurements acquired using different photon energies was firstly reported by Jacobson in 1953 [144]. The concept was eventually translated and applied to the technology of CT by Hounsfield, Rutherford, Alvarez and Macovski [9, 133, 278]. Since then, several techniques and hardware-designs of CT-systems providing spectral information have been proposed, e.g. Dual Source-CT, fast kV-switching CT, and Dual-Layer CT [7, 81, 134]. However, all of these approaches use conventional Energy Integrating Detectors (EIDs) and are realized by the combination of the information obtained by parallel

or subsequent measurements of integrated X-ray signals, rather than by resolving photons' individual energy levels within a polychromatic X-ray spectrum in one single detector.

Recent efforts and developments introduced energy resolving PCDs [146, 159, 302]. Whilst conventional EIDs integrate the X-ray flux over time, discarding the spectral information of the incident signal, PCDs actually count photons exceeding given energy-thresholds. Considering a set of energy-thresholds, energy-bins can be derived leading to the introduction of energy-sensitive measurements.

In spite of the technology's physically inherent limitations [125, 142, 159, 219, 320, 322, 323, 347], PCD-CT provides crucial benefits compared with EID-CT [127, 158, 287, 297, 322]. Whilst high photon flux has been a major challenge in previous studies and systems [142, 157, 284], a research PCD-CT system was eventually introduced, capable to operate with clinically acceptable tube-configurations and detector-setups [159].

The purpose of this study is to demonstrate the application of two image-based post-processing algorithms (Material Decomposition, VNC-imaging) applied on CT-data provided by a research PCD-CT system. The CT-data was acquired in an animal study where two different CAs were applied: a Gd-based CA used for vascular imaging and Xe and air for an assessment of the ventilation of the lungs [172].

5.3 Materials and Methods

he research PCD-CT scanner-layout as used in this study is based on a commercial Dual-Source CT-system (SOMATOM Definition Flash, Siemens Healthcare, Forchheim, Germany). The gantry contains two X-ray tubes and two respective detector systems. The gantry's bore diameter is 780 mm. One detector system is based on conventional energy integration, whereas the other one is a PCD. The two systems, i.e. their detectors and tubes, are offset by 95°. For both systems the source to isocenter distance is 595 mm. The system's rotation time is can be chosen to either 0.5 s or 1.0 s.

The two embedded X-ray tubes, including their filtrations, are both identical in their specifications. Both tubes provide peak voltages of either 80, 100, 120, or 140 kVp. The tube currents range from 25 to 550 mA in steps of 1 mA. The emitted X-ray spectra get filtered by the tube housing. Additional X-ray beam shaping occurs depending on the applied protocol by a carbon and/or an aluminum bowtie-filter.

The GOS-based EID provides a projection matrix of 736 $\times$ 64 with a pixel pitch of 0.6 mm in z-direction in the isocenter. The whole z-coverage is 38.4 mm. The in-plane field of view (FOV) of this system is 500 mm. The scintillating material has a thickness of 1.4 mm and is coupled to photodiodes and charge-integrating electronics.

The research PCD is comprised of a 1.6 mm thick Cadmium Telluride (CdTe) semiconducting material organized in 30 $\times$ 2 single modules; each module contains 64 $\times$ 64 pixels with an individual pitch of 1.125 mm. One pixel encloses 4 $\times$ 4 sub-pixels with an individual pitch of 0.225 mm whereas every fifth pixel in azimuthal direction is covered by the gratings of

a anti-scatter collimator. The PCD has a projection matrix of 480 $\times$ 32, it covers a FOV of 275 mm and has a total longitudinal coverage of 16 mm. In cases where the scanned objects exceed the FOV of the PCD-system, a so-called Data Completion Scan (DCS) can be applied in order to prevent accruing truncation artifacts in the CT-images [362]. Every sub-pixel is supported by readout electronics that provide multi-level comparators and counting units; two energy-thresholds per sub-pixel are provided in this particular research PCD layout, i.e. the lower energy-threshold (T_{low}) and the higher energy-threshold (T_{high}) covering an energy range from 20 to 50 keV and from 50 to 90 keV, respectively. Both of the threshold-values can be adjusted in steps of 1 keV. The pixels can be read out in two different modes:

1. **Macro-Mode**: Two thresholds are applied per sub-pixel. Hereby every single sub-pixel has the same common two energy-threshold-values as its adjacent sub-pixel. The image acquisition in Macro-Mode provides 4 image-volumes: 2 threshold-based image-volumes and 2 bin-based image-volumes. The threshold images are defined by all the photons that exceed the respective threshold, whereas bin-based images are reconstructed based on the photon information of photons which energies lay between two adjacent threshold-values, or, as for the last bin, between the highest threshold and the maximal tube voltage. Bin-based images provide a better spectral separation than threshold-based images.

2. **Chesspattern-Mode**: In this mode every second neighboring sub-pixel provides identical lower and higher thresholds. As a result, 8 image-volumes are obtained per scan, i.e. 4 threshold-based image-volumes and 4 bin-based image-volumes. Applying the Chesspattern-Mode, the quanta-statistics between two neighboring pixels are modified, i.e. altered noise characteristics and covariances with the other images exhibit [147].

The CT-images were acquired in caudo-cranial direction using the Macro-Mode with two energy thresholds of T_{low} = 25 keV and T_{high} = 65 keV, i.e. energy bins of Bin1 = [25, 65] keV and Bin2 = [65, 140] keV, respectively. The X-ray tube was set to provide a peak voltage of 140 kVp with a current of 266 mA, a rotation time of 0.5 s, and a pitch of 0.6 resulting in a pitch normalized tube-current-time-product of 222 mAs. The high tube potential was selected in order to provide a broad energy spectrum and good spectral separation. An additional DCS was performed and used for the reconstruction of the PCD-based images. The images were reconstructed in 1.0 mm thick slices and a 1.0mm increment per image slice. The reconstruction was performed using a medium smooth (D45) kernel. All CT-images used in this study are reconstructed using a Weighted Filtered Back Projection-algorithm (WFBP). [344]

An animal study was conducted on a anesthetized rabbit in order to evaluate it's thoracic vascularization. For that purpose a Gd-based contrast agent material (Gadomer [58] 78 mg Gd/mL) was injected intravenously with a dose of 50 mg Gd/kg and an injection rate of 1 mL/s. Additionally, the rabbit was respirated with Xe (Linde AG, Unterschleißheim, Germany) and air (with an approximate ratio of 1:1) over a duration of 2 min. During the actual scan and end-inspiration breath-hold maneuver was performed. An image based lung segmentation was applied in order to assess local ventilation of the rabbit's lung. Both CAs, Gadomer and Xe, are generally not approved to be used as CA for CT.

The separation of the Gadomer from other materials is based upon the definition of three basis vectors: one for soft tissue, one for fat, and another one for Gd. An eventual basis transformation allows to derive the amount of soft tissue, fat and Gd per pixel. The detection of the Xe inside the lung, however, is based on the assumption, that the measured material is a compound of lung tissue, air, and Xe. The CT-values of these materials under the given spectra and the selected energy thresholds constrain the possible CT-value-ratios in the acquired bin-images of the PCD-CT.

The evaluation of the acquired CT-data was conducted using a modified Siemens *syngo* Multi-modality Workspace (MMWP), which facilitated the processing of image volumes obtained from the respective research system. The modifications allow evaluations of PCD-CT data and take into account image noise, material contrasts, and correlations of CT-values over different patient sizes.

5.4 Results

Two initial bin-based images of the PCD-CT acquisition (fig. 5.1 (a) and (b)) were used to calculate a VNC-image as shown in fig. 5.1 (c). The VNC algorithm successfully suppresses all traces of CA in a final image, imitating a native CT-scan. Fig. 5.1 (d) shows a Gd-image as an enhanced overlay over the VNC image in order to bring it into an anatomical context. Both the ascending aorta and the truncus brachiocephalicus are clearly visible. The color coding of the Gd-image quantitatively indicates the amount and the concentration of the CA in the tissue. The calculated CT-values of different tissue types within the VNC-image showed similar enhancements as the bin-images in corresponding areas (heart tissue: 46.6 HU vs. 46.9 HU and 43.3 HU, liver tissue: 61.5 HU vs. 64.9 HU and 58.7 HU, muscle tissue: 67.5 HU vs. 64.4 HU and 61.2 HU, for the VNC-image against the bin1-image and bin2-image of the native scan, respectively).

The CT-value scatterplot in fig. 5.2 (a) shows the corresponding CT-values as measured in a region of interest (ROI) within lung tissue as measured in the two energy bins. Using the introduced scan parameters (140 kV, T_{low} = 25 keV, T_{high} = 65 keV), the maximum difference in enhancement of the Xe within the two bin-images amounts up to 75 HU. Accordingly to the aforementioned assumption, the measured region qualifies as a material compound of air, Xe and soft tissue (dotted lines). The Xe-image in fig. 5.2 (b) highlights all pixels within a single slice that contain the Xe-based CA. Again, the Xe-image is superimposed on a VNC image, whilst the color coding of the image indicates the relative amount of detected Xe per pixel. The Xe-image shows a normal and non-pathological ventilation of the rabbit's lungs. Fig. 5.2 (c) shows a 3D rendered model of the detected Xe in the lung. It also illustrates the Xe as it was detected in the rabbit's trachea.

5.5 Discussion

We demonstrated the application of image based material decomposing algorithms on CT-images of a anesthetized rabbit obtained using a research PCD-CT scanner. The applied

(a) Bin1-image, $(25, 65)$ keV.

(b) Bin2-image, $(65, 140)$ keV.

(c) VNC image of the heart.

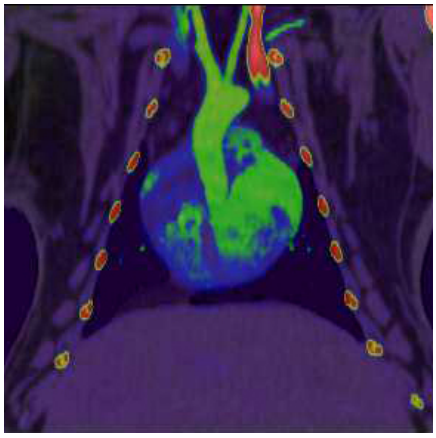

(d) Highlighted gadolinium based CA.

Fig. 5.1. Imaging of the rabbit's heart, C/W = 40/300 HU.

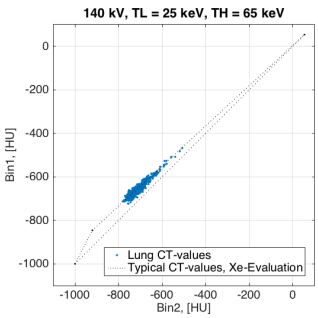

(a) CT-value Scatterplot, lung tissue.

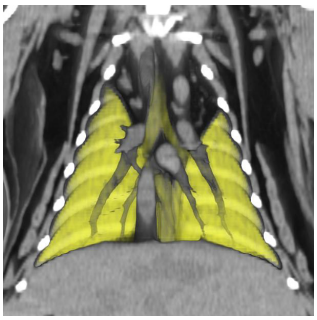

(b) Xe in lung, C/W = 40/300 HU.

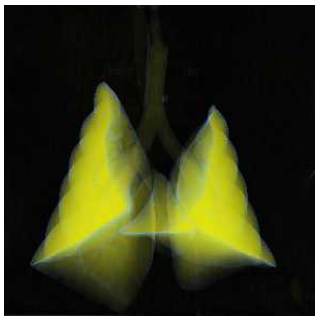

(c) 3D rendered lung.

Fig. 5.2. Xenon imaging of PCD-CT data.

detector technology allows to resolve an incident spectrum in order to generate energy specific images. No adjustment of the acquired sinograms or registration of the obtained image volumes were required. Two CAs, Gadomer and Xe, were applied. A VNC image with and without a Gd enhanced overlay was calculated. The VNC image mimics a native scan where no CA was applied. The obtained CT-values for different tissue types were compared against

the respective CT-values of an actual native scan, showing reasonable CT-values for both energy-bins.

The animal's ventilation was assessed by applying Xe and air as a CA. A Xe-image was generated and superimposed on a VNC image. Also, a 3D rendered image of the animal's lung was generated. The images allow qualitatively assessments of the animal's ventilation and eventual local impairments.

5.6 Conclusion

This study introduces the application of material decomposition algorithms on images obtained by a research PCD-CT system. The CT system's configuration was adjusted to be similar to the configurations used in clinical routine utilizing commercially available CT-systems with EID based detectors. The introduced PCD-CT system offers configurations using tube voltages, tube currents and acquisition speeds as used in clinical routine studies, while providing multi-energy information with every scan. Two CAs, one Gd-based, one Xe-based, were applied on a anesthetized rabbit. Image based material decomposition algorithms provided a VNC image, a Gd enhanced overlay image, as well as a Xe enhanced overlay image and a 3D rendered image of the animal's lung. The results of the applied algorithms were comparable to those of commercially available systems using EID.

5.7 References

[7] A. Altman and R. Carmi. "TU-E-210A-03: a double-layer detector, dual-energy CT—principles, advantages and applications". In: *Medical Physics* 36.6 Part 24 (2009), pp. 2750–2750

[9] R. E. Alvarez and A. Macovski. "Energy-selective reconstructions in x-ray computerised tomography". In: *Physics in Medicine & Biology* 21.5 (1976), p. 733

[81] T. G. Flohr, C. H. McCollough, H. Bruder, M. Petersilka, K. Gruber, C. Süß, M. Grasruck, K. Stierstorfer, B. Krauss, R. Raupach, et al. "First performance evaluation of a dual-source CT (DSCT) system". In: *European Radiology* 16.2 (2006), pp. 256–268

[125] J. A. Heanue, D. A. Pearson, and R. E. Melen. "CdZnTe detector array for a scanning-beam digital x-ray system". In: *Medical Imaging 1999: Physics of Medical Imaging*. Vol. 3659. SPIE. 1999, pp. 718–725

[127] B. J. Heismann, B. T. Schmidt, and T. G. Flohr. "Spectral computed tomography". In: SPIE Bellingham, WA. 2012

[133] G. N. Hounsfield. "Computerized transverse axial scanning (tomography): Part 1. Description of system". In: *The British Journal of Radiology* 46.552 (1973), pp. 1016–1022

[134] J Hsieh. “TU-E-210A-01: Dual-energy CT with fast-kVp switch”. In: *Medical Physics* 36.6Part24 (2009), pp. 2749–2749

[142] J. S. Iwanczyk, E. Nygard, O. Meirav, J. Arenson, W. C. Barber, N. E. Hartsough, N. Malakhov, and J. C. Wessel. “Photon counting energy dispersive detector arrays for x-ray imaging”. In: *IEEE Transactions on Nuclear Science* 56.3 (2009), pp. 535–542

[144] B. Jacobson. “Dichromatic absorption radiography. Dichromography”. In: *Acta Radiologica* 39.6 (1953), pp. 437–452

[147] P. Johns. “Photon-Counting Detectors for Digital Radiography and X-Ray Computed Tomography, 367–369 SPIE”. in: *TD01* (2002)

[159] S Kappler, A Henning, B Krauss, F Schoeck, K Stierstorfer, T Weidinger, and T Flohr. “Multi-energy performance of a research prototype CT scanner with small-pixel counting detector”. In: *International Society for Optics and Photonics Medical Imaging*. International Society for Optics and Photonics. 2013, 86680O–86680O

[161] S Kappler, A Henning, F Schoeck, K Stierstorfer, T Weidinger, and T Flohr. “A Hybrid Research Prototype CT Scanner with Photon Counting Detector”. In: *IEEE Transactions on Medical Imaging: Special Issue On Spectral CT*. IEEE. 2014

[162] S Kappler, D Niederlöhner, K Stierstorfer, and T Flohr. “Contrast-enhancement, image noise, and dual-energy simulations for quantum-counting clinical CT”. in: *International Society for Optics and Photonics Medical Imaging*. International Society for Optics and Photonics. 2010, 76223H–76223H

[219] M. E. Myronakis and D. G. Darambara. “Monte Carlo investigation of charge-transport effects on energy resolution and detection efficiency of pixelated CZT detectors for SPECT/PET applications”. In: *Medical Physics* 38.1 (2011), pp. 455–467

[278] R. Rutherford, B. Pullan, and I Isherwood. “Measurement of effective atomic number and electron density using an EMI scanner”. In: *Neuroradiology* 11.1 (1976), pp. 15–21

[284] J. Schlomka, E Roessl, R Dorscheid, S Dill, G Martens, T Istel, C Bäumer, C Herrmann, R Steadman, G Zeitler, et al. “Experimental feasibility of multi-energy photon-counting K-edge imaging in pre-clinical computed tomography”. In: *Physics in Medicine and Biology* 53.15 (2008), p. 4031

[287] T. G. Schmidt. “Optimal “image-based” weighting for energy-resolved CT”. in: *Medical Physics* 36.7 (2009), pp. 3018–3027

[297] P. M. Shikhaliev. “Computed tomography with energy-resolved detection: a feasibility study”. In: *Physics in Medicine & Biology* 53.5 (2008), p. 1475

[302] P. M. Shikhaliev, T. Xu, and S. Molloi. “Photon counting computed tomography: concept and initial results”. In: *Medical Physics* 32.2 (2005), pp. 427–436

[320] C. Szeles, S. A. Soldner, S. Vydrin, J. Graves, and D. S. Bale. “CdZnTe semiconductor detectors for spectroscopic x-ray imaging”. In: *IEEE Transactions on Nuclear Science* 55.1 (2008), pp. 572–582

[322] K. Taguchi and J. S. Iwanczyk. “Vision 20/20: Single photon counting x-ray detectors in medical imaging”. In: *Medical Physics* 40.10 (2013), p. 100901

[323] K. Taguchi, M. Zhang, E. C. Frey, X. Wang, J. S. Iwanczyk, E. Nygard, N. E. Hartsough, B. M. Tsui, and W. C. Barber. “Modeling the performance of a photon counting x-ray detector for CT: Energy response and pulse pileup effects”. In: *Medical Physics* 38.2 (2011), pp. 1089–1102

[347] L. Wielopolski and R. P. Gardner. “Prediction of the pulse-height spectral distortion caused by the peak pile-up effect”. In: *Nuclear Instruments and Methods* 133.2 (1976), pp. 303–309

6

Dual Energy CT Kidney Stone Differentiation in Photon Counting Computed Tomography

Ralf Gutjahr, MSc,[1,2] Christoph Polster, Dipl.-Phys.,[2,3] André Henning, PhD,[2] Steffen Kappler, PhD,[2] Shuai Leng, PhD,[4] Cynthia H. McCollough, PhD,[4] Martin U. Sedlmair, PhD,[2] Bernhard Schmidt, PhD,[2] Bernhard Krauss, PhD,[2] and Thomas G. Flohr, PhD[2]

[1]Computer Aided Medical Procedures (CAMP), Technical University of Munich, Munich, Germany
[2]Siemens Healthcare, Forchheim, Germany
[3]Institute of Clinical Radiology, Ludwig-Maximilians-University Hospital, Munich, Germany
[4]Department of Radiology, Mayo Clinic, Rochester, MN

Copyright statement

Contributions

The author of this thesis was responsible for the conceptualization of the study, the development of methodology, and prior investigations. He prepared and conducted the experiments while enhancing and utilizing software for spectral analysis. The author carried out formal and statistical analyses and oversaw data curation, including data collection, preparation, evaluation, and visualizations. Furthermore, he engaged in writing, reviewing, and editing the article.

The co-authors participated in the study's conceptualization and assisted with the development of the methodology. They also offered guidance on designing and conducting experiments and took part in the review process. Moreover, they provided necessary resources and supervised the project.

Abstract

This study evaluates the capabilities of a whole-body photon counting CT system to differentiate between four common kidney stone materials, namely uric acid (UA), calcium oxalate monohydrate (COM), cystine (CYS),and apatite (APA) *ex vivo*. Two different x-ray spectra (120 kV and 140 kV) were applied and two acquisition modes were investigated; The macro-mode generates two energy threshold based image-volumes and two energy bin based image-volumes. In the chesspattern-mode, however, four energy thresholds are applied. A virtual low energy image, as well as a virtual high energy image are derived from initial threshold-based images, while considering their statistically correlated nature. The energy bin based images of the macro-mode, as well as the virtual low and high energy image of the chesspattern-mode serve as input for our dual energy evaluation. The dual energy ratio of the individually segmented kidney stones were utilized to quantify the discriminability of the different materials. The dual energy ratios of the two acquisition modes showed high correlation for both applied spectra. Wilcoxon-rank sum tests and the evaluation of the area under the receiver operating characteristics curves suggest that the UA kidney stones are best differentiable from all other materials (AUC $= 1.0$), followed by CYS (AUC ≈ 0.9 compared against COM and APA). COM and APA, however, are hardly distinguishable (AUC between 0.63 and 0.76). The results hold true for the measurements of both spectra and both acquisition modes.

Keywords

CT; Dual-Energy CT; Multi-Energy CT; Spectral CT; Photon-Counting CT; Kidney Stone

6.1 Introduction

The therapeutic treatment of kidney stones strongly depends on their material composition. Several energy selective imaging techniques in Computed Tomography (CT) help to investigate the material characteristics and morphological information of kidney stones. Previous studies elaborate on utilizing kV-switching approaches,[149, 163] Dual Source CT,[61, 102, 254, 257, 329] or Dual Layer CT, [129] in order to characterize common types of kidney stones.

Motivated by recent reports assessing the dual energy capabilities of photon counting detector CT (PDC-CT) systems,[4, 115, 188, 324] this phantom study investigates the differentiability of four different pure kidney stone materials using image information obtained by a research PCD-CT system. The differentiation performance was evaluated comparing the dual energy ratios (DER) of the pure kidney stone materials with respect to two different acquisition modes (macro-mode and chesspattern-mode) and two applied x-ray spectra (120 kV and 140 kV).

6.2 Materials and methods

6.2.1 Scanner configuration

For this study a research whole-body PCD-CT scanner (Somatom CounT, Siemens Healthcare, Forchheim/Germany) was used.[157, 158, 159] The dual source system contains both an energy integrating detector and a PCD. This study focuses on acquisitions of the PCD. The CdTe-based PCD comprises 32 detector rows. Each row contains 480 pixels with an individual pitch of 1.125 mm. A pixel is subdivided into 4×4 so called sub-pixels. Each sub-pixel features two hardware based energy thresholds that allow the generation of signals based on photon energies that just exceed the thresholds as they are set by the user. By considering only photon energies that are found within an energy window (which is determined by two neighboring energy thresholds [322]), so called bin images are generated. The readout occurs either in the macro-mode (MM) or the chesspattern-mode (CM). In the MM every single sub-pixel is configured having the same two energy thresholds(T_L and T_H), resulting in the acquisition of two threshold based images and two energy bin based images (upper limit of highest bin is determined by the maximal energy exposed by the x-ray tube). The energy bin based images inherently provide almost independent photon statistics. In the CM four thresholds are applied (T_{L1}, T_{H1}, T_{L2}, and T_{H2}). However, in this mode only every second sub-pixel features the same low and high energy thresholds. The acquisitions in CM result in four threshold based images and four bin based images. Since the bin based images rely on photons that are measured in two neighboring sub-pixels, there is a non-intuitive statistical correlation among these images.[161]

6.2.2 Phantom preparation

In order to assess the quality of kidney stone material separation using the presented PCD-CT scanner, 40 kidney stones were investigated. The full set of kidney stones consists of four subsets, each consisting of 10 real kidney stones with pure chemical composition. The investigated materials were uric acid (UA, 71.5 – 273.9 mm^3), calcium oxalate monohydrate (COM, 21.4 – 204.2 mm^3), cystine (CYS, 64.3 – 287.1 mm^3), and apatite (APA, 18.0 – 202.73 mm^3). The purity of the materials was earlier determined by infrared spectroscopy. Each subset of stones was arranged in an array of small cups that were half way filled with gelatine. After the stones were separately located in the middle of the gelatines surfaces, the rest of the cups was filled with gelatine. The arrays were placed in a 20 cm wide cylindrical water phantom (positioned at the top of the table) in order to provide a reasonable attenuation of the x-ray spectrum. The arrays were aligned in x/y plane.

6.2.3 Image acquisition and reconstruction

Each array of kidney stones was measured using a tube voltage of 120 kV and 140 kV, both in MM and CM. For the MM acquisition the energy thresholds were set to 25 and 75 keV. For the acquisitions using the CM, however, energy thresholds of 25, 75, 25, 75 keV were applied in order to control the aforementioned correlations typical for CM. All acquisitions were made

following an abdominal sequence protocol with a rotation time of 1.0 s and an effective tube current time product of 102 mAs. The collimation was set to 32 × 0.5 mm. The images were reconstructed in a field of view (FOV) of 110 mm, using a weighted backprojection algorithm with a quantitative medium smooth kernel (D30) [344] resulting in comparatively lower noise levels and coarser structure. Since the diameter of the water container did not exceed the FOV of the system (275 mm), the reconstructions did not require further data completion and were free of truncation artifacts.[361]

6.2.4 Evaluation

In order to discriminate the kidney stone materials out of the acquired CT images, the DER for each kidney stone was calculated. The DER is derived by dividing the mean CT-values of a kidney stone in a CT-image acquired using a lower energy spectrum, and the same stone in a respective higher energy spectrum. In case of the MM acquisition these low and high energy images correspond to the two energy bin based images. Since the CM provides up to eight distinct images, we perform a statistical decorrelation that utilizes the four threshold-based images to generate two images that mime a virtual low energy image and a virtual high energy image, without shedding spectral information. In order to obtain the CT-value statistics of each stone and each image, the stones were segmented and measured individually. The measured DERs per stone material and spectrum were compared against the values of the other stones. Statistical tools used to assess the quality of distinction were a Wilcoxon rank-sum test to test for equal DER medians, and an analysis of the receiver operating characteristic (ROC) and its area under the curve (AUC). The AUC quantifies the differentiability of the measured stones as a case of binary classification. Whilst AUC values around 0.5 imply a random assignation of a class, a value closer to 1.0 indicates high accuracy of distinction.

6.3 Results

Figure 6.1 illustrates the correlation of the DER for the two applied spectra with respect to the two acquisition modes. The correlation is similar for the two spectra. The plot indicates four point accumulations that represent the DER for the particular kidney stone materials. The first accumulation around DER 1.0/1.0 (MM/CM) suggest the measured DER of the UA based stones, the second one around DER 1.1/1.1 represents the CYS material stones, and between DER 1.2/1.18 and 1.22/1.22 depict the COM and APA based kidney stones. This plot also allows to estimate how well the material can be differentiated using the applied spectra.

The boxplots in Figure 6.2 and 6.3 exemplarily show the results of the two acquisitions with a typical 120 kV spectrum and a 140 kV spectrum, respectively, both for MM and CM. The results of the two acquisition modes look similar in terms of their inter-quartile range and the magnitude of the whiskers. The outlying corresponding DER for the CYS measurements can also be seen in the correlation plot. The deviation of that stone appears in all acquisitions. The apparent overlap of the boxes comparing the COM and the APA measurements indicate the difficulty to differentiate the two materials. This observation is confirmed by the application of a pairwise Wilcoxon rank-sum test. For all stone types the DER distribution was found distinct, except for the case of comparing COM and APA, where the null hypothesis (i.e. no difference

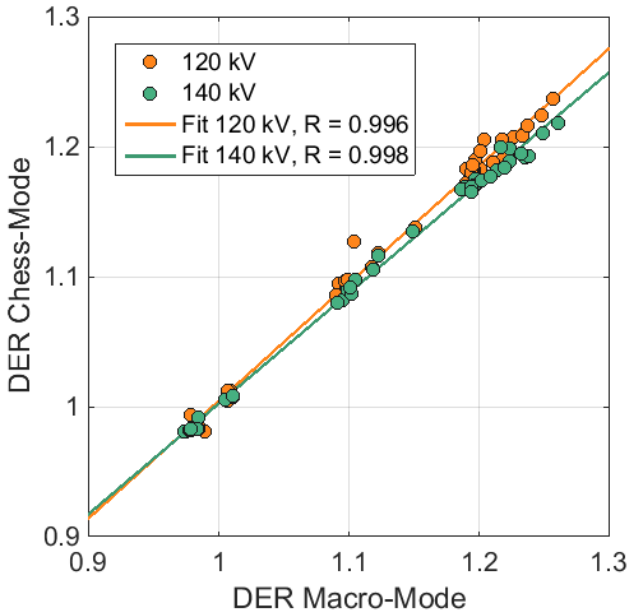

Fig. 6.1. Correlation of DER between Macro-Mode images, and Chess-Mode images

of medians) cannot be rejected (at a 5% significance level). A further validation provides the ROC curves and the AUCs. Figure 6.4 compares the differentiability of UA against CYS. The AUC equals 1.0, which indicates distinct differentiation. The resulting AUC is identical when comparing UA against COM and APA. Whereas CYS and APA (Figure 6.5), CYS and COM (Figure 6.6), and UA against all other materials can be differentiated rather well, this is not the case for COM and APA (AUC values between 0.66 and 0.76, Figure 6.7).

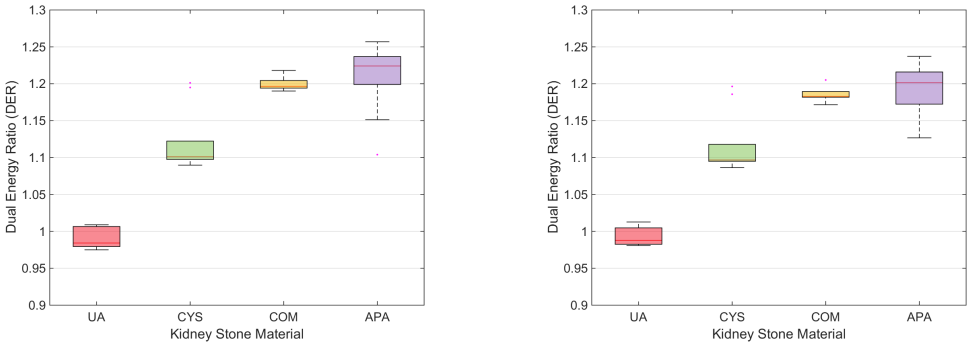

(a) 120 kV, Macro-Mode **(b)** 120 kV, Chesspattern-Mode

Fig. 6.2. Boxplots for mean DERs for all kidney stone materials.

It can also be observed that despite the correlated nature of the CM images, the DER of the derived virtual low energy and virtual high energy image correspond to the DER-values of the MM scans, where the respective spectrum was applied. Among all tested kidney stone materials, UA is the material that is best differentiability from the others (always provides an AUC $= 1.0$), followed by CYS (AUC ≈ 0.9). This is the case for all tested spectra and acquisition modes.

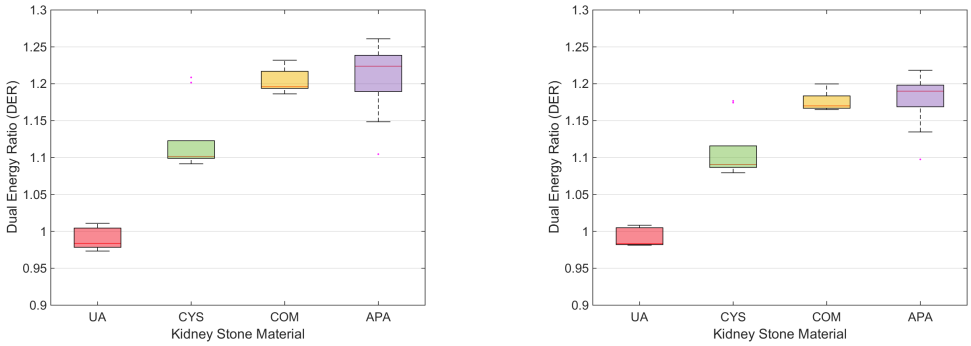

(a) 140 kV, Macro-Mode **(b)** 140 kV, Chesspattern-Mode

Fig. 6.3. Boxplots for mean DERs for all kidney stone materials.

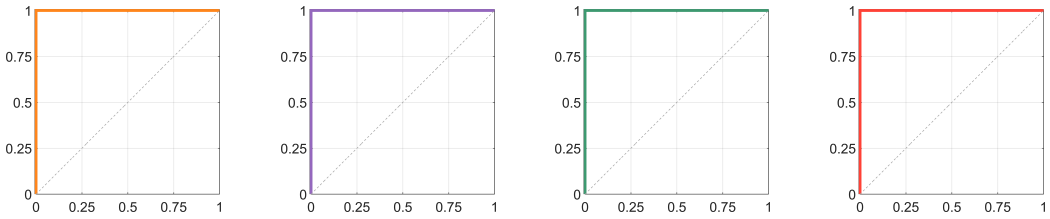

(a) 120 kV, Macro, AUC = 1.0 **(b)** 120 kV, Chess, AUC = 1.0 **(c)** 140 kV, Macro, AUC = 1.0 **(d)** 140 kV, Macro, AUC = 1.0

Fig. 6.4. ROC Curves for UA vs. CYS, sensitivity on the y-axis, 1-specificity on the x-axis.

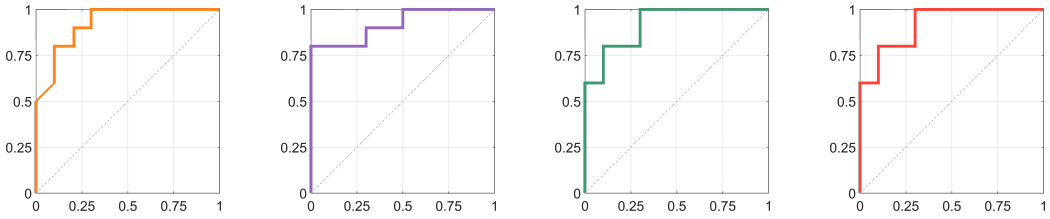

(a) 120 kV, Macro, AUC = 0.93 **(b)** 120 kV, Chess, AUC = 0.92 **(c)** 140 kV, Macro, AUC = 0.93 **(d)** 140 kV, Macro, AUC = 0.92

Fig. 6.5. ROC Curves for CYS vs. APA, sensitivity on the y-axis, 1-specificity on the x-axis.

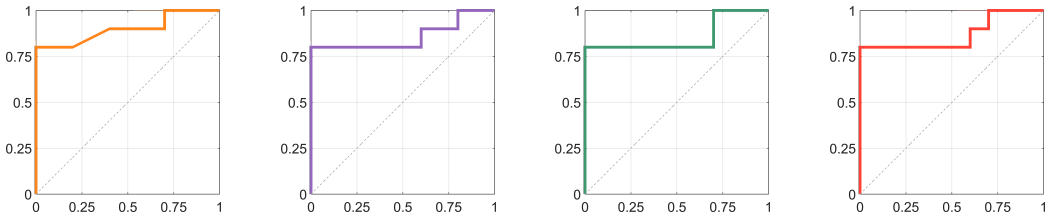

(a) 120 kV, Macro, AUC = 0.90 **(b)** 120 kV, Chess, AUC = 0.86 **(c)** 140 kV, Macro, AUC = 0.86 **(d)** 140 kV, Macro, AUC = 0.87

Fig. 6.6. ROC Curves for CYS vs. COM, sensitivity on the y-axis, 1-specificity on the x-axis.

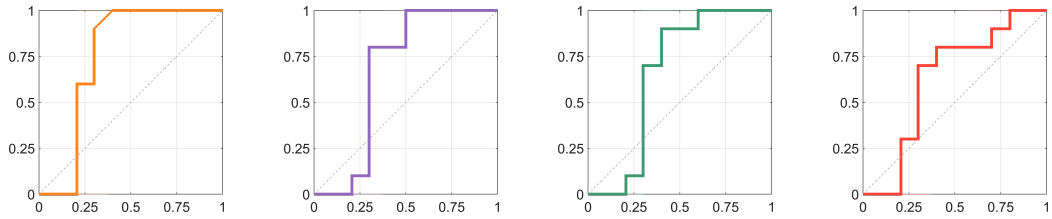

(a) 120 kV, Macro, AUC = 0.76

(b) 120 kV, Chess, AUC = 0.67

(c) 140 kV, Macro, AUC = 0.66

(d) 140 kV, Macro, AUC = 0.63

Fig. 6.7. ROC Curves for COM vs. APA, sensitivity on the y-axis, 1-specificity on the x-axis.

6.4 Discussion

We compared the ability to distinguish between four different kidney stone materials (UA, CYS, COM, APA) based on their DER. All CT images were obtained by a research PCD-CT scanner. The scan parameters included two different scan modes (MM and CM) and two different x-ray spectra (120 kV and 140 kV). Threshold-based images from the CM were processed to generate a virtual low energy image and a virtual high energy image. MM and the decorrelated CM showed similar performances for both tested spectra.

6.5 Conclusion

The material characteristic DER is crucial for differentiation of materials in Dual Energy processing. Four different pure kidney stone materials were compared in two different acquisition modes and two different spectra. For the MM acquisition, the bin based images serve as input for the Dual Energy evaluation. In case of the CM, the resulting threshold images were processed to generate statistically decorrelated virtual low and virtual high energy images. This study demonstrates similar material separation capabilities for all introduced acquisitions. Whereas UA was the most distinguishable material, the differentiation of CYS based kidney stones also showed good results. However, in this study COM based kidney stones couldn't be reliably distinguished from the APA based kidney stones.

6.6 References

[4] A. M. Alessio and L. R. MacDonald. "Quantitative material characterization from multi-energy photon counting CT". in: *Medical Physics* 40.3 (2013), p. 031108

[61] X. Duan, Z. Li, L. Yu, S. Leng, A. F. Halaweish, J. G. Fletcher, and C. H. McCollough. "Characterization of urinary stone composition by use of third-generation dual-source dual-energy CT with increased spectral separation". In: *American Journal of Roentgenology* 205.6 (2015), p. 1203

[102] A. Graser, T. R. Johnson, M. Bader, M. Staehler, N. Haseke, K. Nikolaou, M. F. Reiser, C. G. Stief, and C. R. Becker. “Dual energy CT characterization of urinary calculi: initial in vitro and clinical experience”. In: *Investigative Radiology* 43.2 (2008), pp. 112–119

[115] R. Gutjahr, C. Polster, S. Kappler, H. Pietsch, G. Jost, K. Hahn, F. Schoeck, M. Sedlmair, T. Allmendinger, B. Schmidt, B. Krauss, and T. Flohr. “Material Decomposition and virtual non-contrast imaging in photon counting computed tomography: an animal study”. In: SPIE Medical Imaging (Orlando, Florida, USA, Mar. 2–6, 2016). 2016

[129] G. Hidas, R. Eliahou, M. Duvdevani, P. Coulon, L. Lemaitre, O. N. Gofrit, D. Pode, and J. Sosna. “Determination of Renal Stone Composition with Dual-Energy CT: In Vivo Analysis and Comparison with X-ray Diffraction 1”. In: *Radiology* 257.2 (2010), pp. 394–401

[149] M Joshi, D. Langan, D. Sahani, A Kambadakone, S Aluri, K Procknow, X Wu, R Bhotika, D Okerlund, N Kulkarni, et al. “Effective atomic number accuracy for kidney stone characterization using spectral CT”. in: *International Society for Optics and Photonics Medical Imaging*. International Society for Optics and Photonics. 2010, 76223K–76223K

[157] S Kappler, F Glasser, S Janssen, E Kraft, and M Reinwand. “A research prototype system for quantum-counting clinical CT”. in: *International Society for Optics and Photonics Medical Imaging*. International Society for Optics and Photonics. 2010, 76221Z–76221Z

[158] S Kappler, T Hannemann, E Kraft, B Kreisler, D Niederloehner, K Stierstorfer, and T Flohr. “First results from a hybrid prototype CT scanner for exploring benefits of quantum-counting in clinical CT”. in: *International Society for Optics and Photonics Medical Imaging*. International Society for Optics and Photonics. 2012, pp. 83130X–83130X

[159] S Kappler, A Henning, B Krauss, F Schoeck, K Stierstorfer, T Weidinger, and T Flohr. “Multi-energy performance of a research prototype CT scanner with small-pixel counting detector”. In: *International Society for Optics and Photonics Medical Imaging*. International Society for Optics and Photonics. 2013, 86680O–86680O

[161] S Kappler, A Henning, F Schoeck, K Stierstorfer, T Weidinger, and T Flohr. “A Hybrid Research Prototype CT Scanner with Photon Counting Detector”. In: *IEEE Transactions on Medical Imaging: Special Issue On Spectral CT*. IEEE. 2014

[163] R. K. Kaza, J. F. Platt, R. H. Cohan, E. M. Caoili, M. M. Al-Hawary, and A. Wasnik. “Dual-energy CT with single-and dual-source scanners: current applications in evaluating the genitourinary tract”. In: *Radiographics* 32.2 (2012), pp. 353–369

[188] Z. Li, S. Leng, L. Yu, Z. Yu, and C. H. McCollough. “Image-based material decomposition with a general volume constraint for photon-counting CT”. in: *International Society for Optics and Photonics Medical Imaging*. International Society for Optics and Photonics. 2015, 94120T–94120T

[254] A. N. Primak, J. G. Fletcher, T. J. Vrtiska, O. P. Dzyubak, J. C. Lieske, M. E. Jackson, J. C. Williams Jr, and C. H. McCollough. “Noninvasive differentiation of uric acid versus non–uric acid kidney stones using dual-energy CT”. in: *Academic Radiology* 14.12 (2007), pp. 1441–1447

[257] M. Qu, G. Jaramillo-Alvarez, J. C. Ramirez-Giraldo, Y. Liu, X. Duan, J. Wang, T. J. Vrtiska, A. E. Krambeck, J. Lieske, and C. H. McCollough. “Urinary stone differentiation in patients with large body size using dual-energy dual-source computed tomography”. In: *European Radiology* 23.5 (2013), pp. 1408–1414

[344] “Weighted FBP—a Simple Approximate 3D FBP Algorithm for Multislice Spiral CT With Good Dose Usage for Arbitrary Pitch”. In: *Physics in Medicine and Biology* 49.11 (2004), p. 2209

[322] K. Taguchi and J. S. Iwanczyk. “Vision 20/20: Single photon counting x-ray detectors in medical imaging”. In: *Medical Physics* 40.10 (2013), p. 100901

[324] K. Taguchi, M. Zhang, E. C. Frey, J. Xu, W. P. Segars, and B. M. Tsui. “Image-domain material decomposition using photon-counting CT”. in: *Medical Imaging*. International Society for Optics and Photonics. 2007, pp. 651008–651008

[329] C. Thomas, B. Krauss, D. Ketelsen, I. Tsiflikas, A. Reimann, M. Werner, D. Schilling, J. Hennenlotter, C. D. Claussen, H.-P. Schlemmer, et al. “Differentiation of urinary calculi with dual energy CT: effect of spectral shaping by high energy tin filtration”. In: *Investigative Radiology* 45.7 (2010), pp. 393–398

[361] Z. Yu, S. Leng, S. Kappler, K. Hahn, Z. Li, A. F. Halaweish, A. Henning, E. L. Ritman, and C. H. McCollough. “Low-dose performance of a whole-body research photon-counting CT scanner”. In: *International Society for Optics and Photonics Medical Imaging*. International Society for Optics and Photonics. 2016, 97835Q–97835Q

7

Characterization of Urinary Stone Composition by Use of Whole-body, Photon-counting Detector CT

Andrea Ferrero, PhD,[1] Ralf Gutjahr, MSc,[2,3] Ahmed F. Halaweish, PhD,[3]
Shuai Leng, PhD,[1] and Cynthia H. McCollough, PhD[1]

[1]Department of Radiology, Mayo Clinic, Rochester, MN
[2]Computer Aided Medical Procedures (CAMP), Technical University of Munich, Munich, Germany
[3]Siemens Healthcare–Imaging and Therapy Systems, Malvern, PA

Copyright statement

Contributions

Both authors (A.F. and R.G.) contributed equally in the following parts: They jointly conceptualized the study, developed the methodology, which involved designing, preparing and conducting the necessary experiments. Ideal energy thresholds per kV setting were determined. A.F. and R.G. were also responsible for using and modifying the software for spectral analysis. The formal analysis, including the statistical analysis, was carried out by both authors.

The additional co-authors contributed to the research by refining the conceptual framework and methodology, while providing the resources required to conduct this study, including equipment, software, and facilities. They reviewed and edited the article.

Abstract

Rational and Objectives: This study aims to investigate the performance of a whole-body, photon counting detector (PCD) computed tomography (CT) system in differentiating urinary stone composition.

Materials and Methods: Eighty-seven human urinary stones with pure mineral composition were placed in four anthropomorphic water phantoms (35–50 cm lateral dimension) and scanned on a PCD-CT system at 100, 120, and 140 kV. For each phantom size, tube current was selected to match $CTDI_{vol}$ (volume CT dose index) to our clinical practice. Energy thresholds at [25, 65], [25, 70], and [25, 75] keV for 100, 120, and 140 kV, respectively, were used to generate dual-energy images. Each stone was automatically segmented using in-house software; CT number ratios were calculated and used to differentiate stone types in a receiver operating characteristic (ROC) analysis. A comparison with second- and third-generation dual-source, dual-energy CT scanners with conventional energy integrating detectors (EIDs) was performed under matching conditions.

Results: For all investigated settings and smaller phantoms, perfect separation between uric acid and non–uric acid stones was achieved (area under the ROC curve [AUC] = 1). For smaller phantoms, performance in differentiation of calcium oxalate and apatite stones was also similar between the three scanners: for the 35-cm phantom size, AUC values of 0.76, 0.79, and 0.80 were recorded for the second and third-generation EID-CT and for the PCD-CT, respectively. For larger phantoms, PCD-CT and the third-generation EID-CT outperformed the second-generation EID-CT for both differentiation tasks: for a 50-cm phantom size and a uric acid/non–uric acid differentiating task, AUC values of 0.63, 0.95, and 0.99 were recorded for the second- and third-generation EID-CT and for the PCD-CT, respectively.

Conclusion: PCD-CT provides comparable performance to state-of-the-art EID-CT in differentiating urinary stone composition.

Keywords

CT; photon-counting detector CT; spectral separation; urinary stones

7.1 Introduction

Conventional x-ray computed tomography (CT) systems rely on energy integrating detectors (EIDs), which generate an output signal that is proportional to the amount of energy deposited by the detected x-ray. Therefore, EID-CT systems inherently penalize the contribution of low-energy x-ray photons, which are the photons that carry the most contrast information for biological tissues and contrast media.

In recent years, a number of pre-clinical photon-counting detector (PCD) CT systems were introduced [7, 297, 322]. Unlike EID-CT, PCD-CT systems directly convert each detected x-ray photon into individual pulses with amplitudes proportional to the energy of the incoming photon. Each individual pulse is counted separately through the use of fast electronics. The equal contribution of each detected photon regardless of their energy [95, 287], combined with a reduced influence of electronic noise, results in improved contrast-to-noise ratio for PCD-CT when compared to EID-CT techniques [111]. Additionally, PCD-CT can provide acquisitions with full field-of- view (FOV), fully registered data, stability against motion artifacts, no cross scatter from a second x-ray tube, and the ability to configure more than two energy thresholds. Finally, all measurements provide multi-energy information, enabling the application of dual-energy or multi-energy post-processing algorithms for every scan. The system utilized in this study is a whole-body PCD-CT research system (SOMATOM CounT; Siemens Healthcare, Forchheim, Germany) [157, 159, 359]. Preliminary in vivo animal and human studies demonstrated its ability to provide CT images of diagnostic quality for several applications, including unenhanced and iodine-enhanced abdominal imaging [193, 253]. Renal stone characterization has been one of the most established clinical applications of dual-energy CT to date. Current state-of-the-art dual-energy CT systems can non-invasively separate uric acid (UA) from non–uric acid (NUA) stones, with near 100% accuracy at the same radiation dose as routine, single-energy renal stone CT examinations, providing valuable information to the ordering physician to guide treatment options [337]. Therefore, in this work, we characterized ex-vivo the performance of a PCD-CT system in differentiating the mineral composition of urinary stones and compared it to two commercial dual-energy EID-CT systems. As one of the potential advantages of PCD-CT is the ability to add spectral information to any CT examination and since low-tube potential imaging is a popular and effective method to reduce radiation dose, especially in contrast-enhanced abdominal CT scans, we extended the characterization to lower tube potential.

7.2 Materials and Methods

Institutional Review Board protocol approval was not required for this non-patient study. However, biospecimen approval was obtained from the institutional biospecimen committee.

7.2.1 Stone samples

A set of 87 urinary stones was investigated, including UA ($n = 17$), cystine ($n = 5$), calcium oxalate ($n = 30$), brushite ($n = 5$), and apatite ($n = 30$). Reference composition was given by micro-CT and infrared spectroscopy [365]. Only stones with purity higher than 90% were included in the cohort, with one stone sample selected from each individual patient. The stones were hydrated for 24 hours before being embedded in gelatin in two 60-well ice cube trays and placed in four torso-shaped water tanks with lateral dimensions of 35, 40, 45, and 50 cm, which were used to represent small, average, large, and obese adults, respectively. Figure 7.1 shows the experimental setup.

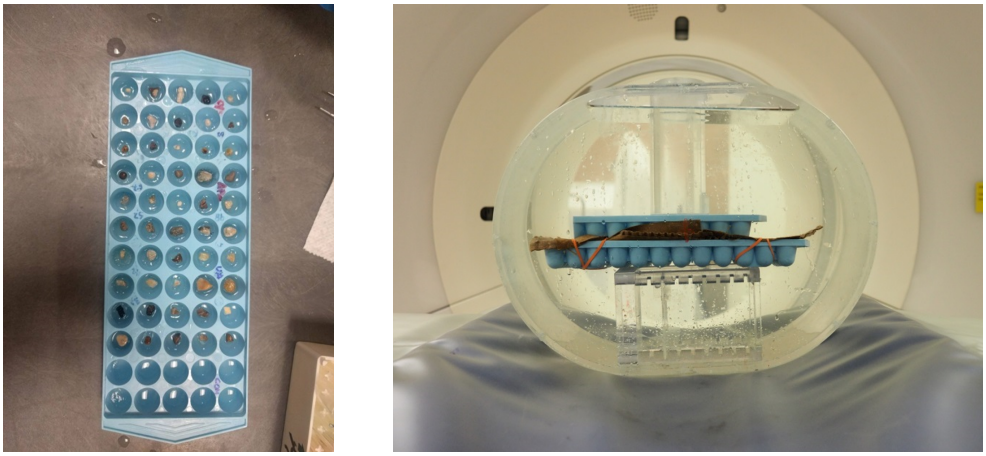

Fig. 7.1. Experimental setup.

7.2.2 PCD-CT Data acquisition and reconstruction

All phantoms were scanned on a whole-body, PCD-CT research system. Three different tube potentials were investigated: 100, 120, and 140 kVp. For each tube potential, the threshold that resulted in the most uniform distributions of the detected x-rays between the low and high bin was selected. Figure 7.2 shows the detected energy spectra for the three settings used.

As the scanned objects exceeded the 275-mm FOV of the PCD subsystem, a data-completion scan from the EID subsystem (500-mm FOV) was used to obtain artifact-free images. This additional scan has been shown to be successfully performed using very low radiation doses [362]. For each phantom size, the tube output was selected to match the volume CT dose index ($CTDI_{vol}$) to our clinical practice. Table 7.1 summarizes the PCD-CT acquisition parameters used for all scans.

Tab. 7.1. Acquisition parameters for photon-counting detector computed tomography scans.

	Tube Potential (kVp)		
	100	**120**	**140**
Phantom sizes scanned (cm)	35, 40	35, 40, 45	35, 40, 45, 50
Energy thresholds (keV)	25, 65	25, 70	25, 75
Detector collimation (mm)		32×0.5	
Rotation time (s)		0.5	
Helical pitch		0.6	

Dual-energy PCD-CT data were obtained whereby the low-energy image included x-rays with energies between the two detector thresholds (eg, 25–65 keV), and the high-energy image included x-rays with energies above the higher detector energy threshold (eg, 65–100 keV). All images were reconstructed using the protocol parameters adopted in our clinical practice for renal stone composition: weighted filtered-backprojection reconstruction, 275-mm

FOV, 1.0-mm thick slices with 0.8-mm slice interval, and a medium-sharp soft-tissue D30f reconstruction kernel.

7.2.3 Image processing and classification analysis

Kidney stones were automatically segmented using previously validated in-house software [63]. Metrics describing morphological, volumetric, and dual-energy features were automatically extracted. Specifically, the CT number ratio (CTR) for each stone was quantitatively assessed as the ratio of the mean CT number within the stone in the low-energy image to that in the high-energy image for each stone.

Receiver operating characteristic (ROC) curves were generated for each combination of phantom size and tube potential by varying values of the CTR threshold used to separate the stone types. Binary classifications between UA and NUA stones were investigated, as well as between calcium oxalate and apatite stones. The area under the ROC curve (AUC) was used as the figure of merit to quantify the performance of the PCDCT system to classify urinary stones based on their mineral composition.

7.2.4 Comparison with state-of-the-art dual-source, dual-energy CT

A comparison of second (SOMATOM Flash, Siemens Healthcare) and third (SOMATOM Force, Siemens Healthcare) generation dual-source, dual-energy CT systems for the task of urinary stone composition was previously reported [61]. In that work, the same stone cohort and experimental setup as in the present study were used. Tube output and reconstruction parameters were also matched. Therefore, a thorough comparison between the three CT systems was possible. Hereafter, we refer to the three scanners as EID-CT1 (SOMATOM Flash), EID-CT2 (SOMATOM Force), and PCD-CT (SOMATOM Count). Figures of merit included the AUC and the absolute difference between mean CTR for the binary classifications that were investigated.

7.3 Results

7.3.1 Dose and image quality for PCD-CT system

As described in the Materials and Methods section, the $CTDI_{vol}$ was the same across all scanners for each phantom size (Table 7.2). No visible artifacts related to beam hardening or photon starvation were appreciated, even for the larger phantoms.

Tab. 7.2. $CTDI_{vol}$ for each of the phantom sizes investigated.

LAT phantom size (cm)	$CTDI_{vol}$ (mGy)
35	13.5
40	19.9
45	33.4
50	45.0

CT, computed tomography; $CTDI_{vol}$, volume CT dose index.

$CTDI_{vol}$ was matched among all three CT systems investigated.

7.3.2 Differentation of kidney stones

In Figure 7.3, the distribution of CTR values for UA and NUA stones across different CT systems and tube potentials is shown for the 35-cm phantom data. ΔCTR - defined as the difference between the mean CTR for UA and NUA stones - varies significantly for the different scanners and tube potential pairs investigated, with the EID-CT2 outperforming the other two scanners at all energy pairs and phantom sizes (Figure 7.3, Table 7.3). However, it is important to notice that the UA and NUA distributions were perfectly separated in all configurations, as shown in Figure 7.4, top-left panel. Data for the EID-CT1 and EID-CT2 dual-energy CT systems were previously reported in Duan et al. [61]. All scanners showed a degradation in separation between UA and NUA (ie, decreased ΔCTR) as phantom size increased. However, the degradation was significantly less pronounced for the PCD-CT, resulting in a better performance compared to the EID-CT1 for larger phantoms (Figure 7.4).

Tab. 7.3. Absolute difference (ΔCTR) between mean CT for uric acid ($n = 17$) vs non–uric acid ($n = 70$) stones.

		Phantom Size (cm)			
CT System	**Tube Potential (kV)**	**35**	**40**	**45**	**50**
EID-CT1	80/Sn140	0.69	0.62	*	*
	100/Sn140	0.42	0.30	0.23	0.05
EID-CT2	70/Sn150	1.03	*	*	*
	80/Sn150	0.83	0.78	*	*
	90/Sn150	0.70	0.64	0.62	*
	100/Sn150	0.58	0.50	0.52	0.43
PCD-CT	100	0.30	0.30	*	*
	120	0.39	0.35	*	*
	140	0.44	0.41	0.37	0.35

* As phantom size increased, not all tube potential pairs could be used.

For smaller phantoms, AUC performance in differentiation of calcium oxalate and apatite stones was similar between the three scanners (Figure 7.5), despite the larger ΔCTR recorded by EID-CT2 for all phantom sizes compared to the other two systems (Table 7.4). For the

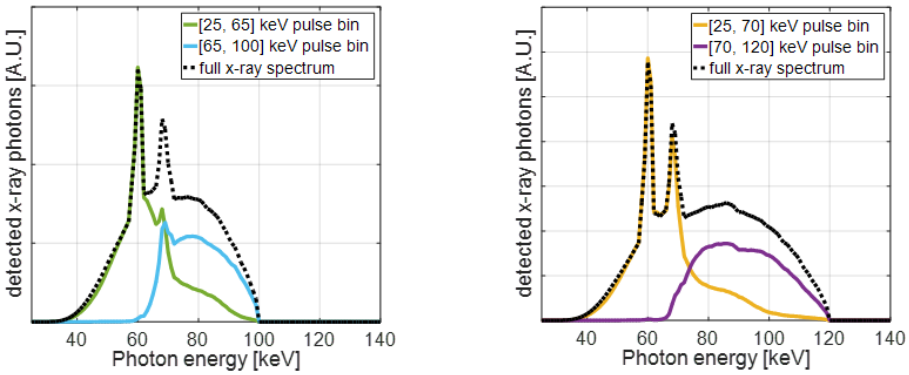

(a) 100 kV, [25, 65] keV

(b) 120 kV, [25, 70] keV

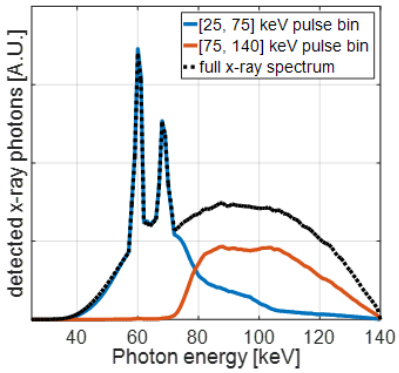

(c) 140 kV, [25, 75] keV

Fig. 7.2. Detected x-ray energy spectra for the different settings investigated. Spectra are simulated for a 35-cm reference phantom and include charge-sharing effects (see Discussion), which result in a finite chance for incoming x-rays of a certain energy to be misclassified and stored in the wrong (lower) energy bin.

35-cm phantom size, AUC values of 0.76, 0.79, and 0.80 were recorded for EIDCT1, EID-CT2, and PCD-CT, respectively. For larger phantoms, PCD-CT and EID-CT2 outperformed EIDCT1 (Figure 7.5). For the 35-cm phantom size, AUC values of 0.65, 0.78, and 0.76 were recorded for EID-CT1, EIDCT2, and PCD-CT, respectively.

7.4 Discussion

In this ex-vivo work, the performance of a whole-body, PCD-CT research system for the characterization of urinary stone composition was investigated. A wide range of patient sizes was mimicked through the use of anthropomorphic water tanks of different size, and used with different tube potential settings available on the CT system. A full comparison with existing dual-energy CT technology was also performed.

Compared to state-of-the-art dual-energy CT systems, reduced CTR differences between UA and NUA stones were measured. In principle, PCD-CT technology offers the possibility to separate the x-ray energy spectrum into two or more energy bins with no overlap.

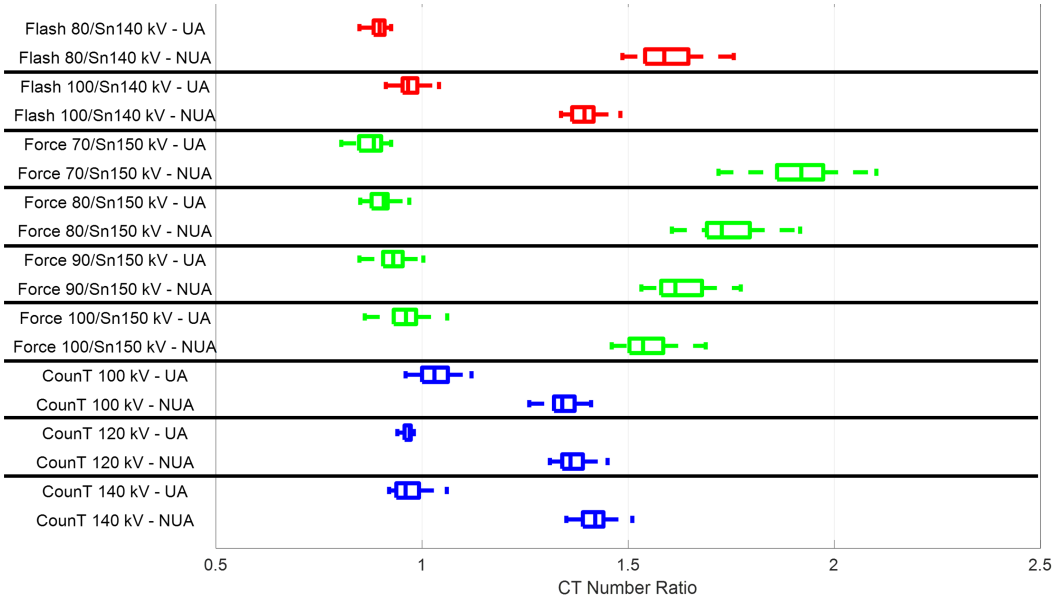

Fig. 7.3. Distribution of CT number ratio values for uric acid (UA) and non–uric acid (NUA) stones for all acquisitions settings tested in the 35-cm water phantom.

However, a number of technology-inherent physical effects reduce the separation of distinct energy bins in PCD-CD, leading to spectral overlap and statistical correlations in the acquired CT images that could potentially negatively impact dual-energy CT applications. The most prominent effect is charge sharing, where several adjacent pixels may "fire-up" in response to x-ray deposited in a single pixel, causing a loss of both spectral and spatial information. For high photon fluxes, which are typical of clinical CT acquisitions, pulse pileup emerged as a substantial limitation for previous PCD-CT systems [297]. In this scenario, two or more low-energy x-ray photons detected within a short time interval create a single, high-energy pulse owing to the finite timing response of the detector in converting x-ray energy into electric pulses. These misclassifications, in turn, result in a certain degree of overlap between the two energy spectra used to generate the low and high-energy images, as shown in the simulations presented in Figure 7.2, which modeled charge sharing (but not pileup).

Despite the reduced spectral separation, the investigated PCD-CT system was able to perfectly differentiate UA from NUA stones across all kilovolt (kV) settings and phantom sizes. Furthermore, PCD-CT was able to differentiate the two most common NUA stone types, calcium oxalate and apatite stones, with good accuracy (AUC = 0.8 at all three investigated kV for the 35-cm phantom). Unlike the second-generation DECT system, the performance of the PCD-CT system was maintained for large patient sizes.

Different kV settings were investigated in this study for the PCD-CT, ranging from 100 to 140 kV. In PCD-CT, a single scan is performed and the recorded data are binned in two energy bins to mimic a low-kV and a high-kV dual-energy acquisition. Therefore, for the PCD-CT scan, a kV below 100 kV would not provide adequate spectral separation between the two energy bins. For reference, clinical EID-CT scanners across manufacturers use a minimum of 120 kV for their high-kV scan.

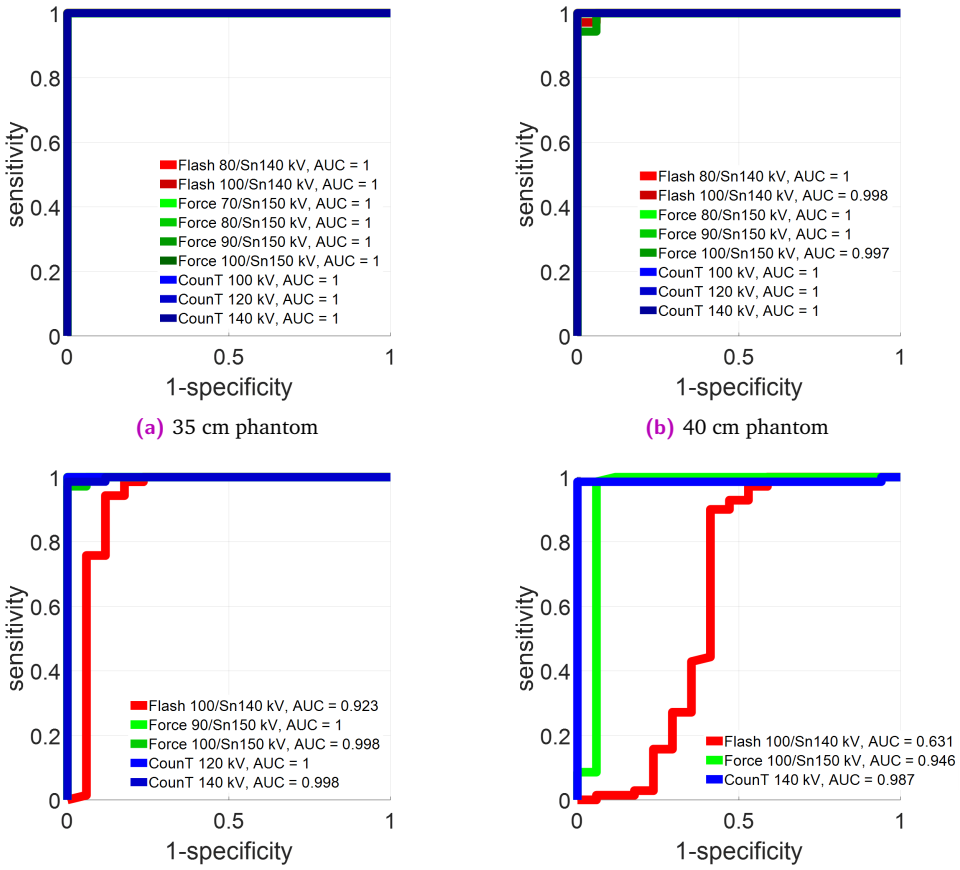

(a) 35 cm phantom **(b)** 40 cm phantom

(c) 45 cm phantom **(d)** 50 cm phantom

Fig. 7.4. Receiver operating characteristic (ROC) analysis to differentiate uric acid from non–uric acid stones for different computed tomography systems and phantom sizes. As phantom size increased, not all tube potential pairs could be used. AUC, area under the ROC curve.

This study has limitations. Only pure stones were included in this study. Although quite common, in our experience, pure (ie, more than 90% of a single mineral) stones account for only approximately 50% of all stones encountered in a clinical setting. Finally, the data reported by Duan et al. defined the CTR for each stone as the average of the CTR computed for each pixel. In this work, however, we computed it as the ratio of the mean low- and high-CT numbers for each stone, as we believe this approach is less affected by noise in the acquired images. This difference could potentially explain the slightly higher variability in CTR for each subset of stones that was observed in the data from Duan et al. compared to our measurements on the PCD-CT.

In conclusion, these ex vivo results add to the developing body of literature showing how PCD-CT is a viable clinical alternative to conventional, EID-based CT for genitourinary applications, showing non-inferiority in several clinical trials [193, 194, 253]. The unique characteristics of PCD technology, including but not limited to the improved sensitivity to low-energy x-ray photons and reduced detector noise, may result in an increased use of routine, multi-energy renal stone characterization CT protocols for the imaging of patients with suspected or established nephrolithiasis, including those with larger body habitus.

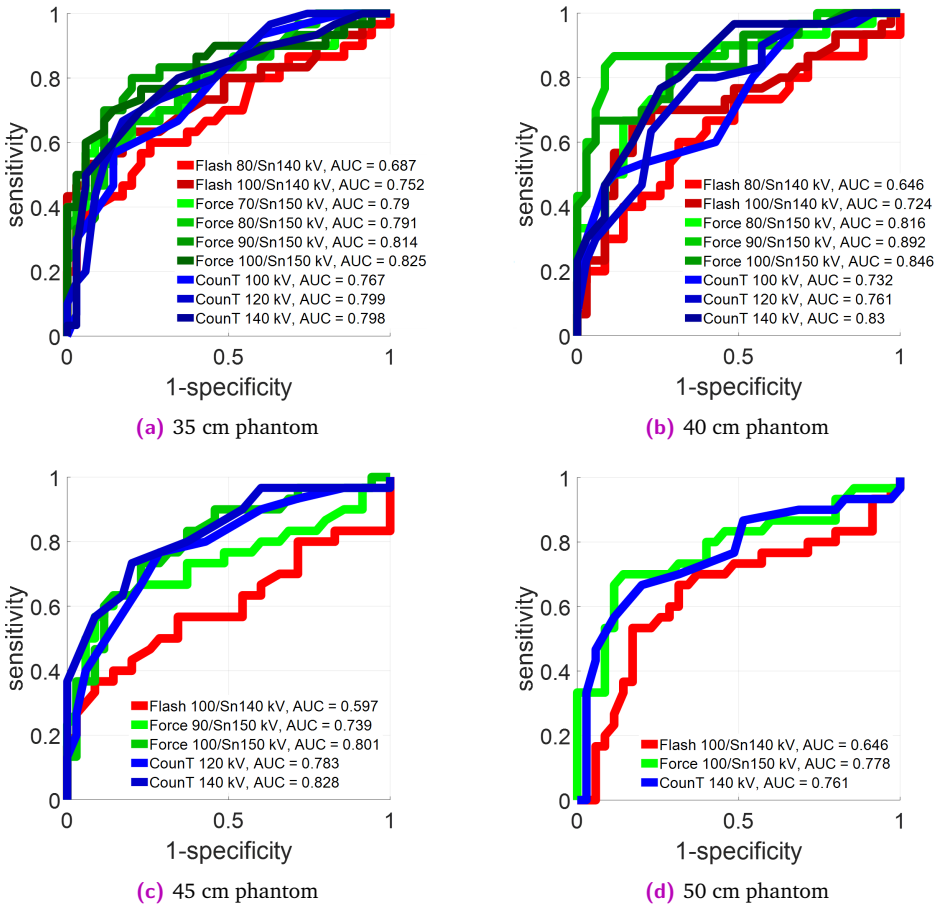

(a) 35 cm phantom **(b)** 40 cm phantom

(c) 45 cm phantom **(d)** 50 cm phantom

Fig. 7.5. Receiver operating characteristic (ROC) analysis to differentiate non–uric acid subtypes calcium oxalate and hydroxyapatite for different computed tomography systems and phantom sizes. As phantom size increased, not all tube potential pairs could be used. AUC, area under the ROC curve.

7.5 References

[7] A. Altman and R. Carmi. "TU-E-210A-03: a double-layer detector, dual-energy CT—principles, advantages and applications". In: *Medical Physics* 36.6 Part 24 (2009), pp. 2750–2750

[61] X. Duan, Z. Li, L. Yu, S. Leng, A. F. Halaweish, J. G. Fletcher, and C. H. McCollough. "Characterization of urinary stone composition by use of third-generation dual-source dual-energy CT with increased spectral separation". In: *American Journal of Roentgenology* 205.6 (2015), p. 1203

[63] X. Duan, J. Wang, M. Qu, S. Leng, Y. Liu, A. Krambeck, and C. H. McCollough. "Kidney stone volume estimation from computerized tomography images using a model based method of correcting for the point spread function". In: *The Journal of Urology* 188.3 (2012), pp. 989–995

[359] Z. Yu, S. Leng, S. M. Jorgensen, Z. Li, R. Gutjahr, B. Chen, A. F. Halaweish, S. Kappler, L. Yu, E. L. Ritman, and C. H. McCollough. “Evaluation of conventional imaging performance in a research whole-body CT system with a photon-counting detector array”. In: *Physics in Medicine and Biology* 61.4 (2016), p. 1572

[95] J. Giersch, D. Niederlöhner, and G. Anton. “The influence of energy weighting on X-ray imaging quality”. In: *Nuclear Instruments and Methods in Physics Research Section A: Accelerators, Spectrometers, Detectors and Associated Equipment* 531.1 (2004), pp. 68–74

[111] R. Gutjahr, A. F. Halaweish, Z. Yu, S. Leng, L. Yu, Z. Li, S. M. Jorgensen, E. L. Ritman, S. Kappler, and C. H. McCollough. “Human Imaging With Photon Counting–Based Computed Tomography at Clinical Dose Levels: Contrast-to-Noise Ratio and Cadaver Studies”. In: *Investigative Radiology* 51.7 (2016), pp. 421–429

[157] S Kappler, F Glasser, S Janssen, E Kraft, and M Reinwand. “A research prototype system for quantum-counting clinical CT”. in: *International Society for Optics and Photonics Medical Imaging*. International Society for Optics and Photonics. 2010, 76221Z–76221Z

[159] S Kappler, A Henning, B Krauss, F Schoeck, K Stierstorfer, T Weidinger, and T Flohr. “Multi-energy performance of a research prototype CT scanner with small-pixel counting detector”. In: *International Society for Optics and Photonics Medical Imaging*. International Society for Optics and Photonics. 2013, 86680O–86680O

[193] R. Marcus, J. G. Fletcher, S. P. Sheedy, J. L. Fidler, Z. Li, Z. Yu, F. Enders, A. Halaweish, and C. H. McCollough. “Photon-counting-detector CT for the evaluation of non-contrast enhanced abdominal imaging in patients”. In: Radiological Society of North America. 102nd Scientific Assembly and Annual Meeting (Chicago IL, USA, Nov. 27–Dec. 2, 2016). 2016

[194] R. Marcus, J. G. Fletcher, T. J. Vrtiska, M. L. Wells, A. Ferrero, J. Montoya, A. Huang, A. Halaweish, F. Enders, S. Leng, and C. H. McCollough. “Detection and characterization of urinary stones using photon-counting-detector CT in a clinical setting”. In: Radiological Society of North America. 102nd Scientific Assembly and Annual Meeting (Chicago IL, USA, Nov. 27–Dec. 2, 2016). 2016

[253] A. Pourmorteza, R. Symons, V. Sandfort, M. Mallek, M. K. Fuld, G. Henderson, E. C. Jones, A. A. Malayeri, L. R. Folio, and D. A. Bluemke. “Abdominal imaging with contrast-enhanced photon-counting CT: first human experience”. In: *Radiology* 279.1 (2016), pp. 239–245

[287] T. G. Schmidt. “Optimal “image-based” weighting for energy-resolved CT”. in: *Medical Physics* 36.7 (2009), pp. 3018–3027

[297] P. M. Shikhaliev. “Computed tomography with energy-resolved detection: a feasibility study”. In: *Physics in Medicine & Biology* 53.5 (2008), p. 1475

[322] K. Taguchi and J. S. Iwanczyk. “Vision 20/20: Single photon counting x-ray detectors in medical imaging”. In: *Medical Physics* 40.10 (2013), p. 100901

[337] T. J. Vrtiska, N. Takahashi, J. G. Fletcher, R. P. Hartman, L. Yu, and A. Kawashima. “Genitourinary applications of dual-energy CT”. in: *AJR. American journal of roentgenology* 194.6 (2010), p. 1434

[362] Z. Yu, S. Leng, Z. Li, A. F. Halaweish, S. Kappler, E. L. Ritman, and C. H. McCollough. “How Low Can We Go in Radiation Dose for the Data-Completion Scan on a Research Whole-Body Photon-Counting Computed Tomography System.” In: *Journal of Computer Assisted Tomography* (2016)

[365] C. A. Zarse, J. A. McAteer, A. J. Sommer, S. C. Kim, E. K. Hatt, J. E. Lingeman, A. P. Evan, and J. C. Williams. “Nondestructive analysis of urinary calculi using micro computed tomography”. In: *BMC Urology* 4.1 (2004), p. 1

Tab. 7.4. Absolute difference (ΔCTR) between mean CTR for calcium oxalate ($n = 35$) vs apatite ($n = 30$) stones.

		Phantom Size (cm)			
CT System	**Tube Potential (kV)**	**35**	**40**	**45**	**50**
EID-CT1	80/Sn140	0.05	0.03	*	*
	100/Sn140	0.04	0.04	0.01	0.01
EID-CT2	70/Sn150	0.11	*	*	*
	80/Sn150	0.08	0.10	*	*
	90/Sn150	0.08	0.09	0.07	*
	100/Sn150	0.04	0.08	0.08	0.08
PCD-CT	100	0.02	0.03	*	*
	120	0.04	0.03	0.04	*
	140	0.03	0.05	0.05	0.03

* As phantom size increased, not all tube potential pairs could be used.

8

Renal stone characterization using high resolution imaging mode on a photon counting detector CT system

Andrea Ferrero, PhD,[1] Ralf Gutjahr, MSc,[2,3] André Henning, PhD,[3] Steffen Kappler, PhD,[3] Ahmed F. Halaweish, PhD,[4] Dilbar Abdurakhimova, PhD,[1] Zachary Peterson, BSc,[1] Juan Montoya, BSc,[1] Shuai Leng, PhD,[1] and Cynthia H. McCollough, PhD[1]

[1]Department of Radiology, Mayo Clinic, Rochester, MN
[2]Computer Aided Medical Procedures (CAMP), Technical University of Munich, Munich, Germany
[3]Siemens Healthcare GmbH, Forchheim, Germany
[4]Siemens Healthcare–Imaging and Therapy Systems, Malvern, PA

Copyright statement

Contributions

The thesis author introduced the idea of using of high-resolution acquisition modes for kidney stone assessment. In collaboration with his co-authors developed a methodology, carried out investigations, and prepared and conducted experiments. The author also adapted a software for spectral analysis, managed data collection, preparation, and assessment, and performed statistical analysis. Furthermore, he created visualizations and contributed to the writing and reviewing of this article.

The co-authors participated in developing the article's concept, working together on the methodology development, and engaging in the investigation and implementation of experi-

ments. Additionally, they were involved in the formal analysis, writing, reviewing, and editing processes of the article. They also supplied resources and provided supervision.

Abstract

In addition to the standard-resolution (SR) acquisition mode, a high-resolution (HR) mode is available on a research photon-counting-detector (PCD) whole-body CT system. In the HR mode each detector consists of a 2 $\times$ 2 array of 0.225 mm $\times$ 0.225 mm subpixel elements. This is in contrast to the SR mode that consists of a 4 $\times$ 4 array of the same sub-elements, and results in 0.25 mm isotropic resolution at iso-center for the HR mode. In this study, we quantified ex vivo the capabilities of the HR mode to characterize renal stones in terms of morphology and mineral composition. Forty pure stones - 10 uric acid (UA), 10 cystine (CYS), 10 calcium oxalate monohydrate (COM) and 10 apatite (APA) - and 14 mixed stones were placed in a 20 cm water phantom and scanned in HR mode, at radiation dose matched to that of routine dual-energy stone exams. Data from micro CT provided a reference for the quantification of morphology and mineral composition of the mixed stones. The area under the ROC curve was 1.0 for discriminating UA from CYS, 0.89 for CYS vs COM and 0.84 for COM vs APA. The root mean square error (RMSE) of the percent UA in mixed stones was 11.0% with a medium-sharp kernel and 15.6% with the sharpest kernel. The HR showed qualitatively accurate characterization of stone morphology relative to micro CT.

Keywords

Computed tomography (CT); photon-counting detector CT (PCD-CT); high resolution CT

8.1 Introduction

Clinical x-ray CT systems are limited in the spatial resolution they can achieve by many physical factors, including, but not limited to: the focal spot size, the detector pixel size and the magnification [135, 151]. While the size of the focal spot is limited by physical constraints, as well as tube output and anode heating considerations, the size of the detector pixels is limited by the need for energy-integrating detectors (EIDs) to have septa between adjacent elements to prevent optical cross-talk. For the vast majority of clinical CT applications, the spatial resolution that can be achieved by conventional EID-CT systems is more than adequate to provide images of diagnostic quality, and noise is rather the limiting factor. However, there are a subset of clinical applications, including but not limited to: imaging of the temporal bone and inner ear, lung imaging, and imaging of the extremities for musculoskeletal applications, for which the spatial resolution that can be achieved with standard focal spot sizes (1–2 mm) and detector pixel sizes (0.5 to 0.625 mm at the iso-center) is suboptimal [201]. To address this limitation, state-of-the-art CT systems offer acquisition modes with enhanced spatial resolution for those specific clinical applications that may benefit from additional anatomical detail. Higher spatial resolution can be achieved on a conventional CT system by selectively

covering part of each detector element with the use of comb or grid z-ray attenuators to reduce the effective detector aperture [78, 182, 201]. However, limiting the detector aperture is dose-inefficient, with only less of 25% of the x-rays contributing to the image formation when half the detector pixel area is covered in both directions, compared to a conventional acquisition mode. This severe dose penalty prevents the use of high resolution CT acquisition modes for large body parts, like the thorax and the abdomen.

In recent years, photon-counting-detector (PCD) technology has been adopted in research CT systems with promising results [142, 157, 284, 297, 299, 300, 301, 322, 333]. In PCDs, detected x-ray photons are individually counted and their energy measured using direct conversion techniques that make possible the use of septa-free detector arrays. Therefore, smaller detector elements - and hence improved spatial resolution - are possible in PCD-CT without compromising the fill-factor and the dose efficiency, opening the door to higher-resolution CT for unexplored clinical applications.

Unenhanced CT is the imaging modality of choice for the diagnosis, monitoring and treatment planning of urinary calculi. Dual-energy CT has emerged as a reliable tool to characterize the mineral composition of urinary stones, effectively discriminating uric acid from non-uric acid stones [102, 163, 315]. However, limited success has been reported in the characterization of small (<3mm) and mixed stones, as well as in the classification of non-uric acid subtypes [61, 185, 256]. The purpose of this study was to investigate the potential of a new high-resolution (HR) acquisition mode available on a research PCD-CT system for the characterization of renal stone composition and morphology.

8.2 Materials and Methods

8.2.1 High resolution PCD-CT

A research whole-body PCD-based CT scanner is available in our lab, which was developed on the platform of a 2nd generation dual-source CT system by replacing one of the two conventional detectors with a PCD [359]. Although the native detector size of the PCD is $225 \times 225\ \mu m^2$, the standard readout mode uses macro pixels that group 4 by 4 native detector elements, resulting in a detector size of $0.9 \times 0.9\ mm^2$. Multi-energy CT data can be acquired in PCD-CT by applying 2 to 4 energy thresholds to the detected photons. A high resolution (HR) mode was recently introduced using 2 by 2 native detector elements. However, preliminary investigations using this mode were limited to only one energy threshold, thus effectively limiting the HR data to single energy applications [183]. An acquisition mode with by 2 detector elements and up to 2 energy thresholds was recently made available by the manufacturer, which enabled the collection of dual-energy HR CT data.

8.2.2 Classification of pure stones

40 stones were used to test the classification capabilities of the HR acquisition mode. The sample consisted of 10 uric acid (UA) stones, 10 cystine (CYS) stones, 10 calcium oxalate

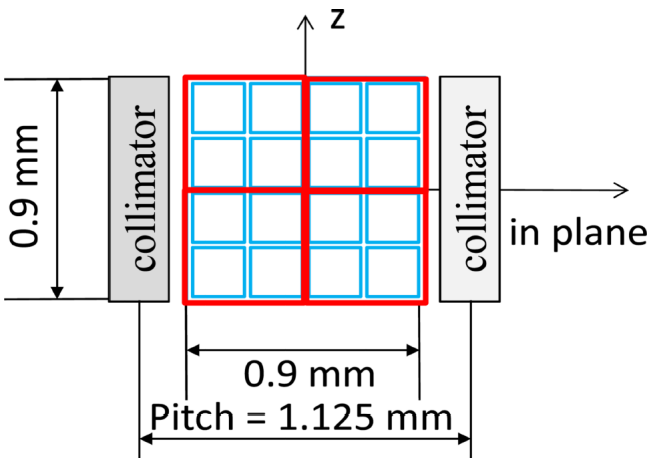

Fig. 8.1. Native pixel (blue) and HR pixel (red) of PCD detector.

monohydrate (COM) and 10 apatite (APA) stones. Reference composition was provided by infrared spectroscopy. Only stones with purity higher than 90% were included in the sample. Each set of stones was placed in a 20 cm water phantom and scanned at the dose level matched to our routine practice (3.8 mGy). Data were acquired in HR mode with 140 kVp tube potential and two energy thresholds (25 and 75 keV) and reconstructed with a small field of view (110 mm) and thin slices, resulting in a voxel size of $0.21 \times 0.21 \times 0.25$ mm^3. A medium-sharp (D50f) and a very sharp (S80) reconstruction kernel were both evaluated. Each stone was subsequently segmented from the water background and single- and dual-energy metrics extracted using custom software. The CT number ratio was computed as the ratio of average CT number of each stone in the two energy bins (CT number of 25–75 keV bin divided by the CT number of the 75–140 keV bin). Using the CT number ratios, receiver operating characteristic (ROC) curves were generated for the classification of stone type. The area under the ROC curve (AUC) was used as the figure of merit to assess the classification performance.

8.2.3 Characterization of mixed stones

14 stones of mixed uric acid (UA) and non-uric acid (nUA) composition were used to determine the accuracy of the HR mode in measuring the morphology and percent of UA in each stone. microCT scans were used to provide an accurate reference [365]. PCD-CT data were acquired in HR mode and processed following the same procedure outlined for the pure stones above. The CT number ratio was computed for each pixel in each stone and the optimal threshold identified as that which resulted in the lowest root mean squared error (RMSE) in the estimation of the percent UA for the stone sample analyzed [185]. Additionally, qualitative analysis of stone morphology was performed by visually assessing the internal structure of the stones.

8.3 Results

8.3.1 Classification of pure stones

In Figure 8.2, we show the ROC curves for the classification of each stone type using the HR mode. Accurate classification of UA and nUA stones (AUC = 1) as well as between nUA subtypes (CYS vs. COM, AUC = 0.89; COM vs APA, AUC = 0.84) was achieved with a medium-sharp kernel despite the small pixel size (Figure 8.2 (a)). Furthermore, no degradation was observed when a very sharp kernel was used (Figure 8.2 (b)). This indicates that the increase in spatial resolution (and associated increase in image noise) did not compromise the ability of the technique to classify stone composition.

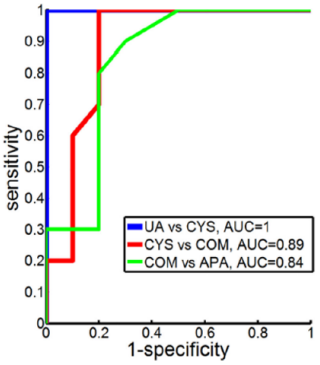

(a) Images reconstructed with a medium-sharp kernel (D50).

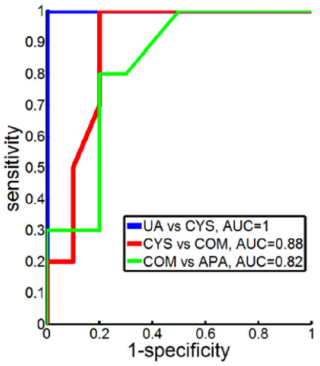

(b) Images reconstructed with a very sharp kernel (S80).

Fig. 8.2. ROC curves for the classification of 4 stone types using the HR mode on a PCD-CT prototype.

8.3.2 Characterization of mixed stones

In Figure 8.3, we show a visual comparison of the HR PCD-CT images of a sample mixed stone (volume, 224 mm^3), together with a reference microCT image. The same medium-sharp and sharp reconstruction kernels (D50 and S80) were used for the PCD-CT image reconstruction. The visual assessment shows significantly improved detail of the internal structures of the stone, with the COM core and the outer UA layer clearly distinguishable in the HR images. Quantification of the UA component of each stone with the optimal CT number threshold resulted in a root-mean-squared-error of 11.0% for the D50 reconstruction kernel [185]. We believe that this value was limited by the increased noise in the CT number ratios when measured on smaller pixels. This hypothesis is supported by the observation that with the sharper kernel, the RMSE increased substantially (Table 8.1). However, the increased detail of the stone internal structure could prove beneficial for the task of classification of mixed stones. In particular, an approach that includes a segmentation step to quantify the percent amount of different components, followed by a classification step using CT number ratios to identify the mineral composition of each sub-region in the stone, could be feasible with the higher spatial resolution offered by the new HR acquisition mode.

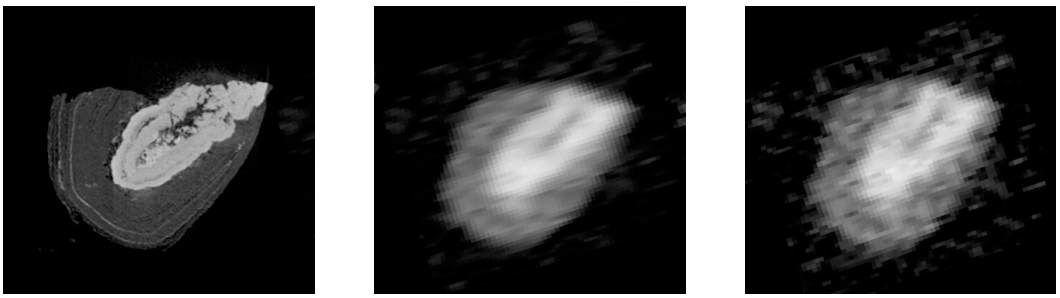

(a) Reference micro CT scan.

(b) Images reconstructed with a medium-sharp kernel (D50).

(c) Images reconstructed with a very sharp kernel (S80).

Fig. 8.3. Visual assessment of internal stone morphology with different reconstruction kernels for the HR mode of the PCD-CT system. Clinical dose level used to obtain HR PCD-CT images.

Tab. 8.1. Root-mean-squared-error for the quantification of the percent UA component of mixed stones for different acquisition modes and reconstruction kernels.

	D50 kernel	**S80 kernel**
RSME (%) vs. micro CT	11.0	15.6

8.4 Conclusions

In this study, we reported the first ex vivo characterization of renal stones using a high resolution imaging mode on a research CT system using a photon-counting detector. Results from this investigation demonstrate that accurate classification of pure renal stones is maintained with the HR mode while providing a detailed characterization of the stone morphology compared to the reference micro-CT data. The additional detail of internal stone structure provided by the HR acquisition mode on PCD-CT might enable more accurate classification of mixed renal stones, which make up to 80% of all renal stones. However, the additional sharpness needs to be balanced against the increased noise associated with using smaller voxels at the same radiation dose. Therefore, appropriate noise reduction techniques may be required to take full advantage of the increased spatial resolution offered by HR PCD-CT.

Acknowledgements

Research reported in this publication was supported by The National Institute of Biomedical Imaging and Bioengineering of the National Institutes of Health under award numbers EB016966 and DK100227, and in collaboration with Siemens Healthcare. The content is solely the responsibility of the authors and does not necessarily represent the official views of the National Institutes of Health. The scanner and algorithm discussed here are not commercially available.

8.5 References

[61] X. Duan, Z. Li, L. Yu, S. Leng, A. F. Halaweish, J. G. Fletcher, and C. H. McCollough. “Characterization of urinary stone composition by use of third-generation dual-source dual-energy CT with increased spectral separation”. In: *American Journal of Roentgenology* 205.6 (2015), p. 1203

[359] Z. Yu, S. Leng, S. M. Jorgensen, Z. Li, R. Gutjahr, B. Chen, A. F. Halaweish, S. Kappler, L. Yu, E. L. Ritman, and C. H. McCollough. “Evaluation of conventional imaging performance in a research whole-body CT system with a photon-counting detector array”. In: *Physics in Medicine and Biology* 61.4 (2016), p. 1572

[78] T. Flohr, K Stierstorfer, C Süss, B Schmidt, A. Primak, and C. McCollough. “Novel ultrahigh resolution data acquisition and image reconstruction for multi-detector row CT”. in: *Medical Physics* 34.5 (2007), pp. 1712–1723

[102] A. Graser, T. R. Johnson, M. Bader, M. Staehler, N. Haseke, K. Nikolaou, M. F. Reiser, C. G. Stief, and C. R. Becker. “Dual energy CT characterization of urinary calculi: initial in vitro and clinical experience”. In: *Investigative Radiology* 43.2 (2008), pp. 112–119

[135] J. Hsieh. “Computed tomography: principles, design, artifacts, and recent advances”. In: SPIE Bellingham, WA. 2009

[142] J. S. Iwanczyk, E. Nygard, O. Meirav, J. Arenson, W. C. Barber, N. E. Hartsough, N. Malakhov, and J. C. Wessel. “Photon counting energy dispersive detector arrays for x-ray imaging”. In: *IEEE Transactions on Nuclear Science* 56.3 (2009), pp. 535–542

[151] W. A. Kalender. *Computertomographie - Grundlagen, Gerätetechnologie, Bildqualität, Anwendungen*. New York: Wiley, 2006

[157] S Kappler, F Glasser, S Janssen, E Kraft, and M Reinwand. “A research prototype system for quantum-counting clinical CT”. in: *International Society for Optics and Photonics Medical Imaging*. International Society for Optics and Photonics. 2010, 76221Z–76221Z

[163] R. K. Kaza, J. F. Platt, R. H. Cohan, E. M. Caoili, M. M. Al-Hawary, and A. Wasnik. “Dual-energy CT with single-and dual-source scanners: current applications in evaluating the genitourinary tract”. In: *Radiographics* 32.2 (2012), pp. 353–369

[182] S Leng, F. Diehn, J. Lane, K. Koeller, R. Witte, R. Carter, and C. McCollough. “Temporal bone CT: improved image quality and potential for decreased radiation dose using an ultra-high-resolution scan mode with an iterative reconstruction algorithm”. In: *American Journal of Neuroradiology* 36.9 (2015), pp. 1599–1603

[183] S Leng, Z Yu, A Halaweish, S Kappler, K Hahn, A Henning, Z Li, J Lane, D. Levin, S Jorgensen, et al. “A high-resolution imaging technique using a whole-body, research photon counting detector CT system”. In: *International Society for Optics and Photonics Medical Imaging*. International Society for Optics and Photonics. 2016, pp. 97831I–97831I

[185] S. Leng, A. Huang, J. M. Cardona, X. Duan, J. C. Williams, and C. H. McCollough. “Dual-Energy CT for Quantification of Urinary Stone Composition in Mixed Stones: A Phantom Study”. In: *American Journal of Roentgenology* (2016), pp. 1–9

[201] C. H. McCollough, S. Leng, J. Sunnegardh, T. J. Vrieze, L. Yu, J. Lane, R. Raupach, K. Stierstorfer, and T. G. Flohr. “Spatial resolution improvement and dose reduction potential for inner ear CT imaging using az-axis deconvolution technique”. In: *Medical Physics* 40.6Part1 (2013), p. 061904

[256] M. Qu, J. C. R. Giraldo, S. Leng, J. C. Williams, T. J. Vrtiska, J. C. Lieske, and C. H. McCollough. “Dual-energy dual-source CT with additional spectral filtration can improve the differentiation of non-uric acid renal stones: an ex vivo phantom study”. In: *American Journal of Roentgenology* 196.6 (2011), p. 1279

[284] J. Schlomka, E Roessl, R Dorscheid, S Dill, G Martens, T Istel, C Bäumer, C Herrmann, R Steadman, G Zeitler, et al. “Experimental feasibility of multi-energy photon-counting K-edge imaging in pre-clinical computed tomography”. In: *Physics in Medicine and Biology* 53.15 (2008), p. 4031

[297] P. M. Shikhaliev. “Computed tomography with energy-resolved detection: a feasibility study”. In: *Physics in Medicine & Biology* 53.5 (2008), p. 1475

[299] P. M. Shikhaliev. “Photon counting spectral CT: improved material decomposition with K-edge-filtered x-rays”. In: *Physics in Medicine and Biology* 57.6 (2012), p. 1595

[300] P. M. Shikhaliev and S. G. Fritz. “Photon counting spectral CT versus conventional CT: comparative evaluation for breast imaging application”. In: *Physics in Medicine and Biology* 56.7 (2011), p. 1905

[301] P. M. Shikhaliev, S. G. Fritz, and J. W. Chapman. “Photon counting multienergy x-ray imaging: Effect of the characteristic x rays on detector performance”. In: *Medical Physics* 36.11 (2009), pp. 5107–5119

[315] P. Stolzmann, M. Kozomara, N. Chuck, M. Müntener, S. Leschka, H. Scheffel, and H. Alkadhi. “In vivo identification of uric acid stones with dual-energy CT: diagnostic performance evaluation in patients”. In: *Abdominal Imaging* 35.5 (2010), pp. 629–635

[322] K. Taguchi and J. S. Iwanczyk. “Vision 20/20: Single photon counting x-ray detectors in medical imaging”. In: *Medical Physics* 40.10 (2013), p. 100901

[333] T. Tumer, M Clajus, G. Visser, S Yin, P. Willson, L D'Aries, K. Parnham, B Glick, J. Perry, T Gamble, et al. "Preliminary results obtained from a novel CdZnTe pad detector and readout ASIC developed for an automatic baggage inspection system". In: *IEEE Nuclear Science Symposium Conference*. Vol. 1. IEEE. 2000, pp. 4–36

[365] C. A. Zarse, J. A. McAteer, A. J. Sommer, S. C. Kim, E. K. Hatt, J. E. Lingeman, A. P. Evan, and J. C. Williams. "Nondestructive analysis of urinary calculi using micro computed tomography". In: *BMC Urology* 4.1 (2004), p. 1

9

Quantitative dual-energy CT material decomposition of holmium microspheres: local concentration determination evaluated in phantoms and a rabbit tumor model

Ralf Gutjahr, MSc,[1,2] Robert C. Bakker, PhD,[3,4] Feiko Tiessens, PhD,[5]
Sebastiaan A. van Nimwegen, PhD,[6] Bernhard Schmidt, PhD,[1]
and Johannes Frank Wilhelmus Nijsen, PhD[5,7]

[1]Computed Tomography, Siemens Healthcare GmbH, Forchheim, Germany
[2]CAMP, Technical University of Munich, Munich, Germany
[3]Department of Radiology and NuclearMedicine, University Medical Center Utrecht, Utrecht, Netherlands
[4]Department of Oral and Maxillofacial Surgery, University Medical Center Utrecht, Utrecht, Netherlands
[5]R&D Imaging & Software, Quirem Medical BV, Deventer, Netherlands
[6]Department of Clinical Sciences of Companion Animals, Faculty of Veterinary Medicine, Utrecht University, Utrecht, Netherlands
[7]Department of Medical Imaging, Radboudumc, Geert Grooteplein-Zuid 10, 6525 GA Nijmegen, Netherlands

Copyright statement

Contributions

The author's contributions included the conceptualization of the study, the development of the methodology, as well as the modification of the original analysis software for optimal data processing. He also participated in upfront investigation, data curation, formal analysis, ensuring the research's validity and robustness. In addition, the author provided the visualization of the results aiming for a informative representations of the findings. His involvement extended to writing, reviewing, and editing the article, ensuring its quality and compliance with publication standards.

The co-authors were responsible in preparing various Holmium solutions used for the system's calibration and the following material quantification. They also prepared the animals, ensuring compliance to the *The Netherlands Experiments on Animals Act (1977) and The European Convention for the Protection of Vertebrate Animals used for Experimental Purposes (Strasbourg, 18.III.1986)*. They also participated in the investigation process ensuring a smooth execution of the research. Their expertise extended to the conceptualization and methodology development, contributing to the study's direction and design.

Abstract

Objectives: The purpose of this study was to assess the feasibility of dual-energy CT-based material decomposition using dual-X-ray spectra information to determine local concentrations of holmium microspheres in phantoms and in an animal model.

Materials and Methods: A spectral calibration phantom with a solution containing 10 mg/mL holmium and various tube settings was scanned using a third-generation dual-energy CT scanner to depict an energy-dependent and material-dependent enhancement vectors. A serial dilution of holmium (microspheres) was quantified by spectral material decomposition and compared with known holmium concentrations. Subsequently, the feasibility of the spectral material decomposition was demonstrated *in-situ* in three euthanized rabbits with injected (radioactive) holmium microspheres.

Results: The measured CT values of the holmium solutions scale linearly to all measured concentrations and tube settings ($R^2 = 1.00$). Material decomposition based on CT acquisitions using the tube voltage combinations of 80/150 Sn kV or 100/150 Sn kV allow the most accurate quantifications for concentrations down to 0.125 mg/mL holmium.

Conclusions: Dual-energy CT facilitates image-based material decomposition to detect and quantify holmium microspheres in phantoms and rabbits.

Keywords

X-ray computed tomography, contrast media, holmium, microspheres

9.1 Introduction

In the 1970s and 1980s, dual-energy CT (DECT) technology demonstrated improved tissue characterization; however, the technique was not widely applied due to limitations like noise in low-kilo voltage (kV) images, acquisition time, and image registration difficulties [55, 94, 204, 207, 278]. Nowadays, DECT technology is clinically established as a result of fast technological developments, such as detectors with fully integrated electronics minimizing electronic noise, improved spectral separation using optimized beam pre-filtration, increased scan speed, and improved post processing techniques [148, 164, 238, 255, 266, 353].

DECT uses two effective X-ray spectra, either generated by a single X-ray tube switching between two different X-ray spectra (kV-switch CT), by using two separated X-ray tubes applying two different voltages (dual-source CT, DSCT), or by resolving an incident spectrum at the scanner (dual-layer CT or photon-counting detector CT). Further image processing enables the quantification of materials by separating their attenuation characteristics into the different contributions of photoelectric absorption and Compton scatter [9, 49, 148, 187, 351]. Nowadays, DECT is clinically used for diagnostic purposes such as classification of uric acid versus non-uric acid urinary stones or to quantify contrast media (CM) uptake, e.g., the local concentration of iodine in liver tissue [26, 91, 102, 238, 254]. Experimental studies also suggest the use of non-approved CM with spectral properties that could be utilized for CTA or cancer theranostics.

A particular therapy that potentially would benefit from DECT quantification is selective internal radiation therapy (SIRT) with beta-emitting radioactive holmium-166 microspheres (^{166}HoMS), which are currently used for radioembolization of liver tumors and intra-tumoral injection in solid malignancies [15, 225, 227, 312]. *In vivo* dosimetry after therapy application, needed to verify the treatment success, can be performed based on SPECT imaging utilizing the holmium-166 gamma radiation or based on magnetic resonance imaging (MRI) utilizing the paramagnetic properties of holmium. Both modalities have shown their possibilities for application in radioembolization therapy; however, for intra-tumoral therapy, their use might be hampered by resolution limitations or detection limits [190, 225, 294, 296].

In intratumoral therapy, high concentrations of microspheres are injected at several locations in the tumor to achieve proper dose levels for the entire tumor. This requires high-resolution dosimetry that cannot be achieved by SPECT and quantification of high holmium concentrations which is challenging for MRI.

Conventional CT for quantification of ^{166}HoMS, utilizing the high attenuation coefficient of holmium, has previously been explored [294, 296]. CT in general would allow for fast ^{166}HoMS quantification of high local concentrations with high spatial resolution and thus accurate local dosimetry at low cost. Although a clear relation was demonstrated between local holmium concentrations and CT signal, discrimination of holmium from, e.g., bone, calcified arteries, or iodinated CM, was found to be difficult [294].

It is expected that DECT can improve the previously identified limitations of conventional CT by utilizing the spectral information that DECT offers combined with the presence of a k-edge

at 56 keV that holmium expresses, leading to a sudden increase in X-ray attenuation at that energy.

The objective of this study was to demonstrate the feasibility of DECT-based quantification of non-radioactive HoMS by means of phantom and measurements of rabbit cadavers.

9.2 Materials and Methods

In this study, the following experiments were performed: Firstly, a spectral calibration was performed to determine the tube voltage combination–dependent and object size–specific spectral properties of the investigated material. Secondly, contrast media quantification measurements were performed to define detection limits and accuracy. Finally, the feasibility of holmium quantification was tested in a pilot study performed *in situ* in VX-2 tumor-bearing rabbits. Since only a very small fraction of holmium-165 is converted to holmium-166 after neutron activation during production (approximately 0.001% [225]), no difference is expected in X-ray attenuation between radioactive and non-radioactive microspheres. Therefore, all experiments were performed using ^{165}HoMS to avoid unnecessary radiation risks.

9.2.1 Spectral calibration

Spectral calibration is required to depict an energy-dependent and material-dependent material vector [9]. For this purpose, a dedicated spectral calibration phantom (QRM GmbH) was scanned using a third-generation dual-energy CT scanner (SOMATOM Force, Siemens Healthcare GmbH). The scans were performed using a dual-energy abdomen protocol; collimation $2 \times 64 \times 0.6$ mm with a flying focal spot in the z-direction, rotation time 0.5 s/rot, and a pitch of 0.6. The images were reconstructed using a weighted filtered backprojection algorithm [344] providing linear handling of contrast, noise, and spatial resolution in order to preserve purely quantitative results. All images were reconstructed with a slice thickness of 1.5 mm, an increment of 1.0 mm, a quantitative medium smooth reconstruction kernel (Qr44f) used for routine reconstruction of DECT images (50% value of the modulation transfer function: ρ_{50} = 4.62 lp/cm, no edge enhancement), and a reconstruction field of view (FOV) of 175 mm. The phantom consists of a 10-cm-wide cylinder comprising a synthetic material exhibiting liquid waterequivalent CT values. Two 2-cm-diameter syringes (Omnifix Solo, B. Braun) were located in the phantom's center and 3 cm horizontally offset, respectively. The centric syringe was filled with holmium (III) chloride hexahydrate (Metal Rare Earth Limited (Holmium content 41.3–45.5% (w/w)) suspended in distilled water (Fresenius SE & Co KGaA). Titration of the holmium chloride revealed a 42.0% holmium content resulting in a final concentration of 10.5 mg/mL. The known concentration served as a reference to facilitate quantitative measurements. The offset syringe contained pure water as a reference to the phantom's original material. In the spectral calibration, the following effects were investigated using an automatic exposure control (CARE, Dose4D, Siemens Healthcare GmbH), the effect of X-ray tube voltage combinations and size-dependent spectral effects (Table 9.1). Measurements were performed using different X-ray tube voltage combinations: 70/150 Sn kV, 80/150 Sn kV, 100/150 Sn kV, and 80/140 kV, whereas Sn denotes the utilization of a 0.6-mm-thick tin pre-filtration used for increased spectral separation [255]. To investigate size-dependent

spectral effects, additional extension rings were used to expand the 10-cm-wide phantom to 15, 20, 25, 30, or 35 cm [164, 190, 226].

Tab. 9.1. Effective tube current-time products regarding the different phantom sizes and all tube voltage combinations as investigated in the calibration measurements.

Tube voltage (system A/B), kV	**Tube current time products for different phantom sizs, mAs**					
	10 cm	15 cm	20 cm	25 cm	30 cm	35 cm
70/150 Sn	16/16	18/16	37/22	80/36	180/16	410/95
80/150 Sn	16/16	16/16	23/22	45/36	95/60	202/95
100/150 Sn	16/16	20/16	34/22	60/36	109/60	195/95
80/140	16/16	16/16	16/16	30/16	65/16	142/24

9.2.2 Material decomposition algorithm

The relationship of the material-specific CT values of corresponding spectral CT acquisitions allows the determination of material vectors unique for the used tube voltages. The used image-based material separation algorithm (syngo.via, VB30A, Siemens Healthcare GmbH) relies on a base transformation and a projection of every measured set of CT values to preselected orthogonalized and linearly independent base vectors [148, 189]. In our study, air (-1000/-1000 HU for the low-kV and high-kV image, respectively), water (0/0 HU) and ^{165}HoMS were selected as base materials. Decomposition into these three materials enables the generation of a material images that constitute local concentrations of ^{165}HoMS, as well as virtual non-contrast images, mimicking a native scan where no CM was applied (Figure 9.1).

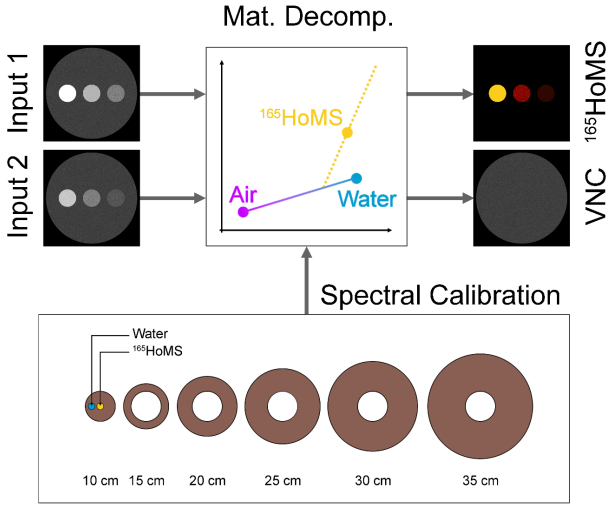

Fig. 9.1. Spectral calibration scans are used to generate energy-dependent and material-dependent material vectors as a prerequisite for the image-based material decomposition. Therefore, the X-ray absorption of holmium on the applied X-ray spectra was investigated in relation to the size of the object (using 10–35-cm extension rings). Based on two different energy input images, inputs 1 and 2, the material decomposition can be calculated and results in material images constituting of local concentrations of ^{165}HoMS, as well as virtual non-contrast images (VNC).

9.2.3 Contrast media quantification measurements

A serial dilution of HoMS (0.125–10.0 mg holmium/mL) was examined to test linearity with various concentrations and the detection limit. The concentration inserts were made of a batch of ^{165}HoMS with a holmium mass percentage of 18.8% (QuiremSpheres, Quirem Medical B.V.). The microspheres were suspended in an injection solution containing 116 mmol phosphate-buffered saline (pH 7.2, 77.0 mmol disodium phosphate dibasic dehydrate, Merck Millipore, and 39.0 mmol sodium phosphate monobasic anhydrous, Sigma Aldrich) with polyoxyethylene-polyoxypropylene block copolymer (Pluronic F-68, Sigma-Aldrich, Chemie B.V.) 2% weight per volume solution. To prevent precipitation of ^{165}HoMS due to their weight (1.4 g/mL), an agar solution (MP Agar, Roche Diagnostics) was added. The agar solution was heated to 90°C for 10 min, resulting in a transparent fluid. The ^{165}HoMS suspension and agar were mixed in a rising concentration of ^{165}HoMS and filled into syringes for the spectral calibration measurements and into 5 mL Eppendorf tubes for the quantitative comparison of measured and known concentration in the CT images. Once cooled to room temperature, the agar became solid.

The experimental setup consisted of a 20-cm-wide (real) water phantom that allowed the positioning of multiple tubes. The solutions were scanned in two groups (0.125–1.0 mg/mL and 2.0–10.0 mg/mL). The inserts were arranged in an equiangular fashion 5 cm distant from the phantom's centerline. In addition to the clinical dose (CARE Dose4D) measurements, a series of high-dose measurements were conducted (Table 9.2). With the first mode, the accuracy of ^{165}HoMS quantification was assessed under clinical conditions, whereas the maximal tube current allows the determination of a contrast agent in a low noise situation. After the image-based material decomposition, the images were quantitatively assessed and ^{165}HoMS concentrations were compared with the known concentrations.

Tab. 9.2. Overview of the effective current, Q_{ref}, and radiation dose for all applied tube voltage combinations for the quantification measurements.

Tube voltages (system A/B), kV	Tube current determination	Effective current, mAs	Q_{ref}, mAs	Dose ($CTDI_{32}$), mGy
70/150 Sn	CARE Dose4D	212 / 55	380 / 95	4.36
	High dose	1083 / 271	-	21.92
80/150 Sn	CARE Dose4D	105 / 54	190 / 95	3.83
	High dose	1083 / 542	-	38.95
100/150 Sn	CARE Dose4D	60 / 53	190 / 95	4.22
	High dose	840 / 420	-	48.91
80/140	CARE Dose4D	73 / 18	132 / 24	3.40
	High dose	997 / 181	-	39.24

Equation 9.1 describes a tolerance term (derived from [308]) discerning as an estimate error for material quantification. The two terms presume the CT value stability and spectral

stability to be two independent types of errors. The tolerance scales with increased known concentration C_{known}.

$$T = \sqrt{\left(0.5\frac{\text{mg}}{\text{mL}}\right)^2 + \left(0.1 \cdot C_{\text{known}}\right)^2} \tag{9.1}$$

9.2.4 Animal preparation

All experiments were performed in conduct with *The Netherlands Experiments on Animals Act (1977) and The European Convention for the Protection of Vertebrate Animals used for Experimental Purposes (Strasbourg, 18.III.1986)*. Approval was obtained from the Utrecht University Animal Experiments Committee (DEC 2011.III.08.080).

The VX-2 tumor model was described previously [226]. Six tumors were induced by subcutaneous injection of three $\pm$ 1 mm^3 viable fragments of VX-2 carcinoma harvested from the donor rabbit. Next, these fragments were injected with 0.1–0.3 mL PBS into three adult female New Zealand White (NZW) rabbits weighting 3–4 kg. All tumor implantations were performed under analgesia with carprofen 4 mg/kg. During the animal experiments, sedation and analgesia were achieved with a mixture of 0.125 mg/kg dexdomitor and 15 mg/kg ketamine.

Subsequently, aliquots with various amounts of ^{166}HoMS were administered intratumorally. The exact administered amount, regarding holmium mass (mg), was calculated by measuring the radioactivity of the syringes with ^{166}HoMS before and after injection using a VDC-404 dose calibrator, Veenstra Instruments B.V. Measurements performed on the DECT are primarily based on ^{165}Ho as only a fraction is converted. Animals were sacrificed and preserved in a shielded freezer to let the radioactive holmium decay prior to scanning with the dual-energy CT scanner. The average water equivalent diameter of the rabbit cadaver ranged from 15 to 20 cm, such that the general quantitative detection of the ^{165}HoMS as from the prior phantom scans can be assumed.

9.2.5 Statistical analysis

After applying the image-based material decomposition algorithm, the quantitative material images were evaluated for ^{165}HoMS quantification. Descriptive statistics (mean concentration, R^2, RMSE, absolute and relative deviation) of the image-based material decomposition measurements were compared with the known concentrations for all tube voltage combinations and dose settings.

9.3 Results

9.3.1 Spectral calibration

Figure 9.2 shows that the X-ray absorption of holmium highly depends on the applied X-ray spectra and the size of the object. With an increased diameter, the mean energy of the X-ray spectrum shifts towards higher energies, which, for lighter atoms (presuming no k-edge in the applied X-ray spectrum), results in a decrease of X-ray attenuation and therefore lower CT values. An increased attenuation and an enhanced CT value are observed when the mean energy of an X-ray spectrum and its spectral barycenter moves closely beyond the K-edge of a material, where the photoelectric effect becomes dominant. The further the energies shift, the more the measured CT values decrease. For all investigated energies, both effects, the decreased X-ray attenuation due to increased object size and the simultaneously mean energy shift towards the k-edge of the material (56 keV for Holmium), result in an increase of total X-ray attenuation at 70 and 80 kV, but eventually to a decrease in absorption at 100–150 Sn kV (Figure 9.2).

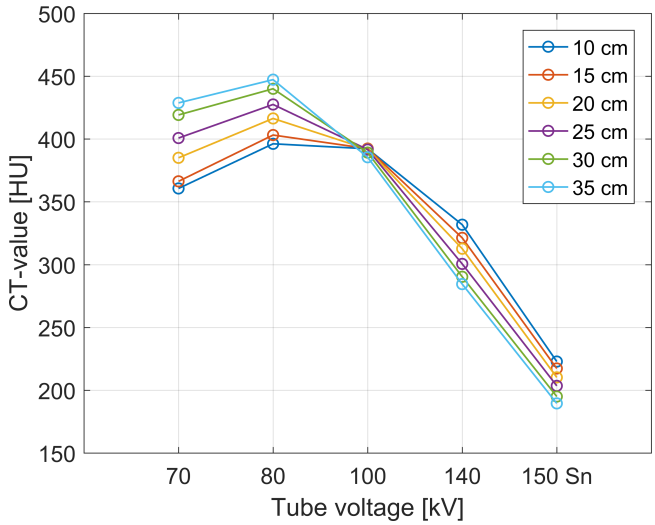

Fig. 9.2. Measured CT values for 10.0 mg ^{165}HoMS/mL with regard to different tube voltages and phantom sizes.

9.3.2 Contrast media quantification measurements

The CT values of the holmium solutions were identical for both dose levels and the image noise level scales square root to the radiation dose reduction (Figure 9.3 a and b). Measured concentrations, in the phantom model, using CT quantification were linear (Table 9.3) and slightly lower than the known concentrations (Figure 9.3 c and d). Figure 9.3 e and f show the increase of deviation with lower holmium concentrations. Given the introduced tolerance term, all quantifications down to 0.125 ^{166}Ho-microspheres mg/mL were sufficient for all tube voltage combinations and for both clinical dose and high doses. The highest accuracy was observed using 80/150 Sn kV, followed by 100/150 Sn, 70/150 Sn, and 80/140 kV tube voltage and high radiation dose.

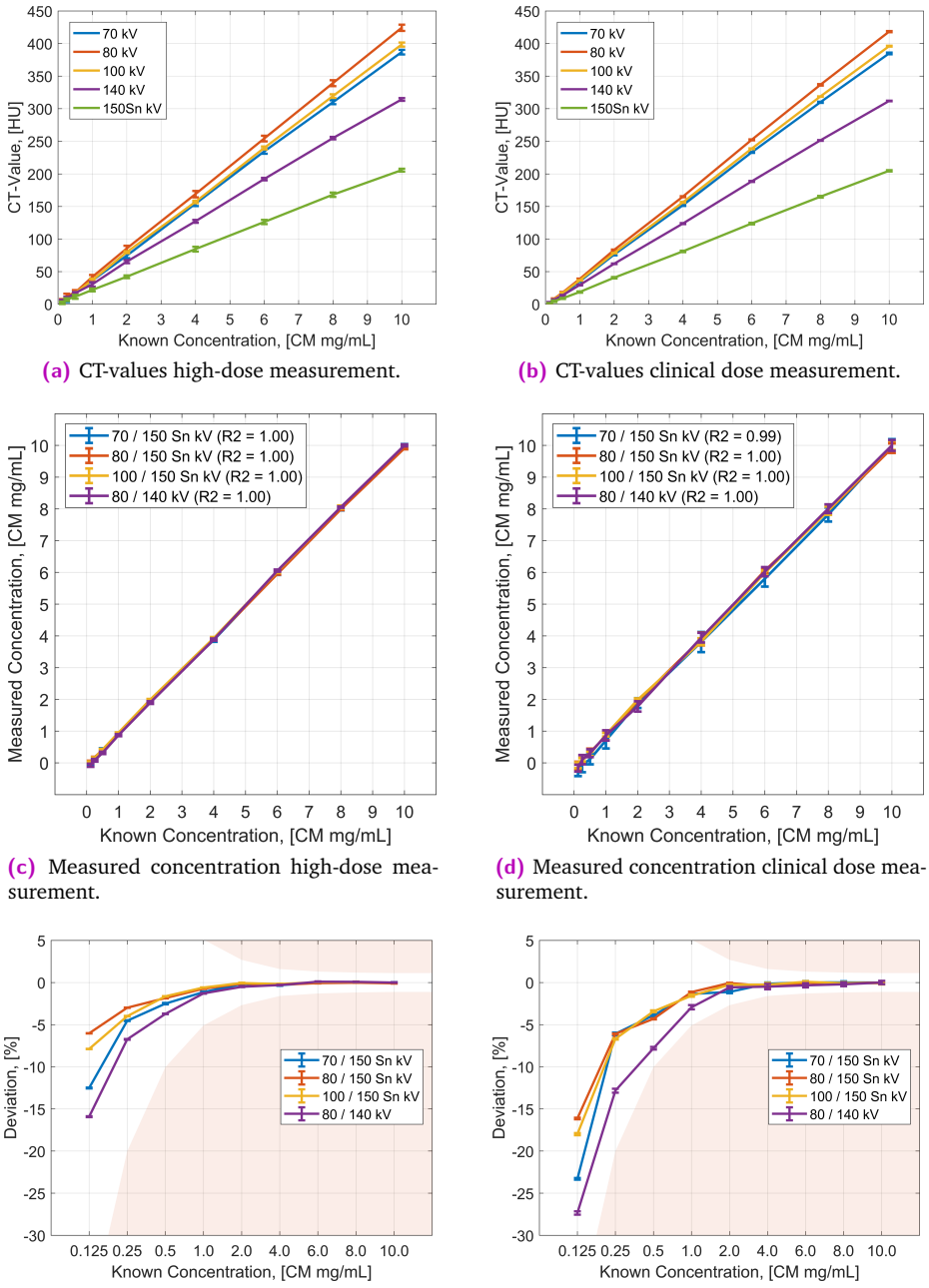

(a) CT-values high-dose measurement.

(b) CT-values clinical dose measurement.

(c) Measured concentration high-dose measurement.

(d) Measured concentration clinical dose measurement.

(e) Relative contrast deviation high-dose measurement.

(f) Relative contrast deviation clinical dose measurement.

Fig. 9.3. Slope and CT values for different ^{165}HoMS mg/mL solutions in a 20-cm-wide water phantom. a High-dose measurements, (b) clinical situation with typical clinical radiation dose using automated exposure control. Accuracy of the measured concentrations compared against the known concentrations for high-dose measurements (c) and measurements using automated exposure control (d). Relative deviations of the measured concentrations compared against the known concentrations for high dose measurements (e) and measurements using automated exposure control (f). The grey area depicts the area where the given tolerance is exceeded.

The measured CT values decreased with lower holmium concentrations, while the noise level remained the same for a tube voltage. This resulted in a factor 3–4 times lower SNR, e.g., from 65.4 to 15.7 for 80 kV with 10 mg/mL holmium (Figure 9.4). The additional value of DECT material decomposition is shown in Figure 9.5, illustrating the output of two

Tab. 9.3. Linear fit parameters (m for slope, b for offset) and errors (R^2 and root mean square error, RMSE) for the comparison of measured and known concentration with respect to different tube voltage combinations and tube currents.

Dose	Tube voltage combination	Fit parameters and errors			
		m	b	R^2	RMSE
CARE Dose 4D	70/150 Sn	1.03	-0.32	0.99	0.25
	80/150 Sn	1.01	-0.16	1.00	0.12
	100/150 Sn	1.02	-0.16	1.00	0.12
	80/140	1.03	-0.21	1.00	0.15
High Dose	70/150 Sn	1.02	-0.13	1.00	0.09
	80/150 Sn	1.00	-0.07	1.00	0.07
	100/150 Sn	1.01	-0.08	1.00	0.06
	80/140	1.02	-0.17	1.00	0.12

separate material decompositions, virtual non-contrast images (Figure 9.5 a and b) and the quantitatively measured mapping of holmium concentrations (Figure 9.5 c and d).

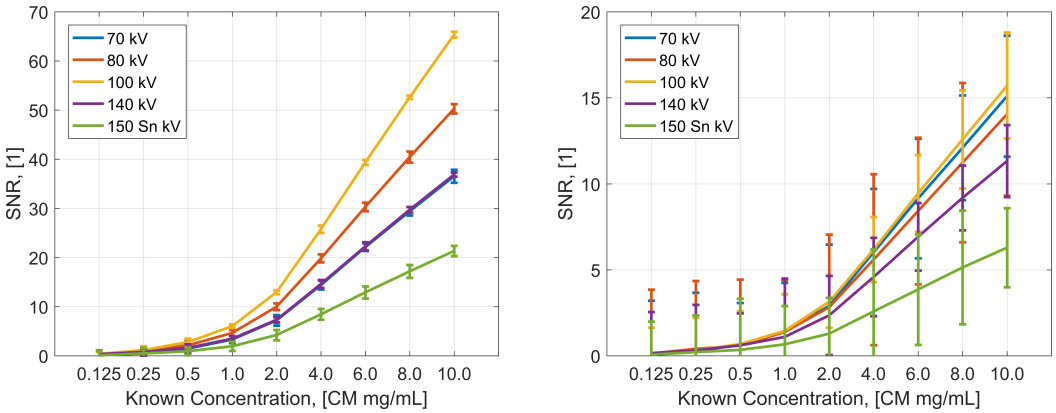

(a) High radiation dose.

(b) Typical clinical radiation dose.

Fig. 9.4. Measured SNRs for all investigated ^{165}HoMS solutions

9.3.3 Animal experiment

Figure 9.6 depicts two acquired coronary slices of a scanned rabbit cadaver using 80 kV (a), 150 Sn kV (b), and a calculated VNC image (c) and a material-specific image (d). The material-specific image segments the holmium and soft tissue to show the exact location of the injected material with respect to the anatomy of the single animals (Figure 9.6 d). The injected and detected amount of ^{165}HoMS corresponded well with relative deviation ranging between 1 and 11% (Table 9.4).

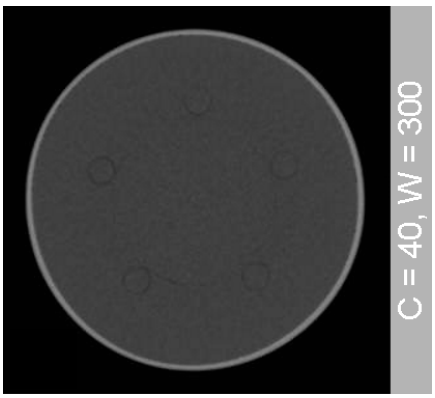

(a) VNC image - high concentrations.

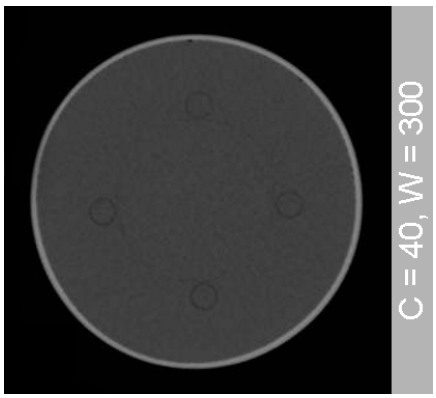

(b) VNC image - low concentrations.

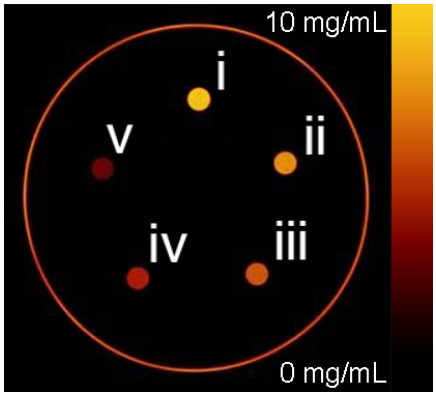

(c) Material image - high concentrations.

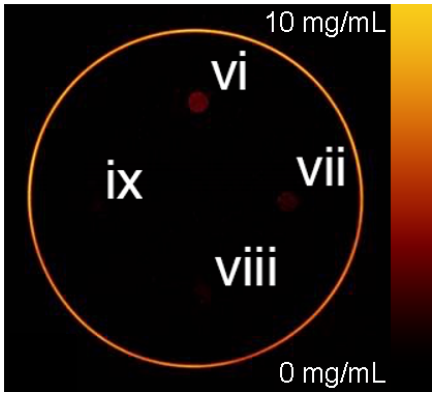

(d) Material image - low concentrations.

Fig. 9.5. a, b VNC images, i.e., images where the ^{165}HoMS is virtually removed. The material images (c, d) facilitate quantitative readout of the investigated ^{165}HoMS concentrations: 10.0, 8.0, 6.0, 4.0, and 2.0 mg ^{165}HoMS/mL; vi–ix show the results for 1.0, 0.5, 0.25, and 0.125 mg ^{165}HoMS/mL.

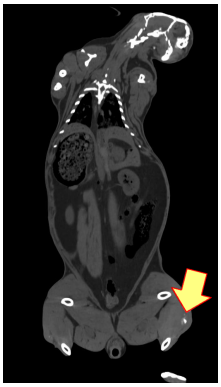

(a) 80 kV

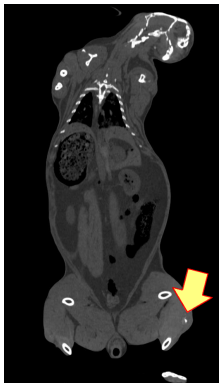

(b) 150 Sn (kV)

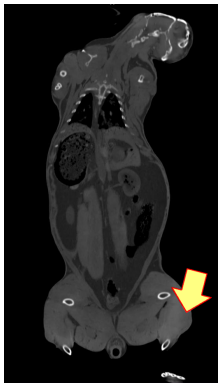

(c) VNC

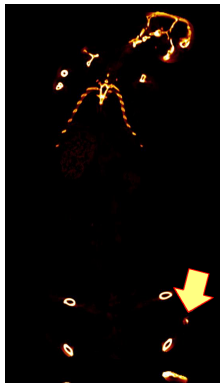

(d)
fig:paper4:figure5:d

Fig. 9.6. Coronary slice of a scanned rabbit cadaver acquired with 80 kV (a) and 150 Sn (kV) (center = 150 HU, window = 600 HU). A VNC image (c) as well as a material-specific image (d) was calculated.

9.4 Discussion

In this article, we presented the first results of DECT-based quantification of holmium microspheres in phantoms and euthanized rabbits.

Tab. 9.4. List of injected amounts of ^{165}HoMS and the detected amounts of ^{165}HoMS after material decomposition and quantification of the animal measurements. The relative deviations (with reference to the injected amounts) are shown in the fourth column.

Injection	Injected amount of ^{165}HoMS, mg	Detected amount of ^{165}HoMS, mg	Relative deviation, %
1	5.61	6.3	-11.4
2	3.34	3.0	-11.7
3	5.96	5.5	-7.7
4	12.59	12.8	1.7

All measurements showed a linear relation between DECT-based holmium concentrations and actual holmium concentrations. This was observed for all investigated X-ray spectra. In the high-dose acquisitions, the accuracy per measurement is superior due to the reduced noise level compared with clinical (low) dose acquisitions. In the case of low concentrations of holmium, the reduced CT value can no longer be distinguished from the background signal anymore. This effect propagates through the applied material decomposition algorithm. Ultimately, the quality of the applied material separations based on the image data of the high-dose measurements outperformed the quality of the respective low-dose measurements.

The measured CT values of the ^{165}HoMS solutions depended on the investigated phantom sizes. For lower energetic X-ray spectra (70 kV and 80 kV), the increased phantom size resulted in a shift of the mean X-ray spectra closer to the k-edge of holmium. The suddenly increased proportion of photoelectric absorption causes an increased total mass attenuation and therefore increased CT values. For higher energetic X- ray spectra (e.g., 140 kV or 150 Sn kV), the mean X-ray energy, as well as the spectral barycenter, moves away from the material's k-edge, leading to reduced mass attenuation and decreased CT values. This effect is different for materials such as iodinated CM (k-edge at 33 keV) because the mean energies of typical X-ray spectra are already beyond that energy.

Material quantification for concentrations down to 0.125 mg/mL holmium was shown for all investigated tube voltage combinations and both evaluated dose levels. In the given experiment, a third-generation dual- source CT scanner was used. This scanner provides additional tube filtration to some tube voltages, which generally improves the spectral separation of dual-energy CT [255]. This option might not be available on all scanners, though. However, it was shown that a tube voltage combination of 80/140 kV could also be used to achieve an acceptable quantification of holmium solutions.

Measurements on three adult female NZW rabbits with subcutaneous VX-2 tumors, which were intratumorally injected with radioactive ^{166}HoMS and imaged post-mortem, demonstrated DECT-based holmium quantification in a scenario that is much closer to clinical reality. Using parameters identical to the calibration scans, the measured amounts of holmium corresponded well with the known injected amount of holmium with a maximum deviation of 11.7%. Hypothetically, in a patient case where a tumor is injected with radioactive microspheres, the quantification is as follows: using the material decomposition method, the amount of holmium in mg per voxel can be calculated, with the known activity per mg at a certain

timestamp given by the company in which the exact amount of activity at time-of-injection can be calculated. The last step is the conversion of an activity map (in MBq) to a dose map (in Gy) which can be realized by using a Monte Carlo–based dose point kernel, which is available in dose evaluation software packages. The dose point kernel takes into account the different radiation types (energies and particles), tissue characteristics, and the volume in which the energy is absorbed. This allows for the evaluation of the absorbed dose distribution on the tumor and can be related to follow-up to tumor-response.

The observation of the characteristic mass attenuation behavior with regard to the photon's energies would facilitate K-edge-sensitive imaging for either dual- or even multi-energetic applications. This could potentially be used for simultaneous imaging of a patient's vascularization and local accumulations of HoMS in tumorous regions within a single CT scan by virtually removing or quantifying one of the materials as shown in Figs. 5 and 6.

Impaired quality of the material separation that was found is largely a consequence of the experimental setup itself. The axial cross-sections of the investigated rabbits were rather elliptical, and the CT scanner did not correct for this shape with adaptive beam shaping. Additionally, the animals were partially frozen resulting in local changes of tissue densities leading to slightly deficiently determined soft tissue base material vectors. In our example, some tumor parts were not detected because of present partial volume effects as well as blooming artifacts caused by adjacent body materials (here: air and bone). In addition, the detection was sub-optimal because third base materials are interpreted as a linear combination of the selected two base material vectors. This limitation could be overcome by extending the amount of applied or resolved X-ray spectra and by adding a third material to the equation, as it can be done using alternative spectral CT technologies such as photon counting detectors (PCD) [70, 318]. Investigating the quantification capability and robustness against clinically realistic artifacts that are per se inherent to a two material separation algorithm using a PCD-CT scanner is considered the next step in holmium microsphere imaging.

In conclusion, the first phantom and *ex vivo* holmium DECT data presented in this paper clearly show the feasibility to detect and quantify concentrations of holmium microspheres. This could lead potentially to the increased clinical utility of DECT imaging for dose verification during and after holmium microspheres internal radiation therapy.

Acknowledgements: The study was supported by Quirem Medical B.V. (Deventer, Netherlands) and Siemens Healthcare GmbH (Forchheim, Germany).

Funding Information: The study was supported by Quirem Medical B.V. (Deventer, Netherlands) and Siemens Healthcare GmbH (Forchheim, Germany).

Compliance with ethical standards

Guarantor: The scientific guarantor of this publication is Frank Nijsen, Radboudumc; frank.nijsen@radboudumc.nl.

Conflict of interests: The authors of this manuscript declare relationships with the following companies: Mr. Ralf Gutjahr and Dr. Bernhard Schmidt are employees of Siemens Healthcare GmbH. R.C. Bakker is funded by the Dutch Cancer Society research grant: 2014-7075 Mr. Feiko Tiessens is an employee of Quirem Medical B.V. J.F.W. Nijsen is the inventor on the patents on and related to the holmium microspheres which are assigned to University Medical Center Utrecht Holding B.V. and/or Quirem Medical (patent families: USA Patent No. 6,373,068 B1, PCT/NL03/00485, EP07112807.8, 10190254.2, P114198PC00, P112614NL00). He is co-founder and chief scientific officer of Quirem Medical and has a minority share in the company Quirem Medical. The activities of J. F.W. Nijsen within Quirem Medical are approved and supported by Dirkjan Masman (Director Technology Transfer Office Radboudumc) and Mathias Prokop (Head of the Department of Medical Imaging at Radboudumc). The Department of Radiology and Nuclear Medicine of the UMC Utrecht receives royalties from Quirem Medical B.V.

Statistics and biometry: This is an observational/experimental study so this is not applicable. No complex statistical methods were necessary for this paper.

Inform consent: Approval from the institutional animal care committee was obtained. All experiments were performed in conduct with "The Netherlands Experiments on Animals Act (1977)" and "The European Convention for the Protection of Vertebrate Animals used for Experimental Purposes (Strasbourg, 18.III.1986)". Approval was obtained from the Utrecht University Animal Experiments Committee (DEC 2011.III.08.080).

Ethical approval: Institutional Review Board approval was obtained. All experiments were performed in conduct with "The Netherlands Experiments on Animals Act (1977)" and "The European Convention for the Protection of Vertebrate Animals used for Experimental Purposes (Strasbourg, 18.III.1986)". Approval was obtained from the Utrecht University Animal Experiments Committee (DEC 2011.III.08.080)..

Methodology: Observational/experimental.

Publisher's note: Springer Nature remains neutral with regard to jurisdictional claims in published maps and institutional affiliations.

9.5 References

[9] R. E. Alvarez and A. Macovski. "Energy-selective reconstructions in x-ray computerised tomography". In: *Physics in Medicine & Biology* 21.5 (1976), p. 733

[15] R. C. Bakker, R. J. van Es, A. J. Rosenberg, S. A. van Nimwegen, R. Bastiaannet, H. W. de Jong, J. F. Nijsen, and M. G. Lam. "Intratumoral injection of radioactive holmium-166 microspheres in recurrent head and neck squamous cell carcinoma". In: *Nuclear Medicine Communications* (Jan. 2018), p. 1

[26] T. Bongartz, K. N. Glazebrook, S. J. Kavros, N. S. Murthy, S. P. Merry, W. B. Franz, C. J. Michet, B. M. A. Veetil, J. M. Davis, T. G. Mason, et al. “Dual-energy CT for the diagnosis of gout: an accuracy and diagnostic yield study”. In: *Annals of the Rheumatic Diseases* 74.6 (2015), pp. 1072–1077

[49] C. A. Coursey, R. C. Nelson, D. T. Boll, E. K. Paulson, L. M. Ho, A. M. Neville, D. Marin, R. T. Gupta, and S. T. Schindera. “Dual-energy multidetector CT: how does it work, what can it tell us, and when can we use it in abdominopelvic imaging?” In: *Radiographics* 30.4 (2010), pp. 1037–1055

[55] G. Di Chiro, R. A. Brooks, R. M. Kessler, G. S. Johnston, A. E. Jones, J. R. Herdt, and W. T. Sheridan. “Tissue signatures with dual-energy computed tomography”. In: *Radiology* 131.2 (1979), pp. 521–523

[70] S. Faby, J. Maier, S. Sawall, D. Simons, H.-P. Schlemmer, M. Lell, and M. Kachelrieß. “An efficient computational approach to model statistical correlations in photon counting x-ray detectors”. In: *Medical Physics* 43.7 (2016), pp. 3945–3960

[91] T. Fukuda, Y. Umezawa, A. Asahina, H. Nakagawa, K. Furuya, and K. Fukuda. “Dual energy CT iodine map for delineating inflammation of inflammatory arthritis”. In: *European Radiology* 27.12 (2017), pp. 5034–5040

[94] H. K. Genant and D. Boyd. “Quantitative bone mineral analysis using dual energy computed tomography.” In: *Investigative Radiology* 12.6 (1977), pp. 545–551

[102] A. Graser, T. R. Johnson, M. Bader, M. Staehler, N. Haseke, K. Nikolaou, M. F. Reiser, C. G. Stief, and C. R. Becker. “Dual energy CT characterization of urinary calculi: initial in vitro and clinical experience”. In: *Investigative Radiology* 43.2 (2008), pp. 112–119

[148] T. R. Johnson, B. Krauss, M. Sedlmair, M. Grasruck, H. Bruder, D. Morhard, C. Fink, S. Weckbach, M. Lenhard, B. Schmidt, et al. “Material differentiation by dual energy CT: initial experience”. In: *European Radiology* 17.6 (2007), pp. 1510–1517

[164] F. Kelcz, P. M. Joseph, and S. K. Hilal. “Noise considerations in dual energy CT scanning”. In: *Medical Physics* 6.5 (1979), pp. 418–425

[187] Y Li, G Shi, S Wang, S Wang, and R Wu. “Iodine quantification with dual-energy CT: phantom study and preliminary experience with VX2 residual tumour in rabbits after radiofrequency ablation”. In: *British Journal of Radiology* 86.1029 (2013), p. 20130143

[189] X. Liu, L. Yu, A. N. Primak, and C. H. McCollough. “Quantitative imaging of element composition and mass fraction using dual-energy CT: three-material decomposition”. In: *Medical Physics* 36.5 (2009), pp. 1602–1609

[190] G. H. van de Maat, P. R. Seevinck, M. Elschot, M. L. Smits, H. de Leeuw, A. D. van het Schip, M. A. Vente, B. A. Zonnenberg, H. W. de Jong, M. G. Lam, et al. “MRI-based biodistribution assessment of holmium-166 poly (L-lactic acid) microspheres after radioembolisation”. In: *European Radiology* 23.3 (2013), pp. 827–835

[204] W. D. McDavid, R. G. Waggener, M. J. Dennis, V. J. Sank, and W. H. Payne. “Estimation of chemical composition and density from computed tomography carried out at a number of energies.” In: *Investigative Radiology* 12.2 (1977), pp. 189–194

[207] M. R. Millner, W. D. McDavid, R. G. Waggener, M. J. Dennis, W. H. Payne, and V. J. Sank. “Extraction of information from CT scans at different energies”. In: *Medical Physics* 6.1 (1979), pp. 70–71

[225] J. F. Nijsen, G. Cornelis Krijger, and A. Dirk van het Schip. “The bright future of radionuclides for cancer therapy”. In: *Anti-Cancer Agents in Medicinal Chemistry* 7.3 (2007), pp. 271–290

[226] J. F. Nijsen, J.-H. Seppenwoolde, T. Havenith, C. Bos, C. J. Bakker, and A. D. van het Schip. “Liver tumors: MR imaging of radioactive holmium microspheres—phantom and rabbit study”. In: *Radiology* 231.2 (2004), pp. 491–499

[227] S. A. van Nimwegen, R. C. Bakker, J. Kirpensteijn, R. J. J. van Es, R. Koole, M. G. E. H. Lam, J. W. Hesselink, and J. F. W. Nijsen. “Intratumoral injection of radioactive holmium (166 Ho) microspheres for treatment of oral squamous cell carcinoma in cats”. In: *Veterinary and Comparative Oncology* 16.1 (2017), pp. 114–124

[238] G. J. Pelgrim, R. W. van Hamersvelt, M. J. Willemink, B. T. Schmidt, T. G. Flohr, A. Schilham, J. Milles, M. Oudkerk, T. Leiner, and R. Vliegenthart. “Accuracy of iodine quantification using dual energy CT in latest generation dual source and dual layer CT”. in: *European Radiology* 27.9 (2017), pp. 3904–3912

[254] A. N. Primak, J. G. Fletcher, T. J. Vrtiska, O. P. Dzyubak, J. C. Lieske, M. E. Jackson, J. C. Williams Jr, and C. H. McCollough. “Noninvasive differentiation of uric acid versus non–uric acid kidney stones using dual-energy CT”. in: *Academic Radiology* 14.12 (2007), pp. 1441–1447

[255] A. N. Primak, J. C. R. Giraldo, C. D. Eusemann, B. Schmidt, B. Kantor, J. G. Fletcher, and C. H. McCollough. “Dual-source dual-energy CT with additional tin filtration: Dose and image quality evaluation in phantoms and in-vivo”. In: *American Journal of Roentgenology* 195.5 (2010), p. 1164

[266] A. J. Reimann, D. Rinck, A. Birinci-Aydogan, M. Scheuering, C. Burgstahler, S. Schroeder, H. Brodoefel, I. Tsiflikas, T. Herberts, T. G. Flohr, et al. “Dual-source computed tomography: advances of improved temporal resolution in coronary plaque imaging”. In: *Investigative Radiology* 42.3 (2007), pp. 196–203

[278] R. Rutherford, B. Pullan, and I Isherwood. “Measurement of effective atomic number and electron density using an EMI scanner”. In: *Neuroradiology* 11.1 (1976), pp. 15–21

[294] P. R. Seevinck, J.-H. Seppenwoolde, T. C. de Wit, W Nijsen, F Johannes, F. J. Beekman, A. D. van het Schip, G Bakker, and J Chris. “Factors affecting the sensitivity and detection limits of MRI, CT, and SPECT for multimodal diagnostic and therapeutic agents”. In: *Anti-Cancer Agents in Medicinal Chemistry* 7.3 (2007), pp. 317–334

[296] J.-H. Seppenwoolde, J. F. Nijsen, L. W. Bartels, S. W. Zielhuis, A. D. van het Schip, and C. J. Bakker. “Internal radiation therapy of liver tumors: Qualitative and quantitative magnetic resonance imaging of the biodistribution of holmium-loaded microspheres in animal models”. In: *Magnetic Resonance in Medicine* 53.1 (2005), pp. 76–84

[308] Siemens Healthcare GmbH. *syngoCT Postprocessing applications - Instructions for Use - syngoCT Workplace syngo CT VB20*. 2017

[312] M. L. Smits, M. Elschot, M. A. van den Bosch, G. H. van de Maat, A. D. van het Schip, B. A. Zonnenberg, P. R. Seevinck, H. M. Verkooijen, C. J. Bakker, H. W. de Jong, M. G. Lam, and J. F. Nijsen. “In vivo dosimetry based on SPECT and MR imaging of 166Ho-microspheres for treatment of liver malignancies”. In: *Journal of Nuclear Medicine* 54.12 (2013), pp. 2093–2100

[344] “Weighted FBP—a Simple Approximate 3D FBP Algorithm for Multislice Spiral CT With Good Dose Usage for Arbitrary Pitch”. In: *Physics in Medicine and Biology* 49.11 (2004), p. 2209

[318] R. Symons, T. E. Cork, M. N. Lakshmanan, R. Evers, C. Davies-Venn, K. A. Rice, M. L. Thomas, C.-Y. Liu, S. Kappler, S. Ulzheimer, et al. “Dual-contrast agent photon-counting computed tomography of the heart: initial experience”. In: *The International Journal of Cardiovascular Imaging* 33.8 (2017), pp. 1253–1261

[351] C.-b. Yang, S. Zhang, Y.-j. Jia, Y. Yu, H.-f. Duan, X.-r. Zhang, G.-m. Ma, C. Ren, and N. Yu. “Dual energy spectral CT imaging for the evaluation of small hepatocellular carcinoma microvascular invasion”. In: *European Journal of Radiology* 95 (2017), pp. 222–227

[353] B. M. Yeh, J. A. Shepherd, Z. J. Wang, H. S. Teh, R. Hartman, and S. Prevrhal. “Dual energy and low kVp CT in the abdomen”. In: *American Journal of Roentgenology* 193.1 (2009), p. 47

Part III

Conclusion and outlook

10 Conclusion and outlook

In conclusion, this thesis provided an in-depth introduction to the history of X-ray and CT, giving a comprehensive overview of CT imaging. This included a detailed discussion of CT geometry, various CT detector technologies, and X-ray generation. Additionally, the most relevant X-ray photon interactions were explored, and the concept of attenuation was explained.

The investigation of several techniques for acquiring spectrally sensitive CT images was an essential aspect of the thesis. The processing of energy selective CT images, both in image-space and projection-space, was discussed to support a better understanding of their function, their computation and their practical applications. Additionally, the thesis presented a wide range of clinical applications for energy selective CT imaging, highlighting the evolution of the field and elaborating on current state-of-the-art approaches.

The significant scientific contributions presented in this thesis include the first CT measurements of a human subject using a pre-clinical photon-counting CT scanner in a clinical setting. The evaluation of image quality, as well as the potential for radiation dose and contrast dose reduction, facilitated comparisons between the PCD CT system and conventional CT systems.

The thesis also demonstrated the feasibility of assessing perfusion and ventilation imaging in a rabbit model using data from a PCD CT scanner, showcasing the potential for functional imaging with application of multiple contrast agents. Furthermore, various evaluations to differentiate kidney stones based on their morphology and composition were reported on.

Another substantial achievement highlighted in the thesis was the application of quantitative evaluations to determine local concentrations of holmium microspheres, facilitating CT dosimetry in SIRT procedures, which may result in improving the precision and accuracy of these treatments.

Ultimately, the findings of this thesis helped to address the questions posed at the beginning of this work:

- **Performance assessment: How does PCD CT compare against other spectral CT imaging techniques?**
  Classifying the performance of new PCD-based CT scanners, especially in comparison to existing technologies, has been and continues to be one of the most important steps in determining their significance for the clinical practice. In this context, thorough evaluations regarding image quality, efficient use of radiation dose, and the level of reliability for consistent results across a wide range of typical diagnostic questions are crucial.

Addressing these aspects was the primary objective of this thesis. An important step was achieved with the first scan of a human subject on a near-clinical PCD CT system in a clinical environment, demonstrating the system's ability to cope with high photon flux rates. Direct comparisons with energy-integrating detector-based CT systems revealed the superior iodine CNR particularly for higher tube potentials, which becomes particularly advantageous in low signal conditions, such as during measurements of heavier patients or low dose scans. The effects on spectral sensitivity when measuring objects of different sizes were carefully evaluated with measurements of representative phantoms. Additionally, it was demonstrated that decreased blooming in high-energy bin images facilitates the assessment of low contrast regions near dense structures. Qualitative evaluations affirmed non-inferiority (e.g. in the differentiation of uric acid-kidney stones and non-uric acid-based kidney stones) and superiority (e.g. with increased CNR values particularly for large patients) for qualitative and quantitative assessments, even for early prototype PCD CT systems with limited measurement fields and constrained detector pixel readout modes. Ultimately, the presented work contributed to the acceptance and further development of this new technology.

- **Which practical benefits come with the use of PCD CT? How can the unique characteristics of this technology be successfully exploited?**
  With the confirmation that PCDs are clinically competitive, it became natural to further foster and evaluate the quality of existing applications using image information from such a CT system. A significant portion of this thesis is dedicated to this evaluation. The assessment of kidney stones in terms of morphology and mineral composition was addressed, along with the ability to differentiate between various stone types — a clinically decisive aspect when determining appropriate therapy. Lung ventilation was assessed by using xenon gas. Simultaneously, and with the same animal model, a virtual separation of gadolinium and soft tissue was performed to assess the object's vasculature. Virtual non-contrast images were calculated, which eventually omit the need for true non-contrast scans and therefore contribute to the saving of radiation dose. As every PCD CT scan is inherently spectrally sensitive, there is no need to decide before the scan whether spectrally processed images are needed or not. Further, spectral processing can aid in standardizing CT images, as traditional non-spectral and polychromatic images could be replaced by beam hardening-free, highly quantitative VMIs. Optimizing the spectral sensitivity of a PCD CT scanner, in terms of the selection of the X-ray spectra and application-specific energy thresholds for given body materials and/or (a combination of) contrast media, remains subject of ongoing investigations [106, 186, 343, 359]. Further endeavors on improving the intrinsic spectral sensitivity of PCDs encompass the use of spectral shaping filters (e.g. by using thin plates of hafnium [246, 247, 248, 249, 250, 299]) and the implementation of probabilistic detection methods, as currently only used in the field of high-energy physics, to compensate for spectrally deteriorating effects like charge sharing [169, 171, 364].

- **Which possible new applications could energy-selective CT bring?**
  Energy-selective high-resolution CT has the potential to introduce several new applications to improve and enhance clinical diagnosis and treatment planning.

  In radiooncology, energy-selective CT can potentially exploit contrast media and their enhancement patterns as biomarkers to assess tumor response to treatment and to

monitor disease progression [92]. The increased fidelity in the separation of effective atomic number and local density enabled by PCD CT also proves to be valuable in particle therapy. This could help improve treatment planning and dose distribution by accounting for tissue heterogeneity more accurately [269].

K-edge imaging takes advantage of the unique energy-dependent absorption characteristics of materials with a K-edge in the relevant energy range of CT, such as alternative high-Z contrast agents. Energy-selective CT with other contrast agents than iodine can enhance the diagnostic quality of CCTA e.g. by better detecting and characterizing calcifications associated with atherosclerosis [150]. This has been demonstrated by using bismuth and tungsten, which have been shown to be better separable from calcium, than iodine-based contrast agents. However, for an actual clinical implementation, certain qualities of the new contrast media must be ensured: biocompatibility, low toxicity, appropriate osmolality, viscosity, particle size, and density.

In-vivo dosimetry, which involves the quantification of activated materials, can benefit significantly from the high spatio-temporal resolution of PCD CT, compared to conventional CT systems. The current challenge lies in transferring the findings of quantifying holmium in an animal model to a human model. This could enable more accurate dose estimations and treatment planning in targeted therapies like SIRT.

The use of multiple contrast media in energy-selective CT has shown promise in experimental setups. However, to make this approach clinically viable, it is crucial to optimize and match the injection patterns and scan timings. As contrast dynamics vary strongly between patients, it is crucial to maintain practicability for such approaches, when applied in real patients.

Lastly, the potential of energy-selective CT for improved resolution and dose efficiency could be further enhanced by incorporating advanced (e.g. AI/DL-based) iterative reconstruction techniques. This can yield to an improved image quality, reduced noise, and optimized dose management in the clinical use.

PCD CT, although subject of research for a long time already, is only at the beginning of its actual application. It remains to be seen whether it will promote the use and acceptance of spectral CT imaging and whether it lives up to the FDA's declaration of the first commercial PCD based CT scanner as the "first major imaging device advancement for computed tomography in nearly a decade." [72] The evidence presented to date is promising.

List of Figures

List of Tables

Bibliography

[1] O. M. Abdel-Rahman and Z. Elsayed. “Yttrium-90 microsphere radioembolisation for unresectable hepatocellular carcinoma”. In: *Cochrane Library* (2016).

[2] I. information for the decisions ahead. “2022 CT Market Outlook Report”. In: *Science and Medicine Group* (2022).

[3] M. H. Albrecht, T. J. Vogl, S. S. Martin, J. W. Nance, T. M. Duguay, J. L. Wichmann, C. N. De Cecco, A. Varga-Szemes, M. van Assen, C. Tesche, et al. “Review of clinical applications for virtual monoenergetic dual-energy CT”. In: *Radiology* 293.2 (2019), pp. 260–271.

[4] A. M. Alessio and L. R. MacDonald. “Quantitative material characterization from multi-energy photon counting CT”. In: *Medical Physics* 40.3 (2013), p. 031108.

[5] I. T. Ali, W. D. Wong, T. Liang, F. Khosa, M. Mian, S. Jalal, and S. Nicolaou. “Clinical Utility of Dual-Energy CT Analysis of Bone Marrow Edema in Acute Wrist Fractures”. In: *American Journal of Roentgenology* 210.4 (2018), pp. 842–847.

[6] T. Allmendinger, T. Nowak, T. G. Flohr, E. Klotz, J. Hagenauer, H. Alkadhi, and B. Schmidt. “Photon-counting detector CT-based vascular calcium removal algorithm: assessment using a cardiac motion phantom”. In: *Investigative Radiology* 57.6 (2022), pp. 399–405.

[7] A. Altman and R. Carmi. “TU-E-210A-03: a double-layer detector, dual-energy CT—principles, advantages and applications”. In: *Medical Physics* 36.6 Part 24 (2009), pp. 2750–2750.

[8] R. E. Alvarez. “Dimensionality and noise in energy selective x-ray imaging”. In: *Medical Physics* 40.11 (2013), p. 111909.

[9] R. E. Alvarez and A. Macovski. “Energy-selective reconstructions in x-ray computerised tomography”. In: *Physics in Medicine & Biology* 21.5 (1976), p. 733.

[10] C. Amato, L. Klein, E. Wehrse, L. T. Rotkopf, S. Sawall, J. Maier, C. H. Ziener, H.-P. Schlemmer, and M. Kachelriess. “Potential of Contrast Agents Based on High-Z Elements for Contrast-Enhanced Photon-Counting Computed Tomography”. In: *Medical Physics* (2020).

[11] M. Andreucci, R. Solomon, and A. Tasanarong. “Side effects of radiographic contrast media: pathogenesis, risk factors, and prevention”. In: *BioMed Research International* 2014 (2014).

[12] H. Atak and P. M. Shikhaliev. “Photon counting x-ray imaging with K-edge filtered x-rays: A simulation study”. In: *Medical Physics* 43.3 (2016), pp. 1385–1400.

[13] B. Aydogan, J. Li, T. Rajh, A. Chaudhary, S. J. Chmura, C. Pelizzari, C. Wietholt, M. Kurtoglu, and P. Redmond. “AuNP-DG: deoxyglucose-labeled gold nanoparticles as X-ray computed tomography contrast agents for cancer imaging”. In: *Molecular imaging and biology* 12 (2010), pp. 463–467.

[14] H. Baker. “Historical vignette: introduction of computed tomography in North America.” In: *American Journal of Neuroradiology* 14.2 (1993), pp. 283–287.

[15] R. C. Bakker, R. J. van Es, A. J. Rosenberg, S. A. van Nimwegen, R. Bastiaannet, H. W. de Jong, J. F. Nijsen, and M. G. Lam. “Intratumoral injection of radioactive holmium-166 microspheres in recurrent head and neck squamous cell carcinoma”. In: *Nuclear Medicine Communications* (Jan. 2018), p. 1.

[16] R Ballabriga, M Campbell, E Heijne, X Llopart, L Tlustos, and W. Wong. “Medipix3: A 64 k pixel detector readout chip working in single photon counting mode with improved spectrometric performance”. In: *Nuclear Instruments and Methods in Physics Research Section A: Accelerators, Spectrometers, Detectors and Associated Equipment* 633 (2011), S15–S18.

[17] F. Bamberg, A. Dierks, K. Nikolaou, M. F. Reiser, C. R. Becker, and T. R. Johnson. “Metal artifact reduction by dual energy computed tomography using monoenergetic extrapolation”. In: *European Radiology* 21.7 (2011), pp. 1424–1429.

[18] W. C. Barber, E. Nygard, J. S. Iwanczyk, M. Zhang, E. C. Frey, B. M. Tsui, J. C. Wessel, N. Malakhov, G. Wawrzyniak, N. E. Hartsough, et al. “Characterization of a novel photon counting detector for clinical CT: count rate, energy resolution, and noise performance”. In: *International Society for Optics and Photonics Medical Imaging*. International Society for Optics and Photonics. 2009, pp. 725824–725824.

[19] B. Barrett and E. Carlisle. “Metaanalysis of the relative nephrotoxicity of high-and low-osmolality iodinated contrast media.” In: *Radiology* 188.1 (1993), pp. 171–178.

[20] M. Baumann, M. Krause, J. Overgaard, J. Debus, S. M. Bentzen, J. Daartz, C. Richter, D. Zips, and T. Bortfeld. “Radiation oncology in the era of precision medicine”. In: *Nature Reviews Cancer* 16.4 (2016), pp. 234–249.

[21] E. C. Beckmann. “CT scanning the early days”. In: *British Journal of Radiology* (2014).

[22] N. Berger, M. Marcon, J. Wieler, D. Vorburger, K. J. Dedes, T. Frauenfelder, Z. Varga, and A. Boss. “Contrast Media-Enhanced Breast Computed Tomography With a Photon-Counting Detector: Initial Experiences on In Vivo Image Quality and Correlation to Histology.” In: *Investigative Radiology* (2022).

[23] J. Beutel, H. L. Kundel, Y. Kim, R. L. Van Metter, and S. C. Horii. *Handbook of medical imaging*. Vol. 3. Spie Press, 2000.

[24] M. Biondi, E. Vanzi, G. De Otto, F. Banci Buonamici, G. M. Belmonte, L. N. Mazzoni, A. Guasti, S. F. Carbone, M. A. Mazzei, A. La Penna, E. Fodera, D. Guerreri, A. Maiolino, and L. Volterrani. “Water/cortical bone decomposition: A new approach in dual energy CT imaging for bone marrow oedema detection. A feasibility study”. In: *Phys Med* 32.12 (2016), pp. 1712–1716.

[25] K Boedeker. “AiCE deep learning reconstruction: bringing the power of ultra-high resolution ct to routine imaging”. In: *Canon Medical Systems Corporation* (2019).

[26] T. Bongartz, K. N. Glazebrook, S. J. Kavros, N. S. Murthy, S. P. Merry, W. B. Franz, C. J. Michet, B. M. A. Veetil, J. M. Davis, T. G. Mason, et al. “Dual-energy CT for the diagnosis of gout: an accuracy and diagnostic yield study”. In: *Annals of the Rheumatic Diseases* 74.6 (2015), pp. 1072–1077.

[27] E. Boote, G. Fent, V. Kattumuri, S. Casteel, K. Katti, N. Chanda, R. Kannan, K. Katti, and R. Churchill. “Gold nanoparticle contrast in a phantom and juvenile swine: models for molecular imaging of human organs using x-ray computed tomography”. In: *Academic Radiology* 17.4 (2010), pp. 410–417.

[28] F. Bouazza, A. Poncelet, C. A. Garcia, P. Delatte, J. L. Engelhom, M. G. Galdon, A. Deleporte, A. Hendlisz, B. Vanderlinden, P. Flamen, et al. “Radioembolisation and portal vein embolization before resection of large hepatocellular carcinoma”. In: *World Journal of Gastroenterology* 21.32 (2015), p. 9666.

[29] D. P. Boyd and M. J. Lipton. “Cardiac computed tomography”. In: *Proceedings of the IEEE* 71.3 (1983), pp. 298–307.

[30] J. Brice. *Radiologists address high expectations for kidney stone evaluations*. https://www.diagnosticimaging.com/view/radiologists-address-high-expectations-kidney-stone-evaluations. (Accessed on 01/06/2009). May 2009.

[31] R. Brooks and G Di Chiro. "Split-detector computed tomography: a preliminary report." In: *Radiology* 126.1 (1978), pp. 255–257.

[32] R. A. Brooks. "A quantitative theory of the Hounsfield unit and its application to dual energy scanning." In: *Journal of computer assisted tomography* 1.4 (1977), pp. 487–493.

[33] R. A. Brooks and G. Di Chiro. "Beam hardening in x-ray reconstructive tomography". In: *Physics in Medicine and Biology* 21.3 (1976), p. 390.

[34] B. Buerke, G. Wittkamp, H. Seifarth, W. Heindel, and S. P. Kloska. "Dual-energy CTA with bone removal for transcranial arteries: intraindividual comparison with standard CTA without bone removal and TOF-MRA". In: *Academic Radiology* 16.11 (2009), pp. 1348–1355.

[35] J. T. Bushberg and J. M. Boone. *The essential physics of medical imaging*. Lippincott Williams & Wilkins, 2011.

[36] J. Butzer, A. Butler, P. Butler, P. Bones, N Cook, and L Tlustos. "Medipix imaging-evaluation of datasets with PCA". In: *2008 23rd International Conference Image and Vision Computing New Zealand*. IEEE. 2008, pp. 1–6.

[37] R. Cahn, B Cederström, M. Danielsson, A Hall, M Lundqvist, and D Nygren. "Detective quantum efficiency dependence on x-ray energy weighting in mammography". In: *Medical Physics* 26.12 (1999), pp. 2680–2683.

[38] Q.-Y. Cai, S. H. Kim, K. S. Choi, S. Y. Kim, S. J. Byun, K. W. Kim, S. H. Park, S. K. Juhng, and K.-H. Yoon. "Colloidal gold nanoparticles as a blood-pool contrast agent for X-ray computed tomography in mice". In: *Investigative Radiology* 42.12 (2007), pp. 797–806.

[39] W. Cai and H. Yoshida. "Electronic cleansing in CT colonography: past, present, and future". In: *Virtual Colonoscopy and Abdominal Imaging. Computational Challenges and Clinical Opportunities: Second International Workshop, Held in Conjunction with MICCAI 2010, Beijing, China, September 20, 2010, Revised Selected Papers 2*. Springer. 2011, pp. 1–8.

[40] J. X. Cao, Y. M. Wang, X. Q. Kong, C. Yang, and P. Wang. "Good interrater reliability of a new grading system in detecting traumatic bone marrow lesions in the knee by dual energy CT virtual non-calcium images". In: *European Journal of Radiology* 84.6 (2015), pp. 1109–15.

[41] D. Cester, M. Eberhard, H. Alkadhi, and A. Euler. "Virtual monoenergetic images from dual-energy CT: systematic assessment of task-based image quality performance". In: *Quantitative Imaging in Medicine and Surgery* 12.1 (2022), p. 726.

[42] E. J. Chae, J. B. Seo, J. Lee, N. Kim, H. W. Goo, H. J. Lee, C. W. Lee, S. W. Ra, Y.-M. Oh, and Y. S. Cho. "Xenon ventilation imaging using dual-energy computed tomography in asthmatics: initial experience". In: *Investigative Radiology* 45.6 (2010), pp. 354–361.

[43] H.-M. Cho, W. C. Barber, H. Ding, J. S. Iwanczyk, and S. Molloi. "Characteristic performance evaluation of a photon counting Si strip detector for low dose spectral breast CT imaging". In: *Medical Physics* 41.9 (2014), p. 091903.

[44] J. A. Christner, K. Stierstorfer, A. N. Primak, C. D. Eusemann, T. G. Flohr, and C. H. McCollough. "Evaluation of-axis resolution and image noise for nonconstant velocity spiral CT data reconstructed using a weighted 3D filtered backprojection (WFBP) reconstruction algorithm". In: *Medical Physics* 37.2 (2010), pp. 897–906.

[45] A. M. Cormack. "Representation of a function by its line integrals, with some radiological applications". In: *Journal of applied physics* 34.9 (1963), pp. 2722–2727.

[46] A. M. Cormack. "Representation of a function by its line integrals, with some radiological applications. II". In: *Journal of Applied Physics* 35.10 (1964), pp. 2908–2913.

[47] D. P. Cormode, E. Roessl, A. Thran, T. Skajaa, R. E. Gordon, J.-P. Schlomka, V. Fuster, E. A. Fisher, W. J. Mulder, R. Proksa, et al. “Atherosclerotic plaque composition: analysis with multicolor CT and targeted gold nanoparticles 1”. In: *Radiology* 256.3 (2010), pp. 774–782.

[48] D. P. Cormode, S. Si-Mohamed, D. Bar-Ness, M. Sigovan, P. C. Naha, J. Balegamire, F. Lavenne, P. Coulon, E. Roessl, M. Bartels, et al. “Multicolor spectral photon-counting computed tomography: in vivo dual contrast imaging with a high count rate scanner”. In: *Scientific reports* 7.1 (2017), pp. 1–11.

[49] C. A. Coursey, R. C. Nelson, D. T. Boll, E. K. Paulson, L. M. Ho, A. M. Neville, D. Marin, R. T. Gupta, and S. T. Schindera. “Dual-energy multidetector CT: how does it work, what can it tell us, and when can we use it in abdominopelvic imaging?” In: *Radiographics* 30.4 (2010), pp. 1037–1055.

[50] J. Dangelmaier, D. Bar-Ness, H. Daerr, D. Muenzel, S. Si-Mohamed, S. Ehn, A. A. Fingerle, M. A. Kimm, F. K. Kopp, L. Boussel, et al. “Experimental feasibility of spectral photon-counting computed tomography with two contrast agents for the detection of endoleaks following endovascular aortic repair”. In: *European Radiology* 28.8 (2018), pp. 3318–3325.

[51] M. Danielsson, M. Persson, and M. Sjölin. “Photon-counting x-ray detectors for CT”. In: *Physics in Medicine & Biology* 66.3 (2021), 03TR01.

[52] M. S. Davenport, M. A. Perazella, J. Yee, J. R. Dillman, D. Fine, R. J. McDonald, R. A. Rodby, C. L. Wang, and J. C. Weinreb. “Use of Intravenous Iodinated Contrast Media in Patients with Kidney Disease: Consensus Statements from the American College of Radiology and the National Kidney Foundation”. In: *Radiology* (Jan. 2020).

[53] P.-R. Derenoncourt, G. J. Felder, H. D. Royal, S. Bhalla, J. A. Lang, M. C. Matesan, and M. Itani. “Ventilation-Perfusion Scan: A Primer for Practicing Radiologists”. In: *RadioGraphics* (2021).

[54] S. Deveci, M. CoŞkun, M.
bibinitperiodI. Tekin, L. PeŞkircioglu, N. Ç. Tarhan, and H. ÖzkardeŞ. “Spiral computed tomography: role in determination of chemical compositions of pure and mixed urinary stones—an in vitro study”. In: *Urology* 64.2 (2004), pp. 237–240.

[55] G. Di Chiro, R. A. Brooks, R. M. Kessler, G. S. Johnston, A. E. Jones, J. R. Herdt, and W. T. Sheridan. “Tissue signatures with dual-energy computed tomography”. In: *Radiology* 131.2 (1979), pp. 521–523.

[56] L. D. Di Maso, J. Huang, M. F. Bassetti, L. A. DeWerd, and J. R. Miller. “Investigating a novel split-filter dual-energy CT technique for improving pancreas tumor visibility for radiation therapy”. In: *Journal of applied clinical Medical Physics* 19.5 (2018), pp. 676–683.

[57] I. M. I. Division. “2021 CT Market Outlook Report”. In: *Science and Medicine Group* (2021), p. 177.

[58] Q. Dong, D. R. Hurst, H. J. Weinmann, T. L. Chenevert, F. J. Londy, and M. R. Prince. “Magnetic resonance angiography with gadomer-17: an animal study”. In: *Investigative Radiology* 33.9 (1998), pp. 699–708.

[59] Y. C. Dong, M. Hajfathalian, P. S. Maidment, J. C. Hsu, P. C. Naha, S. Si-Mohamed, M. Breuilly, J. Kim, P. Chhour, P. Douek, et al. “Effect of gold nanoparticle size on their properties as contrast agents for computed tomography”. In: *Scientific Reports* 9.1 (2019), pp. 1–13.

[60] A. Døssing, F. C. Müller, F. Becce, L. Stamp, H. Bliddal, and M. Boesen. “Dual-Energy Computed Tomography for Detection and Characterization of Monosodium Urate, Calcium Pyrophosphate, and Hydroxyapatite: A Phantom Study on Diagnostic Performance”. In: *Investigative Radiology* (2021).

[61] X. Duan, Z. Li, L. Yu, S. Leng, A. F. Halaweish, J. G. Fletcher, and C. H. McCollough. “Characterization of urinary stone composition by use of third-generation dual-source dual-energy CT with increased spectral separation”. In: *American Journal of Roentgenology* 205.6 (2015), p. 1203.

[62] X. Duan, J. Wang, S. Leng, B. Schmidt, T. Allmendinger, K. Grant, T. G. Flohr, and C. H. McCollough. “Electronic noise in CT detectors: impact on image noise and artifacts”. In: *American Journal of Roentgenology* 201.4 (2013), W626–W632.

[63] X. Duan, J. Wang, M. Qu, S. Leng, Y. Liu, A. Krambeck, and C. H. McCollough. “Kidney stone volume estimation from computerized tomography images using a model based method of correcting for the point spread function”. In: *The Journal of Urology* 188.3 (2012), pp. 989–995.

[64] J. Endrikat, A. Michel, R. Kölbach, P. Lengsfeld, and K. Vogtländer. “Risk of Hypersensitivity Reactions to Iopromide After Intra-Arterial Versus Intravenous Administration: A Nested Case-Control Analysis of 133,331 Patients”. In: *Investigative Radiology* 55.1 (2020), pp. 38–44.

[65] A. Engström. “Quantitative micro-and histochemical elementary analysis by roentgen absorption spectrography”. In: *Acta radiologica* (1946).

[66] A. Euler, A. Parakh, A. L. Falkowski, S. Manneck, D. Dashti, B. Krauss, Z. Szucs-Farkas, and S. T. Schindera. “Initial results of a single-source dual-energy computed tomography technique using a split-filter: assessment of image quality, radiation dose, and accuracy of dual-energy applications in an in vitro and in vivo study”. In: *Investigative Radiology* 51.8 (2016), pp. 491–498.

[67] A. Euler, T. Taslimi, M. Eberhard, A. Kobe, K. Reeve, A. Zimmermann, A. Krauss, R. Gutjahr, B. Schmidt, and H. Alkadhi. “Computed Tomography Angiography of the Aorta—Optimization of Automatic Tube Voltage Selection Settings to Reduce Radiation Dose or Contrast Medium in a Prospective Randomized Trial”. In: *Investigative Radiology* 56.5 (2021), pp. 283–291.

[68] A. P. Evan, L. R. Willis, J. E. Lingeman, and J. A. McAteer. “Renal trauma and the risk of long-term complications in shock wave lithotripsy”. In: *Nephron* 78.1 (1998), pp. 1–8.

[69] S. Faby, S. Kuchenbecker, S. Sawall, D. Simons, H.-P. Schlemmer, M. Lell, and M. Kachelrieß. “Performance of today’s dual energy CT and future multi energy CT in virtual non-contrast imaging and in iodine quantification: a simulation study”. In: *Medical Physics* 42.7 (2015), pp. 4349–4366.

[70] S. Faby, J. Maier, S. Sawall, D. Simons, H.-P. Schlemmer, M. Lell, and M. Kachelrieß. “An efficient computational approach to model statistical correlations in photon counting x-ray detectors”. In: *Medical Physics* 43.7 (2016), pp. 3945–3960.

[71] F. Farhadi, P. Sahbaee, J. R. Rajagopal, M. Nikpanah, B. Saboury, R. Gutjahr, N. M. Biassou, R. Shah, T. G. Flohr, E. Samei, W. F. Pritchard, A. A. Malayeri, D. A. Bluemke, and E. C. Jones. “Virtual monoenergetic imaging in photon-counting CT of the head and neck”. In: *Clinical Imaging* (2023).

[72] FDA. *FDA Clears First Major Imaging Device Advancement for Computed Tomography in Nearly a Decade | FDA*.
urlhttps://www.fda.gov/news-events/press-announcements/fda-clears-first-major-imaging-device-advancement-computed-tomography-nearly-decade. (Accessed on 10/06/2021). 2021.

[73] J. Ferda, M. Novák, H. Mírka, J. Baxa, E. Ferdová, A. Bednářová, T. G. Flohr, B. Schmidt, E. Klotz, and B. Kreuzberg. “The assessment of intracranial bleeding with virtual unenhanced imaging by means of dual-energy CT angiography”. In: *European Radiology* 19.10 (2009), pp. 2518–2522.

[74] A. Ferrero, R. Gutjahr, A. F. Halaweish, S. Leng, and C. H. McCollough. “Characterization of Urinary Stone Composition by Use of Whole-body, Photon-counting Detector CT”. In: *Academic Radiology* 25.10 (Oct. 2018), pp. 1270–1276.

[75] A. Ferrero, R. Gutjahr, A. Henning, S. Kappler, A. F. Halaweish, D. Abdurakhimova, Z Peterson, J. Montoya, S. Leng, and C. H. McCollough. “Renal stone characterization using high resolution imaging mode on a photon counting detector CT system”. In: *SPIE Medical Imaging*. Ed. by T. G. Flohr, J. Y. Lo, and T. G. Schmidt. SPIE, 2017.

[76] S. Feuerlein, E. Roessl, R. Proksa, G. Martens, O. Klass, M. Jeltsch, V. Rasche, H.-J. Brambs, M. H. Hoffmann, and J.-P. Schlomka. “Multienergy photon-counting K-edge imaging: potential for improved luminal depiction in vascular imaging 1”. In: *Radiology* 249.3 (2008), pp. 1010–1016.

[77] A. M. Fischer, J. A. Decker, J. Schoepf, A. Varga-Szemes, T. G. Flohr, B. Schmidt, R. Gutjahr, P. Sahbaee, D. A. Giovagnoli, T. Emrich, et al. “Optimization of contrast material administration for coronary CT angiography using a software-based test-bolus evaluation algorithm”. In: *The British Journal of Radiology* 95.1133 (2022), p. 20201456.

[78] T. Flohr, K Stierstorfer, C Süss, B Schmidt, A. Primak, and C. McCollough. “Novel ultrahigh resolution data acquisition and image reconstruction for multi-detector row CT”. In: *Medical Physics* 34.5 (2007), pp. 1712–1723.

[79] T. G. Flohr, D. D. Cody, and C. H. McCollough. *Advances in Medical Physics: 2006 - Computed Tomography*. Medical Physics Publishing, 2006.

[80] T. G. Flohr, A. Küttner, H. Bruder, K. Stierstorfer, S. S. Halliburton, S. Schaller, and B. M. Ohnesorge. “Performance evaluation of a multi-slice CT system with 16-slice detector and increased gantry rotation speed for isotropic submillimeter imaging of the heart”. In: *Herz* 28.1 (2003), pp. 7–19.

[81] T. G. Flohr, C. H. McCollough, H. Bruder, M. Petersilka, K. Gruber, C. Süß, M. Grasruck, K. Stierstorfer, B. Krauss, R. Raupach, et al. “First performance evaluation of a dual-source CT (DSCT) system”. In: *European Radiology* 16.2 (2006), pp. 256–268.

[82] T. G. Flohr, M. Petersilka, A. Henning, S. Ulzheimer, J. Ferda, and B. Schmidt. “Photon-counting CT review”. In: *Physica Medica* 79 (2020), pp. 126–136.

[83] U. Food and D. Administration. *510(k) Premarket Notification - Naeotom Alpha*. "`https://www.accessdata.fda.gov/scripts/cdrh/cfdocs/cfpmn/pmn.cfm?ID=K211591`". (Accessed on 1225/2022). May 2017.

[84] T. N. Foundation. *Albert Einstein - The Nobel Price in Physics 1921*. `https://www.nobelprize.org/prizes/physics/1921/summary`. (Accessed on 01/02/2023). Nov. 2022.

[85] T. N. Foundation. *Allan M. Cormack and Godfrei N. Hounsfield - The Nobel Price in Physiology or Medicine 1979*. `https://www.nobelprize.org/prizes/medicine/1979/summary/`. (Accessed on 01/02/2023). Nov. 2022.

[86] T. N. Foundation. *Arthur Holly Compton - The Nobel Price in Physics 1927*. `https://www.nobelprize.org/prizes/physics/1927/summary/`. (Accessed on 01/02/2023). Nov. 2022.

[87] T. N. Foundation. *Lord Rayleigh - The Nobel Price in Physics 1904*. `https://www.nobelprize.org/prizes/physics/1904/strutt/facts/`. (Accessed on 01/02/2023). Nov. 2022.

[88] T. N. Foundation. *Wilhelm Conrad Röntgen - The Nobel Price in Physics 1901*. `https://www.nobelprize.org/prizes/physics/1901/summary/`. (Accessed on 01/02/2023). Nov. 2022.

[89] C. Frellesen, M. Azadegan, S. S. Martin, K. Otani, T. D’Angelo, C. Booz, K. Eichler, B. Panahi, M. Kaup, R. W. Bauer, T. J. Vogl, and J. L. Wichmann. “Dual-Energy Computed Tomography-Based Display of Bone Marrow Edema in Incidental Vertebral Compression Fractures: Diagnostic Accuracy and Characterization in Oncological Patients Undergoing Routine Staging Computed Tomography”. In: *Investigative Radiology* 53.7 (2018), pp. 409–416.

[90] T. Fuchs, M. Kachelrieß, and W. A. Kalender. “Direct comparison of a xenon and a solid-state CT detector system: measurements under working conditions”. In: *IEEE transactions on medical imaging* 19.9 (2000), pp. 941–948.

[91] T. Fukuda, Y. Umezawa, A. Asahina, H. Nakagawa, K. Furuya, and K. Fukuda. “Dual energy CT iodine map for delineating inflammation of inflammatory arthritis”. In: *European Radiology* 27.12 (2017), pp. 5034–5040.

[92] Y. Fukukura, Y. Kumagae, R. Higashi, H. Hakamada, H. Nagano, S. Hidaka, K. Kamimura, K. Maemura, S. Arima, and T. Yoshiura. “Visual enhancement pattern during the delayed phase of enhanced CT as an independent prognostic factor in stage IV pancreatic ductal adenocarcinoma”. In: *Pancreatology* 20.6 (2020), pp. 1155–1163.

[93] “Gauss–Markov Theorem”. In: *The Concise Encyclopedia of Statistics*. New York, NY: Springer New York, 2008, pp. 217–218.

[94] H. K. Genant and D. Boyd. “Quantitative bone mineral analysis using dual energy computed tomography.” In: *Investigative Radiology* 12.6 (1977), pp. 545–551.

[95] J. Giersch, D. Niederlöhner, and G. Anton. “The influence of energy weighting on X-ray imaging quality”. In: *Nuclear Instruments and Methods in Physics Research Section A: Accelerators, Spectrometers, Detectors and Associated Equipment* 531.1 (2004), pp. 68–74.

[96] P. GmbH. *IQon Spectral CT CT-Scanner*. "https://www.philips.de/healthcare/product/HC729332/iqon-spectral-ct-ct-scanner/". (Accessed on 12/10/2022). 2022.

[97] S. H. GmbH. *SOMATOM Force - Get two steps ahead with Dual Source CT*. "https://www.siemens-healthineers.com/en-us/computed-tomography/dual-source-ct/somatom-force/". (Accessed on 12/10/2022). 2020.

[98] H. W. Goo. “Initial experience of dual-energy lung perfusion CT using a dual-source CT system in children”. In: *Pediatric radiology* 40.9 (2010), pp. 1536–1544.

[99] H. W. Goo and J. M. Goo. “Dual-energy CT: new horizon in medical imaging”. In: *Korean journal of radiology* 18.4 (2017), pp. 555–569.

[100] R. Grainger. “Osmolality of intravascular radiological contrast media”. In: *British Journal of Radiology* 53.632 (1980), pp. 739–746.

[101] K. L. Grant, T. G. Flohr, B. Krauss, M. Sedlmair, C. Thomas, and B. Schmidt. “Assessment of an advanced image-based technique to calculate virtual monoenergetic computed tomographic images from a dual-energy examination to improve contrast-to-noise ratio in examinations using iodinated contrast media”. In: *Investigative Radiology* 49.9 (2014), pp. 586–592.

[102] A. Graser, T. R. Johnson, M. Bader, M. Staehler, N. Haseke, K. Nikolaou, M. F. Reiser, C. G. Stief, and C. R. Becker. “Dual energy CT characterization of urinary calculi: initial in vitro and clinical experience”. In: *Investigative Radiology* 43.2 (2008), pp. 112–119.

[103] A. Graser, T. R. Johnson, E. M. Hecht, C. R. Becker, C. Leidecker, M. Staehler, C. G. Stief, H. Hildebrandt, M. C. Godoy, M. E. Finn, et al. “Dual-energy CT in patients suspected of having renal masses: can virtual nonenhanced images replace true nonenhanced images?” In: *Radiology* 252.2 (2009), pp. 433–440.

[104] F. Grönberg, J. Lundberg, M. Sjölin, M. Persson, R. Bujila, H. Bornefalk, H. Almqvist, S. Holmin, and M. Danielsson. “Feasibility of unconstrained three-material decomposition: imaging an excised human heart using a prototype silicon photon-counting CT detector”. In: *European Radiology* 30.11 (2020), pp. 5904–5912.

[105] R. Gutjahr. “Predevelopment of Dual-Energy Algorithms for Photon Counting Detector Computed Tomography”. MA thesis. Technische Universität München - Fakultät für Informatik, 2015.

[106] R. Gutjahr. “Technical performance of the macro mode in photon counting detector CT”. In: 2nd Photon Counting Symposium (Mayo Clinic, Rochester, Minnesota, USA, Oct. 6–7, 2016). 2016.

[107] R. Gutjahr, R. C. Bakker, F. Tiessens, S. A. van Nimwegen, B. Schmidt, and J. F. W. Nijsen. “Quantitative dual-energy CT material decomposition of holmium microspheres: local concentration determination evaluated in phantoms and a rabbit tumor model”. In: *European Radiology* (2020), pp. 1–10.

[108] R. Gutjahr, J. G. Fletcher, Y. S. Lee, A. F. Halaweish, V. Suresh, N. M. Weber, T. J. Vrtiska, E. E. Williamson, B. Schmidt, and C. H. McCollough. “Individualized Delay for Abdominal Computed Tomography Angiography Bolus-Tracking Based on Sequential Monitoring: Increased Aortic Contrast Permits Decreased Injection Rate and Lower Iodine Dose”. In: *Journal of Computer Assisted Tomography* 43.4 (2019), pp. 612–618.

[109] R. Gutjahr, A. Halaweish, K. Grant, S. Kappler, Z. Yu, S. Leng, L. Yu, Z. Li, S. M. Jorgensen, E. L. Ritman, and C. McCollough. “Dose Efficiency of a Prototype, Whole-body, Photon-Counting CT System versus a Conventional CT System for Imaging of Iodinated Contrast Media”. In: Radiological Society of North America. 101st Scientific Assembly and Annual Meeting (Chicago IL, USA, Nov. 11–Dec. 4, 2015). 2015.

[110] R. Gutjahr, A. F. Halaweish, J. G. Fletcher, I Duba, Y. S. Lee, N. M. Weber, T. J. Vrtiska, E. Williamson, B. Schmidt, C. H. McCollough, et al. “Individualised delay based on sequential monitoring: increased aortic contrast permits decreased injection rate and lower iodine dose at abdominal CT angiography”. In: European Congress of Radiology-ECR 2019. 2019.

[111] R. Gutjahr, A. F. Halaweish, Z. Yu, S. Leng, L. Yu, Z. Li, S. M. Jorgensen, E. L. Ritman, S. Kappler, and C. H. McCollough. “Human Imaging With Photon Counting–Based Computed Tomography at Clinical Dose Levels: Contrast-to-Noise Ratio and Cadaver Studies”. In: *Investigative Radiology* 51.7 (2016), pp. 421–429.

[112] R. Gutjahr, T. Nowak, M. Sedlmair, H. Pietsch, B. Schmidt, T. G. Flohr, and B. Krauss. “Image-Based Multi-Material Decomposition in Photon Counting Computed Tomography”. In: *European Congress of Radiology*. 2017.

[113] R. Gutjahr, C. Polster, A. Henning, S. Kappler, S. Leng, C. H. McCollough, M. U. Sedlmair, B. Schmidt, B. Krauss, and T. G. Flohr. “Dual energy CT kidney stone differentiation in photon counting computed tomography”. In: *SPIE Medical Imaging*. Ed. by T. G. Flohr, J. Y. Lo, and T. G. Schmidt. SPIE, 2017.

[114] R. Gutjahr, C. Polster, S. Kappler, H. Pietsch, G. Jost, K. Hahn, F. Schöck, M. Sedlmair, T. Allmendinger, B. Schmidt, B. Krauss, and F. Thomas. “Material decomposition and virtual non-contrast imaging in photon counting computed tomography: an animal study”. In: *International Society for Optics and Photonics Medical Imaging*. International Society for Optics and Photonics. 2016, 97831G–97831G.

[115] R. Gutjahr, C. Polster, S. Kappler, H. Pietsch, G. Jost, K. Hahn, F. Schoeck, M. Sedlmair, T. Allmendinger, B. Schmidt, B. Krauss, and T. Flohr. “Material Decomposition and virtual non-contrast imaging in photon counting computed tomography: an animal study”. In: SPIE Medical Imaging (Orlando, Florida, USA, Mar. 2–6, 2016). 2016.

[116] R. Gutjahr, B. Schmidt, M. Sedlmair, T. Flohr, H. Pietsch, B. Krauss, and T. Nowak. “Applied quantitative multi-material decomposition using Photon Counting Detector CT (PCD-CT) image data”. In: Radiological Society of North America. 101st Scientific Assembly and Annual Meeting (Chicago IL, USA, Nov. 26–Dec. 1, 2017). 2017.

[117] R. Gutjahr, B. Schmidt, M. Sedlmair, T. Flohr, H. Pietsch, B. Krauss, and T. Nowak. “Bildbasierte Multimaterialzerlegung – Neue Kontrastmittel für die Spektrale Computertomographie”. In: 49. Jahrestagung der Deutschen Gesellschaft für Medizinische Physik (Nuremberg, Germany, Sept. 19–21, 2018). 2018.

[118] R. Gutjahr, B. Schmidt, M. Sedlmair, T. Flohr, H. Pietsch, B. Krauss, and T. Nowak. “Multi-Material Decomposition of Iodine Mixed with Potential High-Z Contrast Agents in Energy Discriminating Photon Counting Computed Tomography”. In: Radiological Society of North America. 101st Scientific Assembly and Annual Meeting (Chicago IL, USA, Nov. 26–Dec. 1, 2017). 2017.

[119] R. Gutjahr, B. Schmidt, M. Sedlmair, S. Kappler, C. Polster, T. Allmendinger, T. Flohr, and B. Krauss. “Kidney stone differentiation in photon counting computed tomography: a feasibility study”. In: European Congress of Radiology (Vienna, Austria, Mar. 2–6, 2016). 2016.

[120] F. Hagen, J. Hofmann, R. Wrazidlo, R. Gutjahr, B. Schmidt, S. Faby, K. Nikolaou, and M. Horger. "Image quality and dose exposure of contrast-enhanced abdominal CT on a 1st generation clinical dual-source photon-counting detector CT in obese patients vs. a 2nd generation dual-source dual energy integrating detector CT". In: *European Journal of Radiology* 151 (2022), p. 110325.

[121] F. Hagen, L. Walder, J. Fritz, R. Gutjahr, B. Schmidt, S. Faby, F. Bamberg, S. Schoenberg, K. Nikolaou, and M. Horger. "Image Quality and Radiation Dose of Contrast-Enhanced Chest-CT Acquired on a Clinical Photon-Counting Detector CT vs. Second-Generation Dual-Source CT in an Oncologic Cohort: Preliminary Results". In: *Tomography* 8.3 (2022), pp. 1466–1476.

[122] A. Halaweish, S. Leng, B. Krauss, M. Sedlmair, T. Nowak, R. Gutjahr, S. Kappler, B. Schmidt, E. L. Ritman, and C. McCollough. "Quantitative Multi-energy Post-processing of Whole-Body Photon-Counting Computed Tomography Data". In: 4th Workshop on Medical Applications of Spectroscopic X-ray Detectors (CERN, Geneva, Swiss, May 15–15, 2016). 2017.

[123] A. Halaweish, R. Marcus, S. Leng, B. Krauss, M. Sedlmair, T. Allmendinger, R. Gutjahr, S. Kappler, B. Schmidt, E. L. Ritman, and C. McCollough. "Advanced Spectral Analysis of Whole-Body Photon-Counting-Detector Computed Tomography Data". In: Radiological Society of North America. 101st Scientific Assembly and Annual Meeting (Chicago IL, USA, Nov. 27–Dec. 2, 2016). 2016.

[124] L.-A. Hamel and S. Paquet. "Charge transport and signal generation in CdTe pixel detectors". In: *Nuclear Instruments and Methods in Physics Research Section A: Accelerators, Spectrometers, Detectors and Associated Equipment* 380.1-2 (1996), pp. 238–240.

[125] J. A. Heanue, D. A. Pearson, and R. E. Melen. "CdZnTe detector array for a scanning-beam digital x-ray system". In: *Medical Imaging 1999: Physics of Medical Imaging*. Vol. 3659. SPIE. 1999, pp. 718–725.

[126] D Heimbach, D Jacobs, A Hesse, S. Müller, P Zhong, and G. Preminger. "How to improve lithotripsy and chemolitholysis of brushite-stones: an in vitro study". In: *Urological research* 27.4 (1999), pp. 266–271.

[127] B. J. Heismann, B. T. Schmidt, and T. G. Flohr. "Spectral computed tomography". In: SPIE Bellingham, WA. 2012.

[128] W. Hendee and E. Ritenour. *Medical Imaging Physics*. Wiley, 2003.

[129] G. Hidas, R. Eliahou, M. Duvdevani, P. Coulon, L. Lemaitre, O. N. Gofrit, D. Pode, and J. Sosna. "Determination of Renal Stone Composition with Dual-Energy CT: In Vivo Analysis and Comparison with X-ray Diffraction 1". In: *Radiology* 257.2 (2010), pp. 394–401.

[130] R. Hinzpeter, M. Eberhard, R. Gutjahr, K. Reeve, T. Pfammatter, M. Lachat, B. Schmidt, T. G. Flohr, B. Kolb, and H. Alkadhi. "CT Angiography of the Aorta: Contrast Timing by Using a Fixed versus a Patient-specific Trigger Delay". In: *Radiology* 291.2 (2019), pp. 531–538.

[131] E. A. Hoffman and D. Chon. "Computed tomography studies of lung ventilation and perfusion". In: *Proceedings of the American Thoracic Society* 2.6 (2005), pp. 492–498.

[132] F. Holmquist, M. Söderberg, U. Nyman, T. Fält, R. Siemund, and M. Geijer. "80-kVp hepatic CT to reduce contrast medium dose in azotemic patients: a feasibility study". In: *Acta Radiologica* (2019), p. 0284185119866807.

[133] G. N. Hounsfield. "Computerized transverse axial scanning (tomography): Part 1. Description of system". In: *The British Journal of Radiology* 46.552 (1973), pp. 1016–1022.

[134] J Hsieh. "TU-E-210A-01: Dual-energy CT with fast-kVp switch". In: *Medical Physics* 36.6Part24 (2009), pp. 2749–2749.

[135] J. Hsieh. "Computed tomography: principles, design, artifacts, and recent advances". In: SPIE Bellingham, WA. 2009.

[136] J. Hsieh, E. Liu, B. Nett, J. Tang, J.-B. Thibault, and S. Sahney. "A new era of image reconstruction: TrueFidelity™". In: *White Paper (JB68676XX), GE Healthcare* (2019).

[137] S. S. Hsieh, S. Leng, K. Rajendran, S. Tao, and C. H. McCollough. “Photon counting CT: clinical applications and future developments”. In: *IEEE Transactions on Radiation and Plasma Medical Sciences* (2020).

[138] J. H. Hubbell and S. M. Seltzer. *Tables of X-ray mass attenuation coefficients and mass energy-absorption coefficients 1 keV to 20 MeV for elements Z= 1 to 92 and 48 additional substances of dosimetric interest*. Tech. rep. National Institute of Standards and Technology, Gaithersburg, MD (USA), 1995.

[139] W. Huda and R. M. Slone. *Review of Radiologic Physics*. 2nd ed. High-Yield Series. Philadelphia, PA: Lippincott Williams and Wilkins, Feb. 2003.

[140] D. B. Husarik, S. Gordic, L. Desbiolles, B. Krauss, S. Leschka, S. Wildermuth, and H. Alkadhi. “Advanced virtual monoenergetic computed tomography of hyperattenuating and hypoattenuating liver lesions: ex-vivo and patient experience in various body sizes”. In: *Investigative Radiology* 50.10 (2015), pp. 695–702.

[141] I. Isherwood. “Sir Godfrey Hounsfield”. In: *Radiology* 234.3 (2005), pp. 975–976.

[142] J. S. Iwanczyk, E. Nygard, O. Meirav, J. Arenson, W. C. Barber, N. E. Hartsough, N. Malakhov, and J. C. Wessel. “Photon counting energy dispersive detector arrays for x-ray imaging”. In: *IEEE Transactions on Nuclear Science* 56.3 (2009), pp. 535–542.

[143] M. C. Jacobsen, D. Schellingerhout, C. A. Wood, E. P. Tamm, M. C. Godoy, J. Sun, and D. D. Cody. “Intermanufacturer comparison of dual-energy CT iodine quantification and monochromatic attenuation: a phantom study”. In: *Radiology* 287.1 (2018), pp. 224–234.

[144] B. Jacobson. “Dichromatic absorption radiography. Dichromography”. In: *Acta Radiologica* 39.6 (1953), pp. 437–452.

[145] L. Jans, I. De Kock, N. Herregods, K. Verstraete, F. Van den Bosch, P. Carron, E. H. Oei, D. Elewaut, and P. Jacques. “Dual-energy CT: a new imaging modality for bone marrow oedema in rheumatoid arthritis”. In: *Annals of Rheumatic Diseases* 77.6 (2018), pp. 958–960.

[146] P. C. Johns. “Photon-counting detectors for digital radiography and x-ray computed tomography”. In: *Opto-Canada: SPIE Regional Meeting on Optoelectronics, Photonics, and Imaging*. Vol. 10313. SPIE. 2017, pp. 392–394.

[147] P. Johns. “Photon-Counting Detectors for Digital Radiography and X-Ray Computed Tomography, 367–369 SPIE”. In: *TD01* (2002).

[148] T. R. Johnson, B. Krauss, M. Sedlmair, M. Grasruck, H. Bruder, D. Morhard, C. Fink, S. Weckbach, M. Lenhard, B. Schmidt, et al. “Material differentiation by dual energy CT: initial experience”. In: *European Radiology* 17.6 (2007), pp. 1510–1517.

[149] M Joshi, D. Langan, D. Sahani, A Kambadakone, S Aluri, K Procknow, X Wu, R Bhotika, D Okerlund, N Kulkarni, et al. “Effective atomic number accuracy for kidney stone characterization using spectral CT”. In: *International Society for Optics and Photonics Medical Imaging*. International Society for Optics and Photonics. 2010, 76223K–76223K.

[150] G. Jost, M. McDermott, R. Gutjahr, T. Nowak, B. Schmidt, and H. Pietsch. “New Contrast Media for K-Edge Imaging With Photon-Counting Detector CT”. In: *Investigative Radiology - Special issue 2023 - Photon counting CT* (2023), pp. 10–1097.

[151] W. A. Kalender. *Computertomographie - Grundlagen, Gerätetechnologie, Bildqualität, Anwendungen*. New York: Wiley, 2006.

[152] W. A. Kalender, W. Perman, J. Vetter, and E. Klotz. “Evaluation of a prototype dual-energy computed tomographic apparatus. I. Phantom studies”. In: *Medical Physics* 13.3 (1986), pp. 334–339.

[153] W. A. Kalender, W. Seissler, E. Klotz, and P. Vock. “Spiral volumetric CT with single-breath-hold technique, continuous transport, and continuous scanner rotation.” In: *Radiology* 176.1 (1990), pp. 181–183.

[154] A. Kambadakone, V. Baliyan, H. Kordbacheh, R. N. Uppot, A. Thabet, D. A. Gervais, and R. S. Arellano. “Imaging guided percutaneous interventions in hepatic dome lesions: Tips and tricks”. In: *World Journal of Hepatology* 9.19 (2017), p. 840.

[155] T. Kanda, T. Fukusato, M. Matsuda, K. Toyoda, H. Oba, J. Kotoku, T. Haruyama, K. Kitajima, and S. Furui. “Gadolinium-based contrast agent accumulates in the brain even in subjects without severe renal dysfunction: evaluation of autopsy brain specimens with inductively coupled plasma mass spectroscopy”. In: *Radiology* 276.1 (2015), pp. 228–232.

[156] T. Kanda, K. Ishii, H. Kawaguchi, K. Kitajima, and D. Takenaka. “High signal intensity in the dentate nucleus and globus pallidus on unenhanced T1-weighted MR images: relationship with increasing cumulative dose of a gadolinium-based contrast material”. In: *Radiology* 270.3 (2014), pp. 834–841.

[157] S Kappler, F Glasser, S Janssen, E Kraft, and M Reinwand. “A research prototype system for quantum-counting clinical CT”. In: *International Society for Optics and Photonics Medical Imaging*. International Society for Optics and Photonics. 2010, 76221Z–76221Z.

[158] S Kappler, T Hannemann, E Kraft, B Kreisler, D Niederloehner, K Stierstorfer, and T Flohr. “First results from a hybrid prototype CT scanner for exploring benefits of quantum-counting in clinical CT”. In: *International Society for Optics and Photonics Medical Imaging*. International Society for Optics and Photonics. 2012, pp. 83130X–83130X.

[159] S Kappler, A Henning, B Krauss, F Schoeck, K Stierstorfer, T Weidinger, and T Flohr. “Multi-energy performance of a research prototype CT scanner with small-pixel counting detector”. In: *International Society for Optics and Photonics Medical Imaging*. International Society for Optics and Photonics. 2013, 86680O–86680O.

[160] S Kappler, A Henning, B Kreisler, F Schoeck, K Stierstorfer, and T Flohr. “Photon counting CT at elevated X-ray tube currents: contrast stability, image noise and multi-energy performance”. In: *International Society for Optics and Photonics Medical Imaging*. International Society for Optics and Photonics. 2014, pp. 90331C–90331C.

[161] S Kappler, A Henning, F Schoeck, K Stierstorfer, T Weidinger, and T Flohr. “A Hybrid Research Prototype CT Scanner with Photon Counting Detector”. In: *IEEE Transactions on Medical Imaging: Special Issue On Spectral CT*. IEEE. 2014.

[162] S Kappler, D Niederlöhner, K Stierstorfer, and T Flohr. “Contrast-enhancement, image noise, and dual-energy simulations for quantum-counting clinical CT”. In: *International Society for Optics and Photonics Medical Imaging*. International Society for Optics and Photonics. 2010, 76223H–76223H.

[163] R. K. Kaza, J. F. Platt, R. H. Cohan, E. M. Caoili, M. M. Al-Hawary, and A. Wasnik. “Dual-energy CT with single-and dual-source scanners: current applications in evaluating the genitourinary tract”. In: *Radiographics* 32.2 (2012), pp. 353–369.

[164] F. Kelcz, P. M. Joseph, and S. K. Hilal. “Noise considerations in dual energy CT scanning”. In: *Medical Physics* 6.5 (1979), pp. 418–425.

[165] J. Kim, D. Bar-Ness, S. Si-Mohamed, P. Coulon, I. Blevis, P. Douek, and D. P. Cormode. “Assessment of candidate elements for development of spectral photon-counting CT specific contrast agents”. In: *Scientific Reports* 8.1 (2018), p. 12119.

[166] O. Klein and Y. Nishina. “über die Streuung von Strahlung durch freie Elektronen nach der neuen relativistischen Quantendynamik von Dirac”. In: *Zeitschrift für Physik* 52.11-12 (1929), pp. 853–868.

[167] K. Klingenbeck-Regn, S. Schaller, T. G. Flohr, B. Ohnesorge, A. F. Kopp, and U. Baum. “Subsecond multi-slice computed tomography: basics and applications”. In: *European Journal of Radiology* 31.2 (1999), pp. 110–124.

[168] M. Kobayashi, N. Shiragam, Y. Okada, K. Suzuki, K. Sugino, and S. Homma. “Advantage of xenon ventilation CT over conventional low attenuation area measurement for the patients with COPD”. en. In: (2013).

[169] T. Koenig, E. Hamann, S. Procz, R. Ballabriga, A. Cecilia, M. Zuber, X. Llopart, M. Campbell, A. Fauler, T. Baumbach, et al. “Charge summing in spectroscopic x-ray detectors with high-Z sensors”. In: *IEEE Transactions on Nuclear Science* 60.6 (2013), pp. 4713–4718.

[170] T. Koenig, J. Schulze, M. Zuber, K. Rink, J. Butzer, E. Hamann, A. Cecilia, A. Zwerger, A. Fauler, M. Fiederle, et al. “Imaging properties of small-pixel spectroscopic x-ray detectors based on cadmium telluride sensors”. In: *Physics in Medicine and Biology* 57.21 (2012), p. 6743.

[171] T. Koenig, M. Zuber, E. Hamann, A. Cecilia, R. Ballabriga, M. Campbell, M. Ruat, L. Tlustos, A. Fauler, M. Fiederle, et al. “How spectroscopic x-ray imaging benefits from inter-pixel communication”. In: *Physics in Medicine & Biology* 59.20 (2014), p. 6195.

[172] X. Kong, H. X. Sheng, G. M. Lu, F. G. Meinel, K. T. Dyer, U. J. Schoepf, and L. J. Zhang. “Xenon-enhanced dual-energy CT lung ventilation imaging: techniques and clinical applications”. In: *American Journal of Roentgenology* 202.2 (2014), pp. 309–317.

[173] A. E. Krambeck, S. E. Handa, A. P. Evan, and J. E. Lingeman. “Brushite stone disease as a consequence of lithotripsy”. In: *Urological research* 38.4 (2010), pp. 293–299.

[174] P La Rivière and C Crawford. “From EMI to AI: a brief history of commercial CT reconstruction algorithms”. In: *J. Med. Imaging* 8.5 (2021), p. 052111.

[175] R. E. Latchaw, H Yonas, S. Pentheny, and D Gur. “Adverse reactions to xenon-enhanced CT cerebral blood flow determination.” In: *Radiology* 163.1 (1987), pp. 251–254.

[176] R. S. Ledley. *Diagnostic X-ray systems*. 1974.

[177] C.-L. Lee, K. J. Hong, N. Kim, K. Han, D. Kim, H.-S. Jung, S. Lee, J. Park, K.-Y. Lee, J. E. Lee, et al. “Feasibility study of portable multi-energy computed tomography with photon-counting detector for preclinical and clinical applications”. In: *Scientific reports* 11.1 (2021), pp. 1–11.

[178] L. Lehmann, R. Alvarez, A. Macovski, W. Brody, N. Pelc, S. J. Riederer, and A. Hall. “Generalized image combinations in dual KVP digital radiography”. In: *Medical Physics* 8.5 (1981), pp. 659–667.

[179] D. Leithner, J. L. Wichmann, T. J. Vogl, J. Trommer, S. S. Martin, J.-E. Scholtz, B. Bodelle, C. N. De Cecco, T. Duguay, J. W. Nance Jr, et al. “Virtual monoenergetic imaging and iodine perfusion maps improve diagnostic accuracy of dual-energy computed tomography pulmonary angiography with suboptimal contrast attenuation”. In: *Investigative Radiology* 52.11 (2017), pp. 659–665.

[180] M. M. Lell, G. Jost, J. G. Korporaal, A. H. Mahnken, T. G. Flohr, M. Uder, and H. Pietsch. “Optimizing contrast media injection protocols in state-of-the art computed tomographic angiography”. In: *Investigative Radiology* 50.3 (2015), pp. 161–167.

[181] M. M. Lell, M. Kramer, E. Klotz, P. Villablanca, and S. G. Ruehm. “Carotid computed tomography angiography with automated bone suppression: a comparative study between dual energy and bone subtraction techniques”. In: *Investigative Radiology* 44.6 (2009), pp. 322–328.

[182] S Leng, F. Diehn, J. Lane, K. Koeller, R. Witte, R. Carter, and C. McCollough. “Temporal bone CT: improved image quality and potential for decreased radiation dose using an ultra-high-resolution scan mode with an iterative reconstruction algorithm”. In: *American Journal of Neuroradiology* 36.9 (2015), pp. 1599–1603.

[183] S Leng, Z Yu, A Halaweish, S Kappler, K Hahn, A Henning, Z Li, J Lane, D. Levin, S Jorgensen, et al. "A high-resolution imaging technique using a whole-body, research photon counting detector CT system". In: *International Society for Optics and Photonics Medical Imaging*. International Society for Optics and Photonics. 2016, pp. 97831I–97831I.

[184] S. Leng, R. Gutjahr, A. Ferrero, S. Kappler, A. Henning, A. F. Halaweish, W. Zhou, J. Montoya, and C. H. McCollough. "Ultra-high spatial resolution multi-energy CT using photon counting detector technology". In: *SPIE Medical Imaging*. Ed. by T. G. Flohr, J. Y. Lo, and T. G. Schmidt. SPIE, 2017.

[185] S. Leng, A. Huang, J. M. Cardona, X. Duan, J. C. Williams, and C. H. McCollough. "Dual-Energy CT for Quantification of Urinary Stone Composition in Mixed Stones: A Phantom Study". In: *American Journal of Roentgenology* (2016), pp. 1–9.

[186] S. Leng, L. Yu, J. Wang, J. G. Fletcher, C. A. Mistretta, and C. H. McCollough. "Noise reduction in spectral CT: reducing dose and breaking the trade-off between image noise and energy bin selection". In: *Medical Physics* 38.9 (2011), pp. 4946–4957.

[187] Y Li, G Shi, S Wang, S Wang, and R Wu. "Iodine quantification with dual-energy CT: phantom study and preliminary experience with VX2 residual tumour in rabbits after radiofrequency ablation". In: *British Journal of Radiology* 86.1029 (2013), p. 20130143.

[188] Z. Li, S. Leng, L. Yu, Z. Yu, and C. H. McCollough. "Image-based material decomposition with a general volume constraint for photon-counting CT". In: *International Society for Optics and Photonics Medical Imaging*. International Society for Optics and Photonics. 2015, 94120T–94120T.

[189] X. Liu, L. Yu, A. N. Primak, and C. H. McCollough. "Quantitative imaging of element composition and mass fraction using dual-energy CT: three-material decomposition". In: *Medical Physics* 36.5 (2009), pp. 1602–1609.

[190] G. H. van de Maat, P. R. Seevinck, M. Elschot, M. L. Smits, H. de Leeuw, A. D. van het Schip, M. A. Vente, B. A. Zonnenberg, H. W. de Jong, M. G. Lam, et al. "MRI-based biodistribution assessment of holmium-166 poly (L-lactic acid) microspheres after radioembolisation". In: *European Radiology* 23.3 (2013), pp. 827–835.

[191] A. Malusek, M. Karlsson, M. Magnusson, and G. A. Carlsson. "The potential of dual-energy computed tomography for quantitative decomposition of soft tissues to water, protein and lipid in brachytherapy". In: *Physics in Medicine and Biology* 58.4 (2013), p. 771.

[192] S. Mangold, C. Thomas, M. Fenchel, M. Vuust, B. Krauss, D. Ketelsen, I. Tsiflikas, C. D. Claussen, and M. Heuschmid. "Virtual nonenhanced dual-energy CT urography with tin-filter technology: determinants of detection of urinary calculi in the renal collecting system". In: *Radiology* 264.1 (2012), pp. 119–125.

[193] R. Marcus, J. G. Fletcher, S. P. Sheedy, J. L. Fidler, Z. Li, Z. Yu, F. Enders, A. Halaweish, and C. H. McCollough. "Photon-counting-detector CT for the evaluation of non-contrast enhanced abdominal imaging in patients". In: Radiological Society of North America. 102nd Scientific Assembly and Annual Meeting (Chicago IL, USA, Nov. 27–Dec. 2, 2016). 2016.

[194] R. Marcus, J. G. Fletcher, T. J. Vrtiska, M. L. Wells, A. Ferrero, J. Montoya, A. Huang, A. Halaweish, F. Enders, S. Leng, and C. H. McCollough. "Detection and characterization of urinary stones using photon-counting-detector CT in a clinical setting". In: Radiological Society of North America. 102nd Scientific Assembly and Annual Meeting (Chicago IL, USA, Nov. 27–Dec. 2, 2016). 2016.

[195] R. P. Marcus, J. G. Fletcher, A. Ferrero, S. Leng, A. F. Halaweish, R. Gutjahr, T. J. Vrtiska, M. L. Wells, F. T. Enders, and C. H. McCollough. "Detection and Characterization of Renal Stones by Using Photon-Counting–based CT". In: *Radiology* 289.2 (2018), pp. 436–442.

[196] S. S. Martin, F. Trapp, J. L. Wichmann, M. H. Albrecht, L. Lenga, J. Durden, C. Booz, T. J. Vogl, and T. D'Angelo. "Dual-energy CT in early acute pancreatitis: improved detection using iodine quantification". In: *European Radiology* 29.5 (2019), pp. 2226–2232.

[197] W. Mayneord. “The significance of the roentgen”. In: *Acta Int Union Against Cancer* 2 (1937), p. 271.

[198] C. H. McCollough and R. L. Morin. “The technical design and performance of ultrafast computed tomography”. In: *Radiologic Clinics of North America* 32.3 (1994), pp. 521–536.

[199] C. H. McCollough, G. H. Chen, W. Kalender, S. Leng, E. Samei, K. Taguchi, G. Wang, L. Yu, and R. I. Pettigrew. “Achieving routine submillisievert CT scanning: report from the summit on management of radiation dose in CT”. In: *Radiology* 264.2 (2012), p. 567.

[200] C. H. McCollough, S. Leng, R. Gutjahr, Z. yu, Z. Li, A. Halaweish, S. M. Jorgensen, E. L. Ritman, and S. Kappler. “Whole-body Human Imaging with Photon-counting-based CT at Clinically Relevant Doses”. In: Radiological Society of North America. 101st Scientific Assembly and Annual Meeting (Chicago IL, USA, Nov. 11–Dec. 4, 2015). 2015.

[201] C. H. McCollough, S. Leng, J. Sunnegardh, T. J. Vrieze, L. Yu, J. Lane, R. Raupach, K. Stierstorfer, and T. G. Flohr. “Spatial resolution improvement and dose reduction potential for inner ear CT imaging using az-axis deconvolution technique”. In: *Medical Physics* 40.6Part1 (2013), p. 061904.

[202] C. H. McCollough, S. Leng, L. Yu, and J. G. Fletcher. “Dual-and multi-energy CT: principles, technical approaches, and clinical applications”. In: *Radiology* 276.3 (2015), pp. 637–653.

[203] C. H. McCollough and F. E. Zink. “Performance evaluation of a multi-slice CT system”. In: *Medical Physics* 26.11 (1999), pp. 2223–2230.

[204] W. D. McDavid, R. G. Waggener, M. J. Dennis, V. J. Sank, and W. H. Payne. “Estimation of chemical composition and density from computed tomography carried out at a number of energies.” In: *Investigative Radiology* 12.2 (1977), pp. 189–194.

[205] M. F. McNitt-Gray. “AAPM/RSNA Physics Tutorial for Residents: Topics in CT: Radiation Dose in CT 1”. In: *Radiographics* 22.6 (2002), pp. 1541–1553.

[206] C. Miller, K. Lonnroth, G. Sotgiu, and G. B. Migliori. *The long and winding road of chest radiography for tuberculosis detection*. 2017.

[207] M. R. Millner, W. D. McDavid, R. G. Waggener, M. J. Dennis, W. H. Payne, and V. J. Sank. “Extraction of information from CT scans at different energies”. In: *Medical Physics* 6.1 (1979), pp. 70–71.

[208] H. Mitcheson, R. Zamenhof, M. Bankoff, and E. Prien. “Determination of the chemical composition of urinary calculi by computerized tomography.” In: *Journal of Urology* 130.4 (1983), pp. 814–819.

[209] C. Möhler, P. Wohlfahrt, C. Richter, and S. Greilich. “Range prediction for tissue mixtures based on dual-energy CT”. In: *Physics in Medicine & Biology* 61.11 (2016), N268.

[210] R. D. Moore, E. P. Steinberg, N. R. Powe, J. A. Brinker, E. K. Fishman, S. Graziano, and R. Gopalan. “Nephrotoxicity of high-osmolality versus low-osmolality contrast media: randomized clinical trial.” In: *Radiology* 182.3 (1992), pp. 649–655.

[211] C. L. Morgan. *Basic principles of computed tomography*. Philadelphia, PA: Lippincott Williams and Wilkins, Jan. 1983.

[212] D. Morhard, C. Fink, A. Graser, M. F. Reiser, C. Becker, and T. R. Johnson. “Cervical and cranial computed tomographic angiography with automated bone removal: dual energy computed tomography versus standard computed tomography”. In: *Investigative Radiology* 44.5 (2009), pp. 293–297.

[213] S. Mori, T. Obata, N. Nakajima, N. Ichihara, and M. Endo. “Volumetric Perfusion CT Using Prototype 256–Detector Row CT Scanner: Preliminary Study with Healthy Porcine Model”. In: *American Journal of Neuroradiology* 26.10 (2005), pp. 2536–2541.

[214] F. Morsbach, T. Pfammatter, C. S. Reiner, M. A. Fischer, B.-R. Sah, S. Winklhofer, E. Klotz, T. Frauenfelder, A. Knuth, B. Seifert, et al. “Computed tomographic perfusion imaging for the prediction of response and survival to transarterial radioembolization of liver metastases”. In: *Investigative Radiology* 48.11 (2013), pp. 787–794.

[215] G. Motley, N. Dalrymple, C. Keesling, J. Fischer, and W. Harmon. “Hounsfield unit density in the determination of urinary stone composition”. In: *Urology* 58.2 (2001), pp. 170–173.

[216] D. Muenzel, D. Bar-Ness, E. Roessl, I. Blevis, M. Bartels, A. A. Fingerle, S. Ruschke, P. Coulon, H. Daerr, F. K. Kopp, et al. “Spectral Photon-counting CT: Initial Experience with Dual–Contrast Agent K-Edge Colonography”. In: *Radiology* (2016), p. 160890.

[217] D. Muenzel, H. Daerr, R. Proksa, A. A. Fingerle, F. K. Kopp, P. Douek, J. Herzen, F. Pfeiffer, E. J. Rummeny, and P. B. Noël. “Simultaneous dual-contrast multi-phase liver imaging using spectral photon-counting computed tomography: a proof-of-concept study”. In: *European Radiology experimental* 1.1 (2017), pp. 1–9.

[218] D. Muenzel, G. C. Lo, H. S. Yu, A. Parakh, M. Patino, A. Kambadakone, E. J. Rummeny, and D. V. Sahani. “Material density iodine images in dual-energy CT: Detection and characterization of hypervascular liver lesions compared to magnetic resonance imaging”. In: *European Journal of Radiology* 95 (2017), pp. 300–306.

[219] M. E. Myronakis and D. G. Darambara. “Monte Carlo investigation of charge-transport effects on energy resolution and detection efficiency of pixelated CZT detectors for SPECT/PET applications”. In: *Medical Physics* 38.1 (2011), pp. 455–467.

[220] H. Naderi Boldaji, M. Patwari, M. Reymann, R. Gutjahr, R. Raupach, and A. Maier. “Deep Learning based Model Observers for Multi - Modal Imaging”. In: *16th International Meeting on Fully Three-Dimensional Image Reconstruction in Radiology and Nuclear Medicine* (Leuven, Belgium). July 19–23, 2021.

[221] Y Nagayama, T Nakaura, S Oda, N Taguchi, D Utsunomiya, Y Funama, M Kidoh, T Namimoto, D Sakabe, M Hatemura, et al. “Dual-layer detector CT of chest, abdomen, and pelvis with a one-third iodine dose: image quality, radiation dose, and optimal monoenergetic settings”. In: *Clinical Radiology* 73.12 (2018), 1058–e21.

[222] Y. Nagayama, S. Tanoue, T. Inoue, S. Oda, T. Nakaura, D. Utsunomiya, and Y. Yamashita. “Dual-layer spectral CT improves image quality of multiphasic pancreas CT in patients with pancreatic ductal adenocarcinoma”. In: *European Radiology* 30.1 (2020), pp. 394–403.

[223] S. Napel, M. P. Marks, G. D. Rubin, M. D. Dake, C. H. McDonnell, S. M. Song, D. R. Enzmann, and R. Jeffrey Jr. “CT angiography with spiral CT and maximum intensity projection.” In: *Radiology* 185.2 (1992), pp. 607–610.

[224] P. F. New, W. R. Scott, J. A. Schnur, K. R. Davis, and J. M. Taveras. “Computerized axial tomography with the EMI scanner”. In: *Radiology* 110.1 (1974), pp. 109–123.

[225] J. F. Nijsen, G. Cornelis Krijger, and A. Dirk van het Schip. “The bright future of radionuclides for cancer therapy”. In: *Anti-Cancer Agents in Medicinal Chemistry* 7.3 (2007), pp. 271–290.

[226] J. F. Nijsen, J.-H. Seppenwoolde, T. Havenith, C. Bos, C. J. Bakker, and A. D. van het Schip. “Liver tumors: MR imaging of radioactive holmium microspheres—phantom and rabbit study”. In: *Radiology* 231.2 (2004), pp. 491–499.

[227] S. A. van Nimwegen, R. C. Bakker, J. Kirpensteijn, R. J. J. van Es, R. Koole, M. G. E. H. Lam, J. W. Hesselink, and J. F. W. Nijsen. “Intratumoral injection of radioactive holmium (166 Ho) microspheres for treatment of oral squamous cell carcinoma in cats”. In: *Veterinary and Comparative Oncology* 16.1 (2017), pp. 114–124.

[228] T. Nowak, M. Hupfer, R. Brauweiler, F. Eisa, and W. A. Kalender. “Potential of high-Z contrast agents in clinical contrast-enhanced computed tomography”. In: *Medical Physics* 38.12 (2011), pp. 6469–6482.

[229] G. Pache, B. Krauss, P. Strohm, U. Saueressig, P. Blanke, S. Bulla, O. Schäfer, P. Helwig, E. Kotter, M. Langer, et al. “Dual-energy CT virtual noncalcium technique: detecting posttraumatic bone marrow lesions—feasibility study”. In: *Radiology* 256.2 (2010), pp. 617–624.

[230] D. Pan, E. Roessl, J.-P. Schlomka, S. D. Caruthers, A. Senpan, M. J. Scott, J. S. Allen, H. Zhang, G. Hu, P. J. Gaffney, et al. “Computed tomography in color: NanoK-enhanced spectral CT molecular imaging”. In: *Angewandte Chemie* 122.50 (2010), pp. 9829–9833.

[231] M Patwari, R Gutjahr, R Raupach, and A Maier. “Low dose CT denoising with residual convolutional networks and deep learned perceptual loss”. In: European Congress of Radiology-ECR 2020. 2020.

[232] M Patwari, R Gutjahr, R Raupach, A Maier, et al. “Low dose CT denoising with residual convolutional networks and deep learned perceptual loss”. In: European Congress of Radiology-ECR 2020. 2020.

[233] M. Patwari, A. F. Calvarons, R. Gutjahr, R. Marcus, Y. Thali, R. Raupach, and A. Maier. “Reducing the risk of hallucinations with interpretable deep learning models for low-dose CT denoising: comparative performance analysis”. In: *Physics in Medicine and Biology* (2023).

[234] M. Patwari, R. Gutjahr, R. Raupach, and A. Maier. “JBFnet-low dose CT denoising by trainable joint bilateral filtering”. In: *Bildverarbeitung für die Medizin*. 2021.

[235] M. Patwari, R. Gutjahr, R. Raupach, and A. Maier. “Limited parameter denoising for low-dose X-ray computed tomography using deep reinforcement learning”. In: *Medical Physics* (2022).

[236] M. Patwari, R. Gutjahr, R. Raupach, and A. Maier. *Low Dose CT Denoising via Joint Bilateral Filtering and Intelligent Parameter Optimization*. 2020.

[237] M. Patwari, R. Gutjahr, R. Raupach, and A. Maier. “Measuring CT Reconstruction Quality with Deep Convolutional Networks”. In: *Machine Learning for Medical Image Reconstruction* (Shenzhen, China). Oct. 17–17, 2019.

[238] G. J. Pelgrim, R. W. van Hamersvelt, M. J. Willemink, B. T. Schmidt, T. G. Flohr, A. Schilham, J. Milles, M. Oudkerk, T. Leiner, and R. Vliegenthart. “Accuracy of iodine quantification using dual energy CT in latest generation dual source and dual layer CT”. In: *European Radiology* 27.9 (2017), pp. 3904–3912.

[239] M. Persson, B. Huber, S. Karlsson, X. Liu, H. Chen, C. Xu, M. Yveborg, H. Bornefalk, and M. Danielsson. “Energy-resolved CT imaging with a photon-counting silicon-strip detector”. In: *Physics in Medicine and Biology* 59.22 (2014), p. 6709.

[240] M. Persson, A. Wang, and N. J. Pelc. “Detective quantum efficiency of photon-counting CdTe and Si detectors for computed tomography: a simulation study”. In: *Journal of Medical Imaging* 7.4 (2020), pp. 043501–043501.

[241] M Petersilka, K Stierstorfer, H Bruder, and T Flohr. “Strategies for scatter correction in dual source CT”. In: *Medical Physics* 37.11 (2010), pp. 5971–5992.

[242] M. Petersilka, H. Bruder, B. Krauss, K. Stierstorfer, and T. G. Flohr. “Technical principles of dual source CT”. In: *European journal of radiology* 68.3 (2008), pp. 362–368.

[243] B. Petritsch, P. Pannenbecker, A. M. Weng, S. Veldhoen, J.-P. Grunz, T. A. Bley, and A. Kosmala. “Comparison of Dual-and Single-Source Dual-Energy CT for Diagnosis of Acute Pulmonary Artery Embolism”. In: *RöFo-Fortschritte auf dem Gebiet der Röntgenstrahlen und der bildgebenden Verfahren*. Vol. 193. 04. Georg Thieme Verlag KG. 2021, pp. 427–436.

[244] C. Phan, A. Yoo, J. Hirsch, R. Nogueira, and R Gupta. “Differentiation of hemorrhage from iodinated contrast in different intracranial compartments using dual-energy head CT”. In: *American journal of neuroradiology* 33.6 (2012), pp. 1088–1094.

[245] R. E. Pollard and S. M. Puchalski. “Reaction to intraarterial ionic iodinated contrast medium administration in anesthetized horses”. In: *Veterinary Radiology & Ultrasound* 52.4 (2011), pp. 441–443.

[246] C. Polster, R. Gutjahr, M. Berner, T. Flohr, M. Hertel, S. Kappler, K. Stierstorfer, and O. Dietrich. “Improving material separation of high-flux whole-body photon counting computed tomography by K-edge pre-filtration”. In: *SPIE Medical Imaging 2017: Physics of Medical Imaging*. Ed. by T. G. Flohr, J. Y. Lo, and T. G. Schmidt. SPIE, 2017.

[247] C. Polster. “Optimierung der Computertomographie mit photonenzählenden Detektoren durch spektrale Filterung”. PhD thesis. lmu, 2020.

[248] C. Polster, R. Gutjahr, M. Berner, T. Flohr, M. Hertel, S. Kappler, K. Stiersorfer, and O. Dietrich. “High-flux whole-body photon-counting computed tomography: improving material separation by hafnium pre-filtration”. In: 4th Workshop on Medical Applications of Spectroscopic X-ray Detectors (CERN, Geneva, Swiss, May 15–15, 2016). 2017.

[249] C. Polster, K. Hahn, R. Gutjahr, F. Schöck, S. Kappler, K. Stierstorfer, O. Dietrich, and T. G. Flohr. “Improving material decomposition by spectral optimization of photon counting computed tomography”. In: *International Society for Optics and Photonics Medical Imaging*. International Society for Optics and Photonics. 2016, 97831O–97831O.

[250] C. Polster, K. Hahn, R. Gutjahr, F. Schoeck, S. Kappler, K. Stiersorfer, O. Dietrich, and T. Flohr. “Improving material decomposition by spectral optimization of photon counting computed tomography”. In: SPIE Medical Imaging (Orlando, Florida, USA, Mar. 2–6, 2016). 2016.

[251] F. Pontana, M. Remy-Jardin, A. Duhamel, J.-B. Faivre, B. Wallaert, and J. Remy. “Lung perfusion with dual-energy multi-detector row CT: can it help recognize ground glass opacities of vascular origin?” In: *Academic Radiology* 17.5 (2010), pp. 587–594.

[252] A. Pourmorteza, R. Symons, A. Henning, S. Ulzheimer, and D. A. Bluemke. “Dose efficiency of quarter-millimeter photon-counting computed tomography: first-in-human results”. In: *Investigative Radiology* 53.6 (2018), pp. 365–372.

[253] A. Pourmorteza, R. Symons, V. Sandfort, M. Mallek, M. K. Fuld, G. Henderson, E. C. Jones, A. A. Malayeri, L. R. Folio, and D. A. Bluemke. “Abdominal imaging with contrast-enhanced photon-counting CT: first human experience”. In: *Radiology* 279.1 (2016), pp. 239–245.

[254] A. N. Primak, J. G. Fletcher, T. J. Vrtiska, O. P. Dzyubak, J. C. Lieske, M. E. Jackson, J. C. Williams Jr, and C. H. McCollough. “Noninvasive differentiation of uric acid versus non–uric acid kidney stones using dual-energy CT”. In: *Academic Radiology* 14.12 (2007), pp. 1441–1447.

[255] A. N. Primak, J. C. R. Giraldo, C. D. Eusemann, B. Schmidt, B. Kantor, J. G. Fletcher, and C. H. McCollough. “Dual-source dual-energy CT with additional tin filtration: Dose and image quality evaluation in phantoms and in-vivo”. In: *American Journal of Roentgenology* 195.5 (2010), p. 1164.

[256] M. Qu, J. C. R. Giraldo, S. Leng, J. C. Williams, T. J. Vrtiska, J. C. Lieske, and C. H. McCollough. “Dual-energy dual-source CT with additional spectral filtration can improve the differentiation of non-uric acid renal stones: an ex vivo phantom study”. In: *American Journal of Roentgenology* 196.6 (2011), p. 1279.

[257] M. Qu, G. Jaramillo-Alvarez, J. C. Ramirez-Giraldo, Y. Liu, X. Duan, J. Wang, T. J. Vrtiska, A. E. Krambeck, J. Lieske, and C. H. McCollough. “Urinary stone differentiation in patients with large body size using dual-energy dual-source computed tomography”. In: *European Radiology* 23.5 (2013), pp. 1408–1414.

[258] B. Quiney, A. Harris, P. McLaughlin, and S. Nicolaou. “Dual-energy CT increases reader confidence in the detection and diagnosis of hypoattenuating pancreatic lesions”. In: *Abdominal Imaging* 40.4 (2015), pp. 859–64.

[259] O. Rabin, J Manuel Perez, J. Grimm, G. Wojtkiewicz, and R. Weissleder. “An X-ray computed tomography imaging agent based on long-circulating bismuth sulphide nanoparticles”. In: *Nature materials* 5.2 (2006), pp. 118–122.

[260] J. Radon. “Uber die Bestimmung von Funktionen durch ihre Integralwerte langs gewissez Mannigfaltigheiten, Ber”. In: *Verh. Sachs. Akad. Wiss. Leipzig, Math Phys Klass* 69 (1917).

[261] G. L. Raff, M. J. Gallagher, W. W. O’Neill, and J. A. Goldstein. “Diagnostic accuracy of noninvasive coronary angiography using 64-slice spiral computed tomography”. In: *Journal of the American College of Cardiology* 46.3 (2005), pp. 552–557.

[262] P. Rajiah, A. Parakh, F. Kay, D. Baruah, A. R. Kambadakone, and S. Leng. “Update on Multienergy CT: Physics, Principles, and Applications”. In: *Radiographics* (2020), p. 200038.

[263] P. Rajiah, M. Sundaram, and N. Subhas. “Dual-energy CT in musculoskeletal imaging: what is the role beyond gout?” In: *American Journal of Roentgenology* 213.3 (2019), pp. 493–505.

[264] N. Rassouli, M. Etesami, A. Dhanantwari, and P. Rajiah. “Detector-based spectral CT with a novel dual-layer technology: principles and applications”. In: *Insights into Imaging* 8.6 (2017), pp. 589–598.

[265] R. Raupach, H. Bruder, K. Stierstorfer, C. Suess, and T. Flohr. “Novel Approach for Efficient Edge Preserving Noise Reduction in CT Volume Data”. In: Radiological Society of North America. 99th Scientific Assembly and Annual Meeting (Chicago IL, USA). 2005.

[266] A. J. Reimann, D. Rinck, A. Birinci-Aydogan, M. Scheuering, C. Burgstahler, S. Schroeder, H. Brodoefel, I. Tsiflikas, T. Herberts, T. G. Flohr, et al. “Dual-source computed tomography: advances of improved temporal resolution in coronary plaque imaging”. In: *Investigative Radiology* 42.3 (2007), pp. 196–203.

[267] L. Ren, N. Huber, K. Rajendran, J. G. Fletcher, C. H. McCollough, and L. Yu. “Dual-contrast biphasic liver imaging with iodine and gadolinium using photon-counting detector computed tomography: an exploratory animal study”. In: *Investigative Radiology* 57.2 (2022), p. 122.

[268] L. Ren, K. Rajendran, J. G. Fletcher, C. H. McCollough, and L. Yu. “Simultaneous Dual-contrast Imaging of Small Bowel with Iodine and Bismuth using Photon-counting-detector CT: A Feasibility Animal Study”. In: *Investigative Radiology* 55.10 (2020), p. 688.

[269] C. Richter and P. Wohlfahrt. “Dual-Energy CT in Radiation Oncology”. In: *Spectral Imaging*. Springer, 2022, pp. 333–346.

[270] S. J. Riederer and C. Mistretta. “Selective iodine imaging using K-edge energies in computerized x-ray tomography”. In: *Medical Physics* 4.6 (1977), pp. 474–481.

[271] K. Rink, U. Oelfke, M. Fiederle, M. Zuber, and T. Koenig. “Investigating the feasibility of photon-counting K-edge imaging at high x-ray fluxes using nonlinearity corrections”. In: *Medical Physics* 40.10 (2013), p. 101908.

[272] E Roessl and R Proksa. “K-edge imaging in x-ray computed tomography using multi-bin photon counting detectors”. In: *Physics in Medicine and Biology* 52.15 (2007), p. 4679.

[273] E. Roessl et al. “Imaging performance of a photon-counting computed tomography prototype”. In: *Geneva, Switzerland: CERN* (2015).

[274] L. Romans. *Computed Tomography for Technologists: A comprehensive text*. Lippincott Williams and Wilkins, 2018.

[275] J Ronaldson, R Zainon, A Sedayo, N Scott, A Butler, P Butler, and N Anderson. “Toward quantifying the composition of soft tissues by spectral CT with Medipix3”. Radiological Society of North America 2011 Scientific Assembly and Annual Meeting. 2012.

[276] W. C. Röntgen. *Eine neue Art von Strahlen: I und II Mitteilung*. Verlag und Druck der Stahelschen KB Hof. und Universitätsbuch-und Kunsthandlung, 1895.

[277] W. C. Röntgen. *The bones of a hand with a ring on one finger, viewed through x-ray. Photoprint from radiograph by W. C. Röntgen, 1895. Wellcome Library no. 32971i*. https://wellcomecollection.org/works/wjc8ejn2. The hand is possibly the hand of Röntgen's wife, photographed on 22nd December 1895. The print is from one of the first radiographs (x-ray photographs) made by the German physicist, Wilhelm Konrad Röntgen (1845-1923). Röntgen discovered the electro-magnetic rays he named "x-rays" (also known as "Röntgen rays") in Würzburg in November 1895. Röntgen mailed this and other prints to, among others, the British physicist Sir Arthur Schuster, along with an offprint of his article "über eine neue Art von Strahlen" (1895). Dr Nora H. Schuster, Sir Arthur's daughter, presented the prints to the Wellcome Institute Library in 1962. 1895.

[278] R. Rutherford, B. Pullan, and I Isherwood. "Measurement of effective atomic number and electron density using an EMI scanner". In: *Neuroradiology* 11.1 (1976), pp. 15–21.

[279] B. Rutt and A. Fenster. "Split-filter computed tomography: a simple technique for dual energy scanning." In: *Journal of Computer Assisted Tomography* 4.4 (1980), pp. 501–509.

[280] T. Sartoretti, M. Eberhard, T. Nowak, R. Gutjahr, G. Jost, H. Pietsch, B. Schmidt, T. G. Flohr, H. Alkadhi, and A. Euler. "Photon-counting multienergy computed tomography with spectrally optimized contrast media for plaque removal and stenosis assessment". In: *Investigative Radiology* 56.9 (2021), pp. 563–570.

[281] T. Sartoretti, M. Eberhard, J. H. Rüschoff, H. Pietsch, G. Jost, T. Nowak, B. Schmidt, T. G. Flohr, A. Euler, and H. Alkadhi. "Photon-counting CT with tungsten as contrast medium: experimental evidence of vessel lumen and plaque visualization". In: *Atherosclerosis* 310 (2020), pp. 11–16.

[282] T. Sartoretti, V. Mergen, K. Higashigaito, M. Eberhard, H. Alkadhi, and A. Euler. "Virtual noncontrast imaging of the liver using photon-counting detector computed tomography: a systematic phantom and patient study". In: *Investigative Radiology* 57.7 (2022), pp. 488–493.

[283] K. Sato, R. Kageyama, Y. Sawatani, H. Takano, S. Kayano, Y. Takane, and H. Saito. "Accuracy of spectral curves at different phantom sizes and iodine concentrations using dual-source dual-energy computed tomography". In: *Physical and Engineering Sciences in Medicine* (2021), pp. 1–14.

[284] J. Schlomka, E Roessl, R Dorscheid, S Dill, G Martens, T Istel, C Bäumer, C Herrmann, R Steadman, G Zeitler, et al. "Experimental feasibility of multi-energy photon-counting K-edge imaging in pre-clinical computed tomography". In: *Physics in Medicine and Biology* 53.15 (2008), p. 4031.

[285] B. Schmidt, K. Grant, T. Allmendinger, R. Gutjahr, C. McCollough, T. Flohr, and B. Krauss. "Impact of low tube voltage (kVp) selection on spectral data-based coronary CTA calcium plaque removal for Photon Counting Detector CT (PCD-CT)". In: Radiological Society of North America. 101st Scientific Assembly and Annual Meeting (Chicago IL, USA, Nov. 26–Dec. 1, 2017). 2017.

[286] C. Schmidt, B. Baessler, D. Nakhostin, A. Das, M. Eberhard, H. Alkadhi, and A. Euler. "Dual-Energy CT-Based Iodine Quantification in Liver Tumors–Impact of Scan-, Patient-, and Position-Related Factors". In: *Academic Radiology* (2020).

[287] T. G. Schmidt. "Optimal "image-based" weighting for energy-resolved CT". In: *Medical Physics* 36.7 (2009), pp. 3018–3027.

[288] L Schöckel, T Balzer, and H Pietsch. "Erhöhte Signalintensitäten und Gadolinium-Werte im Gehirn nach Gabe Gadolinium-haltiger MR-Kontrastmittel". In: *Der Radiologe* 59.4 (2019), pp. 359–368.

[289] T. Schulman. "Si, CdTe and CdZnTe radiation detectors for imaging applications". PhD thesis. University of Helsinki, Finland, 2006.

[290] B. Schulz, K. Kuehling, W. Kromen, P. Siebenhandl, M. J. Kerl, T. J. Vogl, and R. Bauer. "Automatic bone removal technique in whole-body dual-energy CT angiography: performance and image quality". In: *American Journal of Roentgenology* 199.5 (2012), W646–W650.

[291] B. J. Schwaiger, A. S. Gersing, J. Hammel, K. Mei, F. K. Kopp, J. S. Kirschke, E. J. Rummeny, K. Wörtler, T. Baum, and P. B. Noël. “Three-material decomposition with dual-layer spectral CT compared to MRI for the detection of bone marrow edema in patients with acute vertebral fractures”. In: *Skeletal Radiology* 47 (2018), pp. 1533–1540.

[292] F. Schwartz, J. C. Ramirez-Giraldo, R. Gutjahr, D. Boll, and L. M. Hurwitz Koweek. “Real-Time Patient Specific Scan Initiation for Pulmonary Embolism CTA: Impact on Image Quality”. In: Radiological Society of North America. 104th Scientific Assembly and Annual Meeting (Chicago IL, USA). 2018.

[293] J. A. Scott. *Photon, Electron, Proton and Neutron Interaction Data for Body Tissues: ICRU Report 46. International Commission on Radiation Units and Measurements*. 1993.

[294] P. R. Seevinck, J.-H. Seppenwoolde, T. C. de Wit, W Nijsen, F Johannes, F. J. Beekman, A. D. van het Schip, G Bakker, and J Chris. “Factors affecting the sensitivity and detection limits of MRI, CT, and SPECT for multimodal diagnostic and therapeutic agents”. In: *Anti-Cancer Agents in Medicinal Chemistry* 7.3 (2007), pp. 317–334.

[295] T. Sellerer, P. B. Noël, M. Patino, A. Parakh, S. Ehn, S. Zeiter, J. A. Holz, J. Hammel, A. A. Fingerle, F. Pfeiffer, et al. “Dual-energy CT: a phantom comparison of different platforms for abdominal imaging”. In: *European Radiology* 28.7 (2018), pp. 2745–2755.

[296] J.-H. Seppenwoolde, J. F. Nijsen, L. W. Bartels, S. W. Zielhuis, A. D. van het Schip, and C. J. Bakker. “Internal radiation therapy of liver tumors: Qualitative and quantitative magnetic resonance imaging of the biodistribution of holmium-loaded microspheres in animal models”. In: *Magnetic Resonance in Medicine* 53.1 (2005), pp. 76–84.

[297] P. M. Shikhaliev. “Computed tomography with energy-resolved detection: a feasibility study”. In: *Physics in Medicine & Biology* 53.5 (2008), p. 1475.

[298] P. M. Shikhaliev. “Energy-resolved computed tomography: first experimental results”. In: *Physics in Medicine & Biology* 53.20 (2008), p. 5595.

[299] P. M. Shikhaliev. “Photon counting spectral CT: improved material decomposition with K-edge-filtered x-rays”. In: *Physics in Medicine and Biology* 57.6 (2012), p. 1595.

[300] P. M. Shikhaliev and S. G. Fritz. “Photon counting spectral CT versus conventional CT: comparative evaluation for breast imaging application”. In: *Physics in Medicine and Biology* 56.7 (2011), p. 1905.

[301] P. M. Shikhaliev, S. G. Fritz, and J. W. Chapman. “Photon counting multienergy x-ray imaging: Effect of the characteristic x rays on detector performance”. In: *Medical Physics* 36.11 (2009), pp. 5107–5119.

[302] P. M. Shikhaliev, T. Xu, and S. Molloi. “Photon counting computed tomography: concept and initial results”. In: *Medical Physics* 32.2 (2005), pp. 427–436.

[303] S. Si-Mohamed, D. Bar-Ness, M. Sigovan, V. Tatard-Leitman, D. P. Cormode, P. C. Naha, P. Coulon, L. Rascle, E. Roessl, M. Rokni, et al. “Multicolour imaging with spectral photon-counting CT: a phantom study”. In: *European Radiology Experimental* 2.1 (2018), p. 34.

[304] S. Si-Mohamed, S. Boccalini, P.-A. Rodesch, R. Dessouky, E. Lahoud, T. Broussaud, M. Sigovan, D. Gamondes, P. Coulon, Y. Yagil, et al. “Feasibility of lung imaging with a large field-of-view spectral photon-counting CT system”. In: *Diagnostic and Interventional Imaging* 102.5 (2021), pp. 305–312.

[305] S. Si-Mohamed, V. Tatard-Leitman, A. Laugerette, M. Sigovan, D. Pfeiffer, E. J. Rummeny, P. Coulon, Y. Yagil, P. Douek, L. Boussel, et al. “Spectral Photon-Counting Computed Tomography (SPCCT): in-vivo single-acquisition multi-phase liver imaging with a dual contrast agent protocol”. In: *Scientific reports* 9.1 (2019), pp. 1–8.

[306] S. A. Si-Mohamed, J. Greffier, J. Miailhes, S. Boccalini, P.-A. Rodesch, A. Vuillod, N. van der Werf, D. Dabli, D. Racine, D. Rotzinger, et al. “Comparison of image quality between spectral photon-counting CT and dual-layer CT for the evaluation of lung nodules: A phantom study”. In: *European Radiology* 32.1 (2022), pp. 524–532.

[307] E Siebert, G Bohner, M Dewey, C Bauknecht, and R Klingebiel. “Dose related, comparative evaluation of a novel bone-subtraction algorithm in 64-row cervico-cranial CT angiography”. In: *European journal of radiology* 73.1 (2010), pp. 168–174.

[308] Siemens Healthcare GmbH. *syngoCT Postprocessing applications - Instructions for Use - syngoCT Workplace syngo CT VB20*. 2017.

[309] J. da Silva, F. Grönberg, B. Cederström, M. Persson, M. Sjölin, Z. Alagic, R. Bujila, and M. Danielsson. “Resolution characterization of a silicon-based, photon-counting computed tomography prototype capable of patient scanning”. In: *Journal of Medical Imaging* 6.4 (2019), p. 043502.

[310] B. Sitharaman, K. R. Kissell, K. B. Hartman, L. A. Tran, A. Baikalov, I. Rusakova, Y. Sun, H. A. Khant, S. J. Ludtke, W. Chiu, et al. “Superparamagnetic gadonanotubes are high-performance MRI contrast agents”. In: *Chemical Communications* 31 (2005), pp. 3915–3917.

[311] K. Slebocki, B. Kraus, D.-H. Chang, M. Hellmich, D. Maintz, and C. Bangard. “Incidental findings in abdominal dual-energy computed tomography: correlation between true noncontrast and virtual noncontrast images considering renal and liver cysts and adrenal masses”. In: *Journal of Computer Assisted Tomography* 41.2 (2017), pp. 294–297.

[312] M. L. Smits, M. Elschot, M. A. van den Bosch, G. H. van de Maat, A. D. van het Schip, B. A. Zonnenberg, P. R. Seevinck, H. M. Verkooijen, C. J. Bakker, H. W. de Jong, M. G. Lam, and J. F. Nijsen. “In vivo dosimetry based on SPECT and MR imaging of 166Ho-microspheres for treatment of liver malignancies”. In: *Journal of Nuclear Medicine* 54.12 (2013), pp. 2093–2100.

[313] W. H. Sommer, T. R. Johnson, C. R. Becker, E. Arnoldi, H. Kramer, M. F. Reiser, and K. Nikolaou. “The value of dual-energy bone removal in maximum intensity projections of lower extremity computed tomography angiography”. In: *Investigative Radiology* 44.5 (2009), pp. 285–292.

[314] H. Soo Choi, W. Liu, P. Misra, E. Tanaka, J. P. Zimmer, B. Itty Ipe, M. G. Bawendi, and J. V. Frangioni. “Renal clearance of quantum dots”. In: *Nature Biotechnology* 25.10 (2007), pp. 1165–1170.

[315] P. Stolzmann, M. Kozomara, N. Chuck, M. Müntener, S. Leschka, H. Scheffel, and H. Alkadhi. “In vivo identification of uric acid stones with dual-energy CT: diagnostic performance evaluation in patients”. In: *Abdominal Imaging* 35.5 (2010), pp. 629–635.

[316] M. van Straten, M. Schaap, M. L. Dijkshoorn, M. J. Greuter, A. van der Lugt, G. P. Krestin, and W. J. Niessen. “Automated bone removal in CT angiography: comparison of methods based on single energy and dual energy scans”. In: *Medical Physics* 38.11 (2011), pp. 6128–6137.

[317] M. Sühling, S. Großkopf, R. Gutjahr, M. Schöbinger, C. Schwemmer, A. Wimmer, and T. Flohr. “Artificial Intelligence Integration into the Computed Tomography System”. In: *Artificial Intelligence in Cardiothoracic Imaging*. Ed. by C. N. De Cecco, M. van Assen, and T. Leiner. Cham: Springer International Publishing, 2022, pp. 181–193.

[318] R. Symons, T. E. Cork, M. N. Lakshmanan, R. Evers, C. Davies-Venn, K. A. Rice, M. L. Thomas, C.-Y. Liu, S. Kappler, S. Ulzheimer, et al. “Dual-contrast agent photon-counting computed tomography of the heart: initial experience”. In: *The International Journal of Cardiovascular Imaging* 33.8 (2017), pp. 1253–1261.

[319] R. Symons, B. Krauss, P. Sahbaee, T. E. Cork, M. N. Lakshmanan, D. A. Bluemke, and A. Pourmorteza. “Photon-counting CT for simultaneous imaging of multiple contrast agents in the abdomen: an in vivo study”. In: *Medical Physics* 44.10 (2017), pp. 5120–5127.

[320] C. Szeles, S. A. Soldner, S. Vydrin, J. Graves, and D. S. Bale. “CdZnTe semiconductor detectors for spectroscopic x-ray imaging”. In: *IEEE Transactions on Nuclear Science* 55.1 (2008), pp. 572–582.

[321] K. Taguchi, E. C. Frey, X. Wang, J. S. Iwanczyk, and W. C. Barber. “An analytical model of the effects of pulse pileup on the energy spectrum recorded by energy resolved photon counting x-ray detectors”. In: *Medical Physics* 37.8 (2010), pp. 3957–3969.

[322] K. Taguchi and J. S. Iwanczyk. “Vision 20/20: Single photon counting x-ray detectors in medical imaging”. In: *Medical Physics* 40.10 (2013), p. 100901.

[323] K. Taguchi, M. Zhang, E. C. Frey, X. Wang, J. S. Iwanczyk, E. Nygard, N. E. Hartsough, B. M. Tsui, and W. C. Barber. “Modeling the performance of a photon counting x-ray detector for CT: Energy response and pulse pileup effects”. In: *Medical Physics* 38.2 (2011), pp. 1089–1102.

[324] K. Taguchi, M. Zhang, E. C. Frey, J. Xu, W. P. Segars, and B. M. Tsui. “Image-domain material decomposition using photon-counting CT”. In: *Medical Imaging*. International Society for Optics and Photonics. 2007, pp. 651008–651008.

[325] N. Takahashi, R. P. Hartman, T. J. Vrtiska, A. Kawashima, A. N. Primak, O. P. Dzyubak, J. N. Mandrekar, J. G. Fletcher, and C. H. McCollough. “Dual-energy CT iodine-subtraction virtual unenhanced technique to detect urinary stones in an iodine-filled collecting system: a phantom study”. In: *AJR. American journal of roentgenology* 190.5 (2008), p. 1169.

[326] N. Takahashi, T. J. Vrtiska, A. Kawashima, R. P. Hartman, A. N. Primak, J. G. Fletcher, and C. H. McCollough. “Detectability of urinary stones on virtual nonenhanced images generated at pyelographic-phase dual-energy CT”. In: *Radiology* 256.1 (2010), pp. 184–190.

[327] S. F. Thieme, C. R. Becker, M. Hacker, K. Nikolaou, M. F. Reiser, and T. R. Johnson. “Dual energy CT for the assessment of lung perfusion—correlation to scintigraphy”. In: *European journal of radiology* 68.3 (2008), pp. 369–374.

[328] S. F. Thieme, T. R. Johnson, C. Lee, J. McWilliams, C. R. Becker, M. F. Reiser, and K. Nikolaou. “Dual-energy CT for the assessment of contrast material distribution in the pulmonary parenchyma”. In: *American Journal of Roentgenology* 193.1 (2009), pp. 144–149.

[329] C. Thomas, B. Krauss, D. Ketelsen, I. Tsiflikas, A. Reimann, M. Werner, D. Schilling, J. Hennenlotter, C. D. Claussen, H.-P. Schlemmer, et al. “Differentiation of urinary calculi with dual energy CT: effect of spectral shaping by high energy tin filtration”. In: *Investigative Radiology* 45.7 (2010), pp. 393–398.

[330] M. Toepker, T. Moritz, B. Krauss, M. Weber, G. Euller, T. Mang, F. Wolf, C. J. Herold, and H. Ringl. “Virtual non-contrast in second-generation, dual-energy computed tomography: reliability of attenuation values”. In: *European journal of radiology* 81.3 (2012), e398–e405.

[331] N. Tristan, B. Schmidt, R. Gutjahr, and T. G. Flohr. “Virtual removal of calcified vascular plaques using multi-energy photon counting CT”. In: Radiological Society of North America. 104th Scientific Assembly and Annual Meeting (Chicago IL, USA, Nov. 29–Dec. 5, 2020). 2020.

[332] M. Tsurusaki, K. Sofue, M. Hori, K. Sasaki, K. Ishii, T. Murakami, and M. Kudo. “Dual-Energy Computed Tomography of the Liver: Uses in Clinical Practices and Applications”. In: *Diagnostics* 11.2 (2021), p. 161.

[333] T. Tumer, M Clajus, G. Visser, S Yin, P. Willson, L D’Aries, K. Parnham, B Glick, J. Perry, T Gamble, et al. “Preliminary results obtained from a novel CdZnTe pad detector and readout ASIC developed for an automatic baggage inspection system”. In: *IEEE Nuclear Science Symposium Conference*. Vol. 1. IEEE. 2000, pp. 4–36.

[334] D. Utsunomiya, R. Tanaka, K. Yoshioka, K. Awai, T. Mochizuki, N. Matsunaga, T. Ichikawa, M. Kanematsu, T. Kim, and Y. Yamashita. “Relationship between diverse patient body size-and image acquisition-related factors, and quantitative and qualitative image quality in coronary computed tomography angiography: a multicenter observational study”. In: *Japanese Journal of Radiology* 34.8 (2016), pp. 548–555.

[335] H. W. Venema, F. J. H. Hulsmans, and G. J. den Heeten. “CT angiography of the circle of Willis and intracranial internal carotid arteries: maximum intensity projection with matched mask bone elimination—feasibility study”. In: *Radiology* 218.3 (2001), pp. 893–898.

[336] A. de Vries, E. Roessl, E. Kneepkens, A. Thran, B. Brendel, G. Martens, R. Proska, K. Nicolay, and H. Grüll. “Quantitative spectral K-edge imaging in preclinical photon-counting x-ray computed tomography”. In: *Investigative Radiology* 50.4 (2015), pp. 297–304.

[337] T. J. Vrtiska, N. Takahashi, J. G. Fletcher, R. P. Hartman, L. Yu, and A. Kawashima. “Genitourinary applications of dual-energy CT”. In: *AJR. American journal of roentgenology* 194.6 (2010), p. 1434.

[338] A. S. Wang, D. Harrison, V. Lobastov, and J. E. Tkaczyk. “Pulse pileup statistics for energy discriminating photon counting x-ray detectors”. In: *Medical Physics* 38.7 (2011), pp. 4265–4275.

[339] C.-K. Wang, J.-M. Tsai, M.-T. Chuang, M.-T. Wang, K.-Y. Huang, and R.-M. Lin. “Bone marrow edema in vertebral compression fractures: detection with dual-energy CT”. In: *Radiology* 269.2 (2013), pp. 525–533.

[340] Q. Wang, Z. Sun, S. Li, H. Zhang, J. Li, L. Zhang, H. Xue, and Z. Jin. “Bone Marrow Imaging by Third-generation Dual-source Dual-energy CT Using Virtual Noncalcium Technique for Assessment of Diffuse Infiltrative Lesions of Multiple Myeloma.” In: *Zhongguo yi xue ke xue Yuan xue bao. Acta Academiae Medicinae Sinicae* 39.1 (2017), pp. 114–119.

[341] L Wei, S Li, Q Gao, Y Liu, and X Ma. “Use of low tube voltage and low contrast agent concentration yields good image quality for aortic CT angiography”. In: *Clinical Radiology* 71.12 (2016), 1313–e5.

[342] T Weidinger, T. Buzug, T Flohr, G. Fung, S Kappler, K Stierstorfer, and B. Tsui. “Investigation of ultra low-dose scans in the context of quantum-counting clinical CT”. In: *Medical Imaging 2012: Physics of Medical Imaging*. Vol. 8313. SPIE. 2012, pp. 1207–1215.

[343] T Weidinger, T. Buzug, T Flohr, S Kappler, F Schöck, and K Stierstorfer. “Threshold optimization for efficient contrast imaging with quantum counting CT detectors”. In: *International Society for Optics and Photonics Medical Imaging*. International Society for Optics and Photonics. 2013, 86680Q–86680Q.

[344] “Weighted FBP—a Simple Approximate 3D FBP Algorithm for Multislice Spiral CT With Good Dose Usage for Arbitrary Pitch”. In: *Physics in Medicine and Biology* 49.11 (2004), p. 2209.

[345] N. R. van der Werf, M. J. Greuter, R. Booij, A. van der Lugt, R. P. Budde, and M. van Straten. “Coronary calcium scores on dual-source photon-counting computed tomography: an adapted Agatston methodology aimed at radiation dose reduction”. In: *European Radiology* (2022), pp. 1–9.

[346] D. White, R. Griffith, and I. Wilson. “Report 46”. In: *Journal of the International Commission on Radiation Units and Measurements* 1 (1992), NP–NP.

[347] L. Wielopolski and R. P. Gardner. “Prediction of the pulse-height spectral distortion caused by the peak pile-up effect”. In: *Nuclear Instruments and Methods* 133.2 (1976), pp. 303–309.

[348] M. T. Winkelmann, F. Hagen, L. Le-Yannou, J. Weiss, P. Riffel, R. Gutjahr, S. Faby, K. Nikolaou, and M. Horger. “Myeloma bone disease imaging on a 1st-generation clinical photon-counting detector CT vs. 2nd-generation dual-source dual-energy CT”. In: *European Radiology* (2023), pp. 1–11.

[349] R. Wrazidlo, L. Walder, A. Estler, R. Gutjahr, B. Schmidt, S. Faby, J. Fritz, K. Nikolaou, M. Horger, and F. Hagen. “Radiation dose reduction in contrast-enhanced abdominal CT: comparison of photon-counting detector CT with 2nd generation dual-source dual-energy CT in an oncologic cohort”. In: *Academic Radiology* (2022).

[350] M Yaffe, A Fenster, and H. Johns. “Xenon ionization detectors for fan beam computed tomography scanners”. In: *Journal of Computer Assisted Tomography* 1.4 (1977), pp. 419–428.

[351] C.-b. Yang, S. Zhang, Y.-j. Jia, Y. Yu, H.-f. Duan, X.-r. Zhang, G.-m. Ma, C. Ren, and N. Yu. "Dual energy spectral CT imaging for the evaluation of small hepatocellular carcinoma microvascular invasion". In: *European Journal of Radiology* 95 (2017), pp. 222–227.

[352] B. M. Yeh, P. F. FitzGerald, P. M. Edic, J. W. Lambert, R. E. Colborn, M. E. Marino, P. M. Evans, J. C. Roberts, Z. J. Wang, M. J. Wong, et al. "Opportunities for new CT contrast agents to maximize the diagnostic potential of emerging spectral CT technologies". In: *Advanced drug delivery reviews* 113 (2017), pp. 201–222.

[353] B. M. Yeh, J. A. Shepherd, Z. J. Wang, H. S. Teh, R. Hartman, and S. Prevrhal. "Dual energy and low kVp CT in the abdomen". In: *American Journal of Roentgenology* 193.1 (2009), p. 47.

[354] J. Yu, S. Lin, H. Lu, R. Wang, J. Liu, R. Gutjahr, and J. Gao. "Optimize scan timing in abdominal multiphase CT: Bolus tracking with an individualized post-trigger delay". In: *European Journal of Radiology* 148 (2022), p. 110139.

[355] L. Yu, J. A. Christner, S. Leng, J. Wang, J. G. Fletcher, and C. H. McCollough. "Virtual monochromatic imaging in dual-source dual-energy CT: radiation dose and image quality". In: *Medical Physics* 38.12 (2011), pp. 6371–6379.

[356] L. Yu, S. Leng, and C. H. McCollough. "Dual-energy CT–based monochromatic imaging". In: *American journal of Roentgenology* 199.5_supplement (2012), S9–S15.

[357] Z. Yu, S. Leng, S. M. Jorgensen, Z. Li, R. Gutjahr, B. Chen, X. Duan, A. Halaweish, L. Yu, E. L. Ritman, and C. McCollough. "Initial results from a prototype whole-body photon-counting computed tomography system". In: SPIE Medical Imaging (San Diego, California, USA, Feb. 21–26, 2015). 2015.

[358] Z. Yu, S. Leng, S. M. Jorgensen, Z. Li, R. Gutjahr, B. Chen, X. Duan, A. F. Halaweish, L. Yu, E. L. Ritman, and C. H. McCollough. "Initial results from a prototype whole-body photon-counting computed tomography system". In: *International Society for Optics and Photonics Medical Imaging*. International Society for Optics and Photonics. 2015, 94120W–94120W.

[359] Z. Yu, S. Leng, S. M. Jorgensen, Z. Li, R. Gutjahr, B. Chen, A. F. Halaweish, S. Kappler, L. Yu, E. L. Ritman, and C. H. McCollough. "Evaluation of conventional imaging performance in a research whole-body CT system with a photon-counting detector array". In: *Physics in Medicine and Biology* 61.4 (2016), p. 1572.

[360] Z. Yu, S. Leng, S. Kappler, K. Hahn, Z. Li, A. F. Halaweish, A. Henning, and C. H. McCollough. "Noise performance of low-dose CT: comparison between an energy integrating detector and a photon counting detector using a whole-body research photon counting CT scanner". In: *Journal of Medical Imaging* 3.4 (2016), p. 043503.

[361] Z. Yu, S. Leng, S. Kappler, K. Hahn, Z. Li, A. F. Halaweish, A. Henning, E. L. Ritman, and C. H. McCollough. "Low-dose performance of a whole-body research photon-counting CT scanner". In: *International Society for Optics and Photonics Medical Imaging*. International Society for Optics and Photonics. 2016, 97835Q–97835Q.

[362] Z. Yu, S. Leng, Z. Li, A. F. Halaweish, S. Kappler, E. L. Ritman, and C. H. McCollough. "How Low Can We Go in Radiation Dose for the Data-Completion Scan on a Research Whole-Body Photon-Counting Computed Tomography System." In: *Journal of Computer Assisted Tomography* (2016).

[363] Z. Yu, S. Leng, Z. Li, E. L. Ritman, and C. H. McCollough. "Spectral PICCS Reconstruction for PCCT". In: 2nd Workshop on Medical Applications of Spectroscopic X-ray Detectors (CERN, Geneva, Swiss). 2015.

[364] N. Z. Yussefian and J. Tanguay. "An experimental framework for assessing the detective quantum efficiency of spectroscopic x-ray detectors". In: *Medical Physics* (2022).

[365] C. A. Zarse, J. A. McAteer, A. J. Sommer, S. C. Kim, E. K. Hatt, J. E. Lingeman, A. P. Evan, and J. C. Williams. “Nondestructive analysis of urinary calculi using micro computed tomography”. In: *BMC Urology* 4.1 (2004), p. 1.

[366] L. M. Zatz. “The Effect of the kVp Level on EMI Values: Selective Imaging of Various Materials with Different kVp Settings 1”. In: *Radiology* 119.3 (1976), pp. 683–688.

[367] X. Zhan, R. Zhang, X. Niu, I. Hein, B. Budden, S. Wu, N. Markov, C. Clarke, Y. Qiang, H. Taguchi, et al. “Comprehensive evaluations of a prototype full field-of-view photon counting CT system through phantom studies”. In: *arXiv preprint arXiv:2212.13337* (2022).

[368] D. Zhang, X. Li, and B. Liu. “Objective characterization of GE discovery CT750 HD scanner: gemstone spectral imaging mode”. In: *Medical Physics* 38.3 (2011), pp. 1178–1188.

[369] S. Zhang, D. C. Levin, E. J. Halpern, D. Fischman, M. Savage, P. Walinsky, et al. “Accuracy of MDCT in assessing the degree of stenosis caused by calcified coronary artery plaques.” In: *American Journal of Roentgenology* 191.6 (2008), p. 1676.

[370] W. Zhou, J. Montoya, R. Gutjahr, A. Ferrero, A. Halaweish, S. Kappler, C. H. McCollough, and S. Leng. “Lung nodule volume quantification and shape differentiation with an ultra-high resolution technique on a photon-counting detector computed tomography system”. In: *Journal of Medical Imaging* 4.4 (2017), p. 043502.

[371] Z. Zhou, W. Yan, Y. Zhou, F. Zhang, H. Li, and Z. Ji. “125I low-dose-rate prostate brachytherapy and radical prostatectomy in patients with prostate cancer”. In: *Oncology letters* 18.1 (2019), pp. 72–80.

[372] Y. Zou and M. D. Silver. “Analysis of fast kV-switching in dual energy CT using a pre-reconstruction decomposition technique”. In: *Medical Imaging*. International Society for Optics and Photonics. 2008, pp. 691313–691313.

Reprint permissions

A

Gutjahr, Ralf

From: Karleena Burdick <karleenab@spie.org>
Sent: Wednesday, November 8, 2023 22:50
To: Gutjahr, Ralf
Subject: RE: Permission Request for Article Reprint in Cumulative Doctoral Thesis

Dear Ralf Gutjahr,

Thank you for seeking permission from SPIE to reprint material from our publications. SPIE shares the copyright with you, so as author you retain the right to reproduce your paper in part or in whole.

Publisher's permission is hereby granted under the following conditions:
(1) the material to be used has appeared in our publication without credit or acknowledgment to another source; and
(2) you credit the original SPIE publication. Include the authors' names, title of paper, volume title, SPIE volume number, and year of publication in your credit statement.

Please let me know if I may be of any further assistance.

Best,
Karleena Burdick
Editorial Assistant, Publications
SPIE – the international society for optics and photonics
karleenab@spie.org
1 360 685 5515
SPIE.

From: Gutjahr, Ralf <ralf.gutjahr@siemens-healthineers.com>
Sent: Wednesday, November 8, 2023 10:21 AM
To: reprint_permission <reprint_permission@spie.org>
Subject: Permission Request for Article Reprint in Cumulative Doctoral Thesis

Dear contact from SPIE. Digital Library,

I hope this message finds you well.

I am writing to request permission to reprint the article titled "Material decomposition and virtual non-contrast imaging in photon counting computed tomography: an animal study," which I co-authored and was published in your esteemed journal on March 25, 2016. This article is a significant component of my cumulative doctoral thesis at the Technical University of Munich.

Unfortunately, I encountered difficulty in securing permission through the usual channels, as the article does not appear to be available on the CCC Marketplace, where I was directed by your journal's reprint policies.

Given the circumstances, I am reaching out to you directly to request the necessary permission to include this article in my thesis. My doctoral work is an academic pursuit, and the thesis will be submitted to the university for evaluation and approval. It will not be used for commercial purposes.

Here are the details of the publication in question:

- Title: Material decomposition and virtual non-contrast imaging in photon counting computed tomography: an animal study
- Published on: March 25, 2016
- https://doi.org/10.1117/12.2216861
- SPIE Digital Library URL: https://www.spiedigitallibrary.org/conference-proceedings-of-spie/9783/97831G/Material-decomposition-and-virtual-non-contrast-imaging-in-photon-counting/10.1117/12.2216861.short

To comply with your copyright policy and to appropriately credit the source, I will ensure that the reprinted article includes full citation and attribution as per the journal's requirements. Furthermore, if there are any specific conditions or forms that I need to complete to process this request, please kindly direct me to them or provide me with the necessary documentation.

I deeply appreciate your assistance and the work that your team does in disseminating important scientific research. I am hopeful that you will grant this permission, which will greatly contribute to the scholarly content of my doctoral thesis.

Thank you for considering my request. I look forward to your positive response and any further instructions you may have.

Warm regards,
Ralf Gutjahr

Marketplace

This is a License Agreement between Ralf Gutjahr ("User") and Copyright Clearance Center, Inc. ("CCC") on behalf of the Rightsholder identified in the order details below. The license consists of the order details, the Marketplace Permissions General Terms and Conditions below, and any Rightsholder Terms and Conditions which are included below.

All payments must be made in full to CCC in accordance with the Marketplace Permissions General Terms and Conditions below.

Order Date	08-Jan-2024	**Type of Use**	Republish in a thesis/dissertation
Order License ID	1435480-2		
ISSN	0277-786X	**Publisher**	SPIE
		Portion	Chapter/article

LICENSED CONTENT

Publication Title	Proceedings of SPIE, Regular series	**Publication Type**	Conference Proceeding
		Volume	10132
Article Title	Dual Energy CT Kidney Stone Differentiation in Photon Counting Computed Tomography.	**URL**	https://www.spiedigitallibrary.org/conference-proceedings-of-spie
Date	01/01/1963		
Rightsholder	SPIE		

REQUEST DETAILS

Portion Type	Chapter/article	**Rights Requested**	Main product
Page Range(s)	1-13	**Distribution**	Worldwide
Total Number of Pages	13	**Translation**	Original language of publication
Format (select all that apply)	Print, Electronic	**Copies for the Disabled?**	No
Who Will Republish the Content?	Academic institution	**Minor Editing Privileges?**	No
Duration of Use	Life of current edition	**Incidental Promotional Use?**	No
Lifetime Unit Quantity	Up to 499	**Currency**	EUR

NEW WORK DETAILS

Title	Energy-selective processing of CT images for clinical applications	**Institution Name**	Technical University Munich
		Expected Presentation Date	2024-04-01
Instructor Name	Ralf Gutjahr		

ADDITIONAL DETAILS

The Requesting Person / Organization to Appear on the License	Ralf Gutjahr

REQUESTED CONTENT DETAILS

Title, Description or Numeric Reference of the Portion(s)	Dual Energy CT Kidney Stone Differentiation in Photon Counting Computed Tomography.	**Title of the Article / Chapter the Portion Is From**	Dual Energy CT Kidney Stone Differentiation in Photon Counting Computed Tomography.
Editor of Portion(s)	Gutjahr, R; Polster, C; Henning, A; Kappler, S; Leng, S; McCollough, C H; Sedlmair, M U; Schmidt, B; Krauss, B; Flohr, T G	**Author of Portion(s)**	Gutjahr, R; Polster, C; Henning, A; Kappler, S; Leng, S; McCollough, C H; Sedlmair, M U; Schmidt, B; Krauss, B; Flohr, T G
Volume / Edition	10132	**Publication Date of Portion**	2017-03-01
Page or Page Range of Portion	1-13		

Marketplace Permissions General Terms and Conditions

The following terms and conditions ("General Terms"), together with any applicable Publisher Terms and Conditions, govern User's use of Works pursuant to the Licenses granted by Copyright Clearance Center, Inc. ("CCC") on behalf of the applicable Rightsholders of such Works through CCC's applicable Marketplace transactional licensing services (each, a "Service").

1) **Definitions.** For purposes of these General Terms, the following definitions apply:

"License" is the licensed use the User obtains via the Marketplace platform in a particular licensing transaction, as set forth in the Order Confirmation.

"Order Confirmation" is the confirmation CCC provides to the User at the conclusion of each Marketplace transaction. "Order Confirmation Terms" are additional terms set forth on specific Order Confirmations not set forth in the General Terms that can include terms applicable to a particular CCC transactional licensing service and/or any Rightsholder-specific terms.

"Rightsholder(s)" are the holders of copyright rights in the Works for which a User obtains licenses via the Marketplace platform, which are displayed on specific Order Confirmations.

"Terms" means the terms and conditions set forth in these General Terms and any additional Order Confirmation Terms collectively.

"User" or "you" is the person or entity making the use granted under the relevant License. Where the person accepting the Terms on behalf of a User is a freelancer or other third party who the User authorized to accept the General Terms on the User's behalf, such person shall be deemed jointly a User for purposes of such Terms.

"Work(s)" are the copyright protected works described in relevant Order Confirmations.

2) **Description of Service.** CCC's Marketplace enables Users to obtain Licenses to use one or more Works in accordance with all relevant Terms. CCC grants Licenses as an agent on behalf of the copyright rightsholder identified in the relevant Order Confirmation.

3) **Applicability of Terms.** The Terms govern User's use of Works in connection with the relevant License. In the event of any conflict between General Terms and Order Confirmation Terms, the latter shall govern. User acknowledges that Rightsholders have complete discretion whether to grant any permission, and whether to place any limitations on any grant, and that CCC has no right to supersede or to modify any such discretionary act by a Rightsholder.

4) **Representations; Acceptance.** By using the Service, User represents and warrants that User has been duly authorized by the User to accept, and hereby does accept, all Terms.

5) **Scope of License; Limitations and Obligations.** All Works and all rights therein, including copyright rights, remain the sole and exclusive property of the Rightsholder. The License provides only those rights expressly set forth in the terms and conveys no other rights in any Works

6) **General Payment Terms.** User may pay at time of checkout by credit card or choose to be invoiced. If the User chooses to be invoiced, the User shall: (i) remit payments in the manner identified on specific invoices, (ii) unless otherwise specifically stated in an Order Confirmation or separate written agreement, Users shall remit payments upon receipt of the relevant invoice from CCC, either by delivery or notification of availability of the invoice via the Marketplace platform, and (iii) if the User does not pay the invoice within 30 days of receipt, the User may incur a service charge of 1.5% per month or the maximum rate allowed by applicable law, whichever is less. While User may exercise the rights in the License immediately upon receiving the Order Confirmation, the License is automatically revoked and is null and void, as if it had never been issued, if CCC does not receive complete payment on a timely basis.

7) **General Limits on Use.** Unless otherwise provided in the Order Confirmation, any grant of rights to User (i) involves only the rights set forth in the Terms and does not include subsequent or additional uses, (ii) is non-exclusive and non-transferable, and (iii) is subject to any and all limitations and restrictions (such as, but not limited to, limitations on duration of use or circulation) included in the Terms. Upon completion of the licensed use as set forth in the Order Confirmation, User shall either secure a new permission for further use of the Work(s) or immediately cease any new use of the Work(s) and shall render inaccessible (such as by deleting or by removing or severing links or other locators) any further copies of the Work. User may only make alterations to the Work if and as expressly set forth in the Order Confirmation. No Work may be used in any way that is unlawful, including without limitation if such use would violate applicable sanctions laws or regulations, would be defamatory, violate the rights of third parties (including such third parties' rights of copyright, privacy, publicity, or other tangible or intangible property), or is otherwise illegal, sexually explicit, or obscene. In addition, User may not conjoin a Work with any other material that may result in damage to the reputation of the Rightsholder. Any unlawful use will render any licenses hereunder null and void. User agrees to inform CCC if it becomes aware of any infringement of any rights in a Work and to cooperate with any reasonable request of CCC or the Rightsholder in connection therewith.

8) **Third Party Materials.** In the event that the material for which a License is sought includes third party materials (such as photographs, illustrations, graphs, inserts and similar materials) that are identified in such material as having been used by permission (or a similar indicator), User is responsible for identifying, and seeking separate licenses (under this Service, if available, or otherwise) for any of such third party materials; without a separate license, User may not use such third party materials via the License.

9) **Copyright Notice.** Use of proper copyright notice for a Work is required as a condition of any License granted under the Service. Unless otherwise provided in the Order Confirmation, a proper copyright notice will read substantially as follows: "Used with permission of [Rightsholder's name], from [Work's title, author, volume, edition number and year of copyright]; permission conveyed through Copyright Clearance Center, Inc." Such notice must be provided in a reasonably legible font size and must be placed either on a cover page or in another location that any person, upon gaining access to the material which is the subject of a permission, shall see, or in the case of republication Licenses, immediately adjacent to the Work as used (for example, as part of a by-line or footnote) or in the place where substantially all other credits or notices for the new work containing the republished Work are located. Failure to include the required notice results in loss to the Rightsholder and CCC, and the User shall be liable to pay liquidated damages for each such failure equal to twice the use fee specified in the Order Confirmation, in addition to the use fee itself and any other fees and charges specified.

10) **Indemnity.** User hereby indemnifies and agrees to defend the Rightsholder and CCC, and their respective employees and directors, against all claims, liability, damages, costs, and expenses, including legal fees and expenses, arising out of any use of a Work beyond the scope of the rights granted herein and in the Order Confirmation, or any use of a Work which has been altered in any unauthorized way by User, including claims of defamation or infringement of rights of copyright, publicity, privacy, or other tangible or intangible property.

11) **Limitation of Liability.** UNDER NO CIRCUMSTANCES WILL CCC OR THE RIGHTSHOLDER BE LIABLE FOR ANY DIRECT, INDIRECT, CONSEQUENTIAL, OR INCIDENTAL DAMAGES (INCLUDING WITHOUT LIMITATION DAMAGES FOR LOSS OF BUSINESS PROFITS OR INFORMATION, OR FOR BUSINESS INTERRUPTION) ARISING OUT OF THE USE OR INABILITY TO USE A WORK, EVEN IF ONE OR BOTH OF THEM HAS BEEN ADVISED OF THE POSSIBILITY OF SUCH DAMAGES. In any event, the total liability of the Rightsholder and CCC (including their respective employees and directors) shall not exceed the total amount actually paid by User for the relevant License. User assumes full liability for the actions and omissions of its principals, employees, agents, affiliates, successors, and assigns.

12) **Limited Warranties.** THE WORK(S) AND RIGHT(S) ARE PROVIDED "AS IS." CCC HAS THE RIGHT TO GRANT TO USER THE RIGHTS GRANTED IN THE ORDER CONFIRMATION DOCUMENT. CCC AND THE RIGHTSHOLDER DISCLAIM ALL OTHER WARRANTIES RELATING TO THE WORK(S) AND RIGHT(S), EITHER EXPRESS OR IMPLIED, INCLUDING WITHOUT LIMITATION IMPLIED WARRANTIES OF MERCHANTABILITY OR FITNESS FOR A PARTICULAR PURPOSE. ADDITIONAL RIGHTS MAY BE

REQUIRED TO USE ILLUSTRATIONS, GRAPHS, PHOTOGRAPHS, ABSTRACTS, INSERTS, OR OTHER PORTIONS OF THE WORK (AS OPPOSED TO THE ENTIRE WORK) IN A MANNER CONTEMPLATED BY USER; USER UNDERSTANDS AND AGREES THAT NEITHER CCC NOR THE RIGHTSHOLDER MAY HAVE SUCH ADDITIONAL RIGHTS TO GRANT.

13) **Effect of Breach.** Any failure by User to pay any amount when due, or any use by User of a Work beyond the scope of the License set forth in the Order Confirmation and/or the Terms, shall be a material breach of such License. Any breach not cured within 10 days of written notice thereof shall result in immediate termination of such License without further notice. Any unauthorized (but licensable) use of a Work that is terminated immediately upon notice thereof may be liquidated by payment of the Rightsholder's ordinary license price therefor; any unauthorized (and unlicensable) use that is not terminated immediately for any reason (including, for example, because materials containing the Work cannot reasonably be recalled) will be subject to all remedies available at law or in equity, but in no event to a payment of less than three times the Rightsholder's ordinary license price for the most closely analogous licensable use plus Rightsholder's and/or CCC's costs and expenses incurred in collecting such payment.

14) **Additional Terms for Specific Products and Services.** If a User is making one of the uses described in this Section 14, the additional terms and conditions apply:

a) ***Print Uses of Academic Course Content and Materials (photocopies for academic coursepacks or classroom handouts).*** For photocopies for academic coursepacks or classroom handouts the following additional terms apply:

i) The copies and anthologies created under this License may be made and assembled by faculty members individually or at their request by on-campus bookstores or copy centers, or by off-campus copy shops and other similar entities.

ii) No License granted shall in any way: (i) include any right by User to create a substantively non-identical copy of the Work or to edit or in any other way modify the Work (except by means of deleting material immediately preceding or following the entire portion of the Work copied) (ii) permit "publishing ventures" where any particular anthology would be systematically marketed at multiple institutions.

iii) Subject to any Publisher Terms (and notwithstanding any apparent contradiction in the Order Confirmation arising from data provided by User), any use authorized under the academic pay-per-use service is limited as follows:

A) any License granted shall apply to only one class (bearing a unique identifier as assigned by the institution, and thereby including all sections or other subparts of the class) at one institution;

B) use is limited to not more than 25% of the text of a book or of the items in a published collection of essays, poems or articles;

C) use is limited to no more than the greater of (a) 25% of the text of an issue of a journal or other periodical or (b) two articles from such an issue;

D) no User may sell or distribute any particular anthology, whether photocopied or electronic, at more than one institution of learning;

E) in the case of a photocopy permission, no materials may be entered into electronic memory by User except in order to produce an identical copy of a Work before or during the academic term (or analogous period) as to which any particular permission is granted. In the event that User shall choose to retain materials that are the subject of a photocopy permission in electronic memory for purposes of producing identical copies more than one day after such retention (but still within the scope of any permission granted), User must notify CCC of such fact in the applicable permission request and such retention shall constitute one copy actually sold for purposes of calculating permission fees due; and

F) any permission granted shall expire at the end of the class. No permission granted shall in any way include any right by User to create a substantively non-identical copy of the Work or to edit or in any other way modify the Work (except by means of deleting material immediately preceding or following the entire portion of the Work copied).

iv) Books and Records; Right to Audit. As to each permission granted under the academic pay-per-use Service, User shall maintain for at least four full calendar years books and records sufficient for CCC to determine the numbers of copies made by User under such permission. CCC and any representatives it may designate shall have the right to audit such books and records at any time during User's ordinary business hours, upon two days' prior

notice. If any such audit shall determine that User shall have underpaid for, or underreported, any photocopies sold or by three percent (3%) or more, then User shall bear all the costs of any such audit; otherwise, CCC shall bear the costs of any such audit. Any amount determined by such audit to have been underpaid by User shall immediately be paid to CCC by User, together with interest thereon at the rate of 10% per annum from the date such amount was originally due. The provisions of this paragraph shall survive the termination of this License for any reason.

b) ***Digital Pay-Per-Uses of Academic Course Content and Materials (e-coursepacks, electronic reserves, learning management systems, academic institution intranets).*** For uses in e-coursepacks, posts in electronic reserves, posts in learning management systems, or posts on academic institution intranets, the following additional terms apply:

i) The pay-per-uses subject to this Section 14(b) include:

A) **Posting e-reserves, course management systems, e-coursepacks for text-based content,** which grants authorizations to import requested material in electronic format, and allows electronic access to this material to members of a designated college or university class, under the direction of an instructor designated by the college or university, accessible only under appropriate electronic controls (e.g., password);

B) **Posting e-reserves, course management systems, e-coursepacks for material consisting of photographs or other still images not embedded in text,** which grants not only the authorizations described in Section 14(b)(i)(A) above, but also the following authorization: to include the requested material in course materials for use consistent with Section 14(b)(i)(A) above, including any necessary resizing, reformatting or modification of the resolution of such requested material (provided that such modification does not alter the underlying editorial content or meaning of the requested material, and provided that the resulting modified content is used solely within the scope of, and in a manner consistent with, the particular authorization described in the Order Confirmation and the Terms), but not including any other form of manipulation, alteration or editing of the requested material;

C) **Posting e-reserves, course management systems, e-coursepacks or other academic distribution for audiovisual content,** which grants not only the authorizations described in Section 14(b)(i)(A) above, but also the following authorizations: (i) to include the requested material in course materials for use consistent with Section 14(b)(i)(A) above; (ii) to display and perform the requested material to such members of such class in the physical classroom or remotely by means of streaming media or other video formats; and (iii) to "clip" or reformat the requested material for purposes of time or content management or ease of delivery, provided that such "clipping" or reformatting does not alter the underlying editorial content or meaning of the requested material and that the resulting material is used solely within the scope of, and in a manner consistent with, the particular authorization described in the Order Confirmation and the Terms. Unless expressly set forth in the relevant Order Conformation, the License does not authorize any other form of manipulation, alteration or editing of the requested material.

ii) Unless expressly set forth in the relevant Order Confirmation, no License granted shall in any way: (i) include any right by User to create a substantively non-identical copy of the Work or to edit or in any other way modify the Work (except by means of deleting material immediately preceding or following the entire portion of the Work copied or, in the case of Works subject to Sections 14(b)(1)(B) or (C) above, as described in such Sections) (ii) permit "publishing ventures" where any particular course materials would be systematically marketed at multiple institutions.

iii) Subject to any further limitations determined in the Rightsholder Terms (and notwithstanding any apparent contradiction in the Order Confirmation arising from data provided by User), any use authorized under the electronic course content pay-per-use service is limited as follows:

A) any License granted shall apply to only one class (bearing a unique identifier as assigned by the institution, and thereby including all sections or other subparts of the class) at one institution;

B) use is limited to not more than 25% of the text of a book or of the items in a published collection of essays, poems or articles;

C) use is limited to not more than the greater of (a) 25% of the text of an issue of a journal or other periodical or (b) two articles from such an issue;

D) no User may sell or distribute any particular materials, whether photocopied or electronic, at more than one institution of learning;

E) electronic access to material which is the subject of an electronic-use permission must be limited by means of electronic password, student identification or other control permitting access solely to students and instructors in the class;

F) User must ensure (through use of an electronic cover page or other appropriate means) that any person, upon gaining electronic access to the material, which is the subject of a permission, shall see:

- a proper copyright notice, identifying the Rightsholder in whose name CCC has granted permission,
- a statement to the effect that such copy was made pursuant to permission,
- a statement identifying the class to which the material applies and notifying the reader that the material has been made available electronically solely for use in the class, and
- a statement to the effect that the material may not be further distributed to any person outside the class, whether by copying or by transmission and whether electronically or in paper form, and User must also ensure that such cover page or other means will print out in the event that the person accessing the material chooses to print out the material or any part thereof.

G) any permission granted shall expire at the end of the class and, absent some other form of authorization, User is thereupon required to delete the applicable material from any electronic storage or to block electronic access to the applicable material.

iv) Uses of separate portions of a Work, even if they are to be included in the same course material or the same university or college class, require separate permissions under the electronic course content pay-per-use Service. Unless otherwise provided in the Order Confirmation, any grant of rights to User is limited to use completed no later than the end of the academic term (or analogous period) as to which any particular permission is granted.

v) Books and Records; Right to Audit. As to each permission granted under the electronic course content Service, User shall maintain for at least four full calendar years books and records sufficient for CCC to determine the numbers of copies made by User under such permission. CCC and any representatives it may designate shall have the right to audit such books and records at any time during User's ordinary business hours, upon two days' prior notice. If any such audit shall determine that User shall have underpaid for, or underreported, any electronic copies used by three percent (3%) or more, then User shall bear all the costs of any such audit; otherwise, CCC shall bear the costs of any such audit. Any amount determined by such audit to have been underpaid by User shall immediately be paid to CCC by User, together with interest thereon at the rate of 10% per annum from the date such amount was originally due. The provisions of this paragraph shall survive the termination of this license for any reason.

c) ***Pay-Per-Use Permissions for Certain Reproductions (Academic photocopies for library reserves and interlibrary loan reporting) (Non-academic internal/external business uses and commercial document delivery).*** The License expressly excludes the uses listed in Section (c)(i)-(v) below (which must be subject to separate license from the applicable Rightsholder) for: academic photocopies for library reserves and interlibrary loan reporting; and non-academic internal/external business uses and commercial document delivery.

i) electronic storage of any reproduction (whether in plain-text, PDF, or any other format) other than on a transitory basis;

ii) the input of Works or reproductions thereof into any computerized database;

iii) reproduction of an entire Work (cover-to-cover copying) except where the Work is a single article;

iv) reproduction for resale to anyone other than a specific customer of User;

v) republication in any different form. Please obtain authorizations for these uses through other CCC services or directly from the rightsholder.

Any license granted is further limited as set forth in any restrictions included in the Order Confirmation and/or in these Terms.

d) ***Electronic Reproductions in Online Environments (Non-Academic-email, intranet, internet and extranet).*** For "electronic reproductions", which generally includes e-mail use (including instant messaging or other electronic transmission to a defined group of recipients) or posting on an intranet, extranet or Intranet site (including any display or performance incidental thereto), the following additional terms apply:

i) Unless otherwise set forth in the Order Confirmation, the License is limited to use completed within 30 days for any use on the Internet, 60 days for any use on an intranet or extranet and one year for any other use, all as measured from the "republication date" as identified in the Order Confirmation, if any, and otherwise from the date of the Order Confirmation.

ii) User may not make or permit any alterations to the Work, unless expressly set forth in the Order Confirmation (after request by User and approval by Rightsholder); provided, however, that a Work consisting of photographs or other still images not embedded in text may, if necessary, be resized, reformatted or have its resolution modified without additional express permission, and a Work consisting of audiovisual content may, if necessary, be "clipped" or reformatted for purposes of time or content management or ease of delivery (provided that any such resizing, reformatting, resolution modification or "clipping" does not alter the underlying editorial content or meaning of the Work used, and that the resulting material is used solely within the scope of, and in a manner consistent with, the particular License described in the Order Confirmation and the Terms.

15) **Miscellaneous.**

a) User acknowledges that CCC may, from time to time, make changes or additions to the Service or to the Terms, and that Rightsholder may make changes or additions to the Rightsholder Terms. Such updated Terms will replace the prior terms and conditions in the order workflow and shall be effective as to any subsequent Licenses but shall not apply to Licenses already granted and paid for under a prior set of terms.

b) Use of User-related information collected through the Service is governed by CCC's privacy policy, available online at www.copyright.com/about/privacy-policy/.

c) The License is personal to User. Therefore, User may not assign or transfer to any other person (whether a natural person or an organization of any kind) the License or any rights granted thereunder; provided, however, that, where applicable, User may assign such License in its entirety on written notice to CCC in the event of a transfer of all or substantially all of User's rights in any new material which includes the Work(s) licensed under this Service.

d) No amendment or waiver of any Terms is binding unless set forth in writing and signed by the appropriate parties, including, where applicable, the Rightsholder. The Rightsholder and CCC hereby object to any terms contained in any writing prepared by or on behalf of the User or its principals, employees, agents or affiliates and purporting to govern or otherwise relate to the License described in the Order Confirmation, which terms are in any way inconsistent with any Terms set forth in the Order Confirmation, and/or in CCC's standard operating procedures, whether such writing is prepared prior to, simultaneously with or subsequent to the Order Confirmation, and whether such writing appears on a copy of the Order Confirmation or in a separate instrument.

e) The License described in the Order Confirmation shall be governed by and construed under the law of the State of New York, USA, without regard to the principles thereof of conflicts of law. Any case, controversy, suit, action, or proceeding arising out of, in connection with, or related to such License shall be brought, at CCC's sole discretion, in any federal or state court located in the County of New York, State of New York, USA, or in any federal or state court whose geographical jurisdiction covers the location of the Rightsholder set forth in the Order Confirmation. The parties expressly submit to the personal jurisdiction and venue of each such federal or state court.

Last updated October 2022

Order Date	08-Jan-2024	**Type of Use**	Republish in a thesis/dissertation
Order License ID	1435508-1		
ISSN	1878-4046	**Publisher**	Elsevier
		Portion	Chapter/article

LICENSED CONTENT

Publication Title	Academic radiology	**Publication Type**	e-Journal
Article Title	Characterization of Urinary Stone Composition by Use of Whole-body, Photon-counting Detector CT.	**Start Page**	1270
		End Page	1276
		Issue	10
		Volume	25
Author/Editor	Association of University Radiologists., Society of Chairmen of Academic Radiology Departments., Association of Program Directors in Radiology., American Association of Academic Chief Residents in Radiology., Alliance of Medical Student Educators in Radiology., Radiology Research Alliance., Radiology Alliance for Health Services Research.	**URL**	http://www.sciencedirect.com/science/journal/10766332
Date	01/01/1994		
Language	English		
Country	Netherlands		
Rightsholder	Elsevier Science & Technology Journals		

REQUEST DETAILS

Portion Type	Chapter/article	**Rights Requested**	Main product
Page Range(s)	1-7	**Distribution**	Worldwide
Total Number of Pages	7	**Translation**	Original language of publication
Format (select all that apply)	Print, Electronic	**Copies for the Disabled?**	No
Who Will Republish the Content?	Academic institution	**Minor Editing Privileges?**	No

Duration of Use	Life of current edition	**Incidental Promotional Use?**	No
Lifetime Unit Quantity	Up to 499	**Currency**	EUR

NEW WORK DETAILS

Title	Energy-selective processing of CT images for clinical applications	**Institution Name**	Technical University Munich
Instructor Name	Ralf Gutjahr	**Expected Presentation Date**	2024-04-01

ADDITIONAL DETAILS

Order Reference Number	N/A	**The Requesting Person / Organization to Appear on the License**	Ralf Gutjahr

REQUESTED CONTENT DETAILS

Title, Description or Numeric Reference of the Portion(s)	Characterization of Urinary Stone Composition by Use of Whole-body, Photon-counting Detector CT	**Title of the Article / Chapter the Portion Is From**	Characterization of Urinary Stone Composition by Use of Whole-body, Photon-counting Detector CT.
Editor of Portion(s)	Ralf Gutjahr	**Author of Portion(s)**	Ferrero, Andrea; Gutjahr, Ralf; Halaweish, Ahmed F.; Leng, Shuai; McCollough, Cynthia H.
Volume / Edition	25		
Page or Page Range of Portion	1-9	**Issue, if Republishing an Article From a Serial**	10
		Publication Date of Portion	2018-10-01

RIGHTSHOLDER TERMS AND CONDITIONS

Elsevier publishes Open Access articles in both its Open Access journals and via its Open Access articles option in subscription journals, for which an author selects a user license permitting certain types of reuse without permission. Before proceeding please check if the article is Open Access on http://www.sciencedirect.com and refer to the user license for the individual article. Any reuse not included in the user license terms will require permission. You must always fully and appropriately credit the author and source. If any part of the material to be used (for example, figures) has appeared in the Elsevier publication for which you are seeking permission, with credit or acknowledgement to another source it is the responsibility of the user to ensure their reuse complies with the terms and conditions determined by the rights holder. Please contact permissions@elsevier.com with any queries.

Marketplace Permissions General Terms and Conditions

The following terms and conditions ("General Terms"), together with any applicable Publisher Terms and Conditions, govern User's use of Works pursuant to the Licenses granted by Copyright Clearance Center, Inc. ("CCC") on behalf of the applicable Rightsholders of such Works through CCC's applicable Marketplace transactional licensing services (each, a "Service").

1) **Definitions.** For purposes of these General Terms, the following definitions apply:

"License" is the licensed use the User obtains via the Marketplace platform in a particular licensing transaction, as set forth in the Order Confirmation.

"Order Confirmation" is the confirmation CCC provides to the User at the conclusion of each Marketplace transaction. "Order Confirmation Terms" are additional terms set forth on specific Order Confirmations not set forth in the General Terms that can include terms applicable to a particular CCC transactional licensing service and/or any Rightsholder-specific terms.

"Rightsholder(s)" are the holders of copyright rights in the Works for which a User obtains licenses via the Marketplace platform, which are displayed on specific Order Confirmations.

"Terms" means the terms and conditions set forth in these General Terms and any additional Order Confirmation Terms collectively.

"User" or "you" is the person or entity making the use granted under the relevant License. Where the person accepting the Terms on behalf of a User is a freelancer or other third party who the User authorized to accept the General Terms on the User's behalf, such person shall be deemed jointly a User for purposes of such Terms.

"Work(s)" are the copyright protected works described in relevant Order Confirmations.

2) **Description of Service.** CCC's Marketplace enables Users to obtain Licenses to use one or more Works in accordance with all relevant Terms. CCC grants Licenses as an agent on behalf of the copyright rightsholder identified in the relevant Order Confirmation.

3) **Applicability of Terms.** The Terms govern User's use of Works in connection with the relevant License. In the event of any conflict between General Terms and Order Confirmation Terms, the latter shall govern. User acknowledges that Rightsholders have complete discretion whether to grant any permission, and whether to place any limitations on any grant, and that CCC has no right to supersede or to modify any such discretionary act by a Rightsholder.

4) **Representations; Acceptance.** By using the Service, User represents and warrants that User has been duly authorized by the User to accept, and hereby does accept, all Terms.

5) **Scope of License; Limitations and Obligations.** All Works and all rights therein, including copyright rights, remain the sole and exclusive property of the Rightsholder. The License provides only those rights expressly set forth in the terms and conveys no other rights in any Works

6) **General Payment Terms.** User may pay at time of checkout by credit card or choose to be invoiced. If the User chooses to be invoiced, the User shall: (i) remit payments in the manner identified on specific invoices, (ii) unless otherwise specifically stated in an Order Confirmation or separate written agreement, Users shall remit payments upon receipt of the relevant invoice from CCC, either by delivery or notification of availability of the invoice via the Marketplace platform, and (iii) if the User does not pay the invoice within 30 days of receipt, the User may incur a service charge of 1.5% per month or the maximum rate allowed by applicable law, whichever is less. While User may exercise the rights in the License immediately upon receiving the Order Confirmation, the License is automatically revoked and is null and void, as if it had never been issued, if CCC does not receive complete payment on a timely basis.

7) **General Limits on Use.** Unless otherwise provided in the Order Confirmation, any grant of rights to User (i) involves only the rights set forth in the Terms and does not include subsequent or additional uses, (ii) is non-exclusive and non-transferable, and (iii) is subject to any and all limitations and restrictions (such as, but not limited to, limitations on duration of use or circulation) included in the Terms. Upon completion of the licensed use as set forth in the Order Confirmation, User shall either secure a new permission for further use of the Work(s) or immediately cease any new use of the Work(s) and shall render inaccessible (such as by deleting or by removing or severing links or other locators) any further copies of the Work. User may only make alterations to the Work if and as expressly set forth in the Order Confirmation. No Work may be used in any way that is unlawful, including without limitation if such use would violate applicable sanctions laws or regulations, would be defamatory, violate the rights of third parties (including such third parties' rights of copyright, privacy, publicity, or other tangible or intangible property), or is otherwise illegal, sexually explicit, or obscene. In addition, User may not conjoin a Work with any other material that may result in damage to the reputation of the Rightsholder. Any unlawful use will render any licenses hereunder null and void. User agrees to inform CCC if it becomes aware of any infringement of any rights in a Work and to cooperate with any reasonable request of CCC or the Rightsholder in connection therewith.

8) **Third Party Materials.** In the event that the material for which a License is sought includes third party materials (such as photographs, illustrations, graphs, inserts and similar materials) that are identified in such material as having been used by permission (or a similar indicator), User is responsible for identifying, and seeking separate licenses (under this

Service, if available, or otherwise) for any of such third party materials; without a separate license, User may not use such third party materials via the License.

9) **Copyright Notice.** Use of proper copyright notice for a Work is required as a condition of any License granted under the Service. Unless otherwise provided in the Order Confirmation, a proper copyright notice will read substantially as follows: "Used with permission of [Rightsholder's name], from [Work's title, author, volume, edition number and year of copyright]; permission conveyed through Copyright Clearance Center, Inc." Such notice must be provided in a reasonably legible font size and must be placed either on a cover page or in another location that any person, upon gaining access to the material which is the subject of a permission, shall see, or in the case of republication Licenses, immediately adjacent to the Work as used (for example, as part of a by-line or footnote) or in the place where substantially all other credits or notices for the new work containing the republished Work are located. Failure to include the required notice results in loss to the Rightsholder and CCC, and the User shall be liable to pay liquidated damages for each such failure equal to twice the use fee specified in the Order Confirmation, in addition to the use fee itself and any other fees and charges specified.

10) **Indemnity.** User hereby indemnifies and agrees to defend the Rightsholder and CCC, and their respective employees and directors, against all claims, liability, damages, costs, and expenses, including legal fees and expenses, arising out of any use of a Work beyond the scope of the rights granted herein and in the Order Confirmation, or any use of a Work which has been altered in any unauthorized way by User, including claims of defamation or infringement of rights of copyright, publicity, privacy, or other tangible or intangible property.

11) **Limitation of Liability.** UNDER NO CIRCUMSTANCES WILL CCC OR THE RIGHTSHOLDER BE LIABLE FOR ANY DIRECT, INDIRECT, CONSEQUENTIAL, OR INCIDENTAL DAMAGES (INCLUDING WITHOUT LIMITATION DAMAGES FOR LOSS OF BUSINESS PROFITS OR INFORMATION, OR FOR BUSINESS INTERRUPTION) ARISING OUT OF THE USE OR INABILITY TO USE A WORK, EVEN IF ONE OR BOTH OF THEM HAS BEEN ADVISED OF THE POSSIBILITY OF SUCH DAMAGES. In any event, the total liability of the Rightsholder and CCC (including their respective employees and directors) shall not exceed the total amount actually paid by User for the relevant License. User assumes full liability for the actions and omissions of its principals, employees, agents, affiliates, successors, and assigns.

12) **Limited Warranties.** THE WORK(S) AND RIGHT(S) ARE PROVIDED "AS IS." CCC HAS THE RIGHT TO GRANT TO USER THE RIGHTS GRANTED IN THE ORDER CONFIRMATION DOCUMENT. CCC AND THE RIGHTSHOLDER DISCLAIM ALL OTHER WARRANTIES RELATING TO THE WORK(S) AND RIGHT(S), EITHER EXPRESS OR IMPLIED, INCLUDING WITHOUT LIMITATION IMPLIED WARRANTIES OF MERCHANTABILITY OR FITNESS FOR A PARTICULAR PURPOSE. ADDITIONAL RIGHTS MAY BE REQUIRED TO USE ILLUSTRATIONS, GRAPHS, PHOTOGRAPHS, ABSTRACTS, INSERTS, OR OTHER PORTIONS OF THE WORK (AS OPPOSED TO THE ENTIRE WORK) IN A MANNER CONTEMPLATED BY USER; USER UNDERSTANDS AND AGREES THAT NEITHER CCC NOR THE RIGHTSHOLDER MAY HAVE SUCH ADDITIONAL RIGHTS TO GRANT.

13) **Effect of Breach.** Any failure by User to pay any amount when due, or any use by User of a Work beyond the scope of the License set forth in the Order Confirmation and/or the Terms, shall be a material breach of such License. Any breach not cured within 10 days of written notice thereof shall result in immediate termination of such License without further notice. Any unauthorized (but licensable) use of a Work that is terminated immediately upon notice thereof may be liquidated by payment of the Rightsholder's ordinary license price therefor; any unauthorized (and unlicensable) use that is not terminated immediately for any reason (including, for example, because materials containing the Work cannot reasonably be recalled) will be subject to all remedies available at law or in equity, but in no event to a payment of less than three times the Rightsholder's ordinary license price for the most closely analogous licensable use plus Rightsholder's and/or CCC's costs and expenses incurred in collecting such payment.

14) **Additional Terms for Specific Products and Services.** If a User is making one of the uses described in this Section 14, the additional terms and conditions apply:

a) ***Print Uses of Academic Course Content and Materials (photocopies for academic coursepacks or classroom handouts).*** For photocopies for academic coursepacks or classroom handouts the following additional terms apply:

i) The copies and anthologies created under this License may be made and assembled by faculty members individually or at their request by on-campus bookstores or copy centers, or by off-campus copy shops and other similar entities.

ii) No License granted shall in any way: (i) include any right by User to create a substantively non-identical copy of the Work or to edit or in any other way modify the Work (except by means of deleting material immediately preceding or following the entire portion of the Work copied) (ii) permit "publishing ventures" where any particular anthology would be systematically marketed at multiple institutions.

iii) Subject to any Publisher Terms (and notwithstanding any apparent contradiction in the Order Confirmation arising from data provided by User), any use authorized under the academic pay-per-use service is limited as follows:

A) any License granted shall apply to only one class (bearing a unique identifier as assigned by the institution, and thereby including all sections or other subparts of the class) at one institution;

B) use is limited to not more than 25% of the text of a book or of the items in a published collection of essays, poems or articles;

C) use is limited to no more than the greater of (a) 25% of the text of an issue of a journal or other periodical or (b) two articles from such an issue;

D) no User may sell or distribute any particular anthology, whether photocopied or electronic, at more than one institution of learning;

E) in the case of a photocopy permission, no materials may be entered into electronic memory by User except in order to produce an identical copy of a Work before or during the academic term (or analogous period) as to which any particular permission is granted. In the event that User shall choose to retain materials that are the subject of a photocopy permission in electronic memory for purposes of producing identical copies more than one day after such retention (but still within the scope of any permission granted), User must notify CCC of such fact in the applicable permission request and such retention shall constitute one copy actually sold for purposes of calculating permission fees due; and

F) any permission granted shall expire at the end of the class. No permission granted shall in any way include any right by User to create a substantively non-identical copy of the Work or to edit or in any other way modify the Work (except by means of deleting material immediately preceding or following the entire portion of the Work copied).

iv) Books and Records; Right to Audit. As to each permission granted under the academic pay-per-use Service, User shall maintain for at least four full calendar years books and records sufficient for CCC to determine the numbers of copies made by User under such permission. CCC and any representatives it may designate shall have the right to audit such books and records at any time during User's ordinary business hours, upon two days' prior notice. If any such audit shall determine that User shall have underpaid for, or underreported, any photocopies sold or by three percent (3%) or more, then User shall bear all the costs of any such audit; otherwise, CCC shall bear the costs of any such audit. Any amount determined by such audit to have been underpaid by User shall immediately be paid to CCC by User, together with interest thereon at the rate of 10% per annum from the date such amount was originally due. The provisions of this paragraph shall survive the termination of this License for any reason.

b) ***Digital Pay-Per-Uses of Academic Course Content and Materials (e-coursepacks, electronic reserves, learning management systems, academic institution intranets).*** For uses in e-coursepacks, posts in electronic reserves, posts in learning management systems, or posts on academic institution intranets, the following additional terms apply:

i) The pay-per-uses subject to this Section 14(b) include:

A) **Posting e-reserves, course management systems, e-coursepacks for text-based content,** which grants authorizations to import requested material in electronic format, and allows electronic access to this material to members of a designated college or university class, under the direction of an instructor designated by the college or university, accessible only under appropriate electronic controls (e.g., password);

B) **Posting e-reserves, course management systems, e-coursepacks for material consisting of photographs or other still images not embedded in text,** which grants not only the authorizations described in Section 14(b)(i)(A) above, but also the following authorization: to include the requested material in course materials for use consistent with Section 14(b)(i)(A) above, including any necessary resizing, reformatting or modification of the resolution of such requested material (provided that such modification does not alter the underlying editorial content or meaning of the requested material, and provided that the resulting modified content is used solely within the scope of, and in a manner consistent with, the particular authorization described in the Order Confirmation and the Terms), but not including any other form of manipulation, alteration or editing of the requested material;

C) **Posting e-reserves, course management systems, e-coursepacks or other academic distribution for audiovisual content,** which grants not only the authorizations described in Section 14(b)(i)(A) above, but also the following authorizations: (i) to include the requested material in course materials for use consistent with Section 14(b)(i)(A) above; (ii) to display and perform the requested material to such members of such class in the physical classroom or remotely by means of streaming media or other video formats; and (iii) to "clip" or reformat the requested material for purposes of time or content management or ease of delivery, provided that such "clipping" or reformatting does not alter the underlying editorial content or meaning of the requested material and that the resulting material is used solely within the scope of, and in a manner consistent with, the particular authorization described in the Order Confirmation and the Terms. Unless expressly set forth in the relevant Order Conformation, the License does not authorize any other form of manipulation, alteration or editing of the requested material.

ii) Unless expressly set forth in the relevant Order Confirmation, no License granted shall in any way: (i) include any right by User to create a substantively non-identical copy of the Work or to edit or in any other way modify the Work (except by means of deleting material immediately preceding or following the entire portion of the Work copied or, in the case of Works subject to Sections 14(b)(1)(B) or (C) above, as described in such Sections) (ii) permit "publishing ventures" where any particular course materials would be systematically marketed at multiple institutions.

iii) Subject to any further limitations determined in the Rightsholder Terms (and notwithstanding any apparent contradiction in the Order Confirmation arising from data provided by User), any use authorized under the electronic course content pay-per-use service is limited as follows:

A) any License granted shall apply to only one class (bearing a unique identifier as assigned by the institution, and thereby including all sections or other subparts of the class) at one institution;

B) use is limited to not more than 25% of the text of a book or of the items in a published collection of essays, poems or articles;

C) use is limited to not more than the greater of (a) 25% of the text of an issue of a journal or other periodical or (b) two articles from such an issue;

D) no User may sell or distribute any particular materials, whether photocopied or electronic, at more than one institution of learning;

E) electronic access to material which is the subject of an electronic-use permission must be limited by means of electronic password, student identification or other control permitting access solely to students and instructors in the class;

F) User must ensure (through use of an electronic cover page or other appropriate means) that any person, upon gaining electronic access to the material, which is the subject of a permission, shall see:

- a proper copyright notice, identifying the Rightsholder in whose name CCC has granted permission,
- a statement to the effect that such copy was made pursuant to permission,
- a statement identifying the class to which the material applies and notifying the reader that the material has been made available electronically solely for use in the class, and
- a statement to the effect that the material may not be further distributed to any person outside the class, whether by copying or by transmission and whether electronically or in paper form, and User must also ensure that such cover page or other means will print out in the event that the person accessing the material chooses to print out the material or any part thereof.

G) any permission granted shall expire at the end of the class and, absent some other form of authorization, User is thereupon required to delete the applicable material from any electronic storage or to block electronic access to the applicable material.

iv) Uses of separate portions of a Work, even if they are to be included in the same course material or the same university or college class, require separate permissions under the electronic course content pay-per-use Service.

Unless otherwise provided in the Order Confirmation, any grant of rights to User is limited to use completed no later than the end of the academic term (or analogous period) as to which any particular permission is granted.

v) Books and Records; Right to Audit. As to each permission granted under the electronic course content Service, User shall maintain for at least four full calendar years books and records sufficient for CCC to determine the numbers of copies made by User under such permission. CCC and any representatives it may designate shall have the right to audit such books and records at any time during User's ordinary business hours, upon two days' prior notice. If any such audit shall determine that User shall have underpaid for, or underreported, any electronic copies used by three percent (3%) or more, then User shall bear all the costs of any such audit; otherwise, CCC shall bear the costs of any such audit. Any amount determined by such audit to have been underpaid by User shall immediately be paid to CCC by User, together with interest thereon at the rate of 10% per annum from the date such amount was originally due. The provisions of this paragraph shall survive the termination of this license for any reason.

c) ***Pay-Per-Use Permissions for Certain Reproductions (Academic photocopies for library reserves and interlibrary loan reporting) (Non-academic internal/external business uses and commercial document delivery).*** The License expressly excludes the uses listed in Section (c)(i)-(v) below (which must be subject to separate license from the applicable Rightsholder) for: academic photocopies for library reserves and interlibrary loan reporting; and non-academic internal/external business uses and commercial document delivery.

i) electronic storage of any reproduction (whether in plain-text, PDF, or any other format) other than on a transitory basis;

ii) the input of Works or reproductions thereof into any computerized database;

iii) reproduction of an entire Work (cover-to-cover copying) except where the Work is a single article;

iv) reproduction for resale to anyone other than a specific customer of User;

v) republication in any different form. Please obtain authorizations for these uses through other CCC services or directly from the rightsholder.

Any license granted is further limited as set forth in any restrictions included in the Order Confirmation and/or in these Terms.

d) ***Electronic Reproductions in Online Environments (Non-Academic-email, intranet, internet and extranet).*** For "electronic reproductions", which generally includes e-mail use (including instant messaging or other electronic transmission to a defined group of recipients) or posting on an intranet, extranet or Intranet site (including any display or performance incidental thereto), the following additional terms apply:

i) Unless otherwise set forth in the Order Confirmation, the License is limited to use completed within 30 days for any use on the Internet, 60 days for any use on an intranet or extranet and one year for any other use, all as measured from the "republication date" as identified in the Order Confirmation, if any, and otherwise from the date of the Order Confirmation.

ii) User may not make or permit any alterations to the Work, unless expressly set forth in the Order Confirmation (after request by User and approval by Rightsholder); provided, however, that a Work consisting of photographs or other still images not embedded in text may, if necessary, be resized, reformatted or have its resolution modified without additional express permission, and a Work consisting of audiovisual content may, if necessary, be "clipped" or reformatted for purposes of time or content management or ease of delivery (provided that any such resizing, reformatting, resolution modification or "clipping" does not alter the underlying editorial content or meaning of the Work used, and that the resulting material is used solely within the scope of, and in a manner consistent with, the particular License described in the Order Confirmation and the Terms.

15) **Miscellaneous.**

a) User acknowledges that CCC may, from time to time, make changes or additions to the Service or to the Terms, and that Rightsholder may make changes or additions to the Rightsholder Terms. Such updated Terms will replace the prior terms and conditions in the order workflow and shall be effective as to any subsequent Licenses but shall not apply to Licenses already granted and paid for under a prior set of terms.

b) Use of User-related information collected through the Service is governed by CCC's privacy policy, available online at www.copyright.com/about/privacy-policy/.

c) The License is personal to User. Therefore, User may not assign or transfer to any other person (whether a natural person or an organization of any kind) the License or any rights granted thereunder; provided, however, that, where applicable, User may assign such License in its entirety on written notice to CCC in the event of a transfer of all or substantially all of User's rights in any new material which includes the Work(s) licensed under this Service.

d) No amendment or waiver of any Terms is binding unless set forth in writing and signed by the appropriate parties, including, where applicable, the Rightsholder. The Rightsholder and CCC hereby object to any terms contained in any writing prepared by or on behalf of the User or its principals, employees, agents or affiliates and purporting to govern or otherwise relate to the License described in the Order Confirmation, which terms are in any way inconsistent with any Terms set forth in the Order Confirmation, and/or in CCC's standard operating procedures, whether such writing is prepared prior to, simultaneously with or subsequent to the Order Confirmation, and whether such writing appears on a copy of the Order Confirmation or in a separate instrument.

e) The License described in the Order Confirmation shall be governed by and construed under the law of the State of New York, USA, without regard to the principles thereof of conflicts of law. Any case, controversy, suit, action, or proceeding arising out of, in connection with, or related to such License shall be brought, at CCC's sole discretion, in any federal or state court located in the County of New York, State of New York, USA, or in any federal or state court whose geographical jurisdiction covers the location of the Rightsholder set forth in the Order Confirmation. The parties expressly submit to the personal jurisdiction and venue of each such federal or state court.

Last updated October 2022

CCC Marketplace

Order Number: 1435505
Order Date: 08 Jan 2024

Payment Information

Ralf Gutjahr
ralf.gutjahr@siemens-healthineers.com
Payment method: Invoice

Billing Address:
Mr. Ralf Gutjahr
Siemens Healthineers AG
Siemensstrasse 3
Forchheim, 91301
Germany

+49 15203672851
ralf.gutjahr@siemens-healthineers.com

Customer Location:
Mr. Ralf Gutjahr
Siemens Healthineers AG
Siemensstrasse 3
Forchheim, 91301
Germany

Order Details

1. Proceedings of SPIE, Regular series

Billing Status: Open

Article: Renal Stone Characterization using High Resolution Imaging Mode on a Photon Counting Detector CT System.

Order License ID	1435505-1	**Type of Use**	Republish in a thesis/dissertation
Order detail status	Completed	**Publisher**	SPIE
ISSN	0277-786X	**Portion**	Chapter/article

0,00 EUR
Republication Permission

LICENSED CONTENT

Publication Title	Proceedings of SPIE, Regular series	**Publication Type**	Conference Proceeding
Article Title	Renal Stone Characterization using High Resolution Imaging Mode on a Photon Counting Detector CT System.	**Volume**	10132
		URL	https://www.spiedigitallibrary.org/conference-proceedings-of-spie
Date	01/01/1963		
Rightsholder	SPIE		

REQUEST DETAILS

Portion Type	Chapter/article	**Rights Requested**	Main product
Page Range(s)	1-9	**Distribution**	Worldwide
Total Number of Pages	9	**Translation**	Original language of publication
Format (select all that apply)	Print, Electronic	**Copies for the Disabled?**	No
Who Will Republish the Content?	Academic institution	**Minor Editing Privileges?**	No
		Incidental Promotional Use?	No
Duration of Use	Life of current edition	**Currency**	EUR
Lifetime Unit Quantity	Up to 499		

NEW WORK DETAILS

Title	Energy-selective processing of CT images for clinical applications	**Institution Name**	Technical University Munich
		Expected Presentation Date	2024-04-01
Instructor Name	Ralf Gutjahr		

ADDITIONAL DETAILS

The Requesting Person / Organization to Appear on the License	Ralf Gutjahr

REQUESTED CONTENT DETAILS

Title, Description or Numeric Reference of the Portion(s)	Dual Energy CT Kidney Stone Differentiation in Photon Counting Computed Tomography.	**Title of the Article / Chapter the Portion Is From**	Renal Stone Characterization using High Resolution Imaging Mode on a Photon Counting Detector CT System.
Editor of Portion(s)	Ferrero, A; Gutjahr, R; Henning, A; Kappler, S; Halaweish, A; Abdurakhimova, D; Peterson, Z; Montoya, J; Leng, S; McCollough, C	**Author of Portion(s)**	Ferrero, A; Gutjahr, R; Henning, A; Kappler, S; Halaweish, A; Abdurakhimova, D; Peterson, Z; Montoya, J; Leng, S; McCollough, C
Volume / Edition	10132		
Page or Page Range of Portion	1-9	**Publication Date of Portion**	2017-03-09

Total Items: 1

Subtotal: 0,00 EUR

Order Total: 0,00 EUR

Marketplace Permissions General Terms and Conditions

The following terms and conditions ("General Terms"), together with any applicable Publisher Terms and Conditions, govern User's use of Works pursuant to the Licenses granted by Copyright Clearance Center, Inc. ("CCC") on behalf of the applicable Rightsholders of such Works through CCC's applicable Marketplace transactional licensing services (each, a "Service").

1) **Definitions.** For purposes of these General Terms, the following definitions apply:

"License" is the licensed use the User obtains via the Marketplace platform in a particular licensing transaction, as set forth in the Order Confirmation.

"Order Confirmation" is the confirmation CCC provides to the User at the conclusion of each Marketplace transaction. "Order Confirmation Terms" are additional terms set forth on specific Order Confirmations not set forth in the General Terms that can include terms applicable to a particular CCC transactional licensing service and/or any Rightsholder-specific terms.

"Rightsholder(s)" are the holders of copyright rights in the Works for which a User obtains licenses via the Marketplace platform, which are displayed on specific Order Confirmations.

"Terms" means the terms and conditions set forth in these General Terms and any additional Order Confirmation Terms collectively.

"User" or "you" is the person or entity making the use granted under the relevant License. Where the person accepting the Terms on behalf of a User is a freelancer or other third party who the User authorized to accept the General Terms on the User's behalf, such person shall be deemed jointly a User for purposes of such Terms.

"Work(s)" are the copyright protected works described in relevant Order Confirmations.

2) **Description of Service.** CCC's Marketplace enables Users to obtain Licenses to use one or more Works in accordance with all relevant Terms. CCC grants Licenses as an agent on behalf of the copyright rightsholder identified in the relevant Order Confirmation.

3) **Applicability of Terms.** The Terms govern User's use of Works in connection with the relevant License. In the event of any conflict between General Terms and Order Confirmation Terms, the latter shall govern. User acknowledges that Rightsholders have complete discretion whether to grant any permission, and whether to place any limitations on any grant, and that CCC has no right to supersede or to modify any such discretionary act by a Rightsholder.

4) **Representations; Acceptance.** By using the Service, User represents and warrants that User has been duly authorized by the User to accept, and hereby does accept, all Terms.

5) **Scope of License; Limitations and Obligations.** All Works and all rights therein, including copyright rights, remain the sole and exclusive property of the Rightsholder. The License provides only those rights expressly set forth in the terms and conveys no other rights in any Works

6) **General Payment Terms.** User may pay at time of checkout by credit card or choose to be invoiced. If the User chooses to be invoiced, the User shall: (i) remit payments in the manner identified on specific invoices, (ii) unless otherwise specifically stated in an Order Confirmation or separate written agreement, Users shall remit payments upon receipt of the relevant invoice from CCC, either by delivery or notification of availability of the invoice via the Marketplace platform, and (iii) if the User does not pay the invoice within 30 days of receipt, the User may incur a service charge of 1.5% per month or the maximum rate allowed by applicable law, whichever is less. While User may exercise the rights in the License immediately upon receiving the Order Confirmation, the License is automatically revoked and is null and void, as if it had never been issued, if CCC does not receive complete payment on a timely basis.

7) **General Limits on Use.** Unless otherwise provided in the Order Confirmation, any grant of rights to User (i) involves only the rights set forth in the Terms and does not include subsequent or additional uses, (ii) is non-exclusive and non-transferable, and (iii) is subject to any and all limitations and restrictions (such as, but not limited to, limitations on duration of use or circulation) included in the Terms. Upon completion of the licensed use as set forth in the Order Confirmation, User shall either secure a new permission for further use of the Work(s) or immediately cease any new use of the Work(s) and shall render inaccessible (such as by deleting or by removing or severing links or other locators) any further copies of the Work. User may only make alterations to the Work if and as expressly set forth in the Order Confirmation. No Work may be used in any way that is unlawful, including without limitation if such use would violate applicable sanctions laws or regulations, would be defamatory, violate the rights of third parties (including such third parties' rights of copyright, privacy, publicity, or other tangible or intangible property), or is otherwise illegal, sexually explicit, or obscene. In addition, User may not conjoin a Work with any other material that may result in damage to the reputation of the Rightsholder. Any unlawful use will render any licenses hereunder null and void. User agrees to inform CCC if it becomes aware of any infringement of any rights in a Work and to cooperate with any reasonable request of CCC or the Rightsholder in connection therewith.

8) **Third Party Materials.** In the event that the material for which a License is sought includes third party materials (such as photographs, illustrations, graphs, inserts and similar materials) that are identified in such material as having been used by permission (or a similar indicator), User is responsible for identifying, and seeking separate licenses (under this Service, if available, or otherwise) for any of such third party materials; without a separate license, User may not use such third party materials via the License.

9) **Copyright Notice.** Use of proper copyright notice for a Work is required as a condition of any License granted under the Service. Unless otherwise provided in the Order Confirmation, a proper copyright notice will read substantially as follows: "Used with permission of [Rightsholder's name], from [Work's title, author, volume, edition number and year of copyright]; permission conveyed through Copyright Clearance Center, Inc." Such notice must be provided in a reasonably legible font size and must be placed either on a cover page or in another location that any person, upon gaining access to the material which is the subject of a permission, shall see, or in the case of republication Licenses, immediately adjacent to the Work as used (for example, as part of a by-line or footnote) or in the place where substantially all other credits or notices for the new work containing the republished Work are located. Failure to include the required notice results in loss to the Rightsholder and CCC, and the User shall be liable to pay liquidated damages for each such failure equal to twice the use fee specified in the Order Confirmation, in addition to the use fee itself and any other fees and charges specified.

10) **Indemnity.** User hereby indemnifies and agrees to defend the Rightsholder and CCC, and their respective employees and directors, against all claims, liability, damages, costs, and expenses, including legal fees and expenses, arising out of any use of a Work beyond the scope of the rights granted herein and in the Order Confirmation, or any use of a Work which has been altered in any unauthorized way by User, including claims of defamation or infringement of rights of copyright, publicity, privacy, or other tangible or intangible property.

11) **Limitation of Liability.** UNDER NO CIRCUMSTANCES WILL CCC OR THE RIGHTSHOLDER BE LIABLE FOR ANY DIRECT, INDIRECT, CONSEQUENTIAL, OR INCIDENTAL DAMAGES (INCLUDING WITHOUT LIMITATION DAMAGES FOR LOSS OF BUSINESS PROFITS OR INFORMATION, OR FOR BUSINESS INTERRUPTION) ARISING OUT OF THE USE OR INABILITY TO USE A WORK, EVEN IF ONE OR BOTH OF THEM HAS BEEN ADVISED OF THE POSSIBILITY OF SUCH DAMAGES. In any event, the total liability of the Rightsholder and CCC (including their respective employees and directors) shall not exceed the total amount actually paid by User for the relevant License. User assumes full liability for the actions and omissions of its principals, employees, agents, affiliates, successors, and assigns.

12) **Limited Warranties.** THE WORK(S) AND RIGHT(S) ARE PROVIDED "AS IS." CCC HAS THE RIGHT TO GRANT TO USER THE RIGHTS GRANTED IN THE ORDER CONFIRMATION DOCUMENT. CCC AND THE RIGHTSHOLDER DISCLAIM ALL OTHER WARRANTIES RELATING TO THE WORK(S) AND RIGHT(S), EITHER EXPRESS OR IMPLIED, INCLUDING WITHOUT LIMITATION IMPLIED WARRANTIES OF MERCHANTABILITY OR FITNESS FOR A PARTICULAR PURPOSE. ADDITIONAL RIGHTS MAY BE REQUIRED TO USE ILLUSTRATIONS, GRAPHS, PHOTOGRAPHS, ABSTRACTS, INSERTS, OR OTHER PORTIONS OF THE WORK (AS OPPOSED TO THE ENTIRE WORK) IN A MANNER CONTEMPLATED BY USER; USER UNDERSTANDS AND AGREES THAT NEITHER CCC NOR THE RIGHTSHOLDER MAY HAVE SUCH ADDITIONAL RIGHTS TO GRANT.

13) **Effect of Breach.** Any failure by User to pay any amount when due, or any use by User of a Work beyond the scope of the License set forth in the Order Confirmation and/or the Terms, shall be a material breach of such License. Any breach not cured within 10 days of written notice thereof shall result in immediate termination of such License without further notice. Any unauthorized (but licensable) use of a Work that is terminated immediately upon notice thereof may be liquidated by payment of the Rightsholder's ordinary license price therefor; any unauthorized (and unlicensable) use that is not terminated immediately for any reason (including, for example, because materials containing the Work cannot reasonably be recalled) will be subject to all remedies available at law or in equity, but in no event to a payment of less than three times the Rightsholder's ordinary license price for the most closely analogous licensable use plus Rightsholder's and/or CCC's costs and expenses incurred in collecting such payment.

14) **Additional Terms for Specific Products and Services.** If a User is making one of the uses described in this Section 14, the additional terms and conditions apply:

a) ***Print Uses of Academic Course Content and Materials (photocopies for academic coursepacks or classroom handouts).*** For photocopies for academic coursepacks or classroom handouts the following additional terms apply:

i) The copies and anthologies created under this License may be made and assembled by faculty members individually or at their request by on-campus bookstores or copy centers, or by off-campus copy shops and other similar entities.

ii) No License granted shall in any way: (i) include any right by User to create a substantively non-identical copy of the Work or to edit or in any other way modify the Work (except by means of deleting material immediately preceding or following the entire portion of the Work copied) (ii) permit "publishing ventures" where any particular anthology would be systematically marketed at multiple institutions.

iii) Subject to any Publisher Terms (and notwithstanding any apparent contradiction in the Order Confirmation arising from data provided by User), any use authorized under the academic pay-per-use service is limited as follows:

A) any License granted shall apply to only one class (bearing a unique identifier as assigned by the institution, and thereby including all sections or other subparts of the class) at one institution;

B) use is limited to not more than 25% of the text of a book or of the items in a published collection of essays, poems or articles;

C) use is limited to no more than the greater of (a) 25% of the text of an issue of a journal or other periodical or (b) two articles from such an issue;

D) no User may sell or distribute any particular anthology, whether photocopied or electronic, at more than one institution of learning;

E) in the case of a photocopy permission, no materials may be entered into electronic memory by User except in order to produce an identical copy of a Work before or during the academic term (or analogous period) as to which any particular permission is granted. In the event that User shall choose to retain materials that are the subject of a photocopy permission in electronic memory for purposes of producing identical copies more than one day after such retention (but still within the scope of any permission granted), User must notify CCC of such fact in the applicable permission request and such retention shall constitute one copy actually sold for purposes of calculating permission fees due; and

F) any permission granted shall expire at the end of the class. No permission granted shall in any way include any right by User to create a substantively non-identical copy of the Work or to edit or in any other way modify the Work (except by means of deleting material immediately preceding or following the entire portion of the Work copied).

iv) Books and Records; Right to Audit. As to each permission granted under the academic pay-per-use Service, User shall maintain for at least four full calendar years books and records sufficient for CCC to determine the numbers of copies made by User under such permission. CCC and any representatives it may designate shall have the right to audit such books and records at any time during User's ordinary business hours, upon two days' prior notice. If any such audit shall determine that User shall have underpaid for, or underreported, any photocopies sold or by three percent (3%) or more, then User shall bear all the costs of any such audit; otherwise, CCC shall bear the costs of any such audit. Any amount determined by such audit to have been underpaid by User shall immediately be paid to CCC by User, together with interest thereon at the rate of 10% per annum from the date such amount was originally due. The provisions of this paragraph shall survive the termination of this License for any reason.

b) ***Digital Pay-Per-Uses of Academic Course Content and Materials (e-coursepacks, electronic reserves, learning management systems, academic institution intranets).*** For uses in e-coursepacks, posts in electronic reserves, posts in learning management systems, or posts on academic institution intranets, the following additional terms apply:

i) The pay-per-uses subject to this Section 14(b) include:

A) **Posting e-reserves, course management systems, e-coursepacks for text-based content,** which grants authorizations to import requested material in electronic format, and allows electronic access to this material to members of a designated

college or university class, under the direction of an instructor designated by the college or university, accessible only under appropriate electronic controls (e.g., password);

B) **Posting e-reserves, course management systems, e-coursepacks for material consisting of photographs or other still images not embedded in text,** which grants not only the authorizations described in Section 14(b)(i)(A) above, but also the following authorization: to include the requested material in course materials for use consistent with Section 14(b)(i)(A) above, including any necessary resizing, reformatting or modification of the resolution of such requested material (provided that such modification does not alter the underlying editorial content or meaning of the requested material, and provided that the resulting modified content is used solely within the scope of, and in a manner consistent with, the particular authorization described in the Order Confirmation and the Terms), but not including any other form of manipulation, alteration or editing of the requested material;

C) **Posting e-reserves, course management systems, e-coursepacks or other academic distribution for audiovisual content,** which grants not only the authorizations described in Section 14(b)(i)(A) above, but also the following authorizations: (i) to include the requested material in course materials for use consistent with Section 14(b)(i)(A) above; (ii) to display and perform the requested material to such members of such class in the physical classroom or remotely by means of streaming media or other video formats; and (iii) to "clip" or reformat the requested material for purposes of time or content management or ease of delivery, provided that such "clipping" or reformatting does not alter the underlying editorial content or meaning of the requested material and that the resulting material is used solely within the scope of, and in a manner consistent with, the particular authorization described in the Order Confirmation and the Terms. Unless expressly set forth in the relevant Order Conformation, the License does not authorize any other form of manipulation, alteration or editing of the requested material.

ii) Unless expressly set forth in the relevant Order Confirmation, no License granted shall in any way: (i) include any right by User to create a substantively non-identical copy of the Work or to edit or in any other way modify the Work (except by means of deleting material immediately preceding or following the entire portion of the Work copied or, in the case of Works subject to Sections 14(b)(1)(B) or (C) above, as described in such Sections) (ii) permit "publishing ventures" where any particular course materials would be systematically marketed at multiple institutions.

iii) Subject to any further limitations determined in the Rightsholder Terms (and notwithstanding any apparent contradiction in the Order Confirmation arising from data provided by User), any use authorized under the electronic course content pay-per-use service is limited as follows:

A) any License granted shall apply to only one class (bearing a unique identifier as assigned by the institution, and thereby including all sections or other subparts of the class) at one institution;

B) use is limited to not more than 25% of the text of a book or of the items in a published collection of essays, poems or articles;

C) use is limited to not more than the greater of (a) 25% of the text of an issue of a journal or other periodical or (b) two articles from such an issue;

D) no User may sell or distribute any particular materials, whether photocopied or electronic, at more than one institution of learning;

E) electronic access to material which is the subject of an electronic-use permission must be limited by means of electronic password, student identification or other control permitting access solely to students and instructors in the class;

F) User must ensure (through use of an electronic cover page or other appropriate means) that any person, upon gaining electronic access to the material, which is the subject of a permission, shall see:

- a proper copyright notice, identifying the Rightsholder in whose name CCC has granted permission,
- a statement to the effect that such copy was made pursuant to permission,
- a statement identifying the class to which the material applies and notifying the reader that the material has been made available electronically solely for use in the class, and
- a statement to the effect that the material may not be further distributed to any person outside the class, whether by copying or by transmission and whether electronically or in paper form, and User must also ensure that such cover page or other means will print out in the event that the person accessing the material chooses to print out the material or any part thereof.

G) any permission granted shall expire at the end of the class and, absent some other form of authorization, User is thereupon required to delete the applicable material from any electronic storage or to block electronic access to the applicable material.

iv) Uses of separate portions of a Work, even if they are to be included in the same course material or the same university or college class, require separate permissions under the electronic course content pay-per-use Service. Unless otherwise provided in the Order Confirmation, any grant of rights to User is limited to use completed no later than the end of the academic term (or analogous period) as to which any particular permission is granted.

v) Books and Records; Right to Audit. As to each permission granted under the electronic course content Service, User shall maintain for at least four full calendar years books and records sufficient for CCC to determine the numbers of copies made by User under such permission. CCC and any representatives it may designate shall have the right to audit such books and records at any time during User's ordinary business hours, upon two days' prior notice. If any such audit shall determine that User shall have underpaid for, or underreported, any electronic copies used by three percent (3%) or more, then User shall bear all the costs of any such audit; otherwise, CCC shall bear the costs of any such audit. Any amount determined by such audit to have been underpaid by User shall immediately be paid to CCC by User, together with interest thereon at the rate of 10% per annum from the date such amount was originally due. The provisions of this paragraph shall survive the termination of this license for any reason.

c) ***Pay-Per-Use Permissions for Certain Reproductions (Academic photocopies for library reserves and interlibrary loan reporting) (Non-academic internal/external business uses and commercial document delivery).*** The License expressly excludes the uses listed in Section (c)(i)-(v) below (which must be subject to separate license from the applicable Rightsholder) for: academic photocopies for library reserves and interlibrary loan reporting; and non-academic internal/external business uses and commercial document delivery.

i) electronic storage of any reproduction (whether in plain-text, PDF, or any other format) other than on a transitory basis;

ii) the input of Works or reproductions thereof into any computerized database;

iii) reproduction of an entire Work (cover-to-cover copying) except where the Work is a single article;

iv) reproduction for resale to anyone other than a specific customer of User;

v) republication in any different form. Please obtain authorizations for these uses through other CCC services or directly from the rightsholder.

Any license granted is further limited as set forth in any restrictions included in the Order Confirmation and/or in these Terms.

d) ***Electronic Reproductions in Online Environments (Non-Academic-email, intranet, internet and extranet).*** For "electronic reproductions", which generally includes e-mail use (including instant messaging or other electronic transmission to a defined group of recipients) or posting on an intranet, extranet or Intranet site (including any display or performance incidental thereto), the following additional terms apply:

i) Unless otherwise set forth in the Order Confirmation, the License is limited to use completed within 30 days for any use on the Internet, 60 days for any use on an intranet or extranet and one year for any other use, all as measured from the "republication date" as identified in the Order Confirmation, if any, and otherwise from the date of the Order Confirmation.

ii) User may not make or permit any alterations to the Work, unless expressly set forth in the Order Confirmation (after request by User and approval by Rightsholder); provided, however, that a Work consisting of photographs or other still images not embedded in text may, if necessary, be resized, reformatted or have its resolution modified without additional express permission, and a Work consisting of audiovisual content may, if necessary, be "clipped" or reformatted for purposes of time or content management or ease of delivery (provided that any such resizing, reformatting, resolution modification or "clipping" does not alter the underlying editorial content or meaning of the Work used, and that the resulting material is used solely within the scope of, and in a manner consistent with, the particular License described in the Order Confirmation and the Terms.

15) **Miscellaneous.**

a) User acknowledges that CCC may, from time to time, make changes or additions to the Service or to the Terms, and that Rightsholder may make changes or additions to the Rightsholder Terms. Such updated Terms will replace the prior terms and conditions in the order workflow and shall be effective as to any subsequent Licenses but shall not apply to Licenses already granted and paid for under a prior set of terms.

b) Use of User-related information collected through the Service is governed by CCC's privacy policy, available online at www.copyright.com/about/privacy-policy/.

c) The License is personal to User. Therefore, User may not assign or transfer to any other person (whether a natural person or an organization of any kind) the License or any rights granted thereunder; provided, however, that, where applicable, User may assign such License in its entirety on written notice to CCC in the event of a transfer of all or substantially all of User's rights in any new material which includes the Work(s) licensed under this Service.

d) No amendment or waiver of any Terms is binding unless set forth in writing and signed by the appropriate parties, including, where applicable, the Rightsholder. The Rightsholder and CCC hereby object to any terms contained in any writing prepared by or on behalf of the User or its principals, employees, agents or affiliates and purporting to govern or otherwise relate to the License described in the Order Confirmation, which terms are in any way inconsistent with any Terms set forth in the Order Confirmation, and/or in CCC's standard operating procedures, whether such writing is prepared prior to, simultaneously with or subsequent to the Order Confirmation, and whether such writing appears on a copy of the Order Confirmation or in a separate instrument.

e) The License described in the Order Confirmation shall be governed by and construed under the law of the State of New York, USA, without regard to the principles thereof of conflicts of law. Any case, controversy, suit, action, or proceeding arising out of, in connection with, or related to such License shall be brought, at CCC's sole discretion, in any federal or state court located in the County of New York, State of New York, USA, or in any federal or state court whose geographical jurisdiction covers the location of the Rightsholder set forth in the Order Confirmation. The parties expressly submit to the personal jurisdiction and venue of each such federal or state court.

Last updated October 2022

Order Date	10-Jan-2024	**Type of Use**	Republish in a thesis/dissertation
Order License ID	1436161-1		
ISSN	0938-7994	**Publisher**	SPRINGER-VERLAG
		Portion	Chapter/article

LICENSED CONTENT

Publication Title	European radiology	**Rightsholder**	Springer Nature BV
Article Title	Quantitative dual-energy CT material decomposition of holmium microspheres: local concentration determination evaluated in phantoms and a rabbit tumor model.	**Publication Type**	Journal
		Start Page	139
		End Page	148
		Issue	1
		Volume	31
Author/Editor	EUROPEAN ASSOCIATION OF RADIOLOGY., EUROPEAN CONGRESS OF RADIOLOGY.		
Date	01/01/1991		
Language	English		
Country	Germany		

REQUEST DETAILS

Portion Type	Chapter/article	**Rights Requested**	Main product
Page Range(s)	1-10	**Distribution**	Worldwide
Total Number of Pages	10	**Translation**	Original language of publication
Format (select all that apply)	Print, Electronic	**Copies for the Disabled?**	No
Who Will Republish the Content?	Academic institution	**Minor Editing Privileges?**	No
Duration of Use	Life of current edition	**Incidental Promotional Use?**	No
Lifetime Unit Quantity	Up to 499	**Currency**	EUR

NEW WORK DETAILS

Title	Energy-selective processing of CT images for clinical applications	**Institution Name**	Technical University Munich

Instructor Name	Ralf Gutjahr	**Expected Presentation Date**	2024-04-01

ADDITIONAL DETAILS

The Requesting Person / Organization to Appear on the License	Ralf Gutjahr

REQUESTED CONTENT DETAILS

Title, Description or Numeric Reference of the Portion(s)	Quantitative dual-energy CT material decomposition of holmium microspheres: local concentration determination evaluated in phantoms and a rabbit tumor model.	**Title of the Article / Chapter the Portion Is From**	Quantitative dual-energy CT material decomposition of holmium microspheres: local concentration determination evaluated in phantoms and a rabbit tumor model.
Editor of Portion(s)	Gutjahr, Ralf; Bakker, Robbert C.; Tiessens, Feiko; van Nimwegen, Sebastiaan A.; Schmidt, Bernhard; Nijsen, Johannes Frank Wilhelmus	**Author of Portion(s)**	Gutjahr, Ralf; Bakker, Robbert C.; Tiessens, Feiko; van Nimwegen, Sebastiaan A.; Schmidt, Bernhard; Nijsen, Johannes Frank Wilhelmus
Volume / Edition	31	**Publication Date of Portion**	2021-01-01
Page or Page Range of Portion	139-148		

Marketplace Permissions General Terms and Conditions

The following terms and conditions ("General Terms"), together with any applicable Publisher Terms and Conditions, govern User's use of Works pursuant to the Licenses granted by Copyright Clearance Center, Inc. ("CCC") on behalf of the applicable Rightsholders of such Works through CCC's applicable Marketplace transactional licensing services (each, a "Service").

1) **Definitions.** For purposes of these General Terms, the following definitions apply:

"License" is the licensed use the User obtains via the Marketplace platform in a particular licensing transaction, as set forth in the Order Confirmation.

"Order Confirmation" is the confirmation CCC provides to the User at the conclusion of each Marketplace transaction. "Order Confirmation Terms" are additional terms set forth on specific Order Confirmations not set forth in the General Terms that can include terms applicable to a particular CCC transactional licensing service and/or any Rightsholder-specific terms.

"Rightsholder(s)" are the holders of copyright rights in the Works for which a User obtains licenses via the Marketplace platform, which are displayed on specific Order Confirmations.

"Terms" means the terms and conditions set forth in these General Terms and any additional Order Confirmation Terms collectively.

"User" or "you" is the person or entity making the use granted under the relevant License. Where the person accepting the Terms on behalf of a User is a freelancer or other third party who the User authorized to accept the General Terms on the User's behalf, such person shall be deemed jointly a User for purposes of such Terms.

"Work(s)" are the copyright protected works described in relevant Order Confirmations.

2) **Description of Service.** CCC's Marketplace enables Users to obtain Licenses to use one or more Works in accordance with all relevant Terms. CCC grants Licenses as an agent on behalf of the copyright rightsholder identified in the relevant Order Confirmation.

3) **Applicability of Terms.** The Terms govern User's use of Works in connection with the relevant License. In the event of any conflict between General Terms and Order Confirmation Terms, the latter shall govern. User acknowledges that Rightsholders have complete discretion whether to grant any permission, and whether to place any limitations on any grant, and that CCC has no right to supersede or to modify any such discretionary act by a Rightsholder.

4) **Representations; Acceptance.** By using the Service, User represents and warrants that User has been duly authorized by the User to accept, and hereby does accept, all Terms.

5) **Scope of License; Limitations and Obligations.** All Works and all rights therein, including copyright rights, remain the sole and exclusive property of the Rightsholder. The License provides only those rights expressly set forth in the terms and conveys no other rights in any Works

6) **General Payment Terms.** User may pay at time of checkout by credit card or choose to be invoiced. If the User chooses to be invoiced, the User shall: (i) remit payments in the manner identified on specific invoices, (ii) unless otherwise specifically stated in an Order Confirmation or separate written agreement, Users shall remit payments upon receipt of the relevant invoice from CCC, either by delivery or notification of availability of the invoice via the Marketplace platform, and (iii) if the User does not pay the invoice within 30 days of receipt, the User may incur a service charge of 1.5% per month or the maximum rate allowed by applicable law, whichever is less. While User may exercise the rights in the License immediately upon receiving the Order Confirmation, the License is automatically revoked and is null and void, as if it had never been issued, if CCC does not receive complete payment on a timely basis.

7) **General Limits on Use.** Unless otherwise provided in the Order Confirmation, any grant of rights to User (i) involves only the rights set forth in the Terms and does not include subsequent or additional uses, (ii) is non-exclusive and non-transferable, and (iii) is subject to any and all limitations and restrictions (such as, but not limited to, limitations on duration of use or circulation) included in the Terms. Upon completion of the licensed use as set forth in the Order Confirmation, User shall either secure a new permission for further use of the Work(s) or immediately cease any new use of the Work(s) and shall render inaccessible (such as by deleting or by removing or severing links or other locators) any further copies of the Work. User may only make alterations to the Work if and as expressly set forth in the Order Confirmation. No Work may be used in any way that is unlawful, including without limitation if such use would violate applicable sanctions laws or regulations, would be defamatory, violate the rights of third parties (including such third parties' rights of copyright, privacy, publicity, or other tangible or intangible property), or is otherwise illegal, sexually explicit, or obscene. In addition, User may not conjoin a Work with any other material that may result in damage to the reputation of the Rightsholder. Any unlawful use will render any licenses hereunder null and void. User agrees to inform CCC if it becomes aware of any infringement of any rights in a Work and to cooperate with any reasonable request of CCC or the Rightsholder in connection therewith.

8) **Third Party Materials.** In the event that the material for which a License is sought includes third party materials (such as photographs, illustrations, graphs, inserts and similar materials) that are identified in such material as having been used by permission (or a similar indicator), User is responsible for identifying, and seeking separate licenses (under this Service, if available, or otherwise) for any of such third party materials; without a separate license, User may not use such third party materials via the License.

9) **Copyright Notice.** Use of proper copyright notice for a Work is required as a condition of any License granted under the Service. Unless otherwise provided in the Order Confirmation, a proper copyright notice will read substantially as follows: "Used with permission of [Rightsholder's name], from [Work's title, author, volume, edition number and year of copyright]; permission conveyed through Copyright Clearance Center, Inc." Such notice must be provided in a reasonably legible font size and must be placed either on a cover page or in another location that any person, upon gaining access to the material which is the subject of a permission, shall see, or in the case of republication Licenses, immediately adjacent to the Work as used (for example, as part of a by-line or footnote) or in the place where substantially all other credits or notices for the new work containing the republished Work are located. Failure to include the required notice results in loss to the Rightsholder and CCC, and the User shall be liable to pay liquidated damages for each such failure equal to twice the use fee specified in the Order Confirmation, in addition to the use fee itself and any other fees and charges specified.

10) **Indemnity.** User hereby indemnifies and agrees to defend the Rightsholder and CCC, and their respective employees and directors, against all claims, liability, damages, costs, and expenses, including legal fees and expenses, arising out of

any use of a Work beyond the scope of the rights granted herein and in the Order Confirmation, or any use of a Work which has been altered in any unauthorized way by User, including claims of defamation or infringement of rights of copyright, publicity, privacy, or other tangible or intangible property.

11) **Limitation of Liability.** UNDER NO CIRCUMSTANCES WILL CCC OR THE RIGHTSHOLDER BE LIABLE FOR ANY DIRECT, INDIRECT, CONSEQUENTIAL, OR INCIDENTAL DAMAGES (INCLUDING WITHOUT LIMITATION DAMAGES FOR LOSS OF BUSINESS PROFITS OR INFORMATION, OR FOR BUSINESS INTERRUPTION) ARISING OUT OF THE USE OR INABILITY TO USE A WORK, EVEN IF ONE OR BOTH OF THEM HAS BEEN ADVISED OF THE POSSIBILITY OF SUCH DAMAGES. In any event, the total liability of the Rightsholder and CCC (including their respective employees and directors) shall not exceed the total amount actually paid by User for the relevant License. User assumes full liability for the actions and omissions of its principals, employees, agents, affiliates, successors, and assigns.

12) **Limited Warranties.** THE WORK(S) AND RIGHT(S) ARE PROVIDED "AS IS." CCC HAS THE RIGHT TO GRANT TO USER THE RIGHTS GRANTED IN THE ORDER CONFIRMATION DOCUMENT. CCC AND THE RIGHTSHOLDER DISCLAIM ALL OTHER WARRANTIES RELATING TO THE WORK(S) AND RIGHT(S), EITHER EXPRESS OR IMPLIED, INCLUDING WITHOUT LIMITATION IMPLIED WARRANTIES OF MERCHANTABILITY OR FITNESS FOR A PARTICULAR PURPOSE. ADDITIONAL RIGHTS MAY BE REQUIRED TO USE ILLUSTRATIONS, GRAPHS, PHOTOGRAPHS, ABSTRACTS, INSERTS, OR OTHER PORTIONS OF THE WORK (AS OPPOSED TO THE ENTIRE WORK) IN A MANNER CONTEMPLATED BY USER; USER UNDERSTANDS AND AGREES THAT NEITHER CCC NOR THE RIGHTSHOLDER MAY HAVE SUCH ADDITIONAL RIGHTS TO GRANT.

13) **Effect of Breach.** Any failure by User to pay any amount when due, or any use by User of a Work beyond the scope of the License set forth in the Order Confirmation and/or the Terms, shall be a material breach of such License. Any breach not cured within 10 days of written notice thereof shall result in immediate termination of such License without further notice. Any unauthorized (but licensable) use of a Work that is terminated immediately upon notice thereof may be liquidated by payment of the Rightsholder's ordinary license price therefor; any unauthorized (and unlicensable) use that is not terminated immediately for any reason (including, for example, because materials containing the Work cannot reasonably be recalled) will be subject to all remedies available at law or in equity, but in no event to a payment of less than three times the Rightsholder's ordinary license price for the most closely analogous licensable use plus Rightsholder's and/or CCC's costs and expenses incurred in collecting such payment.

14) **Additional Terms for Specific Products and Services.** If a User is making one of the uses described in this Section 14, the additional terms and conditions apply:

a) ***Print Uses of Academic Course Content and Materials (photocopies for academic coursepacks or classroom handouts).*** For photocopies for academic coursepacks or classroom handouts the following additional terms apply:

i) The copies and anthologies created under this License may be made and assembled by faculty members individually or at their request by on-campus bookstores or copy centers, or by off-campus copy shops and other similar entities.

ii) No License granted shall in any way: (i) include any right by User to create a substantively non-identical copy of the Work or to edit or in any other way modify the Work (except by means of deleting material immediately preceding or following the entire portion of the Work copied) (ii) permit "publishing ventures" where any particular anthology would be systematically marketed at multiple institutions.

iii) Subject to any Publisher Terms (and notwithstanding any apparent contradiction in the Order Confirmation arising from data provided by User), any use authorized under the academic pay-per-use service is limited as follows:

A) any License granted shall apply to only one class (bearing a unique identifier as assigned by the institution, and thereby including all sections or other subparts of the class) at one institution;

B) use is limited to not more than 25% of the text of a book or of the items in a published collection of essays, poems or articles;

C) use is limited to no more than the greater of (a) 25% of the text of an issue of a journal or other periodical or (b) two articles from such an issue;

D) no User may sell or distribute any particular anthology, whether photocopied or electronic, at more than one institution of learning;

E) in the case of a photocopy permission, no materials may be entered into electronic memory by User except in order to produce an identical copy of a Work before or during the academic term (or analogous period) as to which any particular permission is granted. In the event that User shall choose to retain materials that are the subject of a photocopy permission in electronic memory for purposes of producing identical copies more than one day after such retention (but still within the scope of any permission granted), User must notify CCC of such fact in the applicable permission request and such retention shall constitute one copy actually sold for purposes of calculating permission fees due; and

F) any permission granted shall expire at the end of the class. No permission granted shall in any way include any right by User to create a substantively non-identical copy of the Work or to edit or in any other way modify the Work (except by means of deleting material immediately preceding or following the entire portion of the Work copied).

iv) Books and Records; Right to Audit. As to each permission granted under the academic pay-per-use Service, User shall maintain for at least four full calendar years books and records sufficient for CCC to determine the numbers of copies made by User under such permission. CCC and any representatives it may designate shall have the right to audit such books and records at any time during User's ordinary business hours, upon two days' prior notice. If any such audit shall determine that User shall have underpaid for, or underreported, any photocopies sold or by three percent (3%) or more, then User shall bear all the costs of any such audit; otherwise, CCC shall bear the costs of any such audit. Any amount determined by such audit to have been underpaid by User shall immediately be paid to CCC by User, together with interest thereon at the rate of 10% per annum from the date such amount was originally due. The provisions of this paragraph shall survive the termination of this License for any reason.

b) ***Digital Pay-Per-Uses of Academic Course Content and Materials (e-coursepacks, electronic reserves, learning management systems, academic institution intranets).*** For uses in e-coursepacks, posts in electronic reserves, posts in learning management systems, or posts on academic institution intranets, the following additional terms apply:

i) The pay-per-uses subject to this Section 14(b) include:

A) **Posting e-reserves, course management systems, e-coursepacks for text-based content,** which grants authorizations to import requested material in electronic format, and allows electronic access to this material to members of a designated college or university class, under the direction of an instructor designated by the college or university, accessible only under appropriate electronic controls (e.g., password);

B) **Posting e-reserves, course management systems, e-coursepacks for material consisting of photographs or other still images not embedded in text,** which grants not only the authorizations described in Section 14(b)(i)(A) above, but also the following authorization: to include the requested material in course materials for use consistent with Section 14(b)(i)(A) above, including any necessary resizing, reformatting or modification of the resolution of such requested material (provided that such modification does not alter the underlying editorial content or meaning of the requested material, and provided that the resulting modified content is used solely within the scope of, and in a manner consistent with, the particular authorization described in the Order Confirmation and the Terms), but not including any other form of manipulation, alteration or editing of the requested material;

C) **Posting e-reserves, course management systems, e-coursepacks or other academic distribution for audiovisual content,** which grants not only the authorizations described in Section 14(b)(i)(A) above, but also the following authorizations: (i) to include the requested material in course materials for use consistent with Section 14(b)(i)(A) above; (ii) to display and perform the requested material to such members of such class in the physical classroom or remotely by means of streaming media or other video formats; and (iii) to "clip" or reformat the requested material for purposes of time or content management or ease of delivery, provided that such "clipping" or reformatting does not alter the underlying editorial content or meaning of the requested material and that the resulting material is used solely within the scope of, and in a manner consistent with, the particular authorization described in the Order Confirmation and the Terms. Unless expressly set forth in the relevant Order Conformation, the License does not authorize any other form of manipulation, alteration or editing of the requested material.

ii) Unless expressly set forth in the relevant Order Confirmation, no License granted shall in any way: (i) include any right by User to create a substantively non-identical copy of the Work or to edit or in any other way modify the Work (except by means of deleting material immediately preceding or following the entire portion of the Work copied or, in the case of Works subject to Sections 14(b)(1)(B) or (C) above, as described in such Sections) (ii)

permit "publishing ventures" where any particular course materials would be systematically marketed at multiple institutions.

iii) Subject to any further limitations determined in the Rightsholder Terms (and notwithstanding any apparent contradiction in the Order Confirmation arising from data provided by User), any use authorized under the electronic course content pay-per-use service is limited as follows:

A) any License granted shall apply to only one class (bearing a unique identifier as assigned by the institution, and thereby including all sections or other subparts of the class) at one institution;

B) use is limited to not more than 25% of the text of a book or of the items in a published collection of essays, poems or articles;

C) use is limited to not more than the greater of (a) 25% of the text of an issue of a journal or other periodical or (b) two articles from such an issue;

D) no User may sell or distribute any particular materials, whether photocopied or electronic, at more than one institution of learning;

E) electronic access to material which is the subject of an electronic-use permission must be limited by means of electronic password, student identification or other control permitting access solely to students and instructors in the class;

F) User must ensure (through use of an electronic cover page or other appropriate means) that any person, upon gaining electronic access to the material, which is the subject of a permission, shall see:

- a proper copyright notice, identifying the Rightsholder in whose name CCC has granted permission,
- a statement to the effect that such copy was made pursuant to permission,
- a statement identifying the class to which the material applies and notifying the reader that the material has been made available electronically solely for use in the class, and
- a statement to the effect that the material may not be further distributed to any person outside the class, whether by copying or by transmission and whether electronically or in paper form, and User must also ensure that such cover page or other means will print out in the event that the person accessing the material chooses to print out the material or any part thereof.

G) any permission granted shall expire at the end of the class and, absent some other form of authorization, User is thereupon required to delete the applicable material from any electronic storage or to block electronic access to the applicable material.

iv) Uses of separate portions of a Work, even if they are to be included in the same course material or the same university or college class, require separate permissions under the electronic course content pay-per-use Service. Unless otherwise provided in the Order Confirmation, any grant of rights to User is limited to use completed no later than the end of the academic term (or analogous period) as to which any particular permission is granted.

v) Books and Records; Right to Audit. As to each permission granted under the electronic course content Service, User shall maintain for at least four full calendar years books and records sufficient for CCC to determine the numbers of copies made by User under such permission. CCC and any representatives it may designate shall have the right to audit such books and records at any time during User's ordinary business hours, upon two days' prior notice. If any such audit shall determine that User shall have underpaid for, or underreported, any electronic copies used by three percent (3%) or more, then User shall bear all the costs of any such audit; otherwise, CCC shall bear the costs of any such audit. Any amount determined by such audit to have been underpaid by User shall immediately be paid to CCC by User, together with interest thereon at the rate of 10% per annum from the date such amount was originally due. The provisions of this paragraph shall survive the termination of this license for any reason.

c) ***Pay-Per-Use Permissions for Certain Reproductions (Academic photocopies for library reserves and interlibrary loan reporting) (Non-academic internal/external business uses and commercial document delivery).*** The License expressly excludes the uses listed in Section (c)(i)-(v) below (which must be subject to separate license from the

applicable Rightsholder) for: academic photocopies for library reserves and interlibrary loan reporting; and non-academic internal/external business uses and commercial document delivery.

i) electronic storage of any reproduction (whether in plain-text, PDF, or any other format) other than on a transitory basis;

ii) the input of Works or reproductions thereof into any computerized database;

iii) reproduction of an entire Work (cover-to-cover copying) except where the Work is a single article;

iv) reproduction for resale to anyone other than a specific customer of User;

v) republication in any different form. Please obtain authorizations for these uses through other CCC services or directly from the rightsholder.

Any license granted is further limited as set forth in any restrictions included in the Order Confirmation and/or in these Terms.

d) ***Electronic Reproductions in Online Environments (Non-Academic-email, intranet, internet and extranet).*** For "electronic reproductions", which generally includes e-mail use (including instant messaging or other electronic transmission to a defined group of recipients) or posting on an intranet, extranet or Intranet site (including any display or performance incidental thereto), the following additional terms apply:

i) Unless otherwise set forth in the Order Confirmation, the License is limited to use completed within 30 days for any use on the Internet, 60 days for any use on an intranet or extranet and one year for any other use, all as measured from the "republication date" as identified in the Order Confirmation, if any, and otherwise from the date of the Order Confirmation.

ii) User may not make or permit any alterations to the Work, unless expressly set forth in the Order Confirmation (after request by User and approval by Rightsholder); provided, however, that a Work consisting of photographs or other still images not embedded in text may, if necessary, be resized, reformatted or have its resolution modified without additional express permission, and a Work consisting of audiovisual content may, if necessary, be "clipped" or reformatted for purposes of time or content management or ease of delivery (provided that any such resizing, reformatting, resolution modification or "clipping" does not alter the underlying editorial content or meaning of the Work used, and that the resulting material is used solely within the scope of, and in a manner consistent with, the particular License described in the Order Confirmation and the Terms.

15) **Miscellaneous.**

a) User acknowledges that CCC may, from time to time, make changes or additions to the Service or to the Terms, and that Rightsholder may make changes or additions to the Rightsholder Terms. Such updated Terms will replace the prior terms and conditions in the order workflow and shall be effective as to any subsequent Licenses but shall not apply to Licenses already granted and paid for under a prior set of terms.

b) Use of User-related information collected through the Service is governed by CCC's privacy policy, available online at www.copyright.com/about/privacy-policy/.

c) The License is personal to User. Therefore, User may not assign or transfer to any other person (whether a natural person or an organization of any kind) the License or any rights granted thereunder; provided, however, that, where applicable, User may assign such License in its entirety on written notice to CCC in the event of a transfer of all or substantially all of User's rights in any new material which includes the Work(s) licensed under this Service.

d) No amendment or waiver of any Terms is binding unless set forth in writing and signed by the appropriate parties, including, where applicable, the Rightsholder. The Rightsholder and CCC hereby object to any terms contained in any writing prepared by or on behalf of the User or its principals, employees, agents or affiliates and purporting to govern or otherwise relate to the License described in the Order Confirmation, which terms are in any way inconsistent with any Terms set forth in the Order Confirmation, and/or in CCC's standard operating procedures, whether such writing is prepared prior to, simultaneously with or subsequent to the Order Confirmation, and whether such writing appears on a copy of the Order Confirmation or in a separate instrument.

e) The License described in the Order Confirmation shall be governed by and construed under the law of the State of New York, USA, without regard to the principles thereof of conflicts of law. Any case, controversy, suit, action, or

proceeding arising out of, in connection with, or related to such License shall be brought, at CCC's sole discretion, in any federal or state court located in the County of New York, State of New York, USA, or in any federal or state court whose geographical jurisdiction covers the location of the Rightsholder set forth in the Order Confirmation. The parties expressly submit to the personal jurisdiction and venue of each such federal or state court.

Last updated October 2022

B

Selected abstracts of publications not discussed in this thesis

Dose Efficiency of a Prototype, Whole-body, Photon-Counting CT System versus a Conventional CT System for Imaging of Iodinated Contrast Media

Ralf Gutjahr, MSc,[1,2] Ahmed F. Halaweish, PhD,[2] Katharine Grant, PhD,[2] Steffen Kappler, PhD,[3] Zhicong Yu, PhD,[4] Shuai Leng, PhD,[4] Lifeng Yu, PhD,[4] Zhoubo Li, BS,[4] Steven M. Jorgensen, BSEE,[5] Erik L. Ritman, MD, PhD,[5] and Cynthia H. McCollough, PhD[4]

[1]Computer Aided Medical Procedures (CAMP), Technical University of Munich, Munich, Germany
[2]Siemens Healthcare–Imaging and Therapy Systems, Malvern, PA
[3]Siemens Healthcare, Forchheim, Germany
[4]Department of Radiology, Mayo Clinic, Rochester, MN
[5]Department of Physiology and Biomedical Engineering, Mayo Clinic, Rochester, MN

Copyright statement

Contributions

The thesis author played a key role in examining the dose efficiency of a whole-body photon-counting CT scanner compared to a energy-integrating CT system. He contributed to the conceptualization of the study, the investigation of the photon-counting CT prototype system, and the establishment of the methodology for acquiring and analyzing images from the two systems. The author also developed software to process the acquired data and visualizations to effectively present the results, highlighting the increased contrast-to-noise ratio (CNR) values achieved by the photon-counting CT system. He was actively involved in writing, reviewing, and editing the manuscript to ensure clarity and precision.

The co-authors collaborated with the thesis author on various aspects of the project, including the study's conceptualization, the refinement of the methodology, and reviewing the investigation process. They provided valuable resources and supervision throughout the project, ensuring its success, and contributed to the editing process of the manuscript.

Abstract

Purpose: The purpose of this study was to investigate, for the task of iodine imaging, the dose efficiency of a whole-body photon counting CT scanner relative to a commercially available energy-integrating CT system.

Methods and materials: Photon Counting CT (PCCT) imaging was performed on a whole-body prototype system (Siemens Healthcare, Forchheim, Germany), while conventional CT imaging was performed on a commercially available energy-integrating CT system (SOMATOM Definition Flash). The PCCT prototype system is built on a dual-source platform, where the "A" tube/detector uses a conventional energy integrating detector and the "B" tube/detector uses a photon-counting detector. Imaging was performed with similar geometries, identical beam filtration and equivalent tube and detector parameters. Three anthropomorphic phantoms (CIRS, Inc., Norfolk, VA, USA), mimicking a: 10 year old, small adult, and large adult were scanned. Each phantom contained Lucite vials of four different iodine concentrations: 5, 10, 15 and 20 mg/mL. Images were acquired on each system with four different tube voltages (80, 100, 120, 140 kV) and ten different tube currents (50, 100, 150, 200, 250, 300, 350, 400, 500, 550 mA). CT numbers and noise were measured in both tissue-equivalent and iodine regions of interest (ROIs) and averaged over 10 neighboring slices. The calculated CNR values were plotted against CTDIvol(32 cm) for each ROI, tube voltage and phantom size and fitted with a square rootfunction.

Results: At 140 kV, the PCCT system provided increased CNR values (for a given dose) in the 10 year old (+10.7%), small adult (+13.2%), and large adult phantoms (+16.2%). An increase in CNR values (at a given dose) was also observed at 120 kV (10 year old: +10.7%, small adult: +12.9%, large adult: +18.7%) and at 100 kV (10 year old: +9.9%, small adult: +10.9%, large adult: +21.8%).

Conclusion: Relative to conventional CT, PCCT provided increased dose efficiency for iodine imaging for all presented phantom sizes. This is a result of the heavier weighting of the lower energy photons, apparent with PCCT technology.

Clinical relevance/application: PCCT provides greater dose efficiency for iodine imaging relative to conventional energy integrating CT systems.

Whole-body Human Imaging with Photon-counting-based CT at Clinically Relevant Doses

Cynthia H. McCollough, PhD[1] Shuai Leng, PhD,[1] Ralf Gutjahr, MSc,[2,3] Zhicong Yu, PhD,[1]
Zhoubo Li, BS,[1] Ahmed F. Halaweish, PhD,[3] Steven M. Jorgensen, BSEE,[4]
Erik L. Ritman, MD, PhD,[4] and Steffen Kappler, PhD[5]

[1]Department of Radiology, Mayo Clinic, Rochester, MN
[2]Computer Aided Medical Procedures (CAMP), Technical University of Munich, Munich, Germany
[3]Siemens Healthcare–Imaging and Therapy Systems, Malvern, PA
[4]Department of Physiology and Biomedical Engineering, Mayo Clinic, Rochester, MN
[5]Siemens Healthcare, Forchheim, Germany

Copyright statement

Contributions

The thesis author contributed to the study by evaluating human anatomy using cadaveric specimens on a prototype whole-body photon-counting-detector CT scanner. He was involved in the conceptualization of the research idea, the investigation process, and the development of the methodology for acquiring images using both energy-integrating detector (EID) and photon-counting detector (PCD) subsystems of a novel prototype CT system. The author was responsible for creating software to analyze the data and crafting visualizations to showcase the results, which demonstrated equivalent image quality between the two systems. He also reviewed and edited the manuscript, ensuring its quality and accuracy.

The co-authors of this article also provided essential support throughout the study. They contributed to the conceptualization of the research idea and helped refine the methodology. Furthermore, they played an important role in the writing, review, and editing of the manuscript. They also provided essential resources and supervision during the course of the study, ensuring a robust and well-executed investigation.

Abstract

Purpose: The aim of this study was to evaluate and assess human anatomy (using cadaveric specimens) at clinically relevant dose rates on a prototype, whole-body, photon-counting-detector CT scanner.

Method and materials: A prototype, whole-body CT scanner (Siemens Healthcare, Forchheim, Germany) was installed in our laboratory. The system is built on a Definition Flash dual-source platform, where the "A" tube/detector subsystem uses a conventional energy integrating detector (EID) and the "B" tube/detector subsystem uses a photon-counting detector (PCD).

Following biospecimen committee approval and a thorough physics performance evaluation (dose, spatial and low-contrast resolution, CT number accuracy, etc.), a series of scans was performed on a fresh-frozen human cadaver (head and neck, chest, abdomen/pelvis and extremity scans), three cadaveric heads, a cadaveric arm, and a cadaveric leg at clinically relevant doses (140 kV, 200-220 mAs, 0.5 - 1 s rotation time). Images were acquired using two energy thresholds (25 and 65 keV), resulting in the generation of two threshold datasets and two energy bin datasets. Scans were repeated using the EID and identical scan parameters. The EID data were used for data completion to avoid truncation artifacts when the anatomy was outside the PCD field of view (27.5 cm). Side by side comparisons were made between the EID and PCD images.

Results: Phantom measurements of image and dose performance demonstrated equivalent image quality and dose between the two systems, with the exception of section sensitivity profile, which was better on the PCD due to the smaller detector pixel size (0.5 mm vs 0.6 mm). PCD images of the cadaveric anatomy were judged to be equivalent to the EID images, with the exception of improved quality in regard to beam hardening; the high energy [65,140 keV] PCD images demonstrated notably decreased beam hardening, particularly in the skull. Ring artifacts, which are common in PCD CT systems, were not present.

Conclusion: The evaluated prototype whole-body PCD CT system was capable of clinical levels of image quality at clinical dose rates.

Clinical relevance/application: The ability to perform whole-body CT scanning using photon-counting detector technology will facilitate clinical investigations of this new technology.

Initial results from a prototype whole-body photon-counting computed tomography system

Zhicong Yu, PhD,[1] Shuai Leng, PhD,[1] Steven M. Jorgensen, BSEE,[2] Zhoubo Li, BS,[1] Ralf Gutjahr, MSc,[3] Baiyu Chen, PhD,[1] Xiao Duan, PhD,[1] Ahmed F. Halaweish, PhD,[3] Lifeng Yu, PhD,[1] Erik L. Ritman, MD, PhD,[2] and Cynthia H. McCollough, PhD[1]

[1]Department of Radiology, Mayo Clinic, Rochester, MN
[2]Department of Physiology and Biomedical Engineering, Mayo
[3]Siemens Healthcare–Imaging and Therapy Systems, Malvern, PA Clinic, Rochester, MN

Copyright statement

Contributions

The author of this thesis took an active role during the conceptualization of the study that explored the potential of a research prototype PCD CT system by comparing its performance to a EID system. He was instrumental in designing the methodology for evaluating the PCD CT system using phantoms, which led to the discovery of promising characteristics this new detector. His contributions also involved reviewing and editing the manuscript to ensure that the text effectively communicated the study's findings, emphasizing the PCD subsystem's ability to produce clinically-acceptable images in vivo.

Throughout the research process, the co-authors of this article provided invaluable support and expertise. They played a critical role in conceptualizing the research idea and conducting the investigation. In addition, they contributed to the development of the methodology, facilitated the use of appropriate evaluation tools, and resulted in a meaningful visualization of the results. They also ensured the clarity and quality of the manuscript by writing, reviewing and editing it. Their provision of essential resources and oversight facilitated a robust and well-conducted study.

Abstract

X-ray computed tomography (CT) with energy-discriminating capabilities presents exciting opportunities for increased dose efficiency and improved material decomposition analyses. However, due to constraints imposed by the inability of photon-counting detectors (PCD) to respond accurately at high photon flux, to date there has been no clinical application of PCD-CT. Recently, our lab installed a research prototype system consisting of two x-ray sources and two corresponding detectors, one using an energy-integrating detector (EID) and the other using a PCD. In this work, we report the first third-party evaluation of this prototype CT system using both phantoms and a cadaver head. The phantom studies demonstrated several promising characteristics of the PCD sub-system, including improved longitudinal

spatial resolution and reduced beam hardening artifacts, relative to the EID sub-system. More importantly, we found that the PCD sub-system offers excellent pulse pileup control in cases of x-ray flux up to 550 mA at 140 kV, which corresponds to approximately 2.5 $\times$ 1011 photons per cm2 per second. In an anthropomorphic phantom and a cadaver head, the PCD sub-system provided image quality comparable to the EID sub-system for the same dose level. Our results demonstrate the potential of the prototype system to produce clinically-acceptable images in vivo.

Improving material decomposition by spectral optimization of photon counting computed tomography

Polster Christoph, Dipl.-Phys.,[1,2] Katharina Hahn, Dipl.-Phys.,[2] Ralf Gutjahr, MSc,[2,3]
Friederike Schöck, PhD,[2] Steffen Kappler, PhD,[2] Olaf Dietrich,[1] PhD and
Thomas G. Flohr, PhD[2]

[1]Institute for Clinical Radiology, Ludwig-Maximilians-University Hospital, Munich, Germany
[2]Siemens Healthcare GmbH, Forchheim, Germany
[3]CAMP, Technical University of Munich, Garching (Munich), Germany

Copyright statement

Contributions

The thesis author contributed to this specific article by developing the methodology to improve material decomposition in photon-counting CT by adapting the incident X-ray spectrum based on the detector response function. He created visualizations to showcase the results, which demonstrated the benefits of using specific materials as X-ray pre-filtration. He also supported the writing and reviewing of the manuscript.

The co-authors of this article played a crucial role in the research process by participating in the conceptualization of the project and carrying out the investigation. They collaborated in refining the methodology and developing software tools to facilitate data analysis. They also contributed significantly to the creation of visual representations of the results. Throughout the writing process, the co-authors were involved in drafting, reviewing, and editing the manuscript. By providing essential resources and guidance, they provided the necessary support and oversight to ensure the successful completion of the study.

Abstract

Photon counting detectors in computed tomography facilitate measurements of spectral distributions of detected X-ray quanta in discrete energy bins. Along with the dependency on wavelength and atomic number of the mass attenuation coefficient, this information allows for reconstruction of CT images of different material bases. Decomposition of two materials is considered standard in today's dual-energy techniques. With photon-counting detectors the decomposition of more than two materials becomes achievable. Efficient detection of CT-typical X-ray spectra is a hard requirement in a clinical environment. This is fulfilled by only a few sensor materials such as CdTe or CdZnTe. In contrast to energy integrating CT-detectors, the pixel dimensions must be reduced to avoid pulse pile-up problems at clinically relevant count rates. However, reducing pixel sizes leads to increased K-escape and charge sharing effects. As a consequence, the correlation between incident and detected X-ray energy is

reduced. This degradation is quantified by the detector response function. The goal of this study is to improve the achievable material decomposition by adapting the incident X-ray spectrum with respect to the properties (i.e. the detector response function) of a photon counting detector. A significant improvement of a material decomposition equivalent metric is achievable when using specific materials as X-ray pre-filtration (K-edge filtering) while maintaining the applied patient dose and image quality.

Advanced Spectral Analysis of Whole-Body Photon-Counting-Detector Computed Tomography Data

Ahmed F. Halaweish, PhD,[1] Roy P. Marcus, MD,[2] Shuai Leng, PhD,[2]
Bernhard Krauss, PhD,[3] Martin Sedlmair, PhD,[3] Thomas Allmendinger, PhD,[3]
Ralf Gutjahr, MSc,[3,4] Steffen Kappler, PhD,[3] Bernhard Schmidt, PhD,[3]
Erik L. Ritman, MD, PhD,[5] and Cynthia H. McCollough, PhD[2]

[1]Siemens Healthcare–Imaging and Therapy Systems, Malvern, PA
[2]Department of Radiology, Mayo Clinic, Rochester, MN
[3]Siemens Healthcare, Forchheim, Germany
[4]Computer Aided Medical Procedures (CAMP), Technical University of Munich, Munich, Germany
[5]Department of Physiology and Biomedical Engineering, Mayo Clinic, Rochester, MN

Copyright statement

Contributions

The thesis author made noteworthy contributions to the project, specifically by modifying the existing software tools to process the data of the novel PCD CT scanner. This enabled the generation of visualizations to effectively showcase the research outcomes. He also played a key role in scrutinizing the study to ensure its precision and quality.

On the other hand, the article's co-authors were vital in the research process, actively shaping the project's concept and conducting the necessary investigations. They collaborated to refine the methodology and provided the software tools for data analysis purposes. The co-authors also contributed to producing visual displays of the results. They engaged in crafting, reviewing, and editing the manuscript. By providing crucial resources and guidance, they furnished the necessary support and supervision for the successful completion of the research.

Abstract

Purpose: To investigate advanced spectral analysis of whole-body photon-counting-detector (PCD) CT data and compare it to 2nd generation dual-source (DS) dual energy (DE) imaging.

Method and materials: A research, whole-body PCD CT scanner (Somatom CounT, Siemens Healthcare) was utilized to acquire head/neck (H&N) and chest CTA data using 140kV at clinically equivalent doses, following iodine injections (Iohexol 350 at 3 cc/sec: Chest – 45 cc, H&N – 60 cc, Saline chaser – 30 cc) in a swine model. The PCD-CT scanner is based on the footprint of a 2nd generation DSCT scanner (Siemens Healthcare), where the "A" detector/source sub-system uses a conventional energy integrating detector (EID) and the

"B" detector/source sub-system uses a cadmium telluride PCD. PCD-CT acquisitions were performed using a 2-bin (Macro) and a 4-bin (Chess) mode, with energy thresholds set at 25/65 keV and 20/25/57/77 keV for the Macro and Chess modes, respectively. Dose matched DECT acquisitions were performed on a 2nd generation DSCT scanner using 80/Sn140 kV, with the same contrast injection protocol. Spectral post processing algorithms were calibrated for water and iodine and the energy thresholds set for each acquisition. The generated calibration tables were then utilized for the optimization of the PCD-CT analysis. Chess mode data was combined to generate 2 spectrally different datasets for input into the post processing algorithms.

Results: Advanced spectral analysis of the PCD-CT data resulted in the generation of virtual non-contrast and iodine only maps, with qualitatively similar material separation as seen in clinically available techniques. Virtual monoenergetic images further improved upon the already-reported increased contrast-to-noise ratio achievable with PCD-CT. Other spectral analyses optimized for PCD-CT included, optimum contrast, pulmonary perfused blood volume and bone removal. Head and body bone removal algorithms demonstrated similar results as their clinically implemented counterparts.

Conclusion: The advanced spectral analysis of whole-body PCD-CT data provided qualitatively similar results to those attainable utilizing clinically available dual energy technologies, with improved image quality.

Clinical relevance/application: Advanced spectral analysis of whole body PCD-CT allows the extraction of the quantitative spectral information needed to fully assess PCD-CT's capabilities and clinical potential.

Evaluation of conventional imaging performance in a research whole-body CT system with a photon-counting detector array

Zhicong Yu, PhD,[1] Shuai Leng, PhD,[1] Steven M. Jorgensen, BSEE,[2] Zhoubo Li, BS,[1,3] Ralf Gutjahr, MSc,[4] Baiyu Chen, PhD,[1] Ahmed F. Halaweish, PhD,[5] Steffen Kappler, PhD,[4] Lifeng Yu, PhD,[1] Erik L. Ritman, MD, PhD,[2] and Cynthia H. McCollough, PhD[1]

[1]Department of Radiology, Mayo Clinic; Rochester, Minnesota, 55905, USA
[2]Department of Physiology and Biomedical Engineering, Mayo Clinic; Rochester, Minnesota, 55905, USA
[3]Biomedical Engineering and Physiology Graduate Program, Mayo Graduate School; Rochester, Minnesota, 55905, USA
[4]Siemens Healthcare, Forchheim, Bavaria, 91301, Germany
[5]Siemens Healthcare, Malvern, Pennsylvania, 19355, USA

Copyright statement

Contributions

The thesis author contributed effectively to the study, diligently participating in its conceptualization and investigation. He supported the design of the methodology and data analysis.

The co-authors of this article were actively lead this study's conceptualizing and its conduction. The co-authors also contributed to generating visual displays of the research outcomes. Throughout the writing process, they were responsible in drafting, reviewing, and editing the manuscript. By offering crucial resources and direction, the co-authors guaranteed the provision of sufficient support and oversight, leading to the completion of the research project.

Abstract

This study evaluated the conventional imaging performance of a research whole-body photon-counting CT system and investigated its feasibility for imaging using clinically realistic levels of x-ray photon flux. This research system was built on the platform of a 2nd generation dual-source CT system: one source coupled to an energy integrating detector (EID) and the other coupled to a photon-counting detector (PCD). Phantom studies were conducted to measure CT number accuracy and uniformity for water, CT number energy dependency for high-Z materials, spatial resolution, noise, and contrast-to-noise ratio. The results from the EID and PCD subsystems were compared. The impact of high photon flux, such as pulse pile-up, was assessed by studying the noise-to-tube-current relationship using a neonate water phantom and high x-ray photon flux. Finally, clinical feasibility of the PCD subsystem was investigated using anthropomorphic phantoms, a cadaveric head, and a whole-body cadaver,

which were scanned at dose levels equivalent to or higher than those used clinically. Phantom measurements demonstrated that the PCD subsystem provided comparable image quality to the EID subsystem, except that the PCD subsystem provided slightly better longitudinal spatial resolution and about 25% improvement in contrast-to-noise ratio for iodine. The impact of high photon flux was found to be negligible for the PCD subsystem: only subtle high-flux effects were noticed for tube currents higher than 300 mA in images of the neonate water phantom. Results of the anthropomorphic phantom and cadaver scans demonstrated comparable image quality between the EID and PCD subsystems. There were no noticeable ring, streaking, or cupping/capping artifacts in the PCD images. In addition, the PCD subsystem provided spectral information. Our experiments demonstrated that the research whole-body photon-counting CT system is capable of providing clinical image quality at clinically realistic levels of x-ray photon flux.

Kidney stone differentiation in photon counting computed tomography: a feasibility study

Ralf Gutjahr, MSc,[1,2] Bernhard Schmidt, PhD,[1] Martin Sedlmair, PhD,[1]
Steffen Kappler, PhD,[1] Polster Christoph, Dipl.-Phys.,[1,3] Thomas Allmendinger, PhD,[1]
Thomas G. Flohr, PhD,[1] and Bernhard Krauss, PhD[1]

[1]Siemens Healthcare GmbH, Forchheim, Germany
[2]CAMP, Technical University of Munich, Garching (Munich), Germany
[3]Institute for Clinical Radiology, Ludwig-Maximilians-University Hospital, Munich, Germany

Copyright statement

Contributions

In this study, the author played a pivotal role in shaping the research idea of detecting and differentiating kidney stone materials using image information acquired by a research PCD CT-scanner. He conducted comprehensive investigations and conceptualized the research idea, and designed the methodology for the study. His contributions also included developing software for data analysis, creating visualizations to effectively present the results, and writing the manuscript to communicate the findings.

The co-authors of this article collaborated with the thesis author by contributing to the study's conceptualization, investigation process, and methodology refinement. They were involved in the data analysis and in the writing of the manuscript. Their contributions also included reviewing and editing the manuscript, ensuring its quality and accuracy. The co-authors provided essential resources and supervision throughout the project.

Abstract

The medical treatment of a kidney stone strongly depends on its chemical composition, size and its precise location inside the urinary tract of the human body. Yet, kidney stones are highly prevalent and show increased recurrence-rates, therefore an early detection and robust characterization of the crystalline accumulations is desired. Whereas medical imaging technologies became an important tool for kidney stone diagnosis, low dose non-contrast CT is considered as today's gold standard. Several CT-based approaches of kidney stone characterization and differentiation were investigated in previous work. The purpose of this study, however, is to detect and differentiate two particularly prominent kidney stone-materials using image information acquired by a research Photon Counting Detector CT-scanner (PCD-CT). PCD-CT provides scans with a full Field of View, fully registered image data, stability against motion artifacts and no cross scatter from a second X-ray source. Compared to conventional energy integrating CT-detectors, PCD-CT technology promises to provide an increased spatial resolution, due to the absence of optical septa, a negligible level of

electronic noise and an increased dose efficiency especially for materials providing comparably higher absorptions in the lower energy ranges of the energy spectrum. Furthermore, the polychromatic spectrum as emitted by the X-ray tube can be resolved in energy bins by the introduction of energy thresholds; this allows applications of dual/multi energy algorithms as used in this study.

Image-Based Multi-Material Decomposition of Mixed Contrast Agent Solutions in Photon Counting Computed Tomography

Ralf Gutjahr, MSc,[1,2] Bernhard Schmidt, PhD,[1] Martin Sedlmair, PhD,[1]
Hubertus Pietsch, MD,[3] Bernhard Krauss, PhD,[1] and Tristan Nowak, PhD[1]

[1]Siemens Healthcare GmbH, Forchheim, Germany
[2]CAMP, Technical University of Munich, Garching (Munich), Germany
[3]Bayer HealthCare Pharmaceuticals, Berlin, Germany

Copyright statement

Contributions

In this study, the author was crucial in formulating the research concept, carrying out thorough investigations, and establishing a solid methodology. The author's proficiency in software development and data visualization greatly aided in showcasing the study's findings.

The study's co-authors also contributed significantly by collaborating on research conceptualization, investigation, and methodological improvement. They were involved in software development, supplied the contrast media used in this study, and facilitated the writing process. They also provided critical review and support for the writing.

Abstract

The application and assessment of an image-based multi-material decomposition algorithm. The algorithm was applied on multi-energy projection data acquired by a research whole-body high flux photon counting detector CT system (PCD-CT). Three combinations of four different contrast agents (CA) were investigated.

Applied quantitative multi-material decomposition using Photon Counting Detector CT (PCD-CT) image data

Ralf Gutjahr, MSc,[1,2] Bernhard Schmidt, PhD,[1] Martin Sedlmair, PhD,[1]
Thomas G. Flohr, PhD,[1] Hubertus Pietsch, MD,[3] Bernhard Krauss, PhD,[1] and
Tristan Nowak, PhD[1]

[1]Siemens Healthcare GmbH, Forchheim, Germany
[2]CAMP, Technical University of Munich, Garching (Munich), Germany
[3]Bayer HealthCare Pharmaceuticals, Berlin, Germany

Copyright statement

Contributions

The thesis author played a key role in applying and evaluating an image-based decomposition algorithm on three and four materials using single-scan multi-energy data acquired using a research PCD-CT system. He was responsible for devising the research idea, conducting comprehensive inquiries, and constructing a robust methodology. Further, his contributions included developing software for data analysis, creating visualizations to showcase the results, and writing the manuscript revealing the study's outcomes.

The co-authors made meaningful contributions through their collaboration in shaping the research concept, examining various aspects, enhancing the methodology, and by providing the research material, as they furnished the contrast media employed in the study. Ultimately they provided supervision and and support in writing and reviewing.

Abstract

Purpose: To apply and evaluate an image based decomposition algorithm on three and four materials using single scan multi-energy projection data acquired by a research photon counting detector CT (PCD-CT) system.

Method and materials: Six solutions of contrast agents (CAs) in concentrations of 5 and 10 mg/mL were investigated: zirconium (Zr), iodine (I), gadolinium (Gd), dysprosium (Dy), hafnium (Hf), and tungsten (W). The K-edges of all materials lay in the energy range for clinical CT. Multi-energy CT-images were obtained from eight different combinations of sets of three CAs. The solutions, each filled into a 2 cm wide vial, were arranged in an equiangular fashion inside a 20 cm diameter water-equivalent phantom. All CT-images were acquired using a PCD-CT research system (SOMATOM CounT, Siemens Healthcare GmbH, Forchheim) with tube voltages of 100, 120, or 140 kV and respective tube current-time-products of 160, 120, 80 mAs. Four energy thresholds were applied: 25, 45, 65, and 80 keV. The reconstructed energy-threshold images were decomposed into concentration images of three or four materials. For

the first case, the respective materials of the investigated set of CAs were chosen as base materials, for the second case, water was additionally included as a base material. The resulting accuracies were determined by comparing the extracted concentration values to the corresponding known values.

Results: The CAs could be differentiated and quantified in all investigated cases. The mean deviations of the measured concentrations were 8% for 100 kV, 3% for 120 kV, and 9% for 140 kV. The two different concentrations provided linear proportionality in CT-values. CAs with similar x-ray attenuation characteristics showed resembling enhancements throughout the single spectral images and showed greater deviations from the anticipated concentration values (up to -34% for separation of I, Hf, W, and water at 120 kV).

Conclusion: An image-based multi-material decomposition algorithm was applied on CT-data of a PCD-CT research system. The measured concentrations of different CAs showed good correspondence to their known concentrations. The quality of the material separations depend on the selected base materials, the number of base materials, the applied x-ray tube voltage and the selected energy thresholds.

Clinical relevance/application: To demonstrate feasibility of applying and separating multiple contrast agents within a single PCD-CT scan.

Image-Based Multi-Material Decomposition in Photon Counting Computed Tomography

Ralf Gutjahr, MSc,[1,2] Tristan Nowak, PhD,[1] Martin Sedlmair, PhD,[1] Hubertus Pietsch, MD,[3] Bernhard Schmidt, PhD,[1] Thomas G. Flohr, PhD,[1] and Bernhard Krauss, PhD[1]

[1]Siemens Healthcare GmbH, Forchheim, Germany
[2]CAMP, Technical University of Munich, Garching (Munich), Germany
[3]Bayer HealthCare Pharmaceuticals, Berlin, Germany

Copyright statement

Contributions

The thesis author was instrumental in developing, applying and evaluating an image-based material decomposition algorithm using multi-energy image data from a PCD CT scanner. He was responsible for the conceptualization of the research idea, conducting the investigation, and designing the methodology for testing six different contrast agent (CA). The author developed software for processing the acquired data and visualizations to display the results, successfully differentiating K-edge materials. He was also responsible for summarizing the results.

The co-authors collaborated with the thesis author on various aspects of the project, including the research idea's conceptualization, participation in the investigation process, providing the different contrast media, and review of the methodology. They were also involved in editing, providing necessary resources, and offering their supervision.

Abstract

Purpose: To apply and evaluate an image based material decomposition algorithm utilizing multi-energy projection data acquired by a Photon Counting Detector CT (PCD-CT).

Methods and Materials: Six contrast agent (CA) solutions were investigated. All materials provide K-edges in the relevant energy range for clinical CT. Combinations of three CAs were measured in eight different variations. For each measurement three 2 cm wide vials were arranged in an equiangular fashion inside a 20 cm wide water-equivalent phantom. All images were obtained using a PCD-CT research system (SOMATOM CounT, Siemens Healthcare GmbH, Forchheim, Germany) with applied tube voltages of 100, 120, or 140 kV, respective tube current-time-products of 160, 120, 80 mAs and a collimation of 32×0.5 mm. The data was acquired in Chesspattern-mode with energy-thresholds set to 25, 45, 65, and 80 keV. Four energy-threshold images were decomposed into subsets of three pre-selected basis materials while taking into account statistical correlations. The resulting noise levels was reduced by applying a non-linear noise reduction filtration.

Results: The K-edge materials can be successfully differentiated. Amplified noise requires the application of statistical noise reduction algorithms. Present materials that are not determined as basis materials are interpreted as a combination of such.

Conclusion: Material decomposition into pre-selected basis materials is feasible. Noise amplification emerged as an issue the more materials are separated. The result noise level depends on the selected basis-materials.

Quantitative Multi-energy Post-processing of Whole-Body Photon-Counting Computed Tomography Data

Ahmed F. Halaweish, PhD,[1] Shuai Leng, PhD,[2] Bernhard Krauss, PhD,[3]
Martin Sedlmair, PhD,[3] Tristan Nowak, PhD,[3] Ralf Gutjahr, MSc,[3,4] Steffen Kappler, PhD,[3]
Bernhard Schmidt, PhD,[3] Erik L. Ritman, MD, PhD,[5] and Cynthia H. McCollough, PhD[2]

[1]Siemens Healthcare–Imaging and Therapy Systems, Malvern, PA
[2]Department of Radiology, Mayo Clinic, Rochester, MN
[3]Siemens Healthcare, Forchheim, Germany
[4]Computer Aided Medical Procedures (CAMP), Technical University of Munich, Munich, Germany
[5]Department of Physiology and Biomedical Engineering, Mayo Clinic, Rochester, MN

Copyright statement

Contributions

The thesis author made significant contributions to this article by developing software that enabled the calibration required for the utilization and parametrization of Dual Energy algorithms to load and process image data from a PCD CT scanner. He also created visualizations that exemplary results, showing comparable outcomes to dose-matched clinical dual energy acquisitions from conventional EID CT scanners. Furthermore, the author participated in the review process, ensuring the relevance and accuracy of the findings.

The co-authors of this article worked closely in various aspects of the research, such as conceptualizing the investigation of multi-energy image processing. They were also involved in refining the methodology, generating visualizations, writing the manuscript, reviewing the findings, editing the content, providing resources, and offering supervision.

Abstract

The ability to incorporate photon counting detectors into the footprint of a whole body scanner platform has facilitated in depth investigations into the potential impact these novel detectors could have on routine clinical imaging. Several in depths investigations utilizing the Somatom CounT (research whole body photon counting scanner) have already been presented, evaluating spatial resolution, contrast enhancement, image quality, detector stability and artifact reduction. The remaining piece in establishing the full potential of photon counting detectors in routine clinical scenarios is the multi-energy capabilities/processing achievable using photon counting. Rather than creating novel and unique algorithms, without identifying a clinical use scenario, a subset of clinically utilized Dual Energy algorithms was calibrated to accept photon counting data acquired during CT Angiography examinations of the head, chest and abdomen, in a large animal model. Qualitative assessment of the photon counting

multi-energy results demonstrated successful implementation and comparable results to those generated from dose matched clinical dual energy acquisitions, performed on a 2nd generation dual source CT scanner. The collective improvements observed with photon counting detectors, in combination with the ability to perform task specific spectrum adjustments for multi-energy analysis, has the potential to improve upon the already established utility of clinical dual energy scanning.

Improving material decomposition by spectral optimization of photon counting computed tomography

Polster Christoph, Dipl.-Phys.,[1,2] Ralf Gutjahr, MSc,[2,3] Matthias Berner, PhD,[2]
Thomas G. Flohr, PhD,[2] Madeleine Hertel, MSc,[2] Steffen Kappler, PhD,[2]
Karl Stierstorfer, PhD,[2] and Olaf Dietrich,[1] PhD

[1]Institute for Clinical Radiology, Ludwig-Maximilians-University Hospital, Munich, Germany
[2]Siemens Healthcare GmbH, Forchheim, Germany
[3]CAMP, Technical University of Munich, Garching (Munich), Germany

Copyright statement

Contributions

In this article, the thesis author contributed the process for designing and implementing the methodology aimed at improving material decomposition in PCD CT images through the application of an X-ray filtration adapting the incident X-ray spectrum with respect to the properties of the specific CT scanner. He created visualizations that effectively illustrated the impact of using specific materials as X-ray pre-filtration (K-edge filtering) on a specific quality metric. Furthermore, he supported the first author with writing the manuscript and participating in the review and editing process.

The co-authors of the article played a crucial role in various aspects of the research, including the conceptualization of the idea to adapt the incident X-ray spectrum for better material decomposition, guiding the investigation process, refining the methodology, developing the software and visualizations, as well as contributing to the writing, reviewing, and editing of the manuscript. Furthermore, they provided valuable resources and supervision.

Abstract

Photon-counting detectors in computed tomography (CT) allow for measuring the energy of the incident x-ray photons within certain energy windows. This information can be used to enhance contrast or reconstruct CT images of different material bases. Compared to energy-integrating CT-detectors, pixel dimensions have to be smaller to limit the negative effect of pulse pile-up at high X-ray fluxes. Unfortunately, reducing the pixel size leads to increased K-escape and charge sharing effects. As a consequence, an incident X-ray may generate more than one detector signal, and with deteriorated energy information. In earlier simulation studies it has been shown that these limitations can be mitigated by optimizing the X-ray spectrum using K-edge pre-filtration. In the current study, we have used a whole-body research CT scanner with a high-flux capable photon-counting detector, in which for the first time a pre-patient hafnium filter was installed. Our measurement results demonstrate substantial

improvement of the material decomposition capability at comparable dose levels. The results are in agreement with the predictions provided in simulations.

Ultra-high spatial resolution multi-energy CT using photon counting detector technology

Shuai Leng, PhD,[1] Ralf Gutjahr, MSc,[2,3] Andrea Ferrero, PhD,[1] Steffen Kappler, PhD,[3] André Henning, PhD,[3] Ahmed F. Halaweish, PhD,[4] Wei Zhou, PhD,[1] Juan Montoya, BSc,[1] and Cynthia H. McCollough, PhD[1]

[1]Department of Radiology, Mayo Clinic, Rochester, MN
[2]Computer Aided Medical Procedures (CAMP),Technical University of Munich, Munich, Germany
[3]Siemens Healthcare GmbH, Forchheim, Germany
[4]Siemens Healthcare–Imaging and Therapy Systems, Malvern, PA

Copyright statement

Contributions

The author of this thesis has made significant contributions to the research by conceptualizing the study, designing and implementing the methodology, and developing software for the analysis of CT scans to compare the performance of an ultra high resolution acquisition mode against the standard macro mode. They were responsible for the investigation and analysis, as well as the visualization of the results indicating the benefits and limitations of both modes. Furthermore, the author played a key role in the review and editing process of the thesis, ensuring its clarity and accuracy.

The co-authors of this article collaborated effectively in various aspects of the research. They contributed to the conceptualization of the study, the investigation of the imaging modes, and the development of the methodology. They were also involved in creating the software and visualizing the results. Additionally, the co-authors took part in writing, reviewing, and editing the article, ensuring its coherence and quality. They provided valuable resources and expertise for the research, as well as supervision and guidance throughout the entire process.

Abstract

Two ultra-high-resolution (UHR) imaging modes, each with two energy thresholds, were implemented on a research, whole-body photon-counting-detector (PCD) CT scanner, referred to as sharp and UHR, respectively. The UHR mode has a pixel size of 0.25 mm at iso-center for both energy thresholds, with a collimation of 32 $\times$ 0.25 mm. The sharp mode has a 0.25 mm pixel for the low-energy threshold and 0.5 mm for the high-energy threshold, with a collimation of 48 $\times$ 0.25 mm. Kidney stones with mixed mineral composition and lung nodules with different shapes were scanned using both modes, and with the standard imaging mode, referred to as macro mode (0.5 mm pixel and 32 $\times$ 0.5 mm collimation). Evaluation and comparison of the three modes focused on the ability to accurately delineate

anatomic structures using the high-spatial resolution capability and the ability to quantify stone composition using the multi-energy capability. The low-energy threshold images of the sharp and UHR modes showed better shape and texture information due to the achieved higher spatial resolution, although noise was also higher. No noticeable benefit was shown in multi-energy analysis using UHR compared to standard resolution (macro mode) when standard doses were used. This was due to excessive noise in the higher resolution images. However, UHR scans at higher dose showed improvement in multi-energy analysis over macro mode with regular dose. To fully take advantage of the higher spatial resolution in multi-energy analysis, either increased radiation dose, or application of noise reduction techniques, is needed.

Lung Nodule Volume Quantification and Shape Differentiation with an Ultra-High Resolution Technique on a Photon Counting Detector CT System

Wei Zhou, PhD,[1] Juan Montoya, BSc,[1] Ralf Gutjahr, MSc,[2,3] Andrea Ferrero, PhD,[1] Ahmed F. Halaweish, PhD,[4] Steffen Kappler, PhD,[3] Cynthia H. McCollough, PhD[1] and Shuai Leng, PhD[1]

[1]Department of Radiology, Mayo Clinic, Rochester, MN
[2]Computer Aided Medical Procedures (CAMP),Technical University of Munich, Munich, Germany
[3]Siemens Healthcare GmbH, Forchheim, Germany
[4]Siemens Healthcare–Imaging and Therapy Systems, Malvern, PA

Copyright statement

Contributions

The author of this thesis contributed to the study by developing the methodology for applying an ultra high-resolution (UHR) mode on a whole-body PCD CT system and comparing it to the conventional (macro) mode. He also reviewed the manuscript.

The co-authors of this article played a pivotal role in the project by leading the conceptualization of the research idea, participating in the investigation, and refining the methodology. They contributed to software development, visualization creation, and writing the manuscript, while also reviewing and editing the content. The co-authors provided necessary resources and supervision throughout the project.

Abstract

A new ultra high-resolution (UHR) mode has been implemented on a whole body photon counting-detector (PCD) CT system. The UHR mode has a pixel size of 0.25 mm by 0.25 mm at the iso-center, while the conventional (macro) mode is limited to 0.5 mm by 0.5 mm. A set of synthetic lung nodules (two shapes, five sizes, and two radio-densities) was scanned using both the UHR and macro modes and reconstructed with 2 reconstruction kernels (4 sets of images in total). Linear regression analysis was performed to compare measured nodule volumes from CT images to reference volumes. Surface curvature was calculated for each nodule and the full width half maximum (FWHM) of the curvature histogram was used as a shape index to differentiate sphere and star shape nodules. Receiver operating characteristic (ROC) analysis was performed and area under the ROC curve (AUC) was used as a figure of merit for the differentiation task. Results showed strong linear relationship between measured nodule volume and reference standard for both UHR and macro mode. For all nodules, volume

estimation was more accurate using UHR mode with sharp kernel (S80f), with lower mean absolute percent error (MAPE) (6.5%) compared with macro mode (11.1% to 12.9%). The improvement of volume measurement from UHR mode was more evident particularly for small nodule size (3 mm, 5 mm), or star-shape nodules. Images from UHR mode with sharp kernel (S80f) consistently demonstrated the best performance (AUC = 0.85) when separating star from sphere shape nodules among all acquisition and reconstruction modes. Our results showed the advantages of UHR mode on a PCD CT scanner in lung nodule characterization. Various clinical applications, including quantitative imaging, can benefit substantially from this high resolution mode.

Multi-Material Decomposition of Iodine Mixed with Potential High-Z Contrast Agents in Energy Discriminating Photon Counting Computed Tomography

Ralf Gutjahr, MSc,[1,2] Bernhard Schmidt, PhD,[1] Martin Sedlmair, PhD,[1]
Thomas G. Flohr, PhD,[1] Hubertus Pietsch, MD,[3] Bernhard Krauss, PhD,[1] and
Tristan Nowak, PhD[1]

[1]Siemens Healthcare GmbH, Forchheim, Germany
[2]CAMP, Technical University of Munich, Garching (Munich), Germany
[3]Bayer HealthCare Pharmaceuticals, Berlin, Germany

Copyright statement

Contributions

The thesis author made his contributions to this article by conceptualizing the research idea to evaluate the quality of a quantitative image-based multi-material decomposition algorithm for potential CT contrast agents using Photon Counting Detector CT technology. He developed the methodology, created the necessary software to process the acquired CT images, generated visualizations, and wrote the manuscript, which detailed the results of the material decomposition process.

The co-authors of this article collaborated in different capacities, including assisting in conceptualization, participating in the investigation process, reviewing the methodology, editing the manuscript, providing resources, and offering supervision.

Abstract

Purpose: To evaluate the quality of a quantitative image-based multi-material decomposition algorithm on mixtures of potential CT contrast agents (CA) for Photon Counting Detector CT (PCD-CT) technology.

Method and materials: CT-images were obtained using a PCD-CT research scanner (SOMATOM CounT, Siemens Healthcare GmbH, Forchheim). Three tube voltages were applied: 100, 120, and 140 kV using 160, 120, and 80 mAs, respectively. All CT images were acquired using four energy thresholds: 25, 45, 65, and 80 keV. Three mixtures of aqueous solutions of iodine and a high-Z CA, either Gadolinium (Gd), Hafnium (Hf) or Tungsten (W), were investigated. They were placed into vials arranged around the center of a cylindrical 20 cm wide water-equivalent phantom. Both a two and a three material decomposition, including water as a third base material, were applied to the reconstructed energy threshold images.

Identical measurements were repeated 15 times to determine average concentrations and the systematic deviation. The statistical errors were assessed by the evaluation of the dose normalized standard deviations of the measured concentrations.

Results: When decomposing into two base materials the measured concentrations deviated from the known values from -0.5 mg/mL to 0.5 mg/mL. The overall best performance was observed for the differentiation of I and Hf using the 140 kV x-ray spectrum and the given energy thresholds (0.1 mg/mL and 0.0 mg/mL deviation for I and Hf, respectively). By adding water as a third base material, the systematic deviations increased to a range from -2.7 mg/mL to 1.8 mg/mL. Separation into I, water and either Gd or Hf provided more accurate results due to their better energy separation when compared to I, water and W, where especially water and W showed similar attenuation over all selected energies.

Conclusion: For the selected x-ray spectra and energy thresholds, the two-material decompositions provided good results with absolute deviations from the known concentrations under 0.5 mg/mL. By adding water as a third base material the accuracy of the decomposition decreased, especially with tungsten at 100 kV due to its similar spectral characteristics to water at this configuration.

Clinical relevance/application: To separate and quantify mixed CA solutions using image data from a single PCD-CT scan

Detection and characterization of urinary stones using photon-counting-detector CT in a clinical setting

Roy P. Marcus, MD,[1] Joel G. Fletcher, MD,[1] Andrea Ferrero, PhD,[1] Shuai Leng, PhD,[1] Ahmed F. Halaweish, PhD,[3] Ralf Gutjahr, MSc,[4,5] Terri J. Vrtiska, MD,[1] Mike L. Wells, MD,[1] Felicity T. Enders, PhD,[2] and Cynthia H. McCollough, PhD[1]

[1]Department of Radiology, Mayo Clinic, Rochester, MN
[2]Department of Biomedical Statistics and Informatics, Mayo Clinic, Rochester, MN
[3]Siemens Healthcare–Imaging and Therapy Systems, Malvern, PA
[4]Siemens Healthcare, Forchheim, Germany
[5]Computer Aided Medical Procedures (CAMP), Technical University of Munich, Munich, Germany

Copyright statement

Contributions

The author of the thesis contributed to this article by developing the software used in the study to analyze whole-body photon-counting-detector (PCD) CT data and compare it to 2nd generation dual-source (DS) dual energy (DE) imaging. He participated in the review process, ensuring the accuracy and relevance of the findings.

The co-authors of the article made substantial contributions in several areas, such as conceptualizing the research idea to investigate the potential of whole-body PCD-CT data, guiding the investigation process, developing the methodology, creating the software, generating visualizations, writing the manuscript, reviewing the findings, editing the content, providing resources, and offering supervision.

Abstract

Purpose: To compare a research photon-counting–detector (PCD) CT scanner to a dual-source, dual-energy CT scanner for the detection and characterization of renal stones in human participants with known stones.

Materials and Methods: Thirty study participants (median age, 61 years; 10 women) underwent a clinical renal stone characterization scan by using dual-energy CT and a subsequent research PCD CT scan by using the same radiation dose (as represented by volumetric CT dose index). Two radiologists were tasked with detection of stones, which were later characterized as uric acid or non–uric acid by using a commercial dual-energy CT analysis package. Stone size and contrast-to-noise ratio were additionally calculated. McNemar odds ratios and Cohen k were calculated separately for all stones and small stones ($\leq$3 mm).

Results: One-hundred sixty renal stones (91 stones that were $\leq$ 3 mm in axial length) were visually detected. Compared with 1-mm-thick routine images from dual-energy CT, the odds of detecting a stone at PCD CT were 1.29 (95% confidence interval: 0.48, 3.45) for all stones. Stone segmentation and characterization were successful at PCD CT in 70.0% (112 of 160) of stones versus 54.4% (87 of 160) at dual-energy CT, and was superior for stones 3 mm or smaller at PCD CT (45 vs 25 stones, respectively; P = .002). Stone characterization agreement between scanners for stones of all sizes was substantial (k = 0.65).

Conclusion: Photon-counting–detector CT is similar to dual-energy CT for helping to detect renal stones and is better able to help characterize small renal stones.

Bildbasierte Multimaterialzerlegung – Neue Kontrastmittel für die Spektrale Computertomographie

Ralf Gutjahr, MSc,[1,2] Bernhard Schmidt, PhD,[1] Martin Sedlmair, PhD,[1]
Thomas G. Flohr, PhD,[1] Hubertus Pietsch, MD,[3] Gregor Jost, PhD,[3] and
Bernhard Krauss, PhD[1]

[1]Siemens Healthcare GmbH, Forchheim, Germany
[2]CAMP, Technical University of Munich, Garching (Munich), Germany
[3]Bayer HealthCare Pharmaceuticals, Berlin, Germany

Copyright statement

Contributions

In this article, the thesis author played a significant role in conceptualizing the research focused on exploring multi-material decomposition in sets of different contrast agents using a photon counting detector CT scanner. He developed the methodology, created software to process and evaluate the acquired energy-selective CT data, generated visualizations, and wrote the manuscript, which presented the results of the contrast agent differentiation and quantification process and the accuracy of the measured concentrations.

The co-authors of this article collaborated in various ways, including providing assistance in conceptualization, participating in the investigation process, reviewing the methodology, editing the manuscript, offering resources, and providing supervision.

Abstract

Methoden: In dieser Phantomstudie wurden Kombinationen von sechs der folgenden Kontrastmitteln (KM) mit Konzentrationen von 5 und 10 mg/mL untersucht: Zirkonium (Zr), Iod (I), Gadolinium (Gd), Dysprosium (Dy), Hafnium (Hf) und Wolfram (T). Die K-Kanten der Materialien liegen alle im spektralen Bereich typischer Röntgenspektren der Computertomographie. Multienergetische CT-Bilddaten aus acht verschiedenen Gruppen von je drei KMs wurden mit Hilfe eines Photon Counting Detektor CT-scanners (SOMATOM CounT, Siemens Healthcare GmbH, Forchheim) erzeugt (100, 120 und 140 kV). Quantitative Materialbilder wurden auf der Basis von rekonstruierten Energie-Schwellenbildern erstellt. Die Genauigkeit dieser Ergebnisse basieren auf dem Vergleich von gemessenen und bekannten lokalen Konzentrationen.

Ergebnisse: Die Kontrastmittel konnten in allen untersuchten Fällen unterschieden und quantifiziert werden. Die mittlere Abweichung der gemessenen Konzentrationen von den bekannten Konzentrationen beträgt 8% für 100 kV Messungen, 3% für 120 kV Messungen und 9% für 140 kV Messungen. Die zwei verschiedenen untersuchten Konzentrationen skalierten sich linear mit den ermittelten CT-Werten. Die Unterscheidung einzelner KMs mit ähnlichen

Massenschwächungskoeffizienten zeigten größere Abweichungen in den errechneten Konzentrationen. (bis zu -34% für die Zerlegung von I, Hf und W bei 120 kV).

Diskussion: Eine bildbasierte Multimaterialzerlegung wurde auf sets von verschiedenen Kontrastmitteln angewandt. Die verwendeten Bilddaten stammen von einem CT Scanner mit Photon Counting Detektoren. Die gemessenen Konzentrationen korrespondierten mit den bekannten Konzentrationen. Die Qualität der Ergebnisse ist abhängig von den gewählten Basismaterialien, der Anzahl der Materialien, des gewählten Röhrenspektrums und der selektierten Energieschwellen.

New Contrast Media for K-edge Imaging with Photon-Counting Detector CT

Gregor Jost, PhD,[1] Michael McDermott, MSc,[1,2] Ralf Gutjahr, MSc,[3] Tristan Nowak, PhD,[3] Bernhard Schmidt, PhD,[3] Hubertus Pietsch, MD,[3]

[1]Bayer HealthCare Pharmaceuticals, Berlin, Germany
[2]Department of Radiology and Nuclear Medicine, Maastricht University Medical Center, Maastricht, Netherlands
[3]Siemens Healthcare GmbH, Forchheim, Germany

Copyright statement

Contributions

The thesis author contributed significantly by investigating the potential of high atomic number elements in innovative contrast media concepts for photon-counting detector CT (PCD-CT). He designed the methodology to assess the impact of these contrast media for the use of virtual monoenergetic imaging. The author developed software and visualizations to illustrate the results and participated in writing and reviewing the manuscript, ensuring accuracy and relevance.

The co-authors collaborated on various aspects, including the conceptualization of the research idea, participating in the investigation process, and reviewing the methodology. They contributed to software development, visualization creation, and writing the manuscript, while also editing the content. The co-authors offered resources and supervision.

Abstract

The recent technological developments in photon-counting detector CT (PCD-CT) and the introduction of the first commercially available clinical PCD-CT unit opens up new exciting opportunities for contrast media research. With PCD-CT the efficacy of available iodine-based contrast media improves, allowing for a reduction of iodine dosage or, on the other hand, an improvement of image quality in low contrast indications. Virtual monoenergetic image (VMI) reconstructions are routinely available and enable the VMI energy to be adapted to the diagnostic task.

A key property of PCD-CT is the ability for spectral separation in combination with improved material decomposition. Thus, the discrimination of contrast media from intrinsic or pathological tissues and the discrimination of two or more contrasting elements that characterize different tissues, are attractive fields for contrast media research. For these approaches, K-edge

imaging in combination with high atomic number elements such as the lanthanides, tungsten, tantalum, or bismuth plays a central role.

The purpose of this study is to present an overview of innovative contrast media concepts that utilize high atomic number elements. The emphasis is on improving contrast enhancement for cardiovascular plaque imaging, stent visualization, and exploring new approaches using two contrasting elements. Along with the published research, new experimental findings with a contrast medium that incorporates tungsten are included.

Both the literature review and the new experimental data demonstrate the great potential and feasibility for new contrast media to significantly increase diagnostic performance and to enable new clinical fields and indications in combination with PCD-CT.

Virtual monoenergetic imaging in photon-counting CT of the head and neck

Faraz Farhadi, PhD,[1] Pooyan Sahbaee, PhD,[2] Jayasai R. Rajagopal, PhD,[1,3]
Moozhan Nikpanah, PhD,[1] Babak Saboury, PhD,[1] Ralf Gutjahr, MSc,[4]
Nadia M. Biassou, PhD,[1] Ritu Shah, PhD,[1] Thomas G. Flohr, PhD,[4] Ehsan Samei, PhD,[3]
William F. Pritchard, PhD,[1,5] Ashkan A. Malayeria, PhD,[1]
David A. Bluemke, MD, PhD MsB,[6] Elizabeth C. Jones, MD, MPH, MBA,[1]

[1]Radiology and Imaging Sciences, Clinical Center, National Institutes of Health, Bethesda, MD, USA
[2]Siemens Medical Solutions USA, Malvern, PA, USA
[3]Carl E. Ravin Advanced Imaging Laboratories, Department of Radiology, Duke University Medical Center, Durham, NC, USA
[4]Siemens Healthcare GmbH, Forchheim, Germany
[5]Center for Interventional Oncology, Radiology and Imaging Sciences, Clinical Center, National Institutes of Health, Bethesda, MD, USA
[6]Department of Radiology, University of Wisconsin, Madison, WI, USA

Copyright statement

Contributions

The thesis author contributed effectively to the study, participating in its conceptualization and investigation. He supported the design of the methodology and data analysis. He also played a key role in providing calibration and configuration of the evaluation software used.

The article's co-authors took a proactive role in conceptualizing and conducting the study. They also played an essential part in creating visual representations of the research results. Throughout the manuscript's creation, they were integral in drafting, revising, and fine-tuning the content. By providing essential resources and guidance, the co-authors ensured robust support and supervision.

Abstract

Purpose: Advantages of virtual monoenergetic images (VMI) have been reported for dual energy CT of the head and neck, and more recently VMIs derived from photon-counting (PCCT) angiography of the head and neck. We report image quality metrics of VMI in a PCCT angiography dataset, expanding the anatomical regions evaluated and extending observer-based qualitative methods further than previously reported.

Methods: In a prospective study, asymptomatic subjects underwent contrast enhanced PCCT of the head and neck using an investigational scanner. Image sets of low, high, and full spectrum

(Threshold-1) energies; linear mix of low and high energies (Mix); and 23 VMIs (40–150 keV, 5 keV increments) were generated. In 8 anatomical locations, SNR and radiologists' preferences for VMI energy levels were measured using a forced-choice rank method (4 observers) and ratings of image quality using visual grading characteristic (VGC) analysis (2 observers) comparing VMI to Mix and Threshold-1 images.

Results: Fifteen subjects were included (7 men, 8 women, mean 57 years, range 46–75). Among all VMIs, SNRs varied by anatomic location. The highest SNRs were observed in VMIs. Radiologists preferred 50–60 keV VMIs for vascular structures and 75–85 keV for all other structures. Cumulative ratings of image quality averaged across all locations were higher for VMIs with areas under the curve of VMI vs Mix and VMI vs Threshold-1 of 0.67 and 0.68 for the first reader and 0.72 and 0.76 for the second, respectively.

Conclusion: Preferred keV level and quality ratings of VMI compared to mixed and Threshold-1 images varied by anatomical location.

C

Full list of authored and co-authored publications

2023

[233] M. Patwari, A. F. Calvarons, **R. Gutjahr**, R. Marcus, Y. Thali, R. Raupach, and A. Maier. “Reducing the risk of hallucinations with interpretable deep learning models for low-dose CT denoising: comparative performance analysis”. In: *Physics in Medicine and Biology* (2023)

[71] F. Farhadi, P. Sahbaee, J. R. Rajagopal, M. Nikpanah, B. Saboury, **R. Gutjahr**, N. M. Biassou, R. Shah, T. G. Flohr, E. Samei, W. F. Pritchard, A. A. Malayeria, D. A. Bluemke, and E. C. Jones. “Virtual monoenergetic imaging in photon-counting CT of the head and neck”. In: *Clinical Imaging* (2023)

[150] G. Jost, M. McDermott, **R. Gutjahr**, T. Nowak, B. Schmidt, and H. Pietsch. “New Contrast Media for K-edge Imaging with Photon-Counting Detector CT”. In: *Investigative Radiology - Special issue 2023 - Photon counting CT* (2023)

[348] M. T. Winkelmann, F. Hagen, L. Le-Yannou, J. Weiss, P. Riffel, **R. Gutjahr**, S. Faby, K. Nikolaou, and M. Horger. “Myeloma bone disease imaging on a 1st-generation clinical photon-counting detector CT vs. 2nd-generation dual-source dual-energy CT”. In: *European Radiology* (2023).

2022

[121] F. Hagen, L. Walder, J. Fritz, **R. Gutjahr**, B. Schmidt, S. Faby, F. Bamberg, S. Schoenberg, K.Nikolaou, and M. Horger. “Image Quality and Radiation Dose of Contrast-Enhanced Chest-CT Acquired on a Clinical Photon-Counting Detector CT vs. Second-Generation Dual-Source CT in an Oncologic Cohort: Preliminary Results”. In: *Tomography* 8.3 (2022).

[349] R. Wrazidlo, L. Walder, A. Estler, **R. Gutjahr**, B. Schmidt, S. Faby, J. Fritz, K. Nikolaou, M. Horger, and F. Hagen. “Radiation dose reduction in contrast-enhanced abdominal CT: comparison of photon-counting detector CT with 2nd generation dual-source dual-energy CT in an oncologic cohort”. In: *Academic Radiology* (2022) (cit. on p. 12).

[120] F. Hagen, J. Hofmann, R. Wrazidlo, **R. Gutjahr**, B. Schmidt, S. Faby, K. Nikolaou, and M. Horger. “Image quality and dose exposure of contrast-enhanced abdominal CT on a 1st generation clinical dual-source photon-counting detector CT in obese patients vs. a 2nd generation dual-source dual energy integrating detector CT”. In: *European Journal of Radiology* 151 (2022).

[317] M. Sühling, S. Großkopf, **R. Gutjahr**, M. Schöbinger, C. Schwemmer, A. Wimmer, and T. Flohr. “Artificial Intelligence Integration into the Computed Tomography System”. In: *Artificial Intelligence in Cardiothoracic Imaging*. Ed. by C. N. De Cecco, M. van Assen, and T. Leiner. Cham: Springer International Publishing (2022).

[235] M. Patwari, **R. Gutjahr**, R. Raupach, and A. Maier. “Limited parameter denoising for low-dose X-ray computed tomography using deep reinforcement learning”. In: *Medical Physics* (2022).

[77] A. M. Fischer, J. A. Decker, J. Schoepf, A. Varga-Szemes, T. Flohr, B. Schmidt, **R. Gutjahr**, P. Sahbaee, D. A. Giovagnoli, T. Emrich, et al. “Optimization of contrast material administration for coronary CT angiography using a software-based test-bolus evaluation algorithm”. In: *The British Journal of Radiology* 95.1133 (2022).

[354] J. Yu, S. Lin, H. Lu, R. Wang, J. Liu, **R. Gutjahr**, and J. Gao. “Optimize scan timing in abdominal multiphase CT: Bolus tracking with an individualized post-trigger delay”. In: *European Journal of Radiology* 148 (2022).

2021

---

[280] T. Sartoretti, M. Eberhard, T. Nowak, **R. Gutjahr**, G. Jost, H. Pietsch, B. Schmidt, T. Flohr, H. Alkadhi, and A. Euler. “Photon-counting multienergy computed tomography with spectrally optimized contrast media for plaque removal and stenosis assessment”. In: Investigative Radiology 56.9 (2021).

[67] A. Euler, T. Taslimi, M. Eberhard, A. Kobe, K. Reeve, A. Zimmermann, A. Krauss, **R. Gutjahr**, B. Schmidt, and H. Alkadhi. “Computed Tomography Angiography of the Aorta—Optimization of Automatic Tube Voltage Selection Settings to Reduce Radiation Dose or Contrast Medium in a Prospective Randomized Trial”. In: *Investigative Radiology* 56.5 (2021).

2020

[107] **R. Gutjahr**, R. C. Bakker, F. Tiessens, S. A. van Nimwegen, B. Schmidt, and J. F. W. Nijsen. “Quantitative dual-energy CT material decomposition of holmium microspheres: local concentration determination evaluated in phantoms and a rabbit tumor model”. In: European Radiology (2020).

[236] M. Patwari, **R. Gutjahr**, R. Raupach, and A. Maier. "Low Dose CT Denoising via Joint Bilateral Filtering and Intelligent Parameter Optimization". In: *International Conference on Image Formation in X-Ray Computed Tomography* (2020).

2019

[108] **R. Gutjahr**, J. G. Fletcher, Y. S. Lee, A. F. Halaweish, V. Suresh, N. M. Weber, T. J. Vrtiska, E. E. Williamson, B. Schmidt, and C. H. McCollough. “Individualized Delay for Abdominal Computed Tomography Angiography Bolus-Tracking Based on Sequential Monitoring: Increased Aortic Contrast Permits Decreased Injection Rate and Lower Iodine Dose”. In: *Journal of Computer Assisted Tomography* 43.4 (2019).

[130] R. Hinzpeter, M. Eberhard, **R. Gutjahr**, K. Reeve, T. Pfammatter, M. Lachat, B. Schmidt, T. G. Flohr, B. Kolb, and H. Alkadhi. “CT Angiography of the Aorta: Contrast Timing by Using a Fixed versus a Patient-specific Trigger Delay”. In: *Radiology* 291.2 (2019).

2018

[195] R. P. Marcus, J. G. Fletcher, A. Ferrero, S. Leng, A. F. Halaweish, **R. Gutjahr**, T. J. Vrtiska, M. L. Wells, F. T. Enders, and C. H. McCollough. “Detection and Characterization of Renal Stones by Using Photon-Counting–based CT”. In: *Radiology* 289.2 (2018).

[74] A. Ferrero, **R. Gutjahr**, A. F. Halaweish, S. Leng, and C. H. McCollough. “Characterization of Urinary Stone Composition by Use of Whole-body, Photon-counting Detector CT”. In: *Academic Radiology* 25.10 (Oct. 2018).

2017

[370] W. Zhou, J. Montoya, **R. Gutjahr**, A. Ferrero, A. Halaweish, S. Kappler, C. McCollough, and S. Leng. “Lung nodule volume quantification and shape differentiation with an ultra-high resolution technique on a photon counting detector CT system”. In: *Society of Photo-Optical Instrumentation Engineers (SPIE) Medial Imaging Proceedings* (2017).

[113] **R. Gutjahr**, C. Polster, A. Henning, S. Kappler, S. Leng, C. H. McCollough, M. U. Sedlmair, B. Schmidt, B. Krauss, and T. G. Flohr. “Dual energy CT kidney stone differentiation in photon counting computed tomography”. In: *Society of Photo-Optical Instrumentation Engineers (SPIE) Medial Imaging Proceedings* (2017).

[75] A. Ferrero, **R. Gutjahr**, A. Henning, S. Kappler, A. Halaweish, D. Abdurakhimova, Z. Peterson, J. Montoya, S. Leng, and C. McCollough. “Renal stone characterization using high resolution imaging mode on a photon counting detector CT system”. In: *Society of Photo-Optical Instrumentation Engineers (SPIE) Medial Imaging Proceedings* (2017).

[246] C. Polster, **R. Gutjahr**, M. Berner, T. Flohr, M. Hertel, S. Kappler, K. Stierstorfer, and O. Dietrich. “Improving material separation of high-flux whole-body photon counting computed tomography by K-edge pre-filtration”. In: *Society of Photo-Optical Instrumentation Engineers (SPIE) Medial Imaging Proceedings* (2017).

[184] S. Leng, **R. Gutjahr**, A. Ferrero, S. Kappler, A. Henning, A. Halaweish, W. Zhou, J. Montoya, and C. McCollough. “Ultra-high spatial resolution multi-energy CT using photon counting detector technology”. In: *Society of Photo-Optical Instrumentation Engineers (SPIE) Medial Imaging Proceedings* (2017).

2016

[114] **R. Gutjahr**, C. Polster, S. Kappler, H. Pietsch, G. Jost, K Hahn, F Schöck, M. Sedlmair, T. Allmendinger, B. Schmidt, et al. “Material decomposition and virtual non-contrast imaging in photon counting computed tomography: an animal study”. In: *Society of Photo-Optical Instrumentation Engineers (SPIE) Medial Imaging Proceedings* (2016).

[359] Z. Yu, S. Leng, S. M. Jorgensen, Z. Li, **R. Gutjahr**, B. Chen, A. F. Halaweish, S. Kappler, L. Yu, E. L. Ritman, et al. “Evaluation of conventional imaging performance in a research whole-body CT system with a photon-counting detector array”. In: *Physics in Medicine and Biology* 61.4 (2016).

[111] **R. Gutjahr**, A. F. Halaweish, Z. Yu, S. Leng, L. Yu, Z. Li, S. M. Jorgensen, E. L. Ritman, S. Kappler, and C. H. McCollough. “Human Imaging With Photon Counting–Based Computed Tomography at Clinical Dose Levels: Contrast-to-Noise Ratio and Cadaver Studies”. In: *Investigative Radiology* 51.7 (2016).

2015

[357] Z. Yu, S. Leng, S. M. Jorgensen, Z. Li, **R. Gutjahr**, B. Chen, X. Duan, A. Halaweish, L. Yu, E. L. Ritman, and C. McCollough. “Initial results from a prototype whole-body photon-counting computed tomography system”. In: In: *Society of Photo-Optical Instrumentation Engineers (SPIE) Medial Imaging Proceedings* (2015).

Full list of conference posters and presentations

D

2021

[220] H. Naderi Boldaji, M. Patwari, M. Reymann, **R. Gutjahr**, R. Raupach, and A. Maier. “Deep Learning based Model Observers for Multi - Modal Imaging”. In: *16th International Meeting on Fully Three- Dimensional Image Reconstruction in Radiology and Nuclear Medicine* (Leuven, Belgium). July 19–23, 2021.

[234] M. Patwari, **R. Gutjahr**, R. Raupach, and A. Maier. “JBFnet: Low dose CT denoising by trainable joint bilateral filtering”. In: *Bildverarbeitung für die Medizin*. 2021.

2020

[331] T. Nowak, B. Schmidt, **R. Gutjahr**, T. Flohr. "Virtual removal of calcified vascular plaques using multi-energy photon counting CT". In: *Radiological Society of North America. 104th Scientific Assembly and Annual Meeting* (Chicago IL, USA, Nov. 29–Dec. 5, 2020).

[236] M. Patwari, **R. Gutjahr**, R. Raupach, A. Maier. "Low Dose CT Denoising with Joint Bilateral Filtering and Intelligent Parameter Optimization" *CT Meeting*

[232] M. Patwari, **R. Gutjahr**, R. Raupach, A. Maier. “Low dose CT denoising with residual convolutional networks and deep learned perceptual loss”. In: *European Congress of Radiology - ECR* 2020.

[231] M. Patwari, **R. Gutjahr**, R. Raupach, and A. Maier. “Low dose CT denoising with residual convolutional networks and deep learned perceptual loss”. In: *European Congress of Radiology - ECR* 2020.

2019

[237] M. Patwari, **R Gutjahr**, R. Raupach, and A. Maier. “Measuring CT Reconstruction Quality with Deep Convolutional Networks”. In: *Machine Learning for Medical Image Reconstruction* (Shenzhen, China). Oct. 17–17, 2019.

[110] **R. Gutjahr**, A. Halaweish, J. Fletcher, I Duba, Y. Lee, N. Weber, T. Vrtiska, E Williamson, C. McCollough, et al. “Individualised delay based on sequential monitoring: increased aortic contrast permits decreased injection rate and lower iodine dose at abdominal CT angiography”. In: *European Congress of Radiology - ECR* 2019.

2018

[292] F. Schwarz, J.C. Ramirez-Giraldo, **R. Gutjahr**, D.Boll, L.M. Hurwitz. "Real-Time Patient Specific Scan Initiation for Pulmonary Embolism CTA: Impact on Image Quality". In: *Radiological Society of North America. 104th Scientific Assembly and Annual Meeting* (Chicago IL, USA, Nov. 25–30, 2018).

[117] **R Gutjahr**, B. Schmidt, M. Sedlmair, T. Flohr, H. Pietsch, B. Krauss, and T. Nowak. “Bildbasierte Multimaterialzerlegung – Neue Kontrastmittel für die Spektrale Computertomographie”. In: *49. Jahrestagung der Deutschen Gesellschaft für Medizinische Physik*, Nuremberg, Germany, Sept. 19–21, 2018.

2017

[116] **R Gutjahr**, B. Schmidt, M. Sedlmair, T. Flohr, H. Pietsch, B. Krauss, and T. Nowak. “Applied quantitative multi-material decomposition using Photon Counting Detector CT (PCD-CT) image data”. In: *Radiological Society of North America. 101st Scientific Assembly and Annual Meeting* (Chicago IL, USA, Nov. 26–Dec. 1, 2017).

[285] B. Schmidt, K. Grant, T. Allmendinger, **R Gutjahr**, C. McCollough, T. Flohr, and B. Krauss. “Impact of low tube voltage (kVp) selection on spectral data-based coronary CTA calcium plaque removal for Photon Counting Detector CT (PCD-CT)”. In: *Radiological Society of North America. 101st Scientific Assembly and Annual Meeting* (Chicago IL, USA, Nov. 26–Dec. 1, 2017).

[118] **R Gutjahr**, B. Schmidt, M. Sedlmair, T. Flohr, H. Pietsch, B. Krauss, and T. Nowak. "Multi-Material Decomposition of Iodine Mixed with Potential High-Z Contrast Agents in Energy Discriminating Photon Counting Computed Tomography". In: *Radiological Society of North America. 101st Scientific Assembly and Annual Meeting* (Chicago IL, USA, Nov. 26–Dec. 1, 2017).

[122] A. Halaweish, S. Leng, B. Krauss, M. Sedlmair, T. Nowak, **R Gutjahr**, S. Kappler, B. Schmidt, E. L. Ritman, and C. McCollough. "Quantitative Multi-energy Post-processing of Whole-Body Photon-Counting Computed Tomography Data". In: *4th Workshop on Medical Applications of Spectroscopic X-ray Detectors* (CERN, Geneva, Swiss, May 15–15, 2016).

[248] C. Polster, **R Gutjahr**, M. Berner, T. Flohr, M. Hertel, S. Kappler, K. Stiersorfer, and O. Dietrich. "High-flux whole-body photon-counting computed tomography: Improving material separation by hafnium pre-filtration". In: *4th Workshop on Medical Applications of Spectroscopic X-ray Detectors* (CERN, Geneva, Swiss, May 15–15, 2016).

[112] **R Gutjahr**, T. Nowak, M. Sedlmair, H. Pietsch, B. Schmidt, T. Flohr, and B. Krauss. "Image-Based Multi-Material Decomposition in Photon Counting Computed Tomography". In: *European Congress of Radiology - ECR*. 2017

[113] **R Gutjahr**, C. Polster, A. Henning, S. Kappler, S. Leng, C. H. McCollough, M. U. Sedlmair, B. Schmidt, B. Krauss, and T. G. Flohr. "Dual energy CT kidney stone differentiation in photon counting computed tomography". In: *SPIE Medical Imaging*. SPIE, 2017

2016

[106] **R. Gutjahr**. "Technical performance of the macro mode in photon counting detector CT". In: *2nd Photon Counting Symposium* (Mayo Clinic, Rochester, Minnesota, USA, Oct. 6–7, 2016). 2016

[123] A. Halaweish, R. Marcus, S. Leng, B. Krauss, M. Sedlmair, T. Allmendinger, **R Gutjahr**, S. Kappler, B. Schmidt, E. L. Ritman, and C. McCollough. "Advanced Spectral Analysis of Whole-Body Photon- Counting-Detector Computed Tomography Data". In: *Radiological Society of North America. 101st Scientific Assembly and Annual Meeting* (Chicago IL, USA, Nov. 27–Dec. 2, 2016).

[250] C. Polster, K. Hahn, **R Gutjahr**, F. Schoeck, S. Kappler, K. Stiersorfer, O. Dietrich, and T. Flohr. "Improving material decomposition by spectral optimization of photon counting computed tomography". In: *SPIE Medical Imaging* (Orlando, Florida, USA, Mar. 2–6, 2016).

[115] **R Gutjahr**, C. Polster, S. Kappler, H. Pietsch, G. Jost, K. Hahn, F. Schoeck, M. Sedlmair, T. Allmendinger, B. Schmidt, B. Krauss, and T. Flohr. “Material Decomposition and virtual noncontrast imaging in photon counting computed tomography: an animal study”. In: *SPIE Medical Imaging* (Orlando, Florida, USA, Mar. 2–6, 2016).

[119] **R Gutjahr**, B. Schmidt, M. Sedlmair, S. Kappler, C. Polster, T. Allmendinger, T. Flohr, and B. Krauss. “Kidney stone differentiation in photon counting computed tomography: a feasibility study”. In: *European Congress of Radiology* (Vienna, Austria, Mar. 2–6, 2016).

2015

---

[357] Z. Yu, S. Leng, S. M. Jorgensen, Z. Li, **R Gutjahr**, B. Chen, X. Duan, A. Halaweish, L. Yu, E. L. Ritman, and C. McCollough. “Initial results from a prototype whole-body photon-counting computed tomography system”. In: *SPIE Medical Imaging* (San Diego, California, USA, Feb. 21–26, 2015).

[109] **R. Gutjahr**, A. Halaweish, K. Grant, S. Kappler, Z. Yu, S. Leng, L. Yu, Z. Li, S. M. Jorgensen, E. L. Ritman, C. H. McCollough. "Dose Efficiency of a Prototype, Whole-body, Photon-Counting CT system versus a Conventional CT System for Imaging of Iodinated Contrast Media" *Radiological Society of North America Annual Meeting 2015*.

[200] C. H. McCollough, S. Leng, **R. Gutjahr**, Z. Yu, Z. Li, A. Halaweish, S. M. Jorgensen, E. L. Ritman, S. Kappler. "Whole-body Human Imaging with Photon-counting-based CT at Clinically Relevant Doses" *Radiological Society of North America Annual Meeting 2015*.